

PLASMA CHARACTERIZATIONS OF AN ELECTRON CYCLOTRON  
RESONANCE MICROWAVE PLASMA PROCESSING REACTOR

by

*Paul Kevin Shufflebotham*

A Thesis  
Submitted to the Faculty of Graduate Studies  
in Partial Fulfillment of the Requirements  
for the Degree of

DOCTOR OF PHILOSOPHY

Department of Electrical and Computer Engineering  
University of Manitoba  
Winnipeg, Manitoba, Canada

© Copyright 1990 by Paul Kevin Shufflebotham

July 1990



National Library  
of Canada

Bibliothèque nationale  
du Canada

Canadian Theses Service    Service des thèses canadiennes

Ottawa, Canada  
K1A 0N4

The author has granted an irrevocable non-exclusive licence allowing the National Library of Canada to reproduce, loan, distribute or sell copies of his/her thesis by any means and in any form or format, making this thesis available to interested persons.

The author retains ownership of the copyright in his/her thesis. Neither the thesis nor substantial extracts from it may be printed or otherwise reproduced without his/her permission.

L'auteur a accordé une licence irrévocable et non exclusive permettant à la Bibliothèque nationale du Canada de reproduire, prêter, distribuer ou vendre des copies de sa thèse de quelque manière et sous quelque forme que ce soit pour mettre des exemplaires de cette thèse à la disposition des personnes intéressées.

L'auteur conserve la propriété du droit d'auteur qui protège sa thèse. Ni la thèse ni des extraits substantiels de celle-ci ne doivent être imprimés ou autrement reproduits sans son autorisation.

ISBN 0-315-71938-9

Canada

PLASMA CHARACTERIZATIONS OF AN ELECTRON CYCLOTRON  
RESONANCE MICROWAVE PLASMA PROCESSING REACTOR

BY

PAUL KEVIN SHUFFLEBOTHAM

A thesis submitted to the Faculty of Graduate Studies of  
the University of Manitoba in partial fulfillment of the requirements  
of the degree of

DOCTOR OF PHILOSOPHY

© 1990

Permission has been granted to the LIBRARY OF THE UNIVER-  
SITY OF MANITOBA to lend or sell copies of this thesis, to  
the NATIONAL LIBRARY OF CANADA to microfilm this  
thesis and to lend or sell copies of the film, and UNIVERSITY  
MICROFILMS to publish an abstract of this thesis.

The author reserves other publication rights, and neither the  
thesis nor extensive extracts from it may be printed or other-  
wise reproduced without the author's written permission.

## Abstract

This thesis presents a plasma-physical characterisation of an electron cyclotron resonance (ECR) microwave plasma processing reactor. These experiments are intended to provide an empirical connection between the reactor and the plasma as well as the phenomenological roots of a model of reactor-plasma interactions. First, a brief presentation of pertinent background materials and a critical review of the literature concerning plasma characterisations of divergent magnetic field ECR reactors is given. It is concluded that the current understanding of these systems is poor, and that extensive experimentation is required before useful models can be developed.

Several plasma diagnostics are first adapted for use in the ECR system. The stability of the plasma is characterised using visual inspection, reflected versus incident microwave power characteristics, and dynamic measurements of the microwave power or the floating voltage of a probe inserted into the plasma. It is shown that the plasmas occur in the form of stable, quiescent "plasma modes" characterised by unique shapes and power characteristics, and continuous dependences on system variables. Transitions between modes are noisy, discontinuous and often bistable. It is proposed that the plasma modes resulted from the mixing of electromagnetic waveguide modes due to changes in the refractive index of the plasma.

The above diagnostics are then used to select a stable operating regime of the divergent field ECR configuration for detailed characterisation. A computerised data acquisition and analysis system based on a cylindrical orbital-motion limited Langmuir probe is used to measure the axial variation of the plasma density, electron temperature, plasma potential and floating voltage as functions of microwave power, pressure and magnetic field strength. The density is observed to depend primarily on diffusion along the magnetic field away from a source region located at ECR. Increasing the power increases the density, and increasing the pressure reduces the axial diffusion length. The electron temperature shows a spike at ECR due to efficient heating inside the ECR zone, and inelastic collisional cooling outside. Increasing either the power or pressure decreases the temperature slightly. Varying the magnetic field strength simply shifted the electron temperature profile axially along with the location of the ECR zone. The density profile moved only partially since it also depended on the locations of the chamber walls. The potentials were shown to depend on the density and electron temperature.

## Acknowledgements

I wish to thank my advisor, Professor Howard Card, and co-advisor Professor Douglas Thomson, for their patience, encouragement and advice throughout the course of this work. I would particularly like to express my gratitude to Doug for taking over as my advisor during and after Howard's sabbatical leave at Oxford.

I would also like to thank my friends and colleagues for their support as well. In particular, Prof. Greg Bridges, Dr. Vic Herak, Dr. Gord McGonigal and (last but *certainly* not least) Dr. James Schellenberg are to be acknowledged for their many contributions in the form of technical assistance, lunchtime tutorials and a host of valuable discussions.

Financial assistance in the form of postgraduate scholarships from the Natural Sciences and Engineering Research Council of Canada (NSERC) and the University of Manitoba are gratefully acknowledged. NSERC is also acknowledged for their ongoing support of our plasma processing studies.

# Table of Contents

Abstract .....	ii
Acknowledgements .....	iii
Table of Contents .....	iv
<b>CHAPTER 1. INTRODUCTION .....</b>	<b>1</b>
1.1. PLASMA PROCESSING .....	1
1.2. MOTIVATIONS .....	2
1.3. OBJECTIVES .....	3
1.4. ORGANISATION .....	4
References .....	5
<b>CHAPTER 2. REVIEW OF ECR PROCESSING PLASMAS .....</b>	<b>7</b>
2.1. SOME BASIC PLASMA PHYSICS .....	7
2.1.1. Magnetised Microwave Plasmas .....	8
2.1.2. Wave Propagation: Unmagnetised Plasma .....	10
2.1.3. Wave Propagation: Magnetised Plasma .....	11
2.1.4. Boundaries: Diffusion .....	13
2.1.5. Boundaries: Sheaths .....	15
2.2. REACTOR DESIGNS .....	17
2.2.1. Divergent Field Reactors .....	18
2.2.2. Multipolar Reactors .....	19
2.3. PLASMA CHARACTERISATIONS .....	20
2.3.1. Global Parameters .....	21
2.3.2. Plasma Density .....	22
2.3.3. Electron Temperature .....	24
2.3.4. Potentials .....	25
2.3.5. Ion Energy .....	26
2.4. MODELLING ECR PROCESSING PLASMAS .....	27
References .....	31
<b>CHAPTER 3. EXPERIMENTAL APPARATUS AND METHODS .....</b>	<b>35</b>
3.1. VACUUM AND GAS-HANDLING SYSTEM .....	35
3.1.1. Apparatus .....	35

3.1.2. Gas Flow in Vacuum Systems .....	36
3.2. MICROWAVE CIRCUIT .....	37
3.2.1. Apparatus .....	37
3.2.2. Microwave Propagation in Rectangular Waveguides .....	39
3.3. PLASMA CHAMBER .....	40
3.4. LANGMUIR PROBE .....	43
3.4.1. Principles of Operation .....	43
3.4.2. OML Current Equations .....	45
3.4.3. Interpretation of the I-V Characteristic .....	47
3.4.4. Complicating Factors .....	48
3.4.5. Experimental Apparatus .....	49
References .....	51
<b>CHAPTER 4. BEHAVIOUR OF DOWNSTREAM PLASMAS IN A PE-CVD REACTOR .....</b>	<b>52</b>
4.1. EXPERIMENTAL .....	52
4.2. GLOBAL DIAGNOSTICS .....	53
4.3. DOWNSTREAM PLANE LANGMUIR PROBE .....	56
4.3.1. Current Equations .....	56
4.3.2. Interpretation of the I-V Characteristics .....	57
4.3.3. Measurements .....	58
4.4. DISCUSSIONS .....	60
4.4.1. Improvement of the Langmuir Probe Diagnostic .....	61
4.4.2. Global Diagnostics for Global Behaviours .....	62
4.4.3. On the Occurrence of ECR .....	63
References .....	63
<b>CHAPTER 5. DIAGNOSTICS FOR PLASMA STABILITY .....</b>	<b>65</b>
5.1. EXPERIMENTAL .....	65
5.2. RESULTS .....	66
5.3. DISCUSSIONS .....	71
5.3.1. On the Origin of Modes .....	73
References .....	76
<b>CHAPTER 6. PROBE CHARACTERISATION OF THE MAGNETIC BEACH CONFIGURATION .....</b>	<b>78</b>
6.1. EXPERIMENTAL .....	78
6.2. I-V CHARACTERISTICS .....	79
6.3. SPATIAL PROFILES .....	81

6.3.1. Plasma Density .....	81
6.3.2. Electron Temperature .....	84
6.3.3. Plasma and Floating Potentials .....	84
6.4. DISCUSSIONS .....	88
6.4.1. Plasma Generation, Transport and Loss .....	88
6.4.2. Plasma Heating and Cooling .....	90
6.4.3. Potentials .....	91
References .....	93
CHAPTER 7. CONCLUSIONS AND RECOMMENDATIONS .....	95
7.1. CONCERNING THE CHOICE OF GASES .....	95
7.2. CONCERNING THE USE OF LANGMUIR PROBES .....	96
7.3. CONCERNING PLASMA STABILITY .....	97
7.4. CONCERNING BASIC PLASMA PROPERTIES .....	98
7.5. CONCERNING REACTOR DESIGN AND APPLICATION .....	99
References .....	100
APPENDIX A. LANGMUIR PROBE DIAGNOSTIC SYSTEM .....	102
A.1. LANGMUIR PROBE .....	102
A.2. ELECTRICAL SYSTEM .....	102
A.3. SOFTWARE .....	103
A.4. PROGRAM LISTING .....	104
APPENDIX B. LANGMUIR PROBE DATA ANALYSIS SOFTWARE .....	107
B.1. LEVENBERG-MARQUARDT ALGORITHM .....	107
B.2. SOFTWARE .....	109
B.3. PROGRAM USAGE .....	111
B.4. ACCURACY OF RESULTS .....	113
B.5. PROGRAM LISTING .....	116
References .....	130

# CHAPTER 1

## INTRODUCTION

*Basic research is when I'm doing what I don't know what I'm doing.*  
- Werner von Braun

The subject of this thesis is a plasma-physical analysis of an electron cyclotron resonance (ECR) microwave plasma processing reactor. In this chapter some background material is given, as well as a discussion of the factors which motivated this work. The objectives and organisation of the thesis are also described.

### 1.1. PLASMA PROCESSING

In general, plasma processing refers to the synthesis, decomposition or modification of materials using a plasma. More specifically, this term usually implies the use of an electrical discharge to perform various surface modification procedures during the fabrication of microelectronic circuits. These procedures can be grouped into four categories:

- (1) *Cleaning*: A plasma is used to chemically and/or physically remove unwanted surface deposits such as adsorbed contaminants, native oxides or protective coatings.
- (2) *Etching*: A plasma is used to cut specific patterns into a surface through the selective removal of material. This is accomplished through the use of protective masks and plasma conditions which only remove certain substances. While similar to cleaning in principle, it is quite different in intent.
- (3) *Growth*: A plasma is used to generate reactive chemical species which combine directly with the surface to form a modified surface layer (oxidation, for example).
- (4) *Deposition*: A plasma is used to either chemically (through homogeneous or heterogeneous chemical reactions) or physically (through sputtering or beam formation) generate species which will deposit a thin-film (adsorb, nucleate/react, coalesce) on a surface. The essential difference between growth and deposition is that in growth the plasma species react *with* the surface, while in deposition they react *on* the surface.

By far the greatest use of plasma processing takes place in the microelectronics industry; etching applications alone sustain a multi-billion dollar equipment market.<sup>1</sup> The recent adoption of VLSI (very large scale integration) integrated circuit technology has greatly increased the use of plasma processing in integrated circuit fabrication. VLSI circuits require sub-micrometer features which necessitate the use of highly directional and selective etching processes only attainable with plasma techniques.<sup>2</sup> Small feature sizes also mean that conventional growth processes cannot always be used because the high temperatures often involved induce excessive diffusion of, or structural instabilities in, some materials.<sup>3</sup> Plasma deposition can be used to overcome

these problems, since energy is coupled into the plasma rather than the surface, allowing films to be grown at much lower surface temperatures.<sup>2</sup> In addition, some materials can *only* be produced by plasma techniques, such as hydrogenated amorphous silicon, which is used in solar cells and xerographic drums.<sup>4</sup> Plasma processing is compatible with other important vacuum techniques used in integrated circuit fabrication (molecular beam epitaxy, ion implantation), and is safer to use, cleaner and less polluting than older methods, many of which rely on the use of liquid chemicals.<sup>5</sup>

## 1.2. MOTIVATIONS

For mainly historical reasons, the most commonly used plasma processing technique is capacitively coupled, radio-frequency (typically 13.56 MHz) glow discharge (RFGD) with internal parallel-plate electrodes.<sup>6</sup> Such systems are capable of etching features smaller than 1  $\mu\text{m}$  with a high degree of anisotropy and selectivity.<sup>7</sup> They can also produce thin-films of many of the important materials used in integrated circuit fabrication.<sup>8</sup> These reactors achieve anisotropic etching through the production of high energy ions, which bombard the sample surface in the presence of chemically reactive species,<sup>9,10</sup> activating their reaction with the surface. These energetic ions are produced by the large DC electric fields in the electrode sheaths and can damage the etched surfaces.<sup>3,11</sup> This damage (in the form of defect creation, contamination, layer mixing and/or surface roughening), is often not tolerable in VLSI or GaAs circuits. Similar considerations apply to deposition, with the added problem that the substrate temperatures required to produce quality materials are often still too high.<sup>3,12</sup> Thus there appears to be room for improvement, primarily in reducing ion energies and lowering the substrate temperatures required for good thin-film quality.

ECR plasma processing systems are thought to offer improvements over RFGD and other methods in both of these areas.<sup>3,12,13,14,15,16</sup> ECR reactors can perform highly controllable, selective, sub-micron, directional etching with little surface damage.<sup>14</sup> They have also been used to produce quality thin-films at low substrate temperatures and at good deposition rates.<sup>3,12,17,18</sup> In particular, ECR systems are capable of single-pass planarisation (the filling of trenches to produce a flat surface), a process which requires several passes through RFGD systems.<sup>3</sup> ECR reactors typically generate high plasma densities at low pressures which results in high ion fluxes at low energies. These are often desirable properties for both etching and deposition. High densities imply high dissociation rates which, in turn, are often credited with allowing high processing rates to be maintained at low substrate temperatures without sacrificing the quality of the process. High ion fluences appear to activate surface reactions, especially in etching<sup>6</sup> and also perhaps in deposition. If desired, ion energies can be increased separately with DC or RF sample biases,<sup>19,20</sup> a process more versatile and controllable than possible in RFGD, where the bias is inseparable from the method of plasma production.

It therefore appears that ECR plasma processing may be of great importance in the effort to push integrated circuit feature sizes into the submicron regime. This view is reflected in the recent surge of interest in ECR systems in the U.S.A.\*, which had

---

\* Consider, for example, the 12 million dollar (over 5 years) Center for Plasma-Aided Manufacturing started in 1988 at the University of Wisconsin-Madison. Funded mostly by industrial contributions, one of the four key areas targeted for extensive (and largely catch-up)

largely ignored this technology throughout its developmental stages. In Canada, Bell-Northern Research has been studying the application of ECR plasmas to silicon nitride deposition and GaAs etching for several years.<sup>21</sup> Their parent company, Northern Telecom, is now using commercial ECR systems for prototype device fabrication<sup>†</sup>. Mitel S.C.C. is also planning pre-production trials of commercial ECR reactors in 1990 to evaluate their use in advanced IC fabrication processes.<sup>22</sup>

Given that plasma processing is vital to advanced integrated circuit fabrication and that ECR systems are becoming important plasma processing tools, it should be obvious that understanding how ECR plasma processing systems work and what they can do is of great importance. This is the general motivation for this work, as well as the applications research which has been performed in our laboratory for the last six years.

### 1.3. OBJECTIVES

Plasma processing is, by necessity, a largely empirical science\*. All plasma processing systems have a large number of system variables which influence the plasma in a host of complex ways, and which also interact with each other via the plasma. System and applications development *must* proceed primarily by trial-and-error because currently there are no models of these highly complicated systems. However, because of the widespread use and commercial importance of capacitive RFGD systems, considerable effort has recently gone into developing models of these systems. This has been made possible by the appearance of powerful, inexpensive computers with which to perform the extensive numerical computations required for such models, and a large body of experimental data concerning the physical and chemical properties of RF plasmas. Such data is conspicuously absent in the field of ECR plasma processing, a result of the novelty and rarity of these systems. Some ECR plasma characterisation studies have been performed recently (and will be reviewed in chapter 2), but these have only scratched the surface of the immense parameter space available to these machines. Only very recently have any models concerning ECR plasma processing been proposed.<sup>23,24</sup>

The ECR microwave plasma processing reactor that is the subject of this thesis was designed and built by Sergio Mejia and Bob McLeod in order to fabricate amorphous hydrogenated silicon (a-Si:H) thin-films intended for use in solar cells.<sup>25,26,27</sup> The fabrication of microcrystalline silicon ( $\mu$ c-Si:H) thin-films, as a potential replacement for polycrystalline silicon in VLSI integrated circuits, was also studied,<sup>28,29,30,31</sup> as was the etching of Si and SiO<sub>2</sub>.<sup>32,33</sup> Recent efforts have focussed on low-temperature deposition of SiO<sub>2</sub> thin-films for use as a general-purpose dielectric in Si and GaAs integrated circuits, and perhaps as a gate dielectric in VLSI and sub-micron MOSFET's.<sup>17,18,34,35,36</sup> Until this thesis, however, no detailed plasma characterisations

---

research is plasma processing of semiconductors by ECR.

† From employment advertisements and NT job interviews of colleagues.

\* Consider, for example, the following comment contained in the brochure advertising the Massachusetts Institute of Technology's summer course (No. 10.61s, 1989) on plasma processing: "Plasma processes have been developed, largely, by a trial-and-error approach with minimal understanding of the plasma physics and chemistry".

have been undertaken.

The overall purpose of this thesis is to take some of the first serious steps in developing a detailed understanding of the physical processes important in ECR and sub-ECR magnetised microwave processing plasmas. This is to be done through a number of basic plasma-physical (as opposed to plasma-chemical, which are application dependent and thus not considered in this thesis) experiments on a proven research ECR plasma processing reactor, with the intent of answering as many of the following questions in as much detail as possible:

- (1) What kind of information about these plasmas is most important, and what techniques must be used to obtain this information?
- (2) What are the fundamental properties of these plasmas, and how do they depend on important system variables?
- (3) Which plasma mechanisms are, and which are not, important and how do they influence the properties and behaviours of the plasmas?
- (4) What are the basic components that a theoretical model or description of these plasmas should possess?

Specifically, the experiments are to consist of the most basic and informative plasma diagnostic (characterisation) techniques. Some of these will be developed as part of this thesis while others will be standard techniques, modified so that they will function reliably under the conditions found in these plasmas. The aim will be to measure the most immediately informative properties of the ECR plasmas. These include those properties that are both obviously important yet widely neglected, such as visible shape and microwave power absorption, as well as the standard parameters of plasma density and electron temperature. Relative trends as functions of the most important system variables (microwave power, pressure, magnetic field strength and position) will be of primary interest.

Whenever possible, the results will be interpreted in terms of basic theoretical concepts in order to develop a more rigorous understanding of ECR plasma processing systems. The results of these efforts will then be used to make recommendations towards design improvements and process optimisation procedures.

#### 1.4. ORGANISATION

This thesis begins with an introduction to ECR plasma processing and an outline of the motivations and objectives of this thesis. In chapter 2, the background material important to this thesis is presented. A general review of basic plasma physics is given first, followed by a brief description of the design of ECR plasma processing reactors. The last part of chapter 2 consists of a critical review of the literature concerning plasma characterisations in ECR processing reactors.

The specific ECR system studied in this thesis is described in detail in chapter 3, along with the Langmuir probe diagnostic system used to characterise the plasmas. Additional theory pertinent to the system technologies and diagnostic techniques is also given.

Early experiments, which were critical in defining the objectives and methods of this thesis, are presented in chapter 4. Chapter 5 then describes a set of three

complementary, qualitative diagnostics which were found to be very useful in characterising the overall behaviour of ECR and magnetised microwave processing plasmas.

The heart of this thesis is contained in chapter 6. This chapter describes the results of a detailed Langmuir probe characterisation of divergent field ECR processing plasmas, with emphasis on their axial structure and responses to system variables. The theoretical and practical implications of these results are also discussed.

Finally, the conclusions and recommendations of this thesis are presented in chapter 7.

#### References

1. M.F. Leahy, "Superfine IC Geometries," *IEEE Spectrum*, p. 36, Feb. 1985.
2. G.S. Oehrlein, "Applications of RF Plasmas to Etching Processes in Advanced Semiconductor Technology," *AIP Proc. 159: Appl. of RF Power to Plasmas*, p. 442, Kissimmee, Florida, 1987.
3. K.M. Kearney, "ECR Finds Applications in CVD," *Semicond. Intl.*, p. 66, March 1989.
4. M. Hirose, "Glow Discharge," in *Semiconductors and Semimetals Vol. 21: Hydrogenated Amorphous Silicon, Pt. A*, ed. J.I. Pankove, p. 9, Academic, Orlando, 1984.
5. D.J. Elliot, *Integrated Circuit Fabrication Technology*, McGraw-Hill, New York, 1982.
6. J.W. Coburn, *Plasma Etching and Reactive Ion Etching*, Am. Vac. Soc. & Am. Inst. Phys., New York, 1982.
7. K. Suzuki, S. Okudaira, N. Sakudo, and I. Kanomata, "Microwave Plasma Etching," *Jpn. J. Appl. Phys.* 11, p. 1979, 1977.
8. K. Kobayashi and M. Kamoshida, "Plasma Chemical Vapor Deposition," in *Applications of Plasma Processes to VLSI Technology*, ed. T. Sugano, p. 245, John Wiley & Sons, New York, 1985.
9. H.H. Sawin, "A Review of Plasma Processing Fundamentals," *Solid State Technol.*, p. 211, Apl. 1985.
10. J.-I. Nishizawa and H. Hayasaka, "Physical Chemistry of Plasma Etching," in *Applications of Plasma Processes to VLSI Technology*, ed. T. Sugano, p. 42, John Wiley & Sons, New York, 1985.
11. S. Yoshida, "Damage by Plasma Etching," in *Applications of Plasma Processes to VLSI Technology*, ed. T. Sugano, p. 298, John Wiley & Sons, New York, 1985.
12. S. Matsuo and Y. Kiuchi, "Low Temperature Chemical Vapor Deposition Method Utilizing an Electron Cyclotron Resonance Plasma," *Jpn. J. Appl. Phys.* 22, p. L210, 1983.
13. R.R. Burke and C. Pomot, "Microwave Multipolar Plasma for Etching and Deposition," *Solid State Technol.*, p. 67, Feb. 1988.
14. K. Suzuki, K. Ninomiya, and S. Nishimatsu, "Microwave Plasma Etching," *Vacuum* 34, p. 953, 1984.
15. J. Musil, "Microwave Plasma: Its Characteristic and Applications in Thin Films Technology," in *IPAT'85, 5th Int'l. Conf. on Ion & Plasma Assisted Techniques, Munich, 1985*, p. 463, CEP Consultants, Edinburgh, 1985.
16. W. Hale, "ECR - Perspectives on a New Technology," *Micro. Manufac. Testing*, p. 22, November 1989.
17. T.T. Chau, T.V. Herak, D.J. Thomson, S.R. Mejia, D.A. Buchannan, R.D. McLeod, and K.C. Kao, *Silicon Dioxide Films Fabricated by ECR Microwave Plasmas*, Beijing, 1988. Presented at the 2nd Int'l. Conf. Prop. and Appl. of Dielectric Materials
18. T.V. Herak, T.T. Chau, D.J. Thomson, S.R. Mejia, D.A. Buchannan, R.D. McLeod, and K.C. Kao, "Low-Temperature Deposition of Silicon Dioxide Films from ECR Microwave Plasma," *J. Appl. Phys.* 65, p. 2457, 1989.
19. K. Suzuki, K. Ninomiya, S. Nishimatsu, and S. Okudaira, "Radio-Frequency Biased Microwave Plasma Etching Technique: A Method to Increase SiO<sub>2</sub> Etch Rate," *J. Vac. Sci. Technol. B* 3, p. 1025, 1985.
20. Y.H. Lee, J.E. Heidenreich III, and G. Fortuno, "Plasma Characterization of an Electron Cyclotron Resonance-Radio-Frequency Hybrid Plasma Reactor," *J. Vac. Sci. Technol. A* 7, p. 903, 1989.

21. S. Dzioba, Advanced Technology Laboratory, BNR., 1988. Private communication.
22. G. Harling, Director of Process R & D, Mitel S.C.C., 1988. Private communication.
23. M.A. Hussein and G.A. Emmert, "Modeling of Plasma Flow Downstream of an Electron Cyclotron Resonance Plasma Source," *J. Vac. Sci. Technol. A8*, p. 2913, 1990.
24. T.V. Herak, D.J. Thomson, and P.K. Shufflebotham, *A Growth Model for ECR PECVD of SiO<sub>2</sub> Thin Films*, Toronto, Ontario, October 8-12, 1990. Submitted to the American Vacuum Society 37<sup>th</sup> Ann. Symp. and Topical Confs.
25. S.R. Mejia, R.D. McLeod, K.C. Kao, and H.C. Card, "The Effects of Deposition Parameters on a-Si:H Films Fabricated by Microwave Glow Discharge Techniques," *J. Non-Cryst. Solids 59 & 60*, p. 727, 1983.
26. S.R. Mejia, R.D. McLeod, W. Pries, P. Shufflebotham, D.J. Thomson, J. White, J. Schellenberg, K.C. Kao, and H.C. Card, "Fabrication of a-Si:H Films by Microwave Plasmas Under Electron Cyclotron Resonance Conditions," *J. Non-Cryst. Solids 77 & 78*, p. 765, 1985.
27. S.R. Mejia, R.D. McLeod, K.C. Kao, and H.C. Card, "Electron-Cyclotron Resonant Microwave Plasma System for Thin-Film Deposition," *Rev. Sci. Instrum. 57*, p. 493, 1986.
28. J.J. Schellenberg, R.D. McLeod, R.S. Mejia, H.C. Card, and K.C. Kao, "Microcrystalline to Amorphous Transition in Silicon from Microwave Plasmas," *Appl. Phys. Lett 48*, p. 163, 1986.
29. T.V. Herak, T.T. Chau, S.R. Mejia, P.K. Shufflebotham, J.J. Schellenberg, H.C. Card, K.C. Kao, and R.D. McLeod, "Effects of Substrate Bias on Structure and Properties of a-Si:H Films deposited by ECR Microwave Plasmas," *J. Non-Cryst. Solids 97 & 98*, p. 277, 1987.
30. T.V. Herak, J.J. Schellenberg, P.K. Shufflebotham, K.C. Kao, and H.C. Card, "Silicon from Microwave Plasmas: Optical Properties and Their Relation to Structure," *J. Non-Cryst. Solids 103*, p. 125, 1988.
31. T.V. Herak, J.J. Schellenberg, P.K. Shufflebotham, and K.C. Kao, "Investigation of the Amorphous to Microcrystalline Transition of Hydrogenated Silicon Films by Spectroscopic Ellipsometry," *J. Appl. Phys. 64*, p. 688, 1988.
32. S.R. Mejia, T. Chau, R.D. McLeod, K.C. Kao, and H.C. Card, "Electron Cyclotron Resonance Microwave-Plasma Etching," *Can. J. Phys. 65*, p. 856, 1987.
33. S.R. Mejia, *Microwave Plasma Deposition and Etching of Semiconducting and Insulating Thin Films Under ECR Conditions: Systems and Process Characterisation*, Rochester, New York, June 1988. Invited presentation at the 15<sup>th</sup> Ann. Symp. of the American Vacuum Society.
34. T.V. Herak and D.J. Thomson, "Effects of Substrate Temperature on the Electrical and Physical Properties of Silicon Dioxide Films Deposited from Electron Cyclotron Resonant Microwave Plasma," *Accepted for publication in the J. Appl. Phys.*, 1990.
35. D.J. Thomson, *ECR Silicon Dioxide Deposition and Plasma Stability*, Fremont, California, February, 1990. Invited presentation at the Santa Clara Valley CVD User's Symposium held at Lam Research.
36. D.J. Thomson, *Silicon Oxide Deposition by ECR Microwave Plasma*, New Orleans, March, 1988. Invited presentation at the spring meeting of the American Physical Society.

## CHAPTER 2

### REVIEW OF ECR PROCESSING PLASMAS

*There is something fascinating about science.  
One gets such wholesale returns of conjecture  
out of such a trifling investment of fact.  
- Mark Twain, Life on the Mississippi.*

The purpose of this chapter is to introduce the basic physical concepts important in ECR microwave processing plasmas, to describe existing ECR plasma processing reactors and to review the literature concerning the physical plasma properties of these systems.

Throughout this thesis it will be assumed that the reader has at least a passing familiarity with the kinetic theory of gases. In particular, the fact that knowledge of the energy (or velocity) distribution function (EDF) of a gas enables one to calculate virtually all of its macroscopic properties is of fundamental importance. In plasmas of the type used in processing applications it is the electron gas which determines the majority of the plasma properties, so knowledge of the electron EDF (EEDF) is essential in any efforts to model the physics or chemistry of such plasmas. It is also often true in these plasmas that the EEDF is well approximated by the equilibrium *Maxwellian* EDF. This distribution is uniquely specified by two parameters; the particle *density* per unit volume,  $n$ , and the *temperature*,  $T$ , which is a measure of both the average kinetic particle energy and the variance of the distribution about this value. Therefore, knowledge of the electron density,  $n_e$ , and temperature,  $T_e$ , is of fundamental importance in any efforts to model either the plasma or the processes which it is used to perform. Fortunately these are relatively easy parameters to measure, and their determination has been the primary focus of most plasma characterisations of ECR processing plasmas to date, this thesis included.

#### 2.1. SOME BASIC PLASMA PHYSICS

The primary purpose of any processing plasma is to generate chemical reactions within a gas or between a gas and a surface. This is accomplished through the generation of free electrons, ions and photons, as well as molecular, atomic and radical species of varying degrees of excitation. The chemical nature of these products determines the kinds of plasmas that must be used; electron temperatures in the range of 1 to a few tens of eV are required to create viable chemical species and induce reactions, while moderate electron densities of  $n_e > 10^{14} \text{ m}^{-3}$  are needed to produce significant reaction rates.

ECR plasma processing systems produce chemical plasmas using low pressure, flowing, bounded, magnetised microwave discharges. The resulting plasmas are generally *quasi-neutral* and *weakly ionised*. Quasi-neutrality is a defining property of plasmas<sup>1</sup> which requires that  $n$  be large enough that the charged particles are able to

effectively screen out electric fields over distances smaller than those of the containing vessel. This usually means that the *plasma approximation*,  $n_i \approx n_e \approx n$ , can be used, where  $n_i$  is the positive ion density and  $n$  is called the *plasma density*. By weakly ionised it is meant that  $n$  is less than the neutral gas density. This implies that charged particles undergo a significant number of collisions with neutral gas species. Such collisions do not dominate charged particle dynamics in a plasma; electromagnetic interactions do, but they are basic to a number of important plasma phenomena (generation, diffusion and recombination, in particular).

In this section, the basic physical processes thought to be important in ECR microwave processing plasmas will be outlined. The model to be used is basically that of a magnetised *Lorentz gas*.<sup>2,3</sup> This model is a good first approximation to the kinds of plasmas found in ECR systems, and can *qualitatively* account for most of the dominant physical phenomena involved. In this model, electrons are treated as independent particles. Ions and other species are assumed to form a uniformly distributed background of immobile (due to their large mass relative to electrons) charged and neutral scattering centers. Electron-neutral collisions are assumed to be the dominant collision process, characterised by a constant total elastic collision frequency,  $\nu$ . In addition, the electrons may be assumed to be either *cold* ( $T_e = 0$ ) or *temperate* ( $T_e > 0$ ). This is essentially the standard model used to describe plasmas of the type used in processing applications.

The use of a temperature implies a Maxwellian EEDF, and their existence will be assumed throughout this thesis. In a Lorentz gas these would be expected when  $\nu$  is constant,<sup>2,4</sup> an excellent assumption in  $H_2$  and He plasmas.<sup>5</sup> Maxwellian EEDF's also occur when Coulomb collisions (between charged particles) are significant, typically when  $n$  is large. Factors which tend to prevent equilibrium from occurring include inelastic collisions (significant at low  $n$ )<sup>4</sup> and strong electric fields.<sup>4,2</sup> Under such conditions the EEDF tends towards a *Druvestyn* EDF, which is deficient in high energy electrons relative to a Maxwellian at the same "temperature".<sup>4</sup> In ECR plasmas, strong electric fields in the form of microwaves are applied perpendicular to a strong magnetic field. This acts to drive the EEDF towards a Maxwellian since the oscillations induced by the microwaves and the Larmor gyration induced by the magnetic field (see sub-section 2.1.1) imitate the effect of collisions.<sup>1</sup> Thus, the effective value of  $\nu$  is much greater than the plasma and/or gas densities would suggest, and only inelastic collisions should significantly perturb the EEDF from equilibrium.

### 2.1.1. Magnetised Microwave Plasmas

This sub-section gives a brief overview of ECR plasma physics. This simple picture will be made more detailed and exact in sub-sections 2.1.2 to 2.1.5. It is suggested that the reader unfamiliar with ECR plasma processing systems should at least browse section 2.2, especially figures 2.5 and 2.6, to get an idea of what the following discussions are in reference to.

In microwave discharges, plasma is generated by accelerating free electrons into inelastic collisions with neutral gas molecules using microwave electric fields. These collisions produce ions, atoms and radical species of varying degrees of excitation (which may radiate photons as they relax), as well as more electrons with which to sustain the process. Ions are not affected by electric fields oscillating above about 1

MHz because of their large mass.<sup>6</sup> This means that virtually all the microwave energy is coupled directly to electrons, so that ions can be neglected when considering the absorption of microwave power. This also implies that the ion temperature should be near that of the neutral gas, which is determined by the temperature of the vessel walls. This assumption is often made with high frequency plasmas<sup>5</sup> but is in fact untrue.<sup>7</sup> This will be discussed further in sub-section 2.3.5. The microwave field will be assumed to not drive electrons into collisions with the container walls during an oscillation. Thus diffusion phenomena dominate the loss of electrons (and thus of plasma) from these discharges,<sup>5,8</sup> with recombination contributing at high densities.<sup>1</sup>

To ignite a plasma ("break down" the gas), some free electrons must initially be present in the working gas. In ECR systems, the few electrons always present due to cosmic ray ionisation are sufficient to allow the microwaves to initiate a discharge. Breakdown electric fields are quite large since each electron must acquire enough energy to generate many new electrons in order to build up the plasma. In the steady-state, however, each electron must only replace itself before being lost, so maintenance fields are much smaller.<sup>5</sup>

Magnetic fields are used in ECR systems for two purposes; to *confine* the plasma by reducing the diffusive loss of charged particles, thereby permitting operation at lower pressures, and to enable resonant coupling of microwave energy to the plasma electrons through the use of *electron cyclotron resonance*.

Confinement is obtained through the  $q\mathbf{v}\times\mathbf{B}_0$  force exerted by a magnetic field on a particle of charge  $q$ . Here  $\mathbf{B}_0$  is the applied static vector magnetic flux density,  $\mathbf{v}$  is the single particle velocity and  $q \equiv Ze$ , where  $Z$  is the charge state of an ion, or -1 for electrons. This force converts linear motion perpendicular to  $\mathbf{B}_0$  into a circular motion called *cyclotron gyration*.<sup>1</sup> Since motion along  $\mathbf{B}_0$  is unchanged, the motion of a charged particle in such a field describes a helical path. The radius of gyration is the *Larmor radius*,

$$r_L = \frac{|v_\perp|}{\omega_C}, \quad (2.1)$$

and the *cyclotron frequency* is

$$\omega_C \equiv \frac{|q\mathbf{B}_0|}{m}. \quad (2.2)$$

$v_\perp$  is the root-mean-squared speed of the particle in the plane perpendicular to  $\mathbf{B}_0$  and  $m$  is the particle mass.

The occurrence of cyclotron gyration implies that charged particles are "stuck" to the magnetic field lines; in the absence of collisions they cannot move across the magnetic field.<sup>1</sup> If  $r_L$  is much less than the dimensions of the containing vessel, then the magnetic field effectively confines the plasma by preventing charged particles from diffusing across  $\mathbf{B}_0$  to the walls. This decreases the microwave power required to sustain a plasma of given density as compared to the unmagnetised case.

Cyclotron gyration implies that a microwave electric field oscillating at  $\omega = \omega_C$  (with components polarised perpendicularly to  $\mathbf{B}_0$ ) will accelerate electrons continuously throughout their gyro-period. This is called *electron cyclotron resonance* (ECR), and coupled the microwave energy to electrons very efficiently. This allows dense

plasmas to be generated easily over a wide range of conditions. For example, even at a relatively high pressure of 1 Torr, the microwave electric field strength required to break down He at ECR is more than an order of magnitude less than that required with no magnetic field.<sup>5</sup> The motion of a resonating electron forms a spiral, or helix of increasing radius, as  $v_x$  increases.<sup>9</sup>

### 2.1.2. Wave Propagation: Unmagnetised Plasma

In this sub-section it will be assumed that the plasma is cold, homogeneous, unmagnetised and infinite in extent. The effects of boundaries on wave propagation will be addressed at the end of sub-section 2.1.3. The natural frequency of oscillation of the plasma electrons is called the *plasma frequency*:<sup>1</sup>

$$\omega_{pe} = \left[ \frac{ne^2}{\epsilon_0 m_e} \right]^{1/2}, \quad (2.3)$$

where  $\epsilon_0$  is the permittivity of vacuum. These are electrostatic oscillations in the cold plasma assumed here. If electron thermal motions, collisions or fringing fields outside a finite plasma were included, these oscillations would convert to longitudinal (electric field vector parallel to the wave-vector;  $\mathbf{E} \cdot \mathbf{k} \neq 0$ ) electrostatic waves called electron plasma (or Bohm-Gross, Langmuir, Tonks-Langmuir) waves.<sup>1,9</sup> These are basically electronic acoustic waves.

Microwave plasmas are often sustained by launching transverse ( $\mathbf{E} \cdot \mathbf{k} = 0$ ) electromagnetic (TEM) waves from a vacuum region into a non-uniform plasma. Propagation of the wave into the plasma depends solely upon the local value of  $\omega_{pe}$ , which corresponds to a *cutoff* for TEM waves.<sup>1,9</sup> A cutoff is characterised by a vanishing wavevector,  $k \rightarrow 0$ , or refractive index,  $n \equiv ck/\omega \rightarrow 0$ , or a divergent wavelength,  $\lambda \equiv 1/k \rightarrow \infty$ . Any wave incident on a cutoff is totally reflected, with some wave energy leaking into the plasma in the form of an *evanescent* (exponentially decaying) wave with  $\lambda \rightarrow \infty$ . The opposite process is *resonance*, characterised by  $k \rightarrow \infty$ , which totally absorbs an incident wave. In the cold plasma model, a resonantly absorbed wave is converted into non-propagating electrostatic oscillations, since  $\lambda \rightarrow 0$ . Note that  $\omega_{pe}$  is a resonance for longitudinal electrostatic waves and oscillations.<sup>9,10</sup>

Collisions tend to randomise the organised particle motions represented by waves, and thus result in wave damping. The wave energy lost to this damping is, of course, acquired as kinetic energy by the electrons. While both elastic and inelastic collisions cause damping, it is the inelastic collisions, involving the high energy population of electrons, which result in plasma generation. Collisions also allow partial wave transmission through cutoffs and resonances by adding imaginary terms to  $k$  (removing the poles and zeros in the dispersion relation).

The existence of a cutoff at  $\omega_{pe}$  implies that there is an upper limit to the density of plasma which can be sustained by an external TEM wave which depends only on the frequency of the wave. From (2.3) at  $\omega = \omega_{pe}$  we have the so-called *critical plasma density*,

$$n_{pe} = \frac{\omega^2 \epsilon_0 m_e}{e^2}. \quad (2.4)$$

Thus a TEM wave would generate plasma through collisional heating only up to  $n_{pe}$ , after which excess wave energy would be reflected. However, longitudinal electrostatic oscillations (excited between a pair of electrodes, for example) would resonate with the plasma it produced, thus generating an overdense plasma ( $n > n_{pe}$ ).

Though often quoted,  $n_{pe}$  is of little use in plasma processing since, in practice, overdense plasmas are routinely generated. For example, parallel-plate RFGD systems operating in the tens of MHz range should, from the above, only produce  $n$  on the order of  $10^{12} \text{ m}^{-3}$ , but in fact<sup>11</sup> operate above  $10^{16} \text{ m}^{-3}$ . This is partially due to electrostatic resonance at  $\omega_{pe}$ ,<sup>10</sup> but also to other less well understood mechanisms such as multipaction<sup>8</sup> and electron sheath "surfing".<sup>12</sup> In the case of ECR microwave plasmas, the strong magnetic fields present modify the wave propagation characteristics of the plasma so that  $\omega_{pe}$  is not particularly significant by itself.

### 2.1.3. Wave Propagation: Magnetised Plasma

The simple model described in sub-section 2.1.1 might lead one to conclude that ECR occurs wherever  $\omega = \omega_{ce}$ . That this is not so becomes clear when the propagation of waves in magnetised plasmas is examined in detail. Derivations will not be repeated here, only the important results. The interested reader is referred to any of the excellent texts available.<sup>1,3,9,13</sup>

The plasma will be assumed to be temperate and immersed in a uniform (or slowly varying), static magnetic field oriented along the z-axis,  $B_0(z)$ . The waves of interest will be travelling parallel to  $B_0(z)$ , in the same direction as  $B_0$ . The geometry under consideration is shown in figure 2.1.

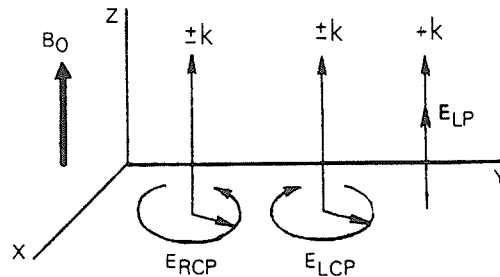


FIGURE 2.1. Geometry for parallel TEM wave propagation in a magnetised plasma. LP, RCP and LCP refer to longitudinal, right-circular and left-circular polarisations, respectively.

There are three solutions to the wave equation in this case. One is just the longitudinal electrostatic wave described in sub-section 2.1.2. Since its electric field vector is parallel to  $B_0$ , this wave mode is unchanged.<sup>1,9</sup> The other two waves are transverse modes corresponding to left and right-hand circularly polarised (LCP, RCP) TEM waves. Each wave has a cutoff at<sup>1,9</sup>

$$\omega_{R,L} = \frac{\pm\omega_{ce} + \left[ \omega_{ce}^2 + 4\omega_{pe}^2 \right]^{1/2}}{2}, \quad (2.5)$$

where the +(-) sign refers to the RCP(LCP) wave. The RCP wave undergoes ECR at  $\omega_{ce}$ , since the electric vector rotates in the same sense as the electrons in their cyclotron gyration. Had ion motions been included, the LCP wave would undergo ion

cyclotron resonance at  $\omega_{Ci} \ll \omega_{Ce}$ . In general there exists one RCP wave for every negative particle species, and one LCP wave for every positive species.<sup>9</sup> At microwave frequencies the electron component dominates. The frequency dispersion of these waves is shown in figure 2.2. This figure shows the normalised (with respect to the vacuum speed of light,  $c$ ) phase velocity of the waves,  $v_\phi \equiv \omega/k$ , (where  $k$  is a function of  $\omega_{pe}$  and  $\omega_{Ce}$ ) versus frequency. This method of plotting the dispersion relation is clearer than the usual  $\omega$  versus  $k$  format in this case. Note that  $v_\phi$  vanishes at a resonance, and diverges at a cutoff.<sup>1</sup>

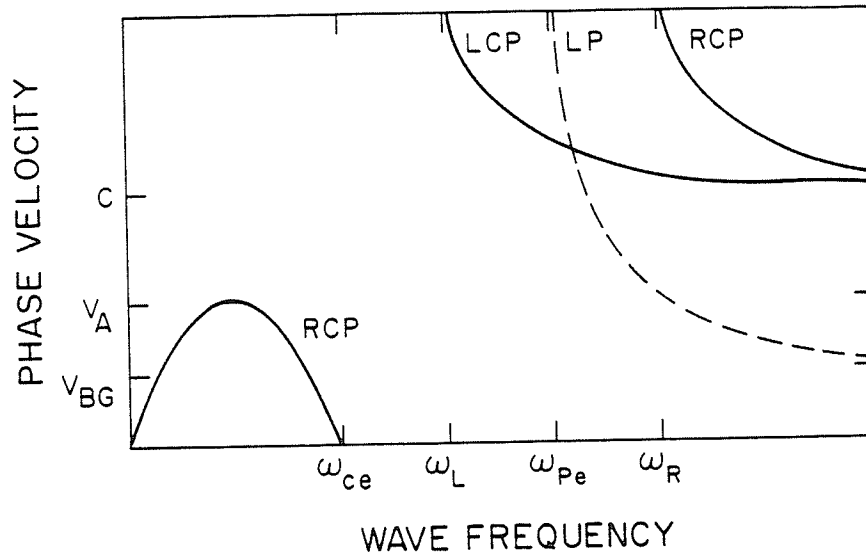


FIGURE 2.2. Sketch of phase velocity vs. angular frequency for plane wave propagation parallel to a static magnetic field in a cold Lorentz gas. LP, LCP and RCP refer to longitudinally polarised electrostatic, left-circularly polarised and right-circularly polarised waves, respectively.  $v_{BG}$  is the Bohm-Gross wave velocity,  $v_A$  is the Alfvén speed<sup>9</sup> and  $c$  is the vacuum speed of light. The LP mode is a wave in a temperate plasma, an electrostatic oscillation at  $\omega_{pe}$  in a cold plasma. Taken from Tanenbaum.<sup>2</sup>

Since only the RCP wave undergoes ECR, the LCP mode will be neglected in the following discussion on how to launch an external wave into ECR. Three different magnetic field configurations could be used;  $B_0(z)$  constant at  $\omega_{Ce} = \omega$ ,  $B_0(z)$  increasing into ECR from  $\omega_{Ce} < \omega$  or  $B_0(z)$  decreasing into ECR from  $\omega_{Ce} > \omega$ . The first case will be considered a limiting form of the decreasing  $B_0(z)$  configuration. To see what happens to a wave launched into a non-uniform plasma, note in figure 2.2 that increasing  $B_0$  moves both  $\omega_{Ce}$  and  $\omega_R$  in the direction of increasing  $\omega$ . Also note that increasing  $n$  separates  $\omega_R$  and  $\omega_{Ce}$ .

For a wave launched from a region of low magnetic field towards a region of high magnetic field,  $\omega$  is initially larger than  $\omega_R$  and  $\omega_{Ce}$ . As the wave approaches ECR, it must first pass through the cutoff at  $\omega_R$ . If  $\omega_{pe}$  is significant, then the cutoff and resonant regions are well separated in space and the wave never reaches the ECR zone.<sup>13</sup> If the conditions are such that the evanescent wave extends into the ECR zone, then the wave can *tunnel* into resonance.<sup>9</sup> In the presence of collisions a larger fraction of the wave will leak through to the resonance region. Clearly, launching a wave through a cutoff is not an efficient way to achieve ECR, so these magnetic field

geometries are not usually used for this purpose.

For a wave launched from a region of high magnetic field towards a region of low magnetic field,  $\omega$  is initially less than  $\omega_{ce}$  and  $\omega_R$ . As the wave moves toward ECR,  $\omega_{ce}$  and  $\omega_R$  decrease towards  $\omega$ . There is no cutoff between  $\omega_{ce}$  and  $\omega$ , and ECR will occur with little reflection.<sup>9,13</sup> This configuration was named the *magnetic beach* by Thomas Stix<sup>13</sup> in analogy to the damping of water waves on a sandy beach. This is the usual method for obtaining ECR, and is widely used in ECR plasma processing reactors.

The behaviour of the LCP wave is straightforward in an increasing magnetic field profile; it has a cutoff like the RCP wave, but at a higher value of  $B_0(z)$ . This value will occur if  $n$  and  $B_0$  are sufficiently large. Unfortunately, figure 2.2 does not clearly indicate that in the magnetic beach case the LCP wave may still experience a cutoff. To see this, imagine that  $\omega_L < \omega_{ce}$ ; if  $n$  increases (spatially) faster than  $B_0(z)$  decreases (a likely situation in the high  $B_0$  region near a microwave input window, for example), then the LCP wave may still undergo a cutoff while the RCP propagates unimpeded into ECR. Thus the LCP and RCP components of a linearly polarised TEM wave are generally subject to quite different propagation properties.

The preceding discussion has been based on the unphysical assumption of a plasma infinite in extent. ECR plasmas, typically generated in waveguides or resonant cavities, obviously introduce boundary conditions which must be considered during the solution of the wave equation. The boundary conditions generally force the continuous plane wave spectrum of the infinite plasma into a discrete set of allowed modes. Each mode exhibits a unique geometric cutoff frequency, standing wave pattern and polarisation.<sup>3</sup>

In principle, the solution of plasma-loaded waveguide problems is an exercise in the tensor solution of a classical boundary value problem. The general procedure has been outlined by Allis, Buschbaum and Bers.<sup>3</sup> In practice this is an extremely difficult task. For the crude approximations required in this thesis, we will assume that the effects due to the plasma and waveguide may be treated separately using the infinite plasma and vacuum waveguide models. It must be recognised, however, that this is a crude approximation which captures only the essence of the problem, but few of its details.

#### 2.1.4. Boundaries: Diffusion

Plasmas used in processing applications are produced in vacuum chambers of various sorts, and are thus bounded. These boundaries have a dramatic influence on the properties and behaviours of a plasma. The most important effect is in supplying a sink for charged particles. Electrons are lost either through recombination on the surface (metals and insulators), absorption into the conduction band (metals) or both. Ions adsorb onto surfaces where they recombine with electrons and desorb back into the plasma as neutrals. These losses result in a diffusive flow of charged particles and corresponding electric fields. The diffusion process will be described in this subsection, and the concurrent formation of potentials in the next.

Other mechanisms may contribute to electron loss under specific conditions. *Attachment* may occur in the presence of species with a high electron affinity, such as

oxygen or fluorine. This involves the capture of electrons by neutral species to form negative ions.<sup>14</sup> This process may be important in applications, where such gases are common, but does not occur in the gases commonly used in plasma characterisations. At high densities various gas-phase *recombination* mechanisms, which involve the capture of electrons by positive ions, may become significant in molecular gases.<sup>14</sup>

Diffusion is a net flow of particles from regions of high to low density which tends to smooth out density variations. This problem is handled analytically by combining the fluid equations of continuity and motion to obtain the *diffusion equation*;

$$\frac{\partial n}{\partial t} - D \nabla^2 n = Q(\mathbf{r}), \quad (2.6)$$

where  $t$  is time,  $\nabla^2$  is the Laplace operator,  $D$  is the *diffusion coefficient* and  $Q(\mathbf{r})$  is a position dependent source term.

The diffusion coefficient is particularly simple in the case of *free* diffusion, which takes place in the absence of space-charge or magnetic fields. In this case<sup>1</sup>

$$D_F = \frac{\kappa T}{m v}. \quad (2.7)$$

However, screening and space charge effects cannot be neglected in a plasma; electrons initially diffuse more rapidly than ions, leaving behind a positive ionic space charge which retards electron loss while accelerating ionic losses. Steady state occurs when the two species diffuse at the same rate, a condition enforced by an *ambipolar* electric field. The ambipolar diffusion coefficient is<sup>1</sup>

$$D_A = \frac{\kappa(T_e + T_i)}{v(m_e + m_i)}. \quad (2.8)$$

Ambipolar diffusion is usually observed for plasma densities<sup>15</sup> above  $10^{14} \text{ m}^{-3}$ , a condition typically satisfied in ECR reactors. Note that ambipolar diffusion is dominated by the colder species (typically the ions) and that it acts as a non-collisional cooling mechanism,<sup>15</sup> since fast electrons can surmount the ambipolar field.

The presence of a magnetic field introduces anisotropy into the diffusion process because of the Larmor gyration perpendicular to  $\mathbf{B}_0$ . In this case  $D$  becomes a tensor. Assuming  $\mathbf{B}_0 = B_0(z)\hat{z}$ , the diffusion tensor in cartesian coordinates becomes

$$\mathbf{D} = \begin{bmatrix} D_{\times} & D_H & 0 \\ -D_H & D_{\times} & 0 \\ 0 & 0 & D_F \end{bmatrix}, \quad (2.9)$$

with elements

$$D_{\times} = \frac{D_F v^2}{\omega_C^2 + v^2} \quad (2.10)$$

and

$$D_H = \frac{D_F \omega_C v}{\omega_C^2 + v^2}. \quad (2.11)$$

The diffusion equation (2.6) now becomes

$$\frac{\partial n}{\partial t} = D_x \left[ \frac{\partial^2 n}{\partial x^2} + \frac{\partial^2 n}{\partial y^2} \right] + D_F \frac{\partial^2 n}{\partial z^2}. \quad (2.12)$$

As long as  $v \ll \omega_C$ , diffusion across  $B_0$  is greatly reduced from the free value; the plasma is confined by the magnetic field.<sup>1</sup> It is interesting to note that while collisions inhibit free diffusion, they *enhance* diffusion across a magnetic field.<sup>1</sup> Plasma confinement with magnetic fields is of fundamental importance in laboratory plasma physics, fusion technology in particular. It is also a standard feature in ECR plasma processing reactors.

Ambipolar diffusion in the presence of a magnetic field is a complex process to which it is not possible to assign a single diffusion coefficient.<sup>1,2</sup> Since only the *total* particle loss must be ambipolar, particle losses in any one direction need not be. Also, magnetic field confinement often does not work as well as expected because of the excitation of various waves and/or instabilities which can dramatically increase charged particle transport across  $B_0$ .<sup>1</sup>

Note that a uniform magnetic field by itself does no net work on a free charged particle because the force is perpendicular to the induced motion. However, there are a host of drift motions which may become important when the magnetic field is non-uniform.<sup>1</sup> Here we will consider only the effects of a gradient in  $B_0$  which is parallel to  $B_0$ . Such configurations do work through the  $\nabla B_0$  force they exert on the magnetic moments of gyrating particles.<sup>1</sup>

We first note that a gyrating charged particle is diamagnetic. The force exerted on the particle along the z-axis is<sup>1</sup>

$$F_z = -\mu \frac{\partial B_0(z)}{\partial z}, \quad (2.13)$$

where the *magnetic moment* is the kinetic energy perpendicular to  $B_0$  divided by  $B_0$ :

$$\mu \equiv \frac{mv_x^2}{2B_0(z)}. \quad (2.14)$$

Though  $r_L$  changes as the particle moves through regions of stronger or weaker  $B_0$ ,  $\mu$  remains constant.<sup>1</sup> As the particle moves into regions of weaker  $B_0$  its Larmor radius increases, so  $v_x$  must necessarily decrease to keep  $\mu$  constant. Since the total kinetic energy of the particle must be conserved, the velocity parallel to  $B_0$  must *increase* as  $v_x$  decreases. Thus the particle is accelerated as it travels down a magnetic beach, or slowed as it travels up the beach. This is the basis of axial plasma confinement with magnetic mirrors<sup>1</sup> (two beaches facing each other) and plasma acceleration (propulsion) with a single beach.

### 2.1.5. Boundaries: Sheaths

Any electric potential appearing in a plasma attracts oppositely charged particles and repels like charges. The resultant space-charge region shields the bulk plasma from the applied potential; this is called *screening* or *Debye shielding*.<sup>1,2</sup> Screening in a plasma is not 100% effective because of the thermal motions of the screening particles. Particles with kinetic energies in excess of a potential will escape that potential and not contribute to screening. On average, for Maxwellian particles, potentials on the

order of  $\kappa T_e/2$  extend into the bulk plasma.

The scale length of a plasma is determined by the characteristic screening length, called the *Debye length*,<sup>1</sup>

$$\lambda_D = \left[ \frac{\epsilon_0 \kappa T_e}{ne^2} \right]^{1/2}. \quad (2.15)$$

For lengths on the order of  $\lambda_D$  or less, the plasma is not quasi-neutral, strong electric fields called micro-fields exist throughout the plasma. Clearly, if the dimensions of the containing vessel are on the order of  $\lambda_D$  or less, screening cannot occur and a plasma cannot be said to exist.<sup>1</sup>

Screening will occur around any biased object in contact with a plasma. The bias is with respect to the plasma and need not be externally applied. The plasma itself can supply the bias through differential losses of charged particles as in ambipolar diffusion to a surface.<sup>1</sup> The non-neutral space-charge region surrounding a biased object in contact with a plasma is called a *sheath*.<sup>1,2</sup>

In general, the structure of a sheath can be very complex. For simplicity assume<sup>1</sup> a one dimensional plasma-wall geometry where the mean free paths of all particles are much larger than  $\lambda_D$  (collisionless sheath). Also assume that the plasma is at zero potential\*, and that all charged particles are lost upon contact with the surface (perfect absorber). Since electrons are lost at a much higher rate than ions, ambipolar diffusion produces a positive space charge layer next to the wall. The wall (or plasma) develops a net negative (positive) potential with respect to the plasma (wall) called the *sheath potential*,  $\phi_s(z)$ , which equalises the loss of charged particles. The sheath has the form shown in figure 2.3.

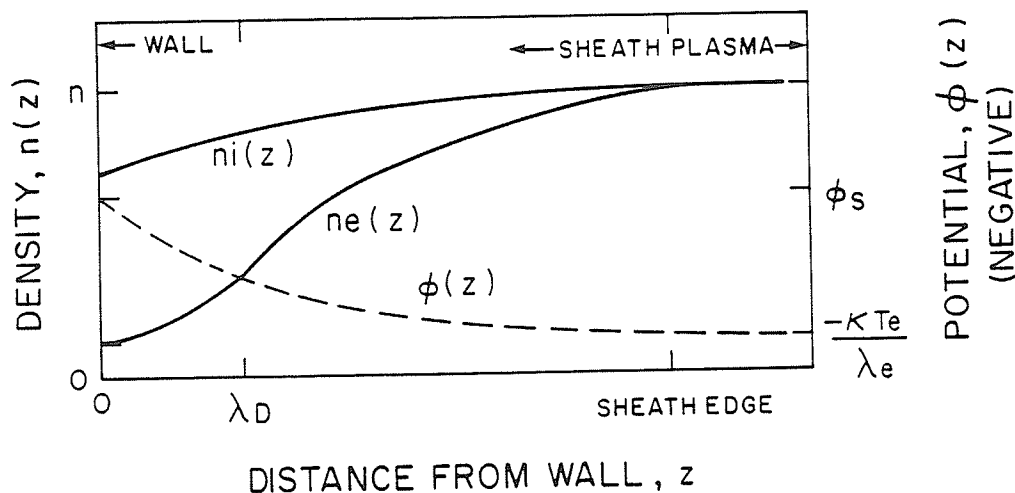


FIGURE 2.3. Structure of a simple one dimensional collisionless sheath. By convention, the plasma is defined to be at zero potential, so  $\phi_s(z)$  is negative. Taken from Tanenbaum.<sup>2</sup>

\* Throughout this thesis, potentials, denoted by  $\phi$ , will be taken with respect to the plasma, while voltages, denoted by  $V$ , will be with respect to the system ground.

Electrons are repelled by  $\phi_S(z)$  and their density within the sheath decreases according to a Boltzmann factor. The ion density also decreases, though less rapidly, as they space out due to their acceleration towards the wall. The "edge" of the sheath is conventionally taken where quasi-neutral conditions begin. Immediately outside the sheath is a quasi-neutral *pre-sheath*, within which exists a potential of approximately  $\kappa T_e/2e$ . This is a result of imperfect screening by thermal electrons.

To get an expression for  $\phi_S(z)$ , the nonlinear Poisson equation for the sheath must be solved.<sup>1</sup> Fortunately, the actual solution is not important here. However, the requirement for a physical solution to exist, known as the *Bohm sheath criterion*, yields important information concerning sheath formation. It states that a positive space charge sheath will form only when<sup>16</sup>

$$\phi_S(z) \leq - \frac{\kappa T_e}{2e} \quad (2.16)$$

or<sup>1</sup>

$$v_i(z) \geq \left[ \frac{\kappa T_e}{m_i} \right]^{1/2}, \quad (2.17)$$

is satisfied. Note that a pre-sheath exists for any  $\phi_S \neq 0$ . Physically, (2.16) implies that only when the potential applied to a surface exceeds a certain value will a space-charge sheath form. The alternative form, (2.17), states that the velocity of the ions impinging on the surface, acquired through acceleration by the pre-sheath, must exceed a critical value (the ion acoustic speed).

A particularly important consequence of sheaths in laboratory plasmas is that the proper reference potential is the *plasma* (or *space*) potential,  $\phi_P$ , assumed by the plasma due to wall sheaths.<sup>17</sup> If the walls are insulating,  $\phi_P$  may vary from point to point.<sup>18</sup> If they are grounded conductors, then  $\phi_P \equiv V_P$  by definition. Any insulator or floating metal object with an area small compared to that of the walls inserted into the plasma will assume the *floating* potential,  $\phi_F$ , which is negative with respect to the plasma potential.  $\phi_F$  arises from the same mechanism as  $\phi_P$ , but is not equal to  $\phi_P$  because it forms in the presence of an existing potential. If the surface area of an object exposed to the plasma is comparable to that of the wall, or perturbs the entire plasma in some manner, then  $\phi_P$  will change.<sup>19</sup> Note that the system ground, if one exists, is independent of both  $\phi_P$  and  $\phi_F$ .

## 2.2. REACTOR DESIGNS

The purpose of this section is to describe the various ECR reactor designs reported in the literature. The host of ECR processing applications will not be included as they are beyond the scope of this thesis.

The reader will probably not be surprised to learn that ECR systems come in a wide variety of styles. Different types of reactors can be distinguished through the different techniques with which ECR is produced. The basic technical issues which must be addressed in all ECR reactor designs are concerned with the magnetic field geometry and how the microwaves should be coupled into the plasma. There are two magnetic field geometries currently in use in ECR systems; the *divergent* and

*multipolar* field geometries, illustrated in figure 2.4. Divergent fields are simply dipole fields generated by solenoids encircling the plasma chamber, while multipole reactors use an arrangement of permanent magnets to form a cusp field configuration.

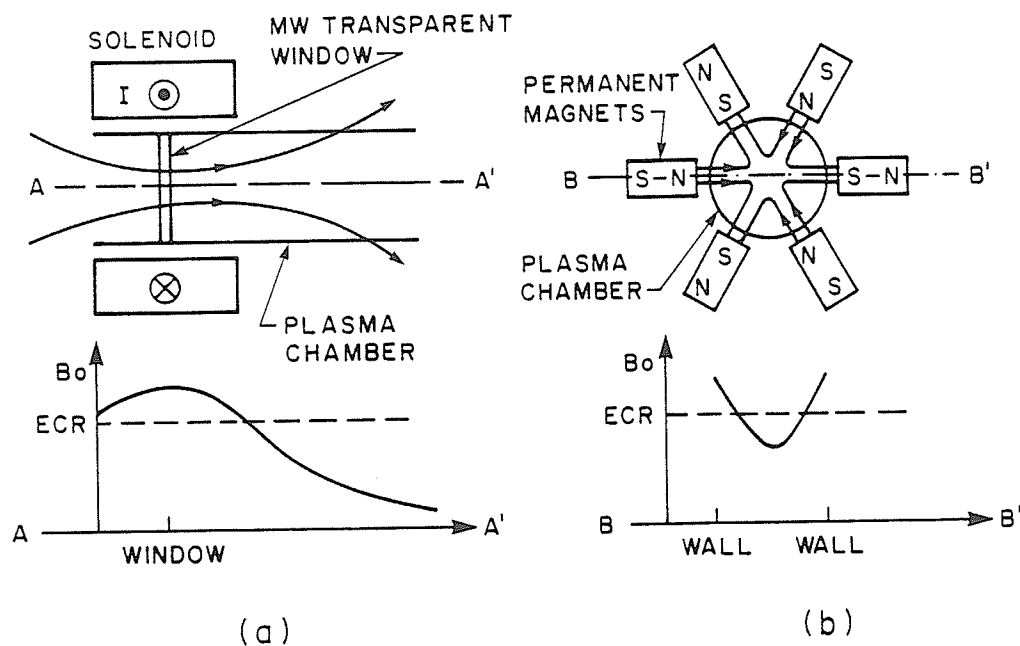


FIGURE 2.4. Basic magnetic field geometries used in ECR plasma processing systems. The top figure shows the basic geometry while the bottom graph shows the magnetic flux density along the noted axes. (a) Divergent field generated by a solenoid to form a magnetic beach. (b) Multipolar (hexapole) field generated by permanent magnets.

The microwaves can be coupled into the plasma using either a waveguide, resonant cavity or antenna. To be specific,<sup>20,21</sup> a waveguide is a hollow conducting pipe which supports a travelling wave, while a resonant cavity is a closed conducting cavity which supports a standing wave of high VSWR (voltage standing wave ratio). The "travelling wave" and "standing wave of high VSWR" provisos are to allow a functional distinction for antenna-based systems, which also use conducting tubes (but not to guide travelling waves) or cavities (but which are not resonant). Note that electrode-based (antenna) systems, which are common at radio frequencies, are generally not used to generate magnetised or ECR microwave plasmas.

### 2.2.1. Divergent Field Reactors

By far the most common type of ECR plasma processing reactor is the divergent field, or "reactive ion beam", type originally developed at Hitachi.<sup>22</sup> Another early design evolved from machines originally used to study problems related to fusion plasmas.<sup>23</sup> Most divergent field reactors in use today appear to be based upon the design developed at Nippon Telephone and Telegraph (NTT).<sup>24,25</sup> One implementation of the NTT design is shown in figure 2.5, in which most of the features of divergent field reactors can be seen. Designs of this type are commercially available from several sources and are widely used in applications.

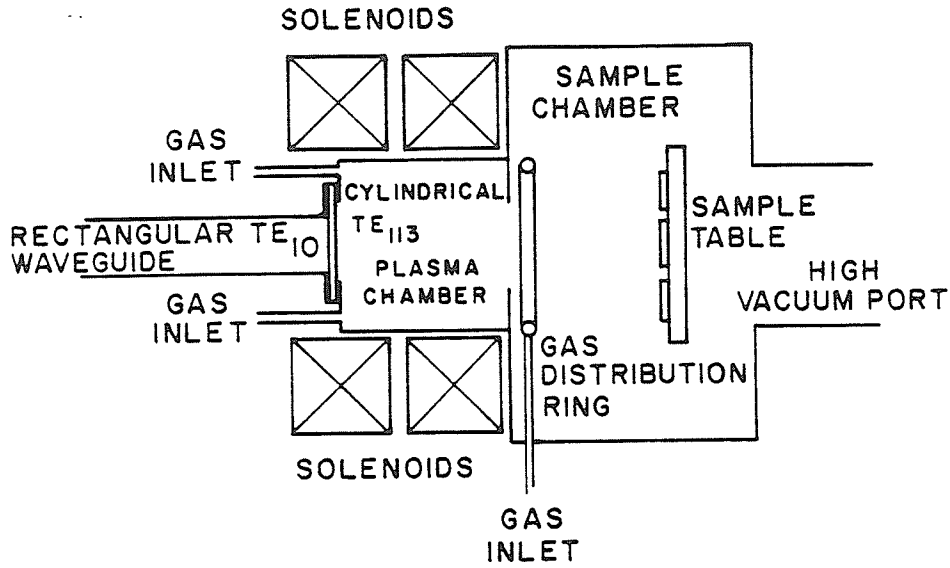


FIGURE 2.5. Representative divergent field ECR microwave plasma processing reactor. Taken from the U.S. NTT patent.<sup>25</sup>

Clearly many variations of this theme are possible, and many have been reported in the literature. The magnetic field profile can be modified through the use of iron structures<sup>25</sup> or additional magnets or coils.<sup>26,27</sup> DC or RF potentials can be applied to the sample table to either control the energy of impinging ions<sup>27,28,29</sup> or modify the plasma in front of the samples.<sup>30</sup> Sputtering targets could be added to provide a supply of material unavailable in gaseous form.<sup>26</sup> A true ion source can be implemented through the addition of an appropriate grid system on the plasma chamber orifice.<sup>31,32</sup> The resonant cavity can be replaced with a section of waveguide,<sup>27,29</sup> or replaced by an antenna structure, such as the Lisitano coil often used in fusion related work.<sup>33,34</sup> Also, the sample and plasma chambers can be combined.<sup>35,36,37,38</sup>

An interesting design has recently been developed by German researchers<sup>39,40</sup> and is being studied at Leybold AG. The plasma is generated across the aperture of a large microwave horn antenna and is used as a large area plasma source. To generate an approximately dipole magnetic field across the large antenna aperture, a circumferential arrangement of permanent magnets is used. However, the actual magnetic field configuration is such that significant microwave propagation occurs perpendicular to the magnetic field. Because of this, and the novelty of the design, it will not be considered further in this thesis.

Finally, a number of systems have been reported<sup>23,41,42</sup> which are basically magnetised versions of the early microwave discharge tube-in-waveguide designs.<sup>43</sup> These systems are not optimised for ECR operation, and are only rarely used.

### 2.2.2. Multipolar Reactors

There have been three multipolar ECR plasma processing systems reported in the literature. Only one, the so-called DECR (distributed ECR) reactor, developed at CNET (Centre National d'Etudes des Télécommunications) in France, is available commercially.<sup>44</sup> Unlike solenoid-based reactors, there is no representative multipolar ECR

system. Fortunately there are fewer variations to be considered. The DECR system is shown in figure 2.6. This system has a potential advantage over divergent field designs because it is a large volume reactor which is easily scaled up. Note that the reactor can be made planar, or with the antennas located on the outer surface of a cylinder to produce a central-source configuration.

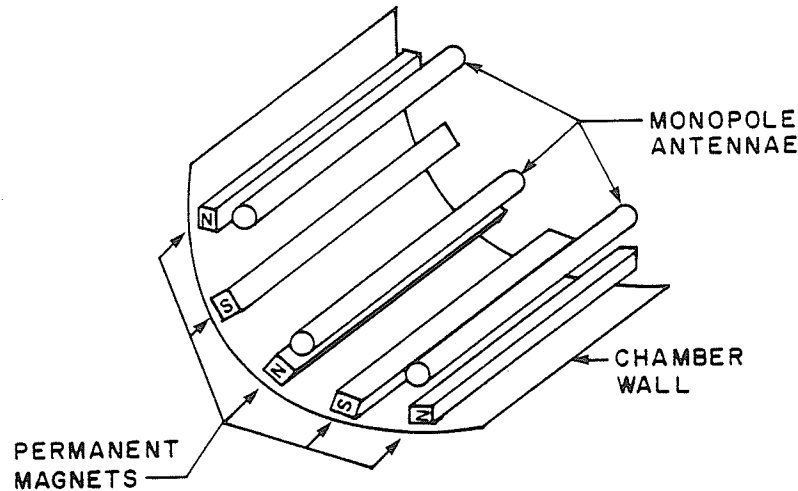


FIGURE 2.6. Design of the DECR multipolar microwave plasma processing reactor. Shown is an interior section of the plasma chamber. The rod antennas are located directly above the permanent magnets where the magnetic field exceeds that required for ECR. Microwaves are launched into the "ECR lobes", from which the plasma diffuses (across the magnetic field) into the center of the chamber. Taken from Pichot and Durandet.<sup>45</sup>

The predecessor of the DECR system was a hybrid multipole-solenoid design, where a standard divergent field plasma source launched plasma into a large multipolar chamber.<sup>46</sup> This system appears to have been abandoned in favour of the DECR design, which produces denser and more uniform plasmas.

The other multipole design consists of a resonant cavity containing a multipolar ring of permanent magnets, within which ECR conditions are produced, at one end of the cavity.<sup>47</sup> The plasma chamber is attached as a plasma source onto a larger chamber, as in divergent field reactors.

### 2.3. PLASMA CHARACTERISATIONS

The ECR plasma processing system studied in this thesis is basically a divergent field reactor. In this section the literature concerning plasma characterisations of divergent field ECR microwave plasma processing systems will be critically reviewed. Multipolar ECR reactors will not be considered here.

Few plasma characterisations of ECR processing systems have been reported in the literature. Given this, it must be noted that a number of these studies were performed by equipment manufacturer's and/or vendors, and that some of these studies may have been subject to a bias (conscious or not) to "play down", neglect or avoid features which may be considered undesirable by potential customers. Such features may include non-uniformities, discontinuous behaviours or anomalous properties.

However, these are often those features which are of most interest in efforts to model the plasma, since they can provide unique clues to the physical mechanisms important in the plasma. Papers from the following manufacturer's and/or vendors should be considered in this light: Hitachi Ltd.<sup>22</sup> Microscience Inc.<sup>48,49</sup> NTT<sup>26,31,50,51,52</sup> and Veeco Instruments Inc.<sup>32</sup>

The primary system variables that have been examined include  $B_0(z)$ , the incident ( $P_I$ ), reflected ( $P_R$ ) and absorbed ( $P_A = P_I - P_R$ ) microwave powers, the plasma chamber dimensions, and the neutral gas pressure ( $p$ ) and composition. The reactors are typically a few centimeters to tens of centimeters in diameter, and several tens of centimeters long. The walls of the plasma chambers are typically clean, electrically grounded stainless steel, although quartz discharge tubes or sleeves are sometimes used to isolate the plasma from the metal walls. The microwave power range extends from near 0 to over 2000 W, but is typically a few hundred Watts. The pressure range covers  $10^{-5}$  to  $10^{-1}$  Torr, but is usually restricted to the  $10^{-4}$  to  $10^{-3}$  range. The most commonly used gas is Ar, with  $H_2$ ,  $N_2$ ,  $O_2$  and  $CF_4$  also used.

### 2.3.1. Global Parameters

A global parameter is one which is characteristic of the plasma as a whole. Included under this label are breakdown and maintenance powers, power characteristics such as  $P_A$  versus  $P_I$ , shape and position.

The electrical breakdown of a gas into a magnetised microwave plasma has been considered in detail by MacDonald.<sup>5</sup> In general, the power required to ignite a plasma decreases drastically when ECR conditions are satisfied within the plasma chamber.<sup>5,23,38,48,53,54</sup> This is true regardless of magnetic field configuration, since this only influences microwave propagation once a plasma has formed. Breakdown powers decrease sharply as  $B_0$  increases towards ECR, but increase only gradually as  $B_0$  becomes greater than that required for ECR.<sup>5,38</sup> The observed width of the resonance, at or below about  $10^{-3}$  Torr, is approximately 0.02 Tesla.<sup>30,38</sup> The pressure range commonly used in ECR reactors ( $10^{-4}$  to  $10^{-2}$  Torr) is such that increasing  $p$  decreases the power required to ignite a plasma.<sup>5,53</sup>

It has been noted that while ECR allows for very efficient plasma generation, magnetic fields above that required for ECR produce significantly denser plasmas.<sup>22,23,31,38,55,56</sup> This is important because the plasma density is more important than the efficiency of generation in processing applications. The reason for the higher densities observed above ECR is not yet understood. Nonetheless, it appears that efficient high density operation requires a magnetic beach with an extended region of strong magnetic field preceding the ECR zone. In such configurations, ECR is primarily used to ignite the plasma, since the microwaves are mostly absorbed (generating dense plasma) before the ECR zone once the plasma has been formed.

The efficiency with which microwave power is absorbed by the plasma can be greatly enhanced through the use of external tuning devices designed to match the plasma chamber to the rest of the microwave circuit (minimise  $P_R$ ).<sup>38,48,49</sup> Matching is also affected by system variables such as  $B_0(z)$ ,  $P_I$ , and  $p$ .<sup>48,49</sup> The degree of matching can affect the visible shape and position of the plasma. The initial (unmatched) ECR plasma may be dim, have a large  $P_R$  and low  $n$ .<sup>48,49</sup> Matching the plasma chamber

impedance with that of the waveguide transmission line causes the plasma to suddenly increase in brightness. This bright plasma also exhibits a low  $P_R$  and high  $n$ .<sup>48,49</sup> The transition from the "dim" to the "bright" plasma exhibits *hysteresis* when accomplished by changing system variables such as  $B_0$ ,  $P_I$  and  $p$ .<sup>48,49</sup> The (radial) shape of the bright, matched plasma could be in the form of a cylindrical axial column, hollow cylindrical torus, or could be uniform.<sup>48,49</sup> The exact shape, size and position of the bright plasma region depends on the matching, and thus on  $P_I$ ,  $p$  and  $B_0(z)$ .

Plasmas like these, which exhibit stable properties over a limited range of conditions, but between which occur discontinuous transitions, will be called plasma *modes*. These modes appear to be a basic property of magnetised and ECR microwave plasmas, but no systematic studies have been reported in the literature. In chapter 5, global plasma properties are used to systematically investigate the modes which occurred in our ECR plasma processing system.

A number of studies found that increasing either  $P_I$  or  $p$  caused the plasma to gradually change shape from a column (no plasma near the walls) to a ring (no plasma on the axis).<sup>48,49</sup> A striking photograph of this phenomena is given by Miyake et al.<sup>57</sup> As will become apparent shortly, these shapes were also manifested in other properties of the plasma. As yet, no explanation has been offered for these observations.<sup>32,37,48,49,58</sup>

### 2.3.2. Plasma Density

The plasma density,  $n$ , in divergent field ECR processing reactors is highly variable since it depends on all system parameters to some degree. The range of  $n$  is about  $10^{16}$  to  $10^{18}$   $m^{-3}$ , averaging on the order of  $10^{17}$  under typical operating conditions.

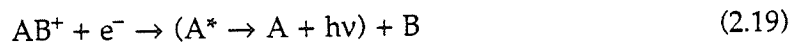
The plasma density was observed to decrease along the axis downstream of the ECR zone.<sup>30,37,48</sup> Indeed, the evidence appears to suggest that  $n$  follows  $B_0(z)$  directly,<sup>30,37,38</sup> especially in the downstream region. However, since the variation of  $B_0$  in this region is roughly exponential, this could merely be a coincidence resulting from the ubiquitous nature of exponential variations in physical phenomena. Nonetheless,  $n$  does increase with  $B_0$ ,<sup>26,30,37,38</sup> although the exact nature of this dependence remains unclear. In chapter 6, a non-simple magnetic field profile will be used in order to eliminate the possibility of a misleading coincidence between  $n$  and  $B_0$ .

Increasing the pressure should eventually eliminate any dependence of  $n$  on  $B_0$  once collisions with neutrals occur sufficiently often to prevent significant Larmor gyration. This was observed in both noble and molecular gases, but with different results in the two cases.<sup>30</sup> In Ar,  $n$  remained essentially constant along the axis, while it decreased significantly in  $O_2$  and  $CF_4$ . Not only does this data suggest that loss processes in noble and molecular gases are different at high  $p$ , but that the mechanism underlying plasma generation may have changed as well (the high  $p$  plasmas appear to be generated at the window, rather than at the ECR zone). As for the loss mechanisms, it was proposed that collision dominated diffusion (with a relatively long mean free path length) was responsible for the flat  $n$  profile in Ar, while

recombination was responsible for the decrease of  $n$  in the molecular gases.<sup>30</sup> Recombination in Ar proceeds through the three-body reaction



which has a very slow reaction rate under the conditions present.<sup>30</sup> However, dissociative recombination of the type<sup>14</sup>



takes place at a sufficiently high rate to account for the observed decay of charged species in the molecular gas plasmas.<sup>30</sup> Here, an \* denotes an excited state and  $h\nu$  a photon. The difference in these two processes implies that rare gases should not be used in plasma characterisations which purport to model the complex molecular gas mixtures used in applications (at least not at high  $p$ ). This is one reason why  $\text{H}_2$  was used in this thesis; it is the simplest of the molecular gases.

Sub-ECR Ar plasmas at low  $p$  also exhibited an  $n$  profile which decayed away from the microwave introduction window.<sup>38</sup> However, this was more likely the result of the formation of an extended region of decreasing plasma generation formed by non-resonant (collisional) absorption of the microwaves, rather than diffusion or recombination processes.

Some anomalous results were found in one study at low  $p$  ( $4 \times 10^{-5}$  Torr), where  $n$  was found to *increase* away from the ECR zone (down a divergent field).<sup>32</sup> The explanation offered for this phenomena is not particularly satisfying since it invokes the standard "magnetic beach" model of wave propagation (described in section 2.1.3) without an explanation of why plasma generation did not occur in, or even near, the ECR zone.

The dependence of  $n$  on the overall magnitude of  $B_0$  appears to be quite complex,<sup>31,32</sup> as the mechanism of plasma generation is affected. It does appear that a substantial increase in  $n$  occurs when the magnitude of the magnetic beach is sufficient for ECR to occur well away from the microwave introduction window,<sup>22</sup> but not so high that other (as yet unknown) effects begin to interfere with the plasma generation process.<sup>31,32</sup>

Different radial  $n$  profiles have been observed which appear correlated with the visible modes described in sub-section 2.3.1. The two most common modes occurring under ECR conditions have either a centrally peaked profile,<sup>30,48,58</sup> or a torus exhibiting a density minimum on the axis.<sup>32,58</sup> The former would be expected from the fundamental diffusion mode and from the fact that most of the radial profiles of system quantities (microwave field, magnetic field, neutral gas density) are either uniform or centrally peaked. No explanation has yet been given for the toroidal mode. However, as far as applications are concerned, it is probably fortunate that it does occur, since appropriate conditions can be chosen so as to "mix" the two modes to form an essentially flat radial density profile.<sup>32,48,58</sup> Such a profile is essential in commercial applications, where large-area uniformity is essential to the function of many end products.

Increasing  $P_A$  causes a linear to sublinear increase in  $n$  measured either directly in the ECR region<sup>23,37,48,49</sup> or downstream.<sup>31,53,58</sup> This result appears to be independent of the gas type ( $\text{Ar}$ ,  $\text{N}_2$ ,  $\text{O}_2$ ). Some evidence of saturation has been found at high power levels.<sup>53,58,23</sup> Some non-monotonic results were also found,<sup>32</sup> which have been

correlated to the formation of the toroidal density mode described above. The rate of increase of  $n$  with  $P_A$  has been observed to either decrease<sup>58</sup> or increase<sup>53</sup> with pressure. The latter results show other behaviours indicative of mode transitions, and so may not be typical.

In a related set of experiments,<sup>48,49</sup> the diameter of the plasma chamber was reduced while  $P_A$  (and all other system variables) was held constant.  $n$  was found to increase. This should have been expected, since it is the *power density*, ( $W/m^2$  or  $W/m^3$ ) which determines  $n$ .<sup>59</sup> Therefore, in scaling experiments such as these the total absorbed power must be reduced along with the chamber dimensions in order to keep the power density constant, otherwise the effects of power and dimension cannot be separated.

Interestingly, it was found that  $n$  in the ECR zone was higher in pulsed plasmas than in plasmas sustained by continuous microwave excitation.<sup>23</sup> No explanation for this result was offered, but somewhat different plasma generation mechanisms, or modes, may be suspected.

The data concerning the variation of  $n$  with  $p$  is quite consistent;  $n$  increases with  $p$  up to about  $10^{-3}$  Torr, above which saturation sets in.<sup>22,48,53,58</sup> This result was largely independent of  $P_A$ ,  $B_0(z)$ , chamber size and the location of the measurement.

Data outside the range of  $10^{-4}$  to  $10^{-2}$  Torr is relatively scarce. However, it does appear that  $n$  begins to decrease as  $p$  increases above  $10^{-3}$  Torr.<sup>58</sup> Below  $10^{-4}$  Torr the data is very non-monotonic and was affected by the formation of toroidal modes, as noted elsewhere in that study.<sup>32</sup>

It has been noted that the total ion current collected downstream can be larger than the flow rate of Ar atoms into the plasma chamber.<sup>58</sup> Thus a significant fraction of the ion population must be due to recycled\* neutrals, a fact which can have serious implications for applications. Since reaction *products* may contribute to  $n$ , but not towards the processing,  $n$  may not be as useful a figure of merit for ECR processing systems as has traditionally been assumed.

### 2.3.3. Electron Temperature

The electron temperature,  $T_e$ , of Ar processing plasmas falls within the range of 2 to 12 eV, averaging about 7 eV.<sup>22,26,30,32,38,48,58</sup> In molecular gases, under similar conditions,  $T_e$  varies over the same range, but with a lower average.<sup>23,30,48,49</sup>

$T_e$  was found to vary substantially along the axis of divergent field plasma chambers. Typically  $T_e$  drops rapidly away from the ECR zone, then decreases more slowly in the downstream plasma.<sup>38,48,49</sup> The rate of decrease increases with pressure, as does the magnitude of the decrease.<sup>38,49</sup> This is because increasing  $p$  increases the collision frequency and thus the rate at which the electrons thermally equilibrate with the neutral gas. Clearly this implies that  $T_e$  in the downstream plasma will depend

---

\* By recycled we mean ions which had previously adsorbed onto the collector, recombined with an electron (thus contributing to the current) and then desorbed back into the plasma as a neutral atom, only to be ionised again. A single atom may undergo this process several times before being evacuated from the plasma chamber. Thus it would appear as though each ion was multiply charged, and the collected current could exceed the input rate of neutral atoms.

upon  $p$ , as has been observed,<sup>58</sup> although it appears that in the ECR zone itself  $T_e$  is independent of  $p$ .<sup>49</sup> Note that one study found  $T_e$  to vary non-monotonically with  $p$  in the downstream region.<sup>22</sup> While no mechanism for this behaviour was given, it was correlated with changes in  $n$ , and may be indicative of mode changes in the plasma. The rate of decrease of  $T_e$  with  $p$  also appears to be less in plasmas where the microwaves are absorbed along an extended region, as in sub-ECR plasmas<sup>38</sup> or in plasmas with long ECR zones.<sup>48</sup> The radial  $T_e$  profile was only examined downstream of a visibly uniform plasma; no radial variation was observed.<sup>48</sup>

Increasing  $P_A$  increases the ionisation fraction, and thus  $n$ , rather than  $T_e$ .<sup>58</sup> No systematic change in  $T_e$  with  $P_A$  has been noted.<sup>58</sup> Only "irregular" variations,<sup>53</sup> in one case over a wide range of power,<sup>32</sup> were found. These may be indicative of mode transitions.

It has been claimed that the downstream magnetic field profile can influence  $T_e$ .<sup>26</sup> Specifically, it was stated that that forming a small mirror in the downstream region reduced  $T_e$  in the plasma behind the mirror. However, what the data actually appears to show is that increasing the *divergence* of the field increased  $T_e$ , but that the magnitude of the mirror had no effect on  $T_e$ . Also, this trend was no larger than scatter due either to error or mode transitions, and is therefore unconvincing. These probe measurements are also suspect for other reasons discussed at the end of this chapter. Since downstream control of  $T_e$  would be of considerable use in many applications, more work on this problem should be undertaken.

Only one study reported electron energy distribution function (EEDF) measurements.<sup>30</sup> Two measurements were made, under extremely different conditions, so the generality of these results is not known. The result was that the form of the EEDF was close to Maxwellian, but with a lower high energy tail. This was also found to be true even in the ECR zone.

#### 2.3.4. Potentials

The plasma potential,  $V_p$ , is a parameter of great practical importance ECR plasma processing reactors. All measurements of  $V_p$  in these systems to date have been made using the current-voltage characteristics of Langmuir probes. However, as will be discussed in sections 3.4.4 and 4.3.2, unless the probe dimensions in the plane perpendicular to  $B_0(z)$  are less than  $r_{Le}$  the true value of  $V_p$  cannot be reliably determined in this manner.<sup>18,60,61,62,63</sup> In this situation electron collection is confined to a *flux tube* consisting of an extended region of electron deficient plasma along  $B_0(z)$  with a cross section given by the intersection of the probe with the lines of magnetic flux.<sup>63</sup> Under these conditions electron collection is dependent on the rate of diffusion of electrons into, and rate of electron generation in, the flux tube. Thus the region of the probe characteristic near and above  $V_p$  is severely perturbed, and parameters extracted directly from this region (such as  $V_p$ ) will exhibit complex dependencies on  $B_0(z)$ ,  $p$  and inelastic collision processes.

Accurate determinations of  $V_p$ , assuming a Maxwellian EEDF, could be made using emissive probes,<sup>18,60</sup> very small Langmuir probes (section 3.4), or simply by calculation from the floating voltage,  $V_F$ , and  $T_e$  obtained from a standard thin-sheath probe (whether or not it satisfies the weak magnetic field condition described above,

see section 4.3). However, to the author's knowledge, none of the studies on ECR processing plasmas used any of these techniques. In fact, none of the studies even provided comparable measurements of  $T_e$  and  $V_P$  (or  $n$ ), even though they can all be obtained from a single probe characteristic!

With the above in mind, the behaviour of  $V_P$  as reported in the literature will now be described. Plasma potentials in ECR processing reactors tend to be low; ranging from 5 to 35 V under typical operating conditions, averaging about 20 V.  $V_P$  has been shown to both decrease<sup>48,49</sup> and to remain constant axially (irrespective of the shape of the downstream magnetic field profile).<sup>26</sup> In the former case,  $V_P$  was observed to follow  $n$ , and thus  $B_0(z)$ . No density measurements were provided for comparison in the latter study, although  $V_P$  was found to increase slowly with  $B_0(z)$ , as did  $n$ .<sup>26</sup> The radial profile of  $V_P$  well downstream of a visibly uniform ECR plasma was constant, as was  $B_0(r)$  and  $n$  (although  $V_P$  remained so over a larger radius than  $n$ ).<sup>48</sup>

$V_P$  appears to be either independent of,<sup>30</sup> or only weakly dependent on,<sup>49</sup>  $P_A$ . A weak dependence in the ECR region was attributed to changes in the radial shape and density profile of the plasma produced by increased power absorption.<sup>49</sup> This same study found that decreasing the size of the chamber enhanced the rate of increase of  $V_P$  over a constant  $P_A$  range. As mentioned earlier, this scaling data was not properly presented; the independent variable should have been the power density, not the total absorbed power. Also, the change in the axial profile of the plasma was not taken into account in this figure, even though several of the chamber radii were such that the waveguide was operating below cutoff.

The pressure dependence of  $V_P$  appears to be relatively straightforward;  $V_P$  decreases in an exponential-like manner over the range of  $10^{-4}$  to  $10^{-3}$  Torr as  $p$  increases.<sup>30,48</sup>

The floating voltage is easily measured with Langmuir probes and is unaffected by the presence of magnetic fields as long as  $r_{Li}$  is much larger than the probe radius. Unfortunately,  $V_F = V_P + \phi_F$  is meaningful only relative to  $V_P$ . Several studies have examined the behaviour of  $V_F$  in ECR plasma processing systems,<sup>23,37,49</sup> but none provided simultaneous reliable measurements of  $V_P$ , or of  $T_e$  from which  $V_P$  could be calculated. Variations in  $V_F$  are impossible to explain unless reliable measurements of the more fundamental quantities are provided. For example,  $V_F$  typically shows a strong decrease in the ECR zone.<sup>37</sup> Assuming  $V_P$  to be constant, probe theory states (see sub-section 4.3.2 for details) that this is a direct result of an increase in  $T_e$ , which is just what is observed.<sup>33</sup>

Considerably more work is called for in the area of potential measurements in ECR processing plasmas, especially given their importance in applications. As will be discussed next, their effect on ion energies is particularly significant.

### 2.3.5. Ion Energy

It is conventionally assumed that the temperature, or mean kinetic energy, of ions in a microwave plasma is near that of the neutral gas, since most of the microwave energy is coupled directly to the electrons.<sup>7</sup> However, measurements have shown that ions in ECR microwave processing plasmas exhibit distinctly non-thermal,

beam-like energy distributions, with mean energies ranging from less than 1 eV to more than 50 eV.<sup>26,38,7,64</sup> These high ion energies can arise from the ion generation process and/or acceleration by spatially non-uniform potentials.

As an example of the first process consider the dissociation of H<sub>2</sub> by electron impact.<sup>65</sup> This is a Franck-Condon\* process with a dissociation energy of 8.8 eV. Since the bond energy is only 4.5 eV, each H atom carries away 2.15 eV of kinetic energy. Subsequent ionisation of the H atoms produces energetic H<sup>+</sup> ions. This process has been invoked to explain the ion energies observed in H<sub>2</sub> plasmas generated with a Lisitano coil,<sup>7</sup> and may have been responsible for the high ion energies observed by optical emission spectroscopy in O<sub>2</sub> divergent field plasmas.<sup>64</sup> In most situations however, this mechanism is probably secondary to direct acceleration by non-uniform electrostatic potentials since large ion energies have also been observed in Ar plasmas.<sup>26,64,67</sup>

The kinetic energy of an ion at an arbitrary point in the plasma,  $r$ , is given by

$$E_i(r) = E_i(r_0) + V_p(r_0) - V_p(r), \quad (2.20)$$

where  $r_0$  denotes the ion's point of origin and  $E_i$  denotes the ion's kinetic energy. The energy of an ion impinging on a surface is given by (2.20) with  $V_p(r)$  replaced by  $V_F$  for a floating or insulating object, or some DC bias value resulting from an applied voltage. Note that the width of the ion energy profile in this model depends directly on the amount of spatial variation of  $E_i(r_0) + V_p(r_0)$  in the ion generation region.<sup>7,26</sup>

Increasing  $p$  decreases both the magnitude of, and variation in,  $E_i$ .<sup>26,7,67</sup> This could be a result of enhanced cooling through collisions with neutrals<sup>7</sup> and/or to a decrease in the magnitude and variation of  $V_p(r_0)$ .<sup>26</sup> Recall from the previous subsection that  $V_p$  does in fact decrease with  $p$ .

Changing the shape and magnitude of  $B_0(z)$  also influences  $E_i$ , through  $V_p$ , by changing the diffusion process from which  $V_p$  develops.<sup>67</sup> In particular, it was found that a magnetic mirror in the downstream plasma could act as an ion energy filter; increasing the strength of the mirror decreased both the magnitude<sup>26,67</sup> and variation<sup>26</sup> of  $E_i$ .

A full understanding of  $E_i$  will require a firm grasp of diffusion in non-uniform, magnetised plasmas, since this determines the potential profiles. The development of such a model will require more accurate and extensive spatially-resolved plasma characterisations. This should be given a high priority in view of the importance of ion energy in applications.<sup>17,58</sup> The spatial variation of the plasma parameters and potentials is the focus of chapter 6.

#### 2.4. MODELLING ECR PROCESSING PLASMAS

In this section the assumptions of the Lorentz gas model of ECR processing plasmas will be examined in the light of the experimental data. Since only order of magnitude estimates are required, it will be convenient to define a "standard" ECR

---

\* The Franck-Condon principle states, in part, that the time required for an electronic transition, such as ionisation, is extremely short compared to the molecular vibrational period, so that the internuclear distance is constant during such a transition.<sup>66</sup>

processing plasma:

neutral gas type	Ar
neutral gas pressure	$p_n = 0.133 \text{ Pa } (10^{-3} \text{ Torr})$
neutral gas temperature	$T_n = 300 \text{ K}$
electron temperature	$T_e \approx 10 \text{ eV (Maxwellian)}$
ion energy	1 eV (non-thermal, beam-like)
plasma density	$n \approx 10^{17} \text{ m}^{-3}$
microwave frequency	$f = 2.45 \text{ GHz}$
magnetic flux density	$B_0 = 0.0875 \text{ Tesla (875 Gauss; ECR)}$
minimum chamber dimension	$L = 10 \text{ cm}$

TABLE 2.1. Parameters of a "standard" ECR microwave processing plasma.

Quasi-neutrality was required in order for the discharge to behave like a plasma and so that the plasma approximation could be used. Quasi-neutrality is guaranteed in an electron-ion plasma if  $\lambda_D \ll L$ . Applying (2.15) for  $\lambda_D$  to the standard plasma yields  $\lambda_D = 75 \mu\text{m}$ , so this condition is well satisfied. In addition, since both positively and negatively charged particles are generated in abundance (there are a large number of each within a sphere of radius  $\lambda_D$ ), screening prevents any significant imbalance of charge from developing in the bulk plasma.

The electron population has been shown by direct measurement to be well described by an approximately Maxwellian distribution with some Druvestyn character.<sup>30</sup> While this conclusion is based on a single pair of measurements, the result is that expected for a magnetised microwave Lorentz gas (see before sub-section 2.1.1). The positive ion population, however, has been shown to exhibit a distinctly beam-like, non-thermal character. Thus the assumption of a cold, immobile ionic background is incorrect. However, the very large mass of the ions as compared to the electrons implies that the electrons can respond essentially instantaneously to ionic motions, so this assumption can still be used to a first approximation when modelling wave phenomena. These ions beams are a product of diffusion-related phenomena, and so cannot be neglected in discussions of this problem, nor can they be ignored when considering the design and interpretation of Langmuir probes, which can be sensitive to plasma flow.

That ECR processing plasmas are weakly ionised can be seen from the degree of ionisation in the plasma, which is given by

$$\alpha \equiv \frac{n}{n_n + n} , \quad (2.21)$$

where  $n_n$  is the density of neutral gas particles. This can be estimated from the Boltzmann form of the ideal gas law;

$$p_n = n_n k T_n , \quad (2.22)$$

which yields  $n_n = 3 \times 10^{19} \text{ m}^{-3}$  in the standard plasma. Thus  $\alpha$  is typically on the order of 1%, and can reach values as high as 10 to 20% under extreme conditions. While this is very high compared to most processing plasmas, it does not correspond to a fully

ionised gas, and collisions with neutrals will play a role in the dynamics of the plasma, as in wave damping and diffusion across  $B_0$ .

The role of collisions is characterised by the collision frequencies,  $\nu_{jk}$  (between a test particle of species  $j$  and a field particle of species  $k$ ), and the mean free path lengths,  $l_{jk}$ . These are related through<sup>1</sup>

$$l_{jk} = \frac{v_j}{\nu_{jk}}, \quad (2.23)$$

where  $v_j$  is the individual test particle speed. This will be assumed to be given by the *most probable* speed for this (Maxwellian distributed) species,<sup>1</sup>

$$v_j = \left( \frac{2kT_j}{m_j} \right)^{1/2}. \quad (2.24)$$

For a 10 eV electron,  $v_e = 2 \times 10^6$  m/s, while for room temperature Ar atoms,  $v_n = 350$  m/s.

For collisions between neutral particles,  $l_{nn}$  can be estimated with good accuracy using the hard-sphere ideal gas relation<sup>68</sup>

$$l_{nn} = \frac{kT_n}{\sqrt{2}\pi\delta^2 p_n}, \quad (2.25)$$

where  $\delta$  is the collision diameter of the neutral molecules. For Ar,  $\delta = 0.364$  nm, for  $H_2$   $\delta = 0.275$  nm. Values of  $\delta$  for other common gases are given by Dushman.<sup>68</sup> Under our standard conditions  $l_{nn} \approx 5$  cm, which is significant in neutral gas flow problems (sub-section 3.1.2). However, the collision frequency between neutral particles,  $\nu_{nn}$ , is a negligible 7 kHz due to the low value of  $T_n$ .

Electron-neutral collision cross sections are generally complex functions of velocity, so it is more convenient to obtain  $\nu_{en}$  from empirical data than from calculation. For this purpose we will use the  $\nu_{en}/p_n$  versus kinetic energy graphs provided by MacDonald.<sup>5</sup> The electron energy will be assumed to be given by the most probable energy of a single electron in a population described by a Maxwellian distribution, which is just  $kT_e$ .<sup>14</sup> It should be pointed out that  $\nu_{en}/p_n$  is essentially constant with respect to energy in  $H_2$ , at approximately  $5 \times 10^9$  (s·Torr)<sup>-1</sup>. This simple behaviour was one reason why  $H_2$  may be preferred over more complex gases such as Ar in fundamental plasma studies. Regardless, for a 10 eV electron in Ar,  $\nu_{en}/p_n = 13.5 \times 10^9$  (s·Torr)<sup>-1</sup>. Therefore at  $10^{-3}$  Torr,  $\nu_{en} = 13.5$  MHz and  $l_{en} = 15$  cm.

Charged particle collisions do not contribute significantly to the dynamics of ECR processing plasmas since  $n$  is too low. This can be seen by calculating  $\nu_{ei}$ ,  $\nu_{ee}$  and  $\nu_{ii}$  from the "handy" formulas provided by Chen.<sup>1</sup> All three parameters are found to be less than 100 kHz. This is much less than  $\nu_{en}$ , which in turn is much less than  $\omega$ . Because of the high velocities involved, the mean free path lengths are on the order of tens of meters, much larger than  $L$ . Also, like-particle collisions do not contribute significantly to diffusion,<sup>1</sup> and so are further reduced in importance.

The net result is that electron-neutral collisions are indeed the dominant collision process. However, since  $\nu_{en} \ll \omega$ ,  $\omega_{pe}$ ,  $\omega_{ce}$ , they can be considered of secondary, though not negligible, importance in wave and diffusion processes.

The fact that  $l_{en} > L$  may, at first glance, suggest that the diffusion equation does not apply to ECR processing plasmas. However, ECR plasmas are strongly magnetised, which means that the mean free path length for charged particles diffusing across  $B_0$  is effectively  $r_L$ , not  $l$ .<sup>1,5</sup> The effect of  $B_0$  on charged particle diffusion can be seen in the ratio

$$\frac{D_x}{D_F} = \frac{v^2}{\omega_c^2 + v^2}, \quad (2.26)$$

which is approximately  $3 \times 10^{-5}$  for electrons in the standard plasma, but only on the order of 1 for the ions. Thus electrons are very well confined, but ions are not. Looking directly at the Larmor radii, applying (2.1) and (2.24) to the standard plasma, we find  $r_{Le} \approx 0.12$  mm and  $r_{Li} \approx 10$  mm. This asymmetry in the transport of charged particles implies that ambipolar diffusion in an ECR reactor will be dominated by the electrons radially (since they are the "slower" species) but by the ions axially (as in the unmagnetised case). In general, any radial confinement at all leads to a larger axial flux of plasma than would result simply from unmagnetised ambipolar diffusion, or from acceleration by  $\nabla B_0$  forces.

Finally, some comments on the problems which need to be addressed by any modelling effort will be made. It should be clear from the previous section that neither the generation or loss mechanisms operating in ECR processing plasmas are well understood. While some attempts have been made to explain the exact nature of the microwave power absorption mechanism(s), the origins of the plasma structures and modes remains unclear at best. Certainly no *predictive* model has been developed. Intimately connected with the generation problem is the question of plasma loss. Developing an accurate model of the diffusion process under the complicated conditions found in ECR processing plasmas will be difficult. Yet this is perhaps the more important modelling task, given the importance of charged particle transport to processing parameters such as uniformity and ion energy.

Unfortunately, there remain more basic problems to be addressed before serious modelling efforts can be undertaken. Though it may appear from the sections 2.3 and 2.4 that the behaviour of the basic plasma properties of divergent field ECR systems are well understood, this is not the case. As should be clear from section 2.3, many of the results are anomalous, inconsistent and/or outright contradictory. The possible influence of plasma "modes", a largely unrecognised problem, only adds to the confusion. Worse still, some results are presented in such a disconnected manner that they bring into question the validity of the results themselves.

Disconnected data sets come in a range of forms. Graphs of plasma parameters such as  $n$  and  $T_e$ , which should have come from the *same* measurements, are sometimes presented under different conditions or at different values of the independent variable. Conspicuous gaps in data which are not accounted for can often be seen. Occasionally, independent variables are mixed, as in obtaining a magnetic field dependence through measurements at different *positions* (since  $B_0$  is a function of  $z$ ), or disguised (as in presenting  $z$  in "arbitrary units") or left out completely (often the case with chamber dimensions).

As an example of the kind of confusion that can arise from incomplete sets of measurements, we consider a study<sup>26</sup> which observed a decrease in  $V_F$  (increased negatively) in the downstream region while  $V_P$  remained essentially constant. These results were presented without any discussion of how extraordinary they were:  $V_F$  depends on  $V_P + \phi_F$ , where  $\phi_F$  is directly proportional to  $-T_e$  (see (4.5) in sub-section 4.3.2). Any increase in  $|V_F - V_P|$  must be a direct result of an increase in  $T_e$ . Therefore, the results reported in this paper imply that  $T_e$  increases in the downstream region by as much as 3 eV, in complete contradiction of both expectation and experiment! Of course, no corresponding spatial results concerning  $T_e$  (which must have been obtainable from the same I-V curves from which the potentials were obtained) were provided.

In this thesis we propose to make some initial efforts in resolving some of these problems. This will be accomplished in three steps. The first involves finding diagnostic procedures which will allow reliable and informative measurements to be made under the complex conditions found in these systems. The next step will be to determine what regimes of operation may be most profitably studied; this primarily means finding a way to either eliminate or deal with the modal behaviours in the plasma. Finally, the chosen regime(s) of operation will be thoroughly characterised, such that a complete and fully consistent set of data are obtained. The hope is that such results will lend themselves to interpretation in terms of theory and other experiments so that our understanding of the physics of ECR processing plasmas is improved.

#### References

1. F.F. Chen, *Introduction to Plasma Physics and Controlled Fusion, Vol. 1: Plasma Physics, 2nd Edn.*, Plenum, New York, 1984.
2. B.S. Tanenbaum, *Plasma Physics*, McGraw-Hill, New York, 1967.
3. W.P. Allis, S.J. Buchsbaum, and A. Bers, *Waves in Anisotropic Plasmas*, M.I.T. Press, Cambridge, 1963.
4. R.N. Franklin, *Plasma Phenomena in Gas Discharges*, Clarendon Press, Oxford, 1976.
5. A.D. MacDonald, *Microwave Breakdown in Gases*, John Wiley & Sons, New York, 1966.
6. M. Hirose, "Glow Discharge," in *Semiconductors and Semimetals Vol. 21: Hydrogenated Amorphous Silicon, Pt. A*, ed. J.I. Pankove, p. 9, Academic, Orlando, 1984.
7. I.G. Brown, "Ion Temperature in a 'Cold' Microwave-Produced Plasma," *Plasma Physics* 18, p. 205, 1976.
8. G. Francis, *Ionization Phenomena in Gases*, Butterworths, London, 1960.
9. D.G. Swanson, *Plasma Waves*, Academic Press, Boston, 1989.
10. W.P. Allis, S.C. Brown, and E. Everhart, "Electron Density Distribution in a High Frequency Discharge in the Presence of Plasma Resonance," *Phys. Rev.* 84, p. 519, 1951.
11. M. Venugopalan and R. Avni, "Analysis of Glow Discharges for Understanding the Process of Film Formation," in *Thin Films from Free Atoms and Particles*, ed. K.J. Klabunde, p. 49, Academic, Orlando, 1985.
12. M.J. Kushner, "Monte-Carlo Simulation of Electron Properties in RF Parallel Plate Capacitively Coupled Discharges," *J. Appl. Phys.* 54, p. 4958, 1983.
13. T.H. Stix, *The Theory of Plasma Waves*, McGraw-Hill, New York, 1962.
14. E. Nasser, *Fundamentals of Gaseous Ionization and Plasma Electronics*, Wiley Interscience, New York, 1971.
15. S.C. Brown, *Introduction to Electrical Discharges in Gases*, John Wiley & Sons, New York, 1966.

16. L. Schott; "Electrical Probes," in *Plasma Diagnostics*, ed. W. Lochte-Holtgreven, p. 668, North-Holland, Amsterdam, 1968.
17. J.W. Coburn, *Plasma Etching and Reactive Ion Etching*, Am. Vac. Soc. & Am. Inst. Phys., New York, 1982.
18. I.H. Hutchinson, *Principles of Plasma Diagnostics*, p. 50, Cambridge University press, Cambridge, U.K., 1987.
19. J.W. Coburn and E. Kay, "Positive Ion Bombardment of Substrates in RF Diode Glow Discharge Sputtering," *J. Appl. Phys.* 43, p. 4965, 1972.
20. R.A. Waldron, in *Theory of Guided Electromagnetic Waves*, Van Nostrand Reinhold, London, 1969.
21. G.C. Southworth, *Principles and Applications of Waveguide Transmission*, D. Van Nostrand, Princeton, 1950.
22. K. Suzuki, S. Okudaira, N. Sakudo, and I. Kanomata, "Microwave Plasma Etching," *Jpn. J. Appl. Phys.* 11, p. 1979, 1977.
23. G. Lončar, J. Musil, and L. Bárdoš, "Present Status of Thin Oxide Films Creation in a Microwave Plasma," *Czech. J. Phys. B* 30, p. 688, 1980.
24. S. Matsuo and Y. Adachi, "Reactive Ion Beam Etching Using a Broad Beam ECR Ion Source," *Jpn. J. Appl. Phys.* 21, p. L4, 1982.
25. S. Matsuo, H. Yoshihara, and S. Yamazaki, *Plasma Deposition Apparatus*, United States Patent No. 4,401,054, 1983.
26. M. Matsuoka and K. Ono, "Magnetic Field Gradient Effects on Ion Energy for Electron Cyclotron Resonance Microwave Plasma Stream," *J. Vac. Sci. Technol. A* 6, p. 25, 1988.
27. K. Suzuki, A. Hiraiwa, S. Takahashi, S. Nishimatsu, K. Ninimiya, and S. Okudaira, *Method for Growing Silicon-Including Film by Employing Plasma Deposition*, United States Patent No. 4,481,229, 1984.
28. K. Suzuki, K. Ninomiya, S. Nishimatsu, and S. Okudaira, "Radio-Frequency Biased Microwave Plasma Etching Technique: A Method to Increase SiO<sub>2</sub> Etch Rate," *J. Vac. Sci. Technol. B* 3, p. 1025, 1985.
29. K. Suzuki, K. Ninomiya, and S. Nishimatsu, "Microwave Plasma Etching," *Vacuum* 34, p. 953, 1984.
30. Y.H. Lee, J.E. Heidenreich III, and G. Fortuno, "Plasma Characterization of an Electron Cyclotron Resonance-Radio-Frequency Hybrid Plasma Reactor," *J. Vac. Sci. Technol. A* 7, p. 903, 1989.
31. Y. Torii, M. Shimada, and I. Watanabe, "Very High Current ECR Ion Source for an Oxygen Ion Implanter," *Nucl. Instrum. Meth. Phys. Res. B* 21, p. 178, 1987.
32. E. Ghanbari, I. Trigor, and T. Nguyen, "A Broad-Beam Electron Cyclotron Resonance Ion Source for Sputtering Etching and Deposition of Material," *J. Vac. Sci. Technol. A* 7, p. 918, 1989.
33. B.W. Rice and J.E. Scharer, "Observation of Localized Electron Cyclotron Resonance Heating in a Magnetic Mirror," *IEEE Trans. Plasma Sci.* PS-14, p. 17, 1986.
34. Y. Suetsugu and Y. Kawai, "RF Field Distribution in a Slotted-Type Lisitano Coil," *Jpn. J. Appl. Phys.* 23, p. 1101, 1984.
35. S.R. Mejia, R.D. McLeod, K.C. Kao, and H.C. Card, "Electron-Cyclotron Resonant Microwave Plasma System for Thin-Film Deposition," *Rev. Sci. Instrum.* 57, p. 493, 1986.
36. J. Musil, "Microwave Plasma: Its Characteristic and Applications in Thin Films Technology," in *IPAT'85, 5th Int'l. Conf. on Ion & Plasma Assisted Techniques, Munich, 1985*, p. 463, CEP Consultants, Edinburgh, 1985.
37. L. Bárdoš and J. Musil, "Axial Decaying of the Microwave ECR Oxygen Plasma," *J. Phys. D: Appl. Phys.* 21, p. 1459, 1988.
38. H. Fujita, H. Handa, M. Nagano, and H. Matsuo, "Characteristics of Microwave Plasma and Preparation of a-Si Thin Film," *Jpn. J. Appl. Phys.* 26, p. 1112, 1987.
39. K.-H. Kretschmer, K. Matl, G. Lorenz, I. Kessler, and B. Dumbacher, "An Electron Cyclotron Resonance (ECR) Plasma Source," *Solid State Technology*, p. 53, February 1990.
40. M. Geisler, J. Kieser, E. Räuchle, and R. Wilhelm, "Elongated Microwave Electron Cyclotron Resonance Heating Plasma Source," *J. Vac. Sci. Technol. A* 8, p. 908, 1990.

41. S. Kato and T. Aoki, "High-Rate Deposition of a-Si:H Using Electron Cyclotron Resonance Plasma," *J. Non-Cryst. Solids* 77 & 78, p. 813, 1985.
42. A. Chayahara, A. Masuda, T. Imura, and Y. Osaka, "Formation of Polycrystalline SiC in ECR Plasma," *Jpn. J. Appl. Phys.* 25, p. L564, 1986.
43. S.R. Goode and K.W. Baughman, "A Review of Instrumentation Used to Generate Microwave-Induced Plasmas," *Appl. Spectroscopy* 38, p. 755, 1984.
44. R.R. Burke and C. Pomot, "Microwave Multipolar Plasma for Etching and Deposition," *Solid State Technol.*, p. 67, Feb. 1988.
45. M. Pichot, A. Durandet, J. Pelletier, Y. Arnal, and L. Vallier, "Microwave Multipolar Plasmas Excited by Distributed Electron Cyclotron Resonance: Concept and Performance," *Rev. sci. Instrum.* 59, p. 1072, 1988.
46. L. Pomathiod, R. Debie, Y. Arnal, and J. Pelletier, "Microwave Excitation of Large Volumes of Plasma at Electron Cyclotron Resonance in Multipolar Confinement," *Physics Letters* 106A, p. 301, 1984.
47. J. Asmussen, "Electron Cyclotron Resonance Microwave Discharges for Etching and Thin-Film Deposition," *J. Vac. Sci. Technol. A* 7, p. 883, 1989.
48. O.A. Popov, "An Electron Cyclotron Resonance Plasma Stream Source for Low Pressure Thin Film Production," *Surf. Coat. Technol.* 36, p. 917, 1988.
49. O.A. Popov, "Characteristics of Electron Cyclotron Resonance Plasma Sources," *J. Vac. Sci. Technol. A* 7, p. 894, 1989.
50. S. Matsuo, M. Kiuchi, and T. Ono, "ECR Low-Energy Ion Equipment and its Application to Deposition and Etching," *Proc. 10th Symp. on Ion Sources and Assoc. Tech. (ISLAT), Tokyo*, p. 471, 1986.
51. M. Matsuoka and K. Ono, "Low-Energy Ion Extraction with Small Dispersion from an Electron Cyclotron Resonance Microwave Plasma Stream," *Appl. Phys. Lett.* 50, p. 1864, 1987.
52. M. Matsuoka and K. Ono, "Ion Energy Analysis for Sputtering-Type Electron-Cyclotron-Resonance Microwave Plasma," *J. Appl. Phys.* 64, p. 5179, 1988.
53. C. Keqiang, Z. Erli, W. Jinfa, Z. Hansheng, G. Zuoyao, and Z. Bangwei, "Microwave Electron Cyclotron Resonance Plasma for Chemical Vapor Deposition and Etching," *J. Vac. Sci. Technol. A* 4, p. 828, 1986.
54. P.K. Shufflebotham, D.J. Thomson, and H.C. Card, "Behavior of Downstream Plasmas Generated in a Microwave Plasma Chemical-Vapor Deposition Reactor," *J. Appl. Phys.* 64, p. 4398, 1988.
55. N. Sakudo, K. Tokiguchi, H. Kioke, and I. Kanomata, "Microwave Ion Source," *Rev. Sci. Instrum.* 48, p. 762, 1977.
56. W. Hale, "ECR - Perspectives on a New Technology," *Micro. Manufac. Testing*, p. 22, November 1989.
57. K. Miyake, S. Kimura, T. Warabisako, H. Sunami, T. Tokuyama, "Microwave Plasma Stream Transport System for Low Temperature Plasma Oxidation," *J. Vac. Sci. Technol. A* 2, p. 496, 1984.
58. J. Forster and W. Holber, "Plasma Characterisation for a Divergent Field Electron Cyclotron Resonance Source," *J. Vac. Sci. Technol. A* 7, p. 899, 1989.
59. M. Moisan and Z. Zakrzewski, "Plasmas Sustained by Surface Waves at Microwave and RF Frequencies: Experimental Investigation and Applications," in *Radiative Processes in Discharge Plasmas*, ed. L.H. Leussen, p. 381, Plenum, 1986.
60. N. Hershkowitz, "How Langmuir Probes Work," in *Plasma Diagnostics Vol. 1; Discharge Parameters and Chemistry*, ed. O. Auciello, D.L. Flamm, p. 113, Academic, Boston, 1989.
61. P.M. Chung, L. Talbot, and K.J. Touryan, *Electric Probes in Stationary and Flowing Plasmas: Theory and Application*, Springer-Verlag, New York, 1975.
62. J.D. Swift and M.J.R. Schwar, *Electrical Probes for Plasma Diagnostics*, Illife, London, 1969.
63. F.F. Chen, "Electric Probes," in *Plasma Diagnostic Techniques*, ed. S.L. Leonard, p. 113, Academic, New York, 1965.
64. J.S. McKillop, J.C. Forster, and W.M. Holber, "Optical Emission Characterisation of a Divergent Magnetic Field Electron Cyclotron Resonance Source," *J. Vac. Sci. Technol. A* 7, p. 908, 1989.

65. A. von Engel, in *Electric Plasmas, Their Nature and Uses*, Taylor & Francis, New York, 1983.
66. S. Glasstone and D. Lewis, *Elements of Physical Chemistry, 2nd Edn.*, D. Van Nostrand, Toronto, 1960.
67. J.S. McKillop, J.C. Forster, and W.M. Holber, "Doppler Profile Measurement of Ar and Ar<sup>+</sup> Translational Energies in a Divergent Magnetic Field Electron Cyclotron Resonance Source," *Appl. Phys. Lett.* 55, p. 30, 1989.
68. S. Dushman, *Scientific Foundations of Vacuum Technique, 2nd Edn.*, John Wiley & Sons, New York, 1962.

## CHAPTER 3

### EXPERIMENTAL APPARATUS AND METHODS

*Though this be madness, yet there is method in't.*  
- William Shakespeare, *Hamlet*.

In this chapter the ECR plasma processing system and associated diagnostic apparatus will be described. This system consisted of four major sub-assemblies; the vacuum and gas-handling system, the microwave circuit, the plasma chamber and the Langmuir probe data acquisition system.

#### 3.1. VACUUM AND GAS-HANDLING SYSTEM

Before beginning this section some comments concerning the pressure measurements reported in this thesis are necessary. After the thesis had been submitted to the examining committee, it was discovered (through the purchase of a second pressure gauge) that the capacitance manometer used for all the experiments reported in this thesis had been mis-calibrated in the factory, and that all pressures were actually *ten times* greater than indicated! All references to, and calculations using, the incorrect pressure values have been corrected by replacing  $p$  with  $10p$ . The effect of this on the thesis is minimal, since the *absolute value* of  $p$  was of little concern as long as it was low enough that collisions did not significantly obscure the Larmor gyration of the electrons (valid for  $p < 10$  Torr).<sup>1</sup>

##### 3.1.1. Apparatus

Figure 3.1 shows a schematic diagram of the main vacuum and gas-handling components of the ECR plasma processing system. All gas and vacuum fittings were constructed of stainless steel in order to minimise the effects of corrosion. Compressed metal-on-metal connections were used throughout (Conflat vacuum flanges and Swagelock gas fittings).

The plasma chamber was evacuated with a turbomolecular pump (Alcatel UM2020 CP) backed by a rotary pump (Alcatel 2012 AC) equipped with an oil (Fomblin) designed for use with chemically reactive gasses. The pressure in the chamber was monitored with a capacitance manometer (MKS Baratron 590) capable of operating accurately above  $10^{-4}$  Torr. The composition of the base vacuum was monitored with a residual gas analyser (Inficon Quadrex 200), which was also used to zero the capacitance manometer. The base vacuum attainable was typically near  $5 \times 10^{-6}$  Torr, and consisted primarily of water vapour. A 200 °C bakeout for a few hours was required to return to these conditions after exposing the chamber to air.

The flow of gas into the chamber was controlled by an electronic flow meter (MKS 2259B) and flow controller (MKS 247B) equipped with gas calibration and automatic set-point controls. All gas lines were filtered to remove particulates larger than 0.2  $\mu\text{m}$ .  $\text{H}_2$  gas, 99.999% pure, chosen for its analytically simple and well

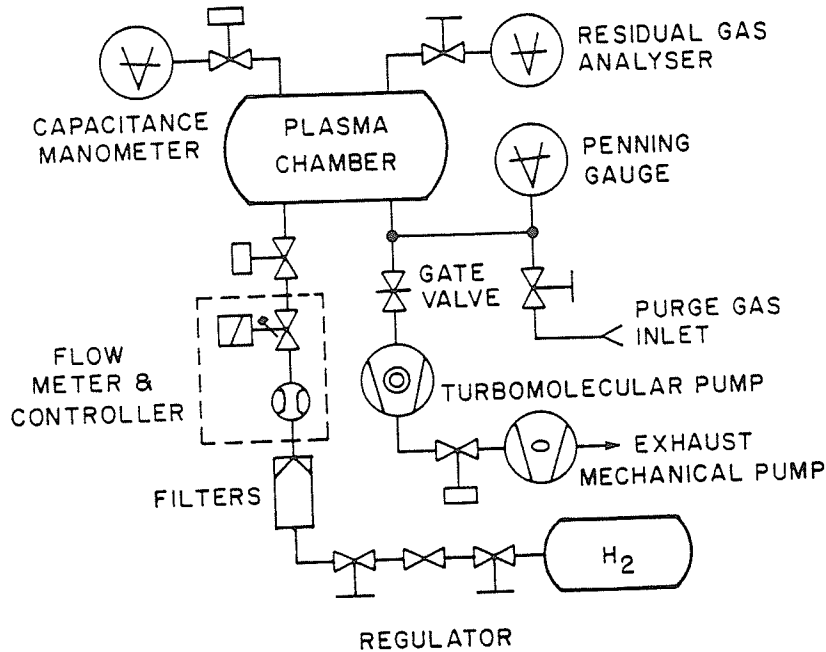


FIGURE 3.1. Schematic diagram of the important gas and vacuum components of the ECR plasma system. Solid lines denote gas or vacuum tubing, dashed lines indicate electrical connections. Symbols are in accordance with international convention.

understood properties, was used for most of the experiments in this thesis.

### 3.1.2. Gas Flow in Vacuum Systems

There are a number of empirical parameters used to characterise the operation of vacuum systems.<sup>2</sup> The *mass flow rate* (or more correctly, *throughput*),  $Q$ , of gas into the chamber could be varied from 2.0 to 100.0 sccm using the flow controller. The *conductance*,  $C$ , of the high vacuum port, and thus the effective *pumping speed*,  $S$ , could be controlled with good accuracy at low pressures with the high vacuum butterfly valve. This meant that the neutral gas pressure,

$$p = \frac{Q}{S}, \quad (3.1)$$

could be varied by changing either  $Q$  or  $S$ . The *residence time* of a typical molecule is given by

$$\tau = \frac{V}{S} = \frac{Vp}{Q}, \quad (3.2)$$

where  $V$  is the volume of the vessel. The volume of the plasma chamber, empty and not including port volumes, was approximately  $1.2 \times 10^{-3} \text{ m}^3$ . In plasma processing applications,  $p$  is usually varied with  $Q$  while  $S$  is held constant, ensuring that waste products are removed as rapidly as possible.<sup>3</sup> This is the technique used in this thesis.

An important property of vacuum systems is the type of gas flow occurring in the system. This depends on the relative magnitudes of the characteristic scale lengths

of the gas and the containing structure\*. This is characterised by the *Knudsen number*,  $Kn$ , which is defined as the mean free path length of the gas molecules divided by the characteristic dimension of the containing vessel or obstructing object. There are three regimes: (1) *viscous* flow for  $Kn < 0.01$ , (2) *molecular* flow for  $Kn > 1.00$  and (3) *transition*, or *Knudsen*, flow for  $0.01 < Kn < 1.00$ . Viscous flow occurs at high (atmospheric) pressures where intermolecular collisions dominate the motion of the gas molecules. Molecular flow occurs at low pressures; the molecules travel independently of each other and collisions with surfaces (adsorption/desorption events) determine their path through the system. The Knudsen regime exists at intermediate pressures.

One consequence of the presence of molecular and/or Knudsen conditions is that it is no longer clear what is meant by a "flow" of gas. However, the locations of the feed and pumping ports imply that the gas molecules must undergo some type of net directed motion from front to back; this is what will be meant by neutral gas flow in this thesis. Note that this "net directed motion" is the cumulative result of independent particles moving in a sequence of straight line paths which change direction randomly upon contact with a surface. A second consequence is that large pressure and density gradients can occur over short distances (typically near inlet and pumping ports) because of an insufficient number of randomising collisions. In addition, the absence of viscous flow implies that neutral gas flow effects (such as eddies or turbulence) cannot account for any plasma structures smaller than the chamber dimensions.

## 3.2. MICROWAVE CIRCUIT

### 3.2.1. Apparatus

The microwave circuit of the ECR plasma processing system is shown in figure 3.2. The frequency of operation was 2.45 GHz. RG-214 coaxial cable connected the source to the waveguide sections at the plasma chamber and the dummy load. These consisted of WR-284 rectangular waveguide components operated in the  $TE_{10}$  (fundamental) mode.

Microwave power was supplied by a magnetron-based power source (Ophos MPG-4M). The output was continuously adjustable from 0 to 120 W (continuous wave). Diode power meters measured the power leaving and entering the source. The power at the plasma chamber was measured directly so that losses leading up to the chamber did not have to be compensated for. No effort was made to match the source to the chamber. A circulator (Microwave Associates 5N43) was placed on the source output to protect the magnetron from reflected power, which was dumped into a dummy load. This precaution increased the magnetron's lifetime and improved its stability by allowing it to operate into a matched load at all times.

The purpose of the  $90^\circ$  H-plane elbow preceding the directional coupler was to allow an unobstructed view into the plasma chamber. The outer wall of the elbow was replaced with a metal screen while the bend removed the coaxial to rectangular

---

\* Note, however, that (3.1) and (3.2) are dimensional relations between empirical quantities and do not depend on the mechanisms underlying the gas flow.

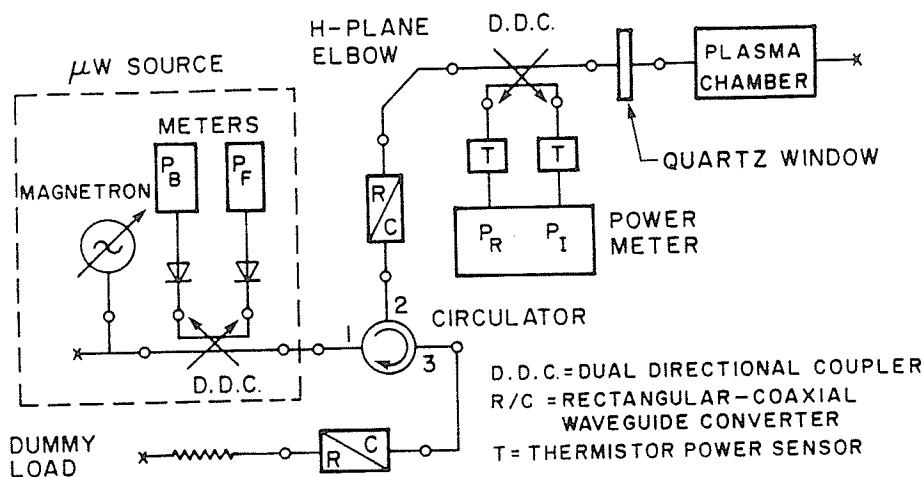


FIGURE 3.2. Schematic diagram of the microwave circuit of the ECR plasma system. The plasma chamber appears as a short-circuited section of plasma-loaded waveguide.

connector's antenna post from the line of sight.

A dual directional coupler (Microwave Technology 2611) sampled the incident,  $P_I$ , and reflected,  $P_R$ , powers at the chamber window with coupling constants of approximately -30 dB.  $P_I$  and  $P_R$  were measured using a dual channel digital power meter (Hewlett Packard 438A) equipped with thermistor power heads (HP 8481A).

The behaviour of the magnetron was carefully examined before being used in the plasma experiments. Peculiarities in the output of the source could easily have resulted in artifacts in the experimental data. For these measurements the reflected power thermistor head was replaced with either a microwave diode detector (Microlab/FXR) to determine the magnetron's power stability, or a frequency counter (Systron Donner 6030) to measure its frequency response. The diode detector rectified the microwave signal into a DC voltage upon which ripple and other fluctuations in the microwave power appeared as corresponding modulations. The incident power was monitored simultaneously with the thermistor head (it was confirmed that the incident and reflected microwave signals exhibited the same behaviours). These measurements were performed with the chamber evacuated.

The frequency of operation varied from 2.453 to 2.460 GHz over the range of 3 to 120 W. The measurement was precise to better than 1 MHz. This frequency variation was negligible. Ripple above 12 W consisted of 120 and 360 Hz line frequency harmonics and was always  $\leq 1\%$  of the signal level.

Some notable features were observed below 12 W. Below 3 W the microwave signal consisted mainly of high frequency "hash" which changed in both magnitude and average level as the "power output" was increased. The result was that as the power output variac was steadily increased from zero,  $P_I$  first increased (to 450 mW), then decreased (to 250 mW) and then increased again. The noise level in these regions varied from 50 to 100% of the signal level. Above 3 W the noise remained constant in

magnitude while the signal level steadily increased. Between 10 and 12 W this noise was broken by randomly occurring pulses with random duty cycles but constant magnitude. The pulses consisted of the very low noise operation associated with the higher power level operation described in the previous paragraph. These pulses of "normal" operation of the magnetron appeared at about 10 W and increased in number with power until operation was fully normal above 12 W. As a consequence of these behaviours of the magnetron, any unusual *universal* behaviours in the plasmas over the ranges of 0 to 3 or 10-12 W  $P_I$  should be considered artifacts.

### 3.2.2. Microwave Propagation in Rectangular Waveguides

A major focus of this thesis was to understand how microwave power propagated through, and coupled into, the plasma. Since the plasma chamber was basically a short-circuited section of plasma-loaded waveguide, the first step was to ensure that the properties of the system in the absence of plasma were clearly understood. Discussions of rectangular waveguides can be found in any advanced undergraduate electromagnetics text.<sup>4,5</sup> The classic work on the practical aspects of waveguides is by Southworth.<sup>6</sup>

The geometry being considered here is shown in figure 3.3. The  $TE_{10}$  electric and magnetic fields are the real parts of<sup>4</sup>

$$\mathbf{E} = \hat{y} E_{RMS} \sin(k_x x) e^{i(\omega t - k_z z)}, \quad (3.3a)$$

$$\mathbf{H} = E_{RMS} \left[ \hat{x} \frac{-k_z}{\omega \mu} \sin(k_x x) + \hat{z} \frac{ik_x}{\omega \mu} \cos(k_x x) \right] e^{i(\omega t - k_z z)}, \quad (3.3b)$$

where  $k_x = \pi/X$  is the wavevector in the  $\hat{x}$  direction.  $E_{RMS}$  is the root-mean-squared electric field strength at the waveguide axis and  $\mu$  is the magnetic permeability of the (homogeneous, isotropic) medium filling the waveguide.  $\mathbf{E}$  and  $\mathbf{H}$  represent a linearly polarised (in the  $\hat{y}$  direction) wave traveling in the positive  $\hat{z}$  direction. The electric field strength varies as a 1/2 period of a sine function across the waveguide cross-section ( $\hat{x}$  direction).

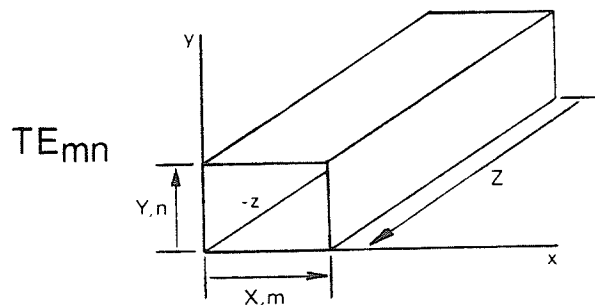


FIGURE 3.3. Rectangular waveguide geometry in a right-handed coordinate system.  $X, Y, Z$  refer to the dimensions of the waveguide, while  $m$  and  $n$  give the number of vacuum half-wavelengths which fit along  $X$  and  $Y$ , respectively.

The dispersion relation for the  $TE_{10}$  mode is<sup>4</sup>

$$k_z^2 = \omega^2 \mu \epsilon - \left( \frac{\pi}{X} \right)^2, \quad (3.4)$$

where  $\epsilon$  is the dielectric permittivity of the (homogeneous, isotropic) medium filling the waveguide. The guide wavelength is given by<sup>4</sup>

$$\lambda_G = \frac{2\pi}{k_z}. \quad (3.5)$$

The cutoff frequency of this mode,<sup>4</sup>

$$f_{CO} = \frac{1}{2X\sqrt{\mu\epsilon}}, \quad (3.6)$$

is obtained from  $k_z = 0$ . With the plasma chamber assumed to be evacuated,  $\lambda_G = 23.2$  cm and  $f_{CO} = 2.08$  GHz. The chamber was about  $2 \lambda_G$  long.

The time-averaged power transmitted through an arbitrary cross-section of waveguide is given by<sup>4</sup>

$$P = \frac{E_{RMS}^2 XY k_z}{4\omega\mu}. \quad (3.7)$$

$E_{RMS}$  could be estimated by assuming that all reflection occurred at the entrance to the chamber, so that the absorbed power,  $P_A = P_I - P_R$ , could be assumed to be transmitted across that plane. In fact, however, reflection was probably distributed continuously and nonuniformly along a major fraction of the chamber length.

Attenuation of the wave due to losses in the waveguide walls, a result of the finite wall conductivity, have so far been ignored in this discussion. The attenuation coefficient due to such losses is<sup>6</sup>

$$\alpha = \left[ 1 + \frac{2Yf_{CO}^2}{Xf^2} \right] \left[ \frac{\pi\epsilon_0\mu_m f^3}{\mu_0\sigma_m Y^2(f^2 - f_{CO}^2)} \right]^{1/2} \quad (3.8)$$

where  $\sigma_m$  is the DC conductivity of the wall metal. This attenuation appears as an extra  $e^{-\alpha z}$  factor multiplying the field equations.  $\alpha$  can be expressed in dB/m by multiplying by 8.686. The fraction of the power lost to the walls can be obtained from

$$\frac{P_{LOST}}{P_{TOTAL}} = 10^{-\alpha z/10}, \quad (3.9)$$

where  $\alpha$  is in dB/m. If the microwave power measurements were to be meaningful, the chamber walls should not have absorbed a substantial fraction of the incident power. Using the conductivity of (clean) 304 steel and assuming that its relative permeability was unity,  $\alpha = 0.18$  dB/m was found. As an estimate of the wall losses to be expected in plasma experiments we note that in traveling the length of the chamber (46.5 cm), less than 2% of the incident power was lost to the walls.

### 3.3. PLASMA CHAMBER

A sketch of the plasma chamber is shown in figure 3.4. The chamber was constructed of AISI 304 stainless steel; a non-magnetic steel with a conductivity of approximately  $1.4 \times 10^6 (\Omega \cdot m)^{-1}$ . The cross sectional dimensions were those of WR-284 rectangular waveguide; 7.21 by 3.40 cm. The interior length of the evacuated section

was 46.5 cm. The chamber and associated gas and vacuum lines were wrapped in flexible heater ribbon and could be baked to 300 °C.

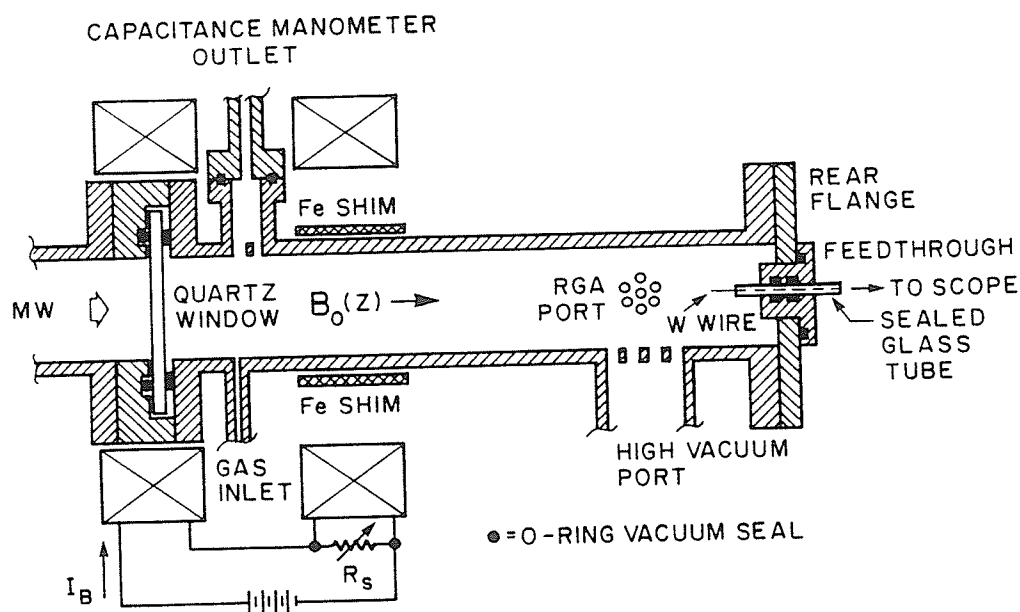


FIGURE 3.4. Cutaway side view of the ECR plasma chamber. The RGA port projects into the page.

The quartz window was used to provide a vacuum seal transparent to near-UV, visible and microwave radiation. Access to the chamber was through the rear flange, onto which either a sample table or probe feedthrough was usually mounted. All large ports were constructed as a cluster of smaller holes in order to contain the microwave field. The vacuum seals at the window and the rear flange were made with Viton O-rings. Note that the plasma chamber, even in the absence of internal structures, was not a perfect short due to the small cylindrical "cavity" within which the quartz window was mounted. Thus the evacuated plasma chamber typically reflected approximately 40% of  $P_I$ .

The DC current supplied to the magnetic field coils,  $I_B$ , could be varied continuously from 0 to 27 A using a variac. The coils, immersed in transformer oil, were cooled by water flowing through copper tubing wound into the coils. In addition to the obvious choices of coil configurations and positions, the shape of the magnetic field profile could be adjusted by adding a variable shunt resistor in parallel with either coil. Fine tuning of the profile was achieved through the judicious use of iron shims wrapped around the chamber.

The magnetic flux density,  $B_0(z)$ , was measured as a function of position and  $I_B$  with a Gaussmeter (Bell 610) equipped with a Hall effect probe. These measurements were made with the rear flange removed. Axial magnetic field profiles as a function of  $I_B$  for various coil configurations are shown in figure 3.5. The cross-sectional profiles were uniform to within  $\pm 2\%$ , except under the shims, where a 4% increase was

observed near the walls. This was presumably due to concentration of the magnetic field lines near the shim.

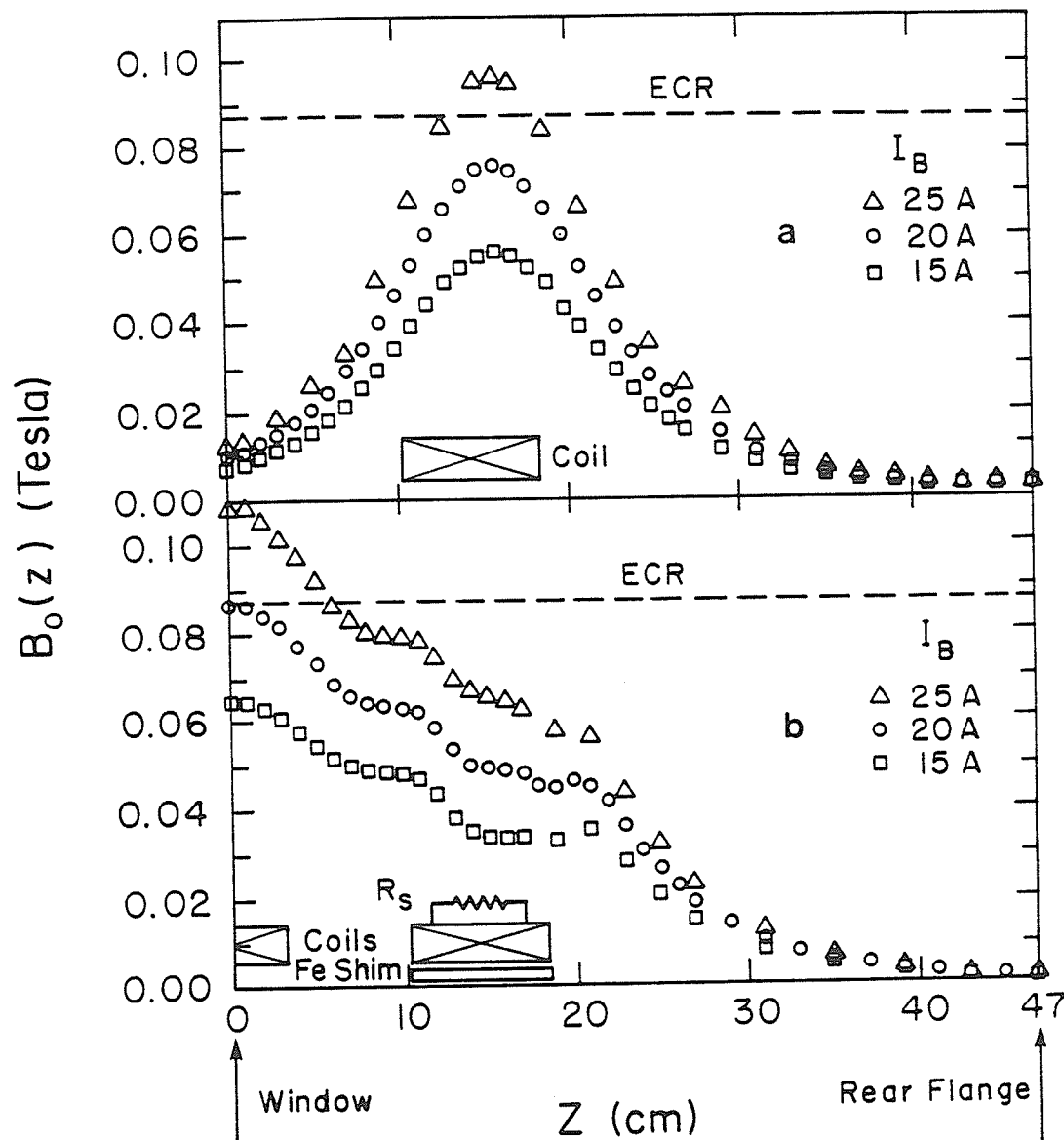


FIGURE 3.5. Magnetic field profiles as a function of  $I_B$ . The insets show the arrangement of devices used to obtain each configuration. (a) Peaked configuration. (b) Magnetic beach configuration.

The gas flow regimes of the plasma chamber will now be estimated. The characteristic dimension for gas flow through a cylindrical vessel is the radius; for the rectangular plasma chamber an effective radius of 2.7 cm will be used. For  $H_2$  at 300 K,  $Kn > 1$  for  $p < 3.5 \times 10^{-3}$  Torr. This thesis was concerned with the range  $10^{-3} < p < 10^{-1}$  Torr, which corresponds to Knudsen gas flow conditions.

### 3.4. LANGMUIR PROBE

Langmuir probes are the oldest and experimentally simplest plasma diagnostic technique; a small electrode is inserted into the plasma and its current-voltage (I-V) characteristic is measured. The price of this experimental simplicity is difficulty of interpretation, a result of sheath formation. The theory and technique of Langmuir probe diagnostics has been reviewed by many authors. The primary references used here were the monographs by Swift and Schwar<sup>7</sup> and Chung, Talbot and Touryan,<sup>8</sup> and the reviews by Hershkowitz,<sup>9</sup> Schott<sup>10</sup> and Chen.<sup>11</sup>

The first Langmuir probes used in the ECR system were of the planar type, as described in section 4.3. That design was chosen for its analytical simplicity and apparent immunity to complicating factors. The results obtained replaced educated guesses as to the basic parameters of the plasma with experimental data, thus allowing a proper determination of the best type of probe design to be used in more sophisticated experiments. It was decided that a long, thin cylindrical probe satisfying the orbital-motion limit (OML) condition would be used. In addition to the advantages to be described below, the OML analysis could always be replaced by Laframboise's exact numerical calculations for cylindrical probes, should this be necessary.<sup>12,13</sup>

#### 3.4.1. Principles of Operation

A basic probe I-V measurement circuit is shown in figure 3.6. The probe voltage,  $V = \phi_S + \phi_P$ , is with respect to the system ground\*. The important quantity here is the probe-to-plasma (sheath) potential,  $\phi_S$ . Note that  $\phi_P \equiv V_P$  since the chamber walls consisted of clean, grounded metal surfaces. The probe current,  $I(V)$ , is the sum of the ionic and electronic components, and is defined to be positive when flowing *into* the probe<sup>†</sup>. This means that pure electron (positive ion) collection results in positive (negative) current.

Probe theory makes a number of assumptions about both the probe and plasma. The probes used in this thesis were designed to satisfy all of these conditions. In this regard, it should be recognised that the conditions seen by the probe at the mesoscopic level are not necessarily equivalent to those at the macroscopic level.

The Langmuir probe was made small. Obviously, the probe was smaller than the volume of plasma in so that quasi-neutrality held, and so that the probe did not perturb the bulk plasma. The chamber walls, which formed the reference electrode of the probe circuit, were clean conductors, and had a much larger surface area than the probe. The probe was also marginally smaller than the scale lengths of the inhomogeneities in the plasma, so that the plasma could be assumed to be locally homogeneous. The sheath could be assumed to be collisionless since all mean free path lengths were larger than the largest probe dimensions. In addition, probe dimensions perpendicular to the magnetic field were made smaller than the Larmor radii so that the effect of  $B_0(z)$  could be neglected. This is discussed in more detail in sub-section 3.4.4.

---

\* Throughout this thesis, an arbitrary potential difference will be denoted by  $\phi$ , while a voltage,  $V$ , will refer specifically to a potential with respect to the system ground.

† In agreement with convention, if not with all authors or physical intuition.

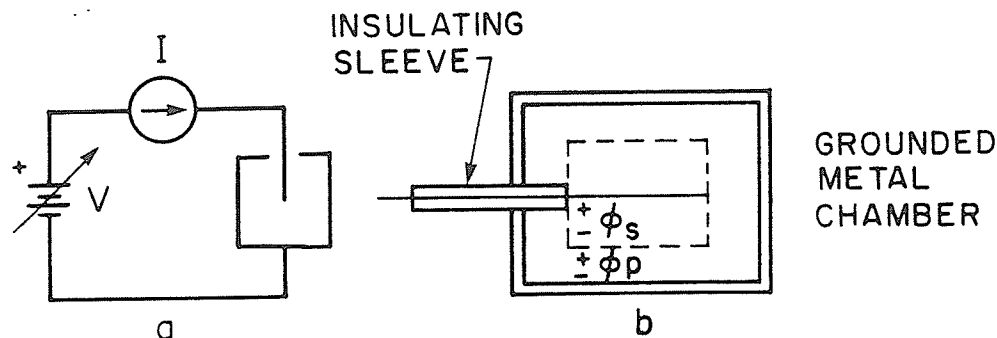


FIGURE 3.6. (a) Schematic diagram of a basic Langmuir probe I-V measurement circuit. The direction of positive current flow is in accordance with convention. (b) Sketch of the potential profile within the plasma chamber for ion collection, defining the sheath ( $\phi_s$ ) and plasma ( $\phi_p$ ) potentials.

The glass shielding sleeves of the probe were also made as small as possible so that fringing fields could be neglected.

While no restrictions need be made concerning the number of positive ion species, the effect of negative ions will be neglected. This is valid except in strongly attaching plasmas,<sup>7</sup> and was certainly valid in the  $H_2$  plasmas examined in this thesis. Probe theory does assume that each charged particle species is in thermal equilibrium. This was probably not true of the ions, but the effect of ion beams and/or plasma flow can be dealt with separately, as discussed in sub-section 3.4.4. That sub-section also considers the effect of microwave electric fields and plasma noise on the probe measurements.

The most commonly used probe material, and the one used in this thesis, is tungsten. This material is preferred because it is a relatively unreactive, refractory metal (melting point  $3410\text{ }^\circ\text{C}$ ), is mechanically strong and is a good electrical conductor (conductivity  $1.85 \times 10^5\text{ }(\Omega\text{-cm})^{-1}$ ). It also has a relatively high ionisation potential (7.98 eV) and work function (4.55 eV). These properties allow the probe model to assume that the probe is a perfect conductor and absorber of charged particles, and that it does not display surface complications such as deposition, electron emission, sputtering, etc. Tungsten is not, however, easily machined. Thus molybdenum, which is easily machined and has properties similar to tungsten, was used for the disc probe described in chapter 4.

The I-V characteristics of an OML cylindrical probe have the form shown in figure 3.7. The probe is assumed to be have a large aspect ratio, so that it appears to be an infinite cylinder (negligible fringing fields and end collection). Additional assumptions required specifically to satisfy OML conditions will be described in the next sub-section.

The overall form of the I-V characteristic can be explained as follows. Let the probe be initially biased at  $V_p$ ; it is *unbiased* with respect to the plasma ( $\phi_s = 0$ ), has no sheath and collects the full random thermal flux of ions and electrons. Since the electron flux is typically much larger than that of the ions (due to the smaller mass and higher temperature of the electrons),  $I$  is large and positive;  $I = I_{0e} + I_{0i} \approx I_{0e}$ .

Here  $I_{0j}$  is the "saturation" current of the  $j$ 'th species, which corresponds to the random thermal flux incident on the probe. Now decrease  $V$  below  $V_P$ . After approximately  $-\kappa T_e/2e$  an ion sheath forms ( $\phi_S < 0$ ). Note that as a result of screening by the sheath, the plasma never experiences a potential significantly larger than  $\kappa T_e/2e$ , so only the random thermal fluxes are collected at the sheath edge.  $I$  changes because electrons are *repelled* by  $\phi_S < 0$ . As  $V$  decreases,  $\phi_S$  increases negatively, expanding the sheath and reflecting a larger fraction of the electron population, thus decreasing  $I$ . If the electrons have a Maxwellian distribution, this decrease is exponential, and depends only on  $T_e$ . Eventually the floating potential,  $\phi_F = V_F - V_P$ , where the electron and ion currents cancel ( $I = 0$ ), is reached. Finally all electrons are reflected;  $I = I_{0i}$  and further decreases in  $V$  only increase the ion sheath thickness. This is the ion saturation region of the I-V characteristic. In general the surface area of the sheath continues to increase so that  $I_{0i}$  does not remain constant. The rate of increase then depends on the geometry of the probe and its size relative to the Debye length.

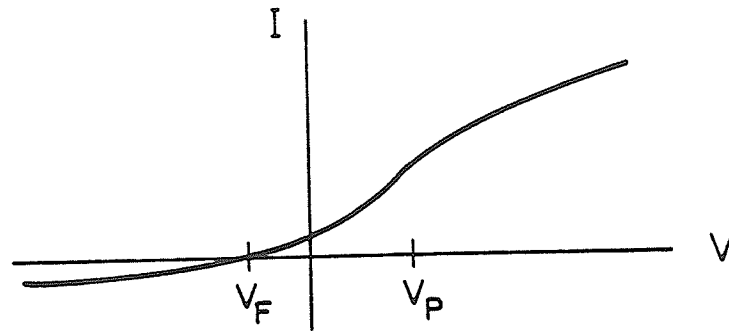


FIGURE 3.7. Sketch of the I-V characteristic of a cylindrical OML Langmuir probe. Note that the sign convention for  $I$  results in positive current when electron collection dominates.

As  $V$  is increased above  $V_P$  the same process takes place, except that an electron sheath forms ( $\phi_S > 0$ ) and  $I_i$  is reduced to zero. This happens almost as soon as the sheath is established because of the low ion temperature. For all practical purposes, electron saturation exists at any  $V > V_P$ . This makes it impossible to obtain  $T_i$  from probe I-V characteristics. In addition, when  $T_i < T_e$ , the ion velocity is modified by the probe pre-sheath in order to satisfy the Bohm sheath criterion (see sub-section 2.1.5).

### 3.4.2. OML Current Equations

The exact theory of current collection by a cylindrical probe under the assumptions listed above is Laframboise's<sup>12</sup> extension of the exact mono-energetic analysis of Bernstein and Rabinowitz<sup>14</sup> to include Maxwellian electron and ion distributions. This model does not yield analytic results, but must be calculated numerically. Fortunately, the conditions found in the ECR system were such that the original OML model of Mott-Smith and Langmuir<sup>15</sup> could be used\*. The following discussion is a distillation

\* Note, however, the missing  $e^n$  factor in the third term of (the critical) equation (28a) of this reference, and that the "error function" used is actually the complementary error function in modern usage.

of the presentations given in the reviews and monographs cited earlier.

OML refers to the case where the probe collects the maximum current possible for its geometry at an arbitrary potential. In Laframboise's theory, as in practice, this occurs when the sheath thickness is much larger than the probe radius,  $R$ . This is parameterised through the ratio  $\xi \equiv R/\lambda_D$ , so that OML occurs as  $\xi \rightarrow 0$ . In fact, current collection by OML cylinders depends only on the distribution functions, not the exact probe geometry; the OML equations for all convex cylindrical probe shapes are the same, provided they are not short compared to  $\lambda_D$ .<sup>16</sup> The only assumption required in addition to  $\xi \rightarrow 0$  and those listed at the start of this section is that the potential in the sheath must vary less steeply than an inverse square power of the radius; an assumption satisfied by all OML cylindrical probes with *collisionless* sheaths.<sup>16</sup> From the exact results of Laframboise<sup>12</sup> (figures 44 and 45), it can be seen that the OML model for cylinders is valid up to  $\xi \approx 1$ .

The current equations will not be derived here; the interested reader is referred to the substantial literature on this subject,<sup>7,10,11,15</sup> and the elegant derivation given by Laframboise and Parker in particular.<sup>16</sup> The current collected by any probe is given by

$$I = \sum_j I_j, \quad (3.10)$$

where the current of the  $j^{\text{th}}$  particle species is

$$I_j = I_{0j} e^{\chi_j} \quad (3.11)$$

for *repelling* potentials, or

$$I_j = I_{0j} \Psi(\chi_j) \quad (3.12)$$

for *attracting* potentials. Note that (3.11) applies for *any* convex probe shape.<sup>7</sup> The "saturation" currents collected from the quasi-neutral plasma (at  $V_p$ ) are

$$I_{0j} = \frac{-A n q_j}{2} \left[ \frac{2 \kappa T_j}{\pi m_j} \right]^{1/2}, \quad (3.13)$$

where the square-root factor is the one-dimensional Maxwellian average speed and  $A = 2\pi RL$  is the surface area of the cylindrical probe.  $R$  and  $L$  are the probe radius and length, respectively. The minus sign is required by the current convention, and the  $1/2$  because only particles going *towards* the probe contribute to the collected flux. The sheath potential has been normalised to the particle energy;

$$\chi_j = \frac{-q_j (V - V_p)}{\kappa T_j}. \quad (3.14)$$

The function  $\Psi$  is given by

$$\Psi(\chi_j) = \frac{2}{\sqrt{\pi}} \sqrt{\chi_j} + e^{\chi_j} \text{erfc}(\sqrt{\chi_j}), \quad (3.15)$$

where the complementary error function is defined as<sup>17</sup>

$$\text{erfc}(x) \equiv \frac{2}{\sqrt{\pi}} \int_x^\infty e^{-t^2} dt \approx \frac{1}{\sqrt{\pi}} \frac{\exp(-x^2)}{x} \quad \text{large } x. \quad (3.16)$$

The function  $\Psi$  can be accurately approximated by using the asymptotic form of  $\text{erfc}(x)$  and recognising the result as the first two terms of a binomial expansion. The result can be expressed as<sup>7,11</sup>

$$\Psi(\chi_j) \approx \frac{2}{\sqrt{\pi}} \left[ \chi_j + 1 \right]^{1/2}. \quad (3.17)$$

This equation is essentially exact for  $\chi \leq 2$ . At worst, when  $\chi = 0$ , it overestimates  $\Psi$  by a factor of  $2/\sqrt{\pi} = 12\%$ . Thus the region near  $V_p$  should not be relied upon in any analysis procedure.<sup>7</sup>

### 3.4.3. Interpretation of the I-V Characteristic

There are four unknown plasma parameters which appear in the current equations:  $V_p$ ,  $T_e$ ,  $T_i$  and  $n$ . In addition,  $V_F$ , (which is an important parameter in practice) can simply be read off of the measured I-V characteristic at the voltage where  $I = 0$ . Ideally,  $V_p$  can also be obtained directly from the I-V characteristic at the "knee" joining the electron retarding and attracting regions. However, this knee is rarely well defined and is often completely unrelated to  $V_p$  due to the influence of non-ideal factors (several of which occur in ECR plasmas). In such cases  $V_p$  must be obtained by extrapolation from the unperturbed I-V characteristic well below electron saturation. As already mentioned, the I-V curve does not contain sufficient information for an accurate determination of  $T_i$ .

The plasma parameters were determined by fitting the OML current equations (3.10) to (3.14) and (3.17) to the measured I-V characteristics. This was accomplished using the Levenberg-Marquardt modelling technique. This method is a nonlinear generalised least-squares technique, and is described in detail in *Numerical Recipes*,<sup>17</sup> which includes Fortran and Pascal programs for implementing this procedure. A complete description of the analysis procedure as implemented in this thesis is given in appendix B. Basically, a model function is supplied by the user, which the program fits to the data by minimising a chi-squared merit parameter. It should be recognised that this procedure simultaneously fits all plasma parameters of the model to the data in a self-consistent manner. There were three primary reasons for using this technique: (1) speed, since this procedure can be completely automated, and requires a minimum of operator intervention; (2) versatility, in that different model functions could be investigated; and (3) accuracy, in that the presence and nature of any non-idealities could be easily determined (by graphically comparing the data and model), and could possibly be incorporated into the model function. The precision of the analysis procedure is discussed in detail in appendix B.

In order to extract the plasma parameters, the mass(es) of the positive ion species must be specified. In  $H_2$  plasmas, only two positive ion species are produced;  $H^+$  and  $H_2^+$ . Since no independent means of determining the relative concentrations of these ions was available, the worst case, which is that *all* ions were  $H^+$ , was assumed. This *underestimated* the density by a factor of  $\sqrt{2}$  at most.

### 3.4.4. Complicating Factors

A problem arises if the distribution function is not Maxwellian; the electron current does not decrease exponentially and the OML equations are not correct. However, measurements have shown that ECR microwave plasmas are reasonably well described by a Maxwellian EEDF,<sup>18</sup> so this should not be a serious problem. If necessary, the approximate form of the electron EDF can be obtained directly from the I-V characteristics by taking the second derivative of  $I_e(V)$  with respect to  $V$ .<sup>7</sup> Note however, that experimental errors could make a Maxwellian EEDF appear to decrease non-exponentially or vice versa. In this case the Druvestyn method, being subject to the same errors, will not resolve the problem.

The non-uniform, strong magnetic field present in the ECR system posed two potential difficulties: anisotropic current collection and flow of the bulk plasma into the downstream region. The first problem can be dispensed with by making the probe dimension across  $B_0$  much smaller than the Larmor radii. Note that this has the additional benefit of reinforcing OML conditions. Experiment<sup>19</sup> indicates that  $R \leq 0.25 r_{Le}$  is sufficient, assuming  $r_{Le} < r_{Li}$ . This is the criteria used in this thesis. However, more recent results<sup>20</sup> based on the calculations of Rubinstein and Laframboise<sup>21</sup> indicate that the size of the *sheath*, relative to  $r_L$ , must also be considered. These results are in the form of least upper bounds on the attracted particle currents<sup>21</sup> and so are not useful in modelling experimental data, but they do indicate when the effects of magnetic fields will be significant. For the conditions encountered in this thesis, the electrons are collected through a *transition magnetosheath*, while the ions are collected through an essentially unmagnetised sheath.<sup>20</sup> Thus, provided the region above  $V_p$  is avoided, the unmagnetised OML equations should accurately model the experimental data. Perturbations to be expected from an electron transition magnetosheath are a reduction of the magnitude and slope of the electron "saturation" current, and a rounding of the knee near  $V_p$ .<sup>21</sup> These are exactly the phenomena observed in the experimental data (see sections 4.3.3 and 6.2, and figures 6.1 and B.1 in particular).

The effect of any flow in the plasma could be made negligible by aligning the probe parallel to the flow (which was along  $B_0$ ), and by ensuring that  $L$  was large enough to satisfy<sup>8</sup>

$$\frac{L}{u\lambda_D} \left[ \frac{\kappa T_e}{m_i} \right]^{1/2} \geq 50. \quad (3.18)$$

Here  $u$  is the flow velocity of the plasma as a whole, which may arise from the  $\nabla B_0$  force, for example. A worst case value of  $u$  was estimated from (2.13) using the maximum slope of the magnetic beach profile at  $I_B = 25$  A and assuming that the ions determined the net ambipolar flow rate. A value on the order of  $10^4$  m/s, approximately equal to  $\sqrt{\kappa T_e/m_i}$ , was obtained. Thus  $L \geq 50 \lambda_D$  was required. Unfortunately, the more serious problem posed by ion "beaming" could not be compensated for in this way. The ion beams will tend to enhance collection at the end of the probe tip; a contribution which has been ignored in the analysis thus far. Such end collection will take place through a more or less hemispherical sheath, and will thus contribute a spherical character to the measured I-V curves. This should appear as a *linear* contribution to  $I(V)$ , since spherical probes collect saturation currents linear in  $V$ .<sup>7,16</sup> This

was in fact observed, and was accounted for using the technique described in appendix B and section 6.2.

Another potential problem arises if oscillations occur in the plasma.<sup>11,7</sup> A good discussion of this problem is given by Hershkowitz.<sup>9</sup> Oscillations could be due to fluctuations in any of the plasma parameters or to the electric fields produced by waves or instabilities. The non-linear properties of the probe sheath rectifies these signals into voltages which contribute to the unperturbed I-V characteristic. Typically, this shifts the I-V characteristics to more negative voltages and depress the currents collected near  $V_p$ .<sup>9</sup> As long as the fluctuations are small, most of the original characteristic remains intact, and determinations of  $n$  and  $T_e$  are unaffected. Fortunately, inspection of the I-V curve clearly reveals when noise is a problem, and what portion of the curve has been affected.

### 3.4.5. Experimental Apparatus

A sketch of the probe and feedthrough is shown in figure 3.8. The construction of the probe is described in detail in appendix A. The probe tip consisted of a 1 cm length of 25  $\mu\text{m}$  diameter tungsten wire. The outside diameter of the glass shield at the tip was approximately 100  $\mu\text{m}$ . The location of the probe is denoted by  $z$ , the distance of the *center* of the probe tip from the inside surface of the quartz window. Thus at  $z = 1.5$  cm the probe sampled plasma along the axis from  $z = 1$  to 2 cm.

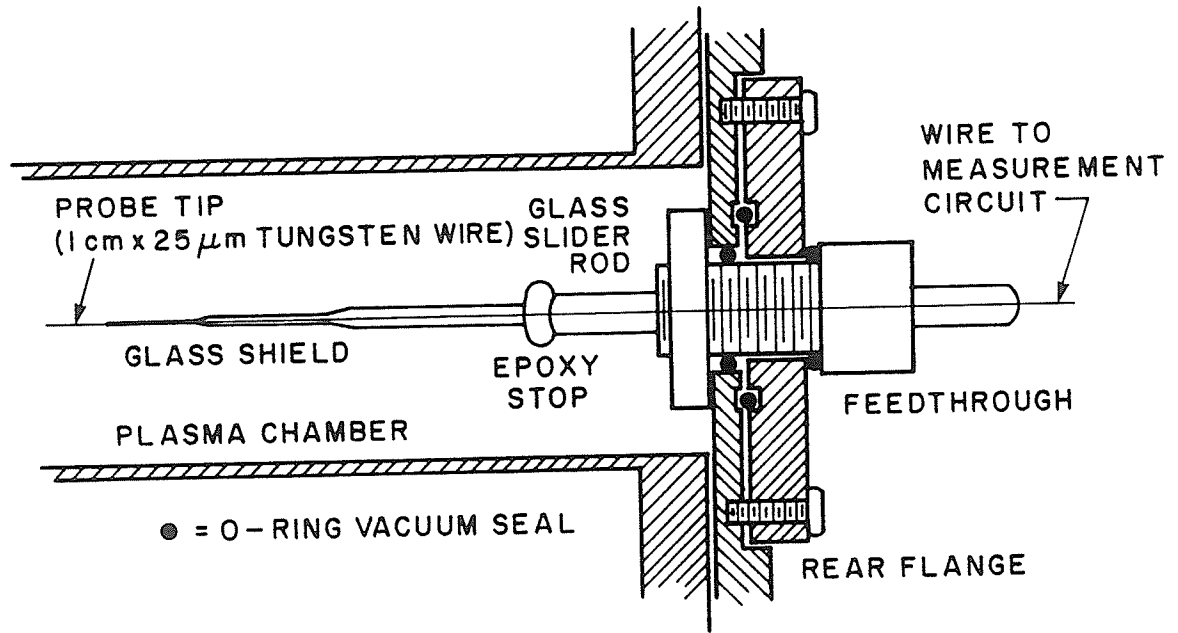


FIGURE 3.8. Sketch of the Langmuir probe and sliding feedthrough used to position it in the plasma chamber.

The dimensions of the probe were chosen to satisfy the constraints discussed in the previous sub-sections using the data obtained from the preliminary measurements described in section 4.1. Assuming operation in  $\text{H}_2$  at 300 °K, with  $T_e \approx 3$  eV,  $n \approx 10^{16}$   $\text{m}^{-3}$  and the probe dimensions given above, OML theory was satisfied for  $B_0 \leq 0.1$

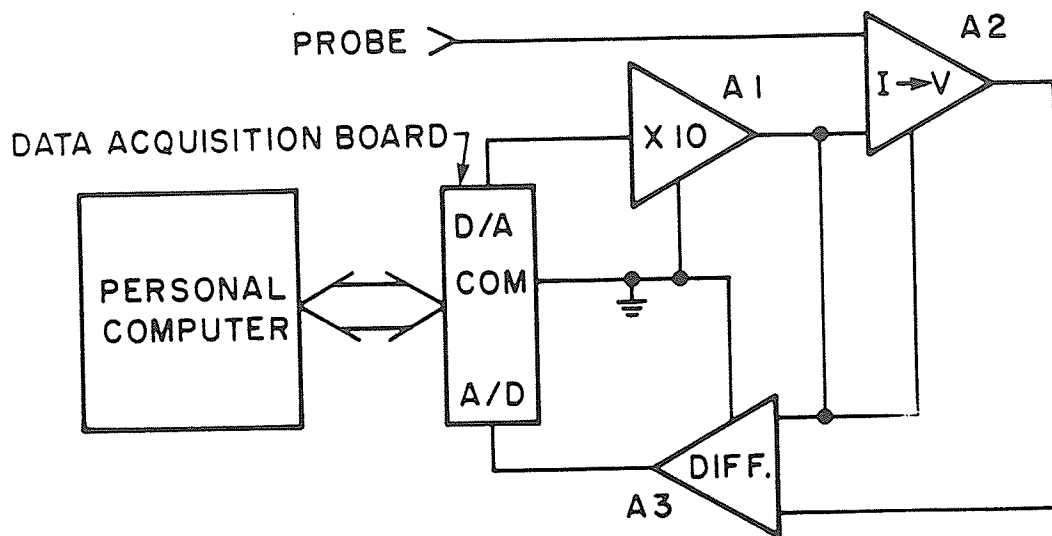


FIGURE 3.9. Block diagram of the Langmuir probe I-V data acquisition system. The lines projecting from the sides of the amplifier symbols indicate which voltage their ground was taken with respect to.

Tesla and  $p \leq 10^{-2}$  Torr. The pressure criteria reflects the fact that, strictly speaking,  $l_{en} \geq L \gg \lambda_D$ . This is a weak restriction, since only very energetic electrons arriving at grazing angles of incidence will travel distances on the order of  $L$  within the probe sheath. Thus violations of this condition do not become significant until  $l_{en} \approx \lambda_D$  is approached. This qualification is important (and very fortunate), since pressures as large as 0.1 Torr were examined in this thesis, due to the factory miscalibration of the capacitance manometer discussed at the start of section 3.1. Even at these high pressures, the OML theory described above should remain valid.

A block diagram of the probe measurement circuit is shown in figure 3.9. A detailed description is given in appendix A. The circuit consisted of a data acquisition board (Metra-Byte Dascon-1) mounted in a personal computer (IBM XT clone). A  $\pm 5$  V digital-to-analog, D/A, converter sent its output into the 10x non-inverting amplifier A1, which could output up to  $\pm 50$  V. The output of A1 was applied to the probe, one input of A3 and the common for A2's power supply. A2 was a current-to-voltage converter which transformed  $I$  into a proportional voltage. The outputs of A1 and A2 went into the unity gain differential amplifier A3 which converted the output of A2 (with respect to  $V$ ) into a signal with respect to ground which was in turn measured by an analog-to-digital, A/D, converter on the data acquisition board.

A BASIC program was written to control the data acquisition system. Analysis of the data was performed separately upon completion of the experiments. Each I-V curve was stored on the hard disk and then plotted on the monitor. The data was acquired in four interlaced low resolution scans, from negative to positive  $V$ . Thus the final characteristic was a high resolution time average. A current limiter was implemented in software to prevent excessive fluxes onto the probe. Details of the controller program are given in appendix A.

## References

1. A.D. MacDonald, *Microwave Breakdown in Gases*, John Wiley & Sons, New York, 1966.
2. S. Dushman, *Scientific Foundations of Vacuum Technique, 2nd Edn.*, John Wiley & Sons, New York, 1962.
3. J.W. Coburn, *Plasma Etching and Reactive Ion Etching*, Am. Vac. Soc. & Am. Inst. Phys., New York, 1982.
4. L.C. Shen and J.A. Kong, *Applied Electromagnetism*, Brooks/Cole, Monterey, 1983.
5. E.C. Jordan and K.G. Balmain, *Electromagnetic Waves and Radiating Systems, 2nd Edn.*, Prentice-Hall, Englewood Cliffs, 1968.
6. G.C. Southworth, *Principles and Applications of Waveguide Transmission*, D. Van Nostrand, Princeton, 1950.
7. J.D. Swift and M.J.R. Schwar, *Electrical Probes for Plasma Diagnostics*, Illife, London, 1969.
8. P.M. Chung, L. Talbot, and K.J. Touryan, *Electric Probes in Stationary and Flowing Plasmas: Theory and Application*, Springer-Verlag, New York, 1975.
9. N. Hershkowitz, "How Langmuir Probes Work," in *Plasma Diagnostics Vol. 1; Discharge Parameters and Chemistry*, ed. O. Auciello, D.L. Flamm, p. 113, Academic, Boston, 1989.
10. L. Schott, "Electrical Probes," in *Plasma Diagnostics*, ed. W. Lochte-Holtgreven, p. 668, North-Holland, Amsterdam, 1968.
11. F.F. Chen, "Electric Probes," in *Plasma Diagnostic Techniques*, ed. S.L. Leonard, p. 113, Academic, New York, 1965.
12. J.G. Laframboise, *UTIAS Report 100: Theory of Spherical and Cylindrical Langmuir Probes in a Collisionless, Maxwellian Plasma at Rest*, University of Toronto Institute for Aerospace Studies, Toronto, 1966.
13. M.B. Hopkins and W.G. Graham, "Langmuir Probe Technique for Plasma Parameter Measurement in a Medium Density Discharge," *Rev. Sci. Instrum.* 57, p. 2210, 1986.
14. I.B. Bernstein and I.N. Rabinowitz, "Theory of Electrostatic Probes in a Low-Density Plasma," *Phys. Fluids* 2, p. 112, 1959.
15. H.M. Mott-Smith and I. Langmuir, "The Theory of Collectors in Gaseous Discharges," *Phys. Rev.* 28, p. 727, 1926.
16. J.G. Laframboise and L.W. Parker, "Probe Design for Orbit-Limited Current Collection," *Phys. Fluids* 16, p. 629, 1973.
17. W.H. Press, B.P. Flannery, S.A. Teukolsky, and W.T. Vetterling, *Numerical Recipes, The Art of Scientific Computing*, Cambridge University Press, Cambridge, England, 1986.
18. Y.H. Lee, J.E. Heidenreich III, and G. Fortuno, "Plasma Characterization of an Electron Cyclotron Resonance-Radio-Frequency Hybrid Plasma Reactor," *J. Vac. Sci. Technol. A* 7, p. 903, 1989.
19. F.F. Chen, C. Etievant, and D. Mosher, "Measurements of Low Plasma Densities in a Magnetic Field," *Phys. Fluids* 11, p. 811, 1968.
20. E.P. Szuszcwicz and P.T. Takacs, "Magnetosheath Effects on Cylindrical Langmuir Probes," *Phys. Fluids* 22, p. 2424, 1979.
21. J. Rubinstein and J.G. Laframboise, "Theory of Axially Symmetric Probes in a Collisionless Magnetoplasma: Aligned Spheroids, Finite Cylinders, and Disks," *Phys. Fluids* 26, p. 3624, 1983.

## CHAPTER 4

### BEHAVIOUR OF DOWNSTREAM PLASMAS IN A PE-CVD REACTOR\*

*The cause is hidden, but the effect is known.*  
- Ovid, *Metamorphoses*

In this chapter, some early experiments on the ECR plasma processing system will be described. The system was configured in the form used in most applications; as a downstream plasma-enhanced chemical-vapour deposition (PE-CVD) reactor using a singly peaked magnetic field profile. The focus of these experiments was a planar Langmuir probe mounted on a sample table located at the rear of the plasma chamber. This chapter describes our earliest plasma characterisation efforts, and is "out of step" with the rest of the thesis as a result. This chapter is included largely for completeness, since the objectives and methods of this thesis arose primarily out of these early experiments.

#### 4.1. EXPERIMENTAL

The ECR system used in this study differed somewhat from that described in chapter 3. A diffusion pump (NRC) was connected to the plasma chamber through a longer and more convoluted (lower conductance) pipe. The capacitance manometer was attached to the side of this pipe; a poor location for operation in the molecular flow regime. The pressures measured in these experiments were approximately one-half the values indicated by the same meter located properly as described in chapter 3. Due to the additional corrections to the pressure readings described in section 3.1, the values of  $p$  quoted in this chapter are *20 times* those reported in the published paper.<sup>1</sup> The magnetic field profile was in the form of a single peak, shown in figure 3.5(a). Another important difference was that the power meter was mis-calibrated. This was corrected for in this section by increasing the reflected powers by 15% over the values reported in the published paper.<sup>1</sup> The relative trends, which were of primary interest in this study, were unaffected by this change.

The microwave source used in these experiments (MW Technology) was intended for high power (kilowatt) applications. After these experiments were completed, it was found that the output of the magnetron (Phillips YJ1160) was highly oscillatory. The consequences of this behaviour (aside from the obvious) are discussed in sub-section 4.4.3. Unfortunately, the magnetron was accidentally destroyed during efforts to eliminate these very oscillations (the cure was worse than the disease...), so no detailed characterisation of these behaviours was made.

---

\* This chapter is an extensively revised version of: P.K. Shufflebotham, D.J. Thomson, H.C. Card, "Behavior of Downstream Plasmas Generated in a Microwave Plasma Chemical-Vapor Deposition Reactor", *Journal of Applied Physics* 64, pp. 4398-4403, 1988.

When used as a PE-CVD reactor, the sample table shown in figure 4.1 was mounted on the rear flange of the plasma chamber. This table contained an internal heater, thermocouple, and two gas injection nozzles, and could be biased relative to the surrounding waveguide. The planar Langmuir probe used in this experiment was mounted on one corner of the table, with the probe tip centered in the waveguide and oriented normal to the waveguide axis.

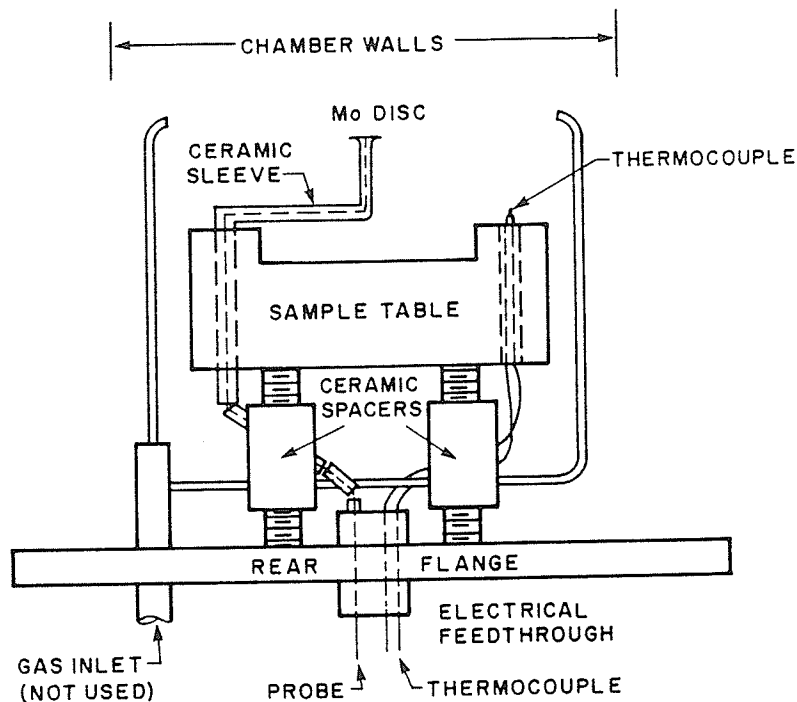


FIGURE 4.1. Sketch of the downstream sample table and planar Langmuir probe.

Most measurements were performed at  $P_A = 4$  W, but some were also made at 2 and 6 W. The primary variable of interest was  $I_B$ . The operating pressure was  $10^{-2}$  Torr at a flow rate of 29.0 sccm of  $H_2$ . The chamber and table were at room temperature. The waveguide was grounded while the sample table was allowed to float in order to minimise perturbation of the plasma. Microwave power readings, optical emission spectra and probe I-V characteristics were recorded for each point, as was the shape, colour and location of the plasma as observed visually. The reproducibility of a number of representative points was repeatedly checked throughout the experiment.

## 4.2. GLOBAL DIAGNOSTICS

Global diagnostics refers to those which characterise the entire plasma, in contrast to the local measurements made by probes. These include visual inspection, microwave power absorption and optical emission spectroscopy (OES).

Two quite different plasma shapes were observed depending upon whether  $I_B$  was above or below that required to produce ECR (22.5 A). Looking down the axis, plasmas below ECR appeared as small discs or rectangular rings centered on the axis.

As  $I_B$  increased the discs first spread into rings, which then expanded in diameter. Above 22 A the plasma suddenly switched to a complicated but relatively uniform structure which completely filled the waveguide cross-section. In the transitional region around 22 A the plasma was unstable; flickering and randomly switching between the two types. Sketches of typical plasmas are given in figure 4.2. Plasmas under all conditions were a pale pink colour with a purple tint.

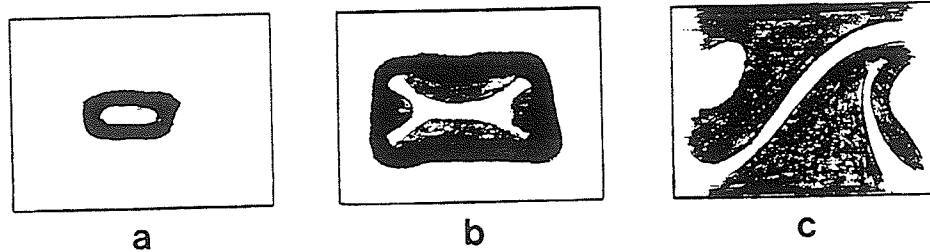


FIGURE 4.2. Typical appearances of the plasmas to visual inspection down the chamber axis. (a) and (b) are sub-ECR plasmas at  $I_B = 18$  and 20 A respectively, while (c) is an ECR plasma at  $I_B \geq 23$  A.

The visual appearance of the plasmas demonstrated some of the most basic features of these plasmas. Below ECR, the principal effect of  $B_0$  was to confine charged particles radially, hence the non-uniform, symmetric, axis-centered shapes. Increasing confinement would explain the radial expansion of these plasmas with  $I_B$  since better confinement would allow the plasma to be maintained by weaker electric fields and nearer to boundaries which acted as sinks of charged particles. Thus increasing confinement allowed the plasma column to expand, as observed. However, at ECR the principal effect of  $B_0$  was to generate axially localised regions of resonance within which most plasma generation occurred. In these resonant zones plasma generation was so efficient that the plasma expanded to fill virtually the entire waveguide cross-section. Thus a large and essentially uniform plasma was available for processing.

These simple magnetic field effects do not explain the fine structures observed in these shapes, especially in the ECR plasmas, which should not exhibit any such structure at all. It is also not apparent why there should be rings below ECR, when larger discs should be all that was required. These questions have a direct bearing on processing applications, since the reproducibility and uniformity of the process are largely determined by the reproducibility and uniformity of the plasma.

A complete set of OES spectra (covering the near-UV and visible spectral ranges) were taken as part of these experiments. It was originally thought that useful information regarding the ionisation and reaction paths followed in the plasma could be obtained as functions of system variables. However, the fact that the plasma was a non-uniform, diffuse optical source made it impossible to measure localised optical emissions from the plasma with the existing system. This would not be a problem if the plasma were uniform; in this case changes in spectra could reasonably be expected to be correlated with changes in fundamental plasma properties such as density and electron temperature. However, in a non-uniform plasma the measured spectra depends on the relative *amounts* of the different plasma regions that contribute to the

image focussed on the monochromator slit, as well as their basic plasma properties. Thus, OES was unable to distinguish between variations due to changes in the basic properties of a given region of plasma from changes in the relative area occupied by these regions. Efforts to provide the spectrometer with localised imaging capabilities are currently underway. Until this problem is satisfactorily solved, the spectrometer cannot be used as an effective plasma characterisation tool. Therefore, although a large number of spectra were recorded and analysed as part of these experiments, the results were of little use to this thesis.

Figure 4.3 shows the values of  $P_I$  required to maintain a given  $P_A$  as a function of  $I_B$ . The range of  $I_B$  shown was limited to the values for which a plasma could be sustained. Specifically, plasmas could not be supported at values of  $I_B$  less than 21, 18 and 17 A for  $P_A$ 's of 2, 4 and 6 W, respectively. The minimum power plasma that could be maintained was at  $P_A = 0.046$  W at  $P_I = 0.07 \pm 0.005$  W for  $I_B$  between 23 and 25 A. The plasmas became noisier and less stable above  $P_A = 6$  W.

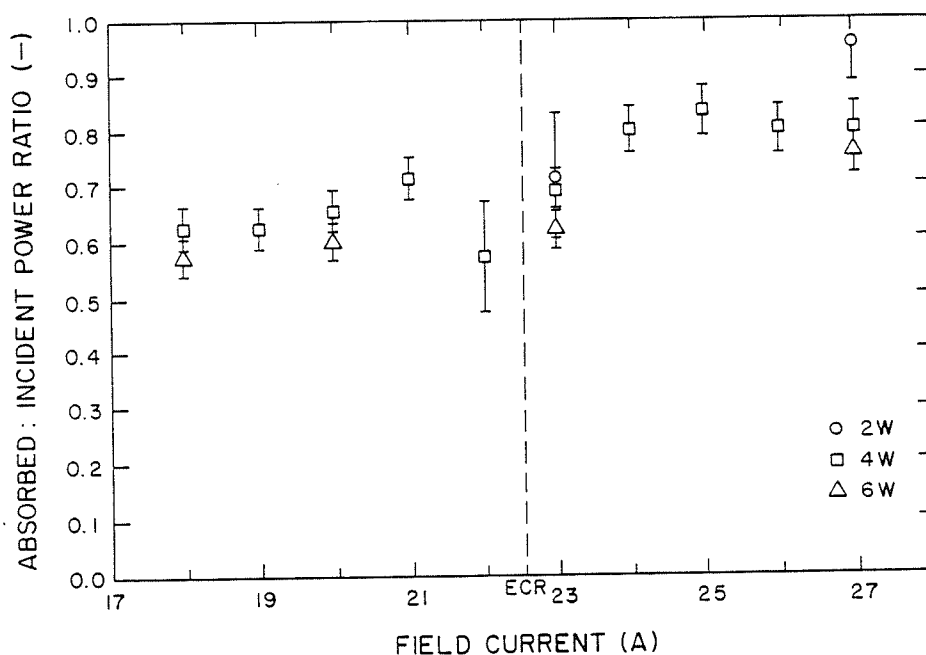


FIGURE 4.3.  $P_A/P_I$  for  $P_A = 2, 4$  and  $6$  W vs.  $I_B$ . The dashed line indicates the lowest value of  $I_B$  capable of producing ECR in the chamber.

By a fortunate accident, it was observed that the thermocouple mounted on the substrate table could act as a sensitive microwave "antenna". Microwaves incident on the table caused a dramatic increase in the reading of the thermocouple. Because the temperature responded almost instantaneously to variations in the power, it was assumed that only the exposed tip of the thermocouple was being heated, or acting as a high frequency rectifier. Also, withdrawing the thermocouple deep into its mounting hole in the sample table (see figure 4.1) eliminated this effect, thereby ruling out rapid heating of the entire table. Using this device, it was found that no power reached the table once a plasma was struck. This was later confirmed by replacing the rear flange

with a screened window assembly. After striking a plasma, the screen was removed and the microwave field measured with a survey meter (Microwave Technology SM1800); no microwaves were detected.

#### 4.3. DOWNSTREAM PLANE LANGMUIR PROBE

This diagnostic was the focus of these experiments. Its purpose was to sample the downstream plasma impinging on the sample table, not the active core under the magnetic field coil. The theory of plane probes, which differs slightly from that of OML probes (section 3.4), will be reviewed in sub-sections 4.3.1 and 4.3.2. The results will be presented in sub-section 4.3.3.

The form of the probe, shown in figure 4.1, was a Mo disc 0.1 mm thick and 3.8 mm in diameter. The probe was located 2 cm in front of the sample table and 7 cm from the center of the magnetic field coil. Only the front surface was uninsulated. The probe I-V characteristics were recorded with an X-Y recorder (HP 7035B) attached to the analog output of an electrometer (Keithly 610C), which measured the current. The voltage was ramped from -18 to +18 volts over approximately 10 seconds, 10 times for each curve. The linearity of the ion saturation current was checked out to -50 V separately. The raw data was digitised and loaded into a spreadsheet for presentation and analysis.

##### 4.3.1. Current Equations

Plane probe theory is straightforward and analytic; this was one of the main reasons for choosing this type of probe for these preliminary measurements. Other reasons were experimental simplicity and an obvious immunity to most of the complications in the ECR system that (originally) appeared to present problems in the analysis of other probe geometries. The theory of plane probe current collection is discussed in detail by Hutchinson<sup>2</sup> and Schott.<sup>3</sup>

Plane probe theory uses the same assumptions as the OML theory except that the probe is assumed to appear locally as an *infinite plane*, so that the sheath is *thin* compared to the lateral probe dimensions. The problem is therefore one dimensional. The I-V characteristics of a plane Langmuir probe are shown in figure 4.4. The equations describing the I-V characteristic in the electron retarding region ( $V < V_p$ ) are simpler than those of OML probes. The current is given by<sup>2</sup>

$$I = I_{0i} + I_{0e} e^{\chi_e} \quad (4.1)$$

where

$$I_{0i} = - (0.61) A n e \left( \frac{\kappa T_e}{m_i} \right)^{1/2} \quad (4.2)$$

and

$$I_{0e} = \frac{A n e}{2} \left( \frac{2 \kappa T_e}{\pi m_e} \right)^{1/2} \quad (4.3)$$

The normalised potential is still given by (3.14);

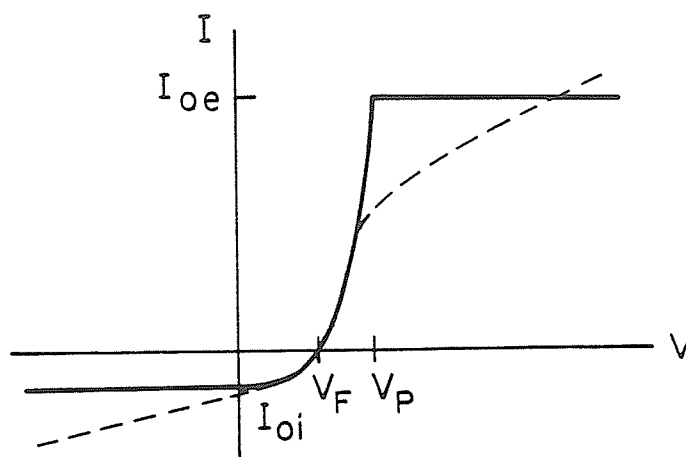


FIGURE 4.4. Sketch of the I-V characteristic of a plane Langmuir probe. The ion saturation current is exaggerated for clarity. The solid line shows an ideal characteristic while the dashed line shows the effect of a moderate magnetic field (oriented with the lines of flux perpendicular to the probe surface) and fringing fields in the probe sheath.

$$\chi_e = \frac{e(V - V_P)}{\kappa T_e} \quad (4.4)$$

$A$  is the surface area of the sheath, which was assumed to be equal to the surface area of the probe;  $A = \pi R^2$ , where  $R$  is the radius of the probe disc. The numerical factor 0.61 is actually  $\exp(-1/2)$ . The other symbols have the same meanings as in chapter 3. Note that appropriate geometrical factors must be included in the saturation currents if fringing fields produce significant sidewalls on the planar sheath. These would, for example, make  $I_{0i}$  a function of voltage,  $I_i(V)$ , in which case the true ion saturation current should be taken at  $I_{0i} \equiv I_i(V = V_P)$ .

#### 4.3.2. Interpretation of the I-V Characteristics

The plane probe analysis procedure involved fitting a line,  $I_i(V)$ , to the current at large negative biases.<sup>4</sup> This is equivalent to assuming that the sheath had some spherical character due to fringing fields, since spherical probes collect saturation currents linear in  $V$ . This line was then subtracted from  $I(V)$  to obtain  $I_e(V)$ . Observe that  $T_e$ , in eV, is the inverse of the derivative with respect to  $V$  of the logarithm of  $I_e(V < V_P)$ . Graphically, this is the inverse of the slope of the line  $|\ln(I - I_i)|$  versus  $V$ . Once  $T_e$  was known,  $n$  could be obtained from (4.2) by extrapolation of the line  $I_i(V)$  to  $V_P$ . Here there is no sheath and  $I_{0i}$  and  $I_{0e}$  are collected directly. Thus we define  $I_{0i} \equiv I_i(V_P)$ .  $V_F$  was read directly off of the I-V characteristic at the point where  $I = 0$ . In non-ideal cases, as occurred here,  $V_P$  must be calculated from  $V_F$  and  $T_e$  as described below. Note that if  $\ln[I_e(V)]$  was not linear, then the electron energy distribution function was not Maxwellian. In such cases the approximate form of the EEDF can be obtained from the second derivative of  $I_e(V)$  with respect to  $V$ .<sup>4,5</sup>

Magnetic fields produce several complications in the interpretation of plane probe I-V characteristics.<sup>2,4,6,7</sup> In this case the magnetic field strength was typically

such that  $r_{Le} < R \ll r_{Li}$ ; the so-called "moderate" magnetic field condition.<sup>6</sup> Under these conditions ion collection is essentially unaffected by  $B_0$ , and  $I_{0i}$  is still given by (4.2).<sup>2</sup> Electron collection well below  $V_p$  is also not significantly affected, so  $T_e$  and  $V_F$  are obtained as before.<sup>2</sup> However, near and above  $V_p$  the I-V characteristic was strongly distorted by  $B_0$  and ideal theory no longer applies.

The effect of  $B_0$  on electron collection (above  $V_p$ ) is to constrict the electron presheath to a *flux tube* parallel to  $B_0$  with a radius of about  $R+r_{Le}$ . This arises because  $B_0$  forces collection to take place primarily along the magnetic field lines. A flux tube reduces the electron collecting area of any convex probe to its equivalent planar projection perpendicular to the field lines. While this reinforces the planar condition, it also creates several theoretical difficulties.<sup>2,6,7,8</sup> The first is that  $I_{0e}$  is now determined by the limiting rate of cross-field diffusion into the sides of the flux tube, so it is not simply related to the random thermal flux of electrons. This is because the high rate of collection in this region depletes the flux tube of plasma, which must be replaced by diffusion across the magnetic field lines. Also,  $I_{0e}$  does not saturate since the surface area of the flux tube expands with  $V$ . The flux tube may expand in length enough to enclose significant volumes of charged particle generation or loss, in which case  $I_{0e}$  also becomes dependent on inelastic collision processes.<sup>7</sup>

The result is that  $I_{0e}$  is reduced (see figure 4.4) in a largely unpredictable manner, meaning that (4.3) cannot be used to obtain the plasma density, although (4.2) can still be used. The range of the I-V characteristic which may be used to determine  $T_e$  is also reduced, and the "saturation" knee in the I-V characteristic becomes blurred and unrelated to  $V_p$ . Thus  $V_p$  cannot be obtained graphically and must be calculated from  $V_p = V_F - \phi_F$  once  $V_F$  and  $T_e$  have been determined. An expression for  $\phi_F$  can be obtained from (4.1) with  $I(V_F) = 0$ ;

$$\phi_F = \frac{\kappa T_e}{2e} \left[ \ln \left[ 2\pi \frac{m_e}{m_i} \right] - 1 \right]. \quad (4.5)$$

Flow of the plasma towards the rear of the chamber was not a problem for the single-sided plane probe used in these studies, since it was oriented normal to the direction of flow.<sup>6,4</sup> Exposure to microwaves was also not a problem as the probe was always situated in a region free of microwaves (sub-section 4.4.2). However, other oscillations in the plasma may have produced small perturbations of the I-V characteristics as described in sub-section 3.4.1.

### 4.3.3. Measurements

Figure 4.5 shows example I-V characteristics for  $P_A = 4$  W plasmas above and below ECR. Corresponding  $|\ln[I_e(V)]|$  curves are also shown. The latter were all linear within error over the range of approximately -10 to 0 V; above the noise floor in  $I_i(V)$  and below the magnetic field-induced roll-off below  $V_p$ .

The floating voltages are shown in figure 4.6. The plasma potentials, as calculated from (4.4), are also shown. Both  $V_F$  and  $V_p$  confirm the gross trends observed in the bulk plasma by visual observation and power measurements; that there were different types of plasmas above and below ECR. The unstable region between the two may have manifested itself through the unexpected jumps in  $V_F$  and  $V_p$  at 21 and 23 A,

although why 22 A seems to have been unaffected is not known.

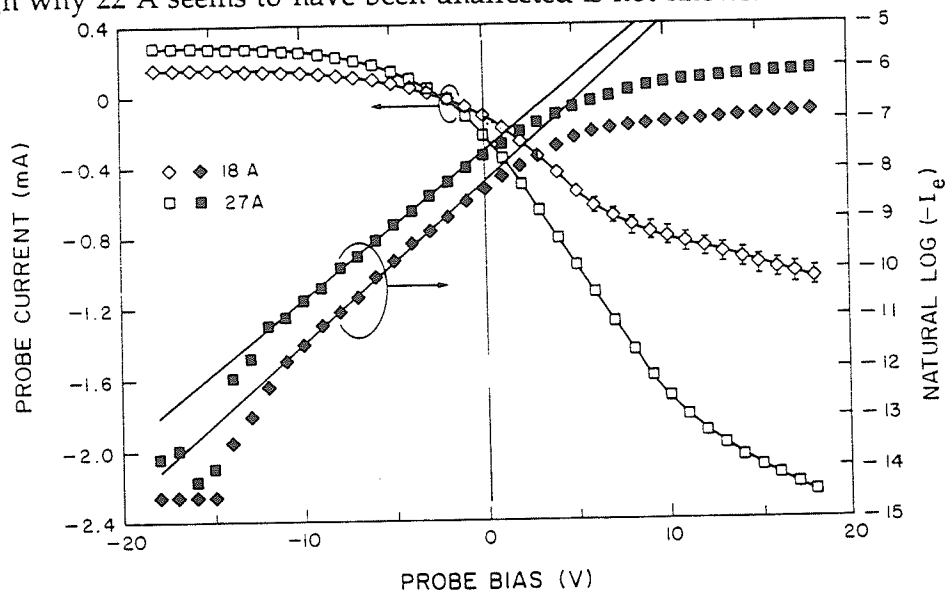


FIGURE 4.5. Probe I-V characteristics of  $P_A = 4$  W plasmas above and below ECR. Measurement error, except where otherwise indicated, was less than the symbol size. The open symbols are the raw data, while the closed symbols are  $|\ln[I_e(V)]|$ . For I-V characteristics taken below ECR, noise increased dramatically near and above electron saturation.

Above ECR both  $V_F$  and  $V_P$  varied smoothly, increasing slowly with  $I_B$ . Since all plasmas above ECR should have been similar except for their location, such a trend would be expected. This is because plasma generation should occur primarily in the axially localised ECR planes centered at  $B_0(z) = 0.0875$  Tesla. Thus resonance, rather than confinement, would dominate the properties of the plasma, and all ECR plasmas should have been essentially the same except for their axial location. As  $I_B$  increased, the spacing between the probe and the rear ECR plane decreased. This should have resulted in gradual increases in all the parameters measured by the probe<sup>9</sup> (until the probe entered the resonant zone, where large changes would presumably occur). This is exactly what was observed with  $V_F$  and  $V_P$ , and possibly in  $T_e$  and  $n$  also. The behaviour of  $V_F$  and  $V_P$  below ECR is not clear; there is insufficient data.

The electron temperatures are presented in figure 4.7, which shows additional evidence of distinct types of plasmas occurring above and below ECR. A gradual increase with  $I_B$  above ECR, perhaps due to movement of the ECR planes may also be indicated. The origin of the larger variations below ECR is not clear; it could have been due to shape or position changes, or simply to data scatter. In any case,  $T_e$  does not vary much with either  $I_B$  or  $P_A$ , either above or below ECR.  $T_e$  averages approximately 3.5 eV.

The plasma densities are shown in figure 4.8. The precision of this data was only sufficient to discern the gross features noted previously; distinct plasmas above and below ECR and, perhaps, a gradual increase in  $n$  with  $I_B$  above ECR. Average values were approximately  $4 \times 10^{15} \text{ m}^{-3}$  below ECR and  $10^{16} \text{ m}^{-3}$  above.

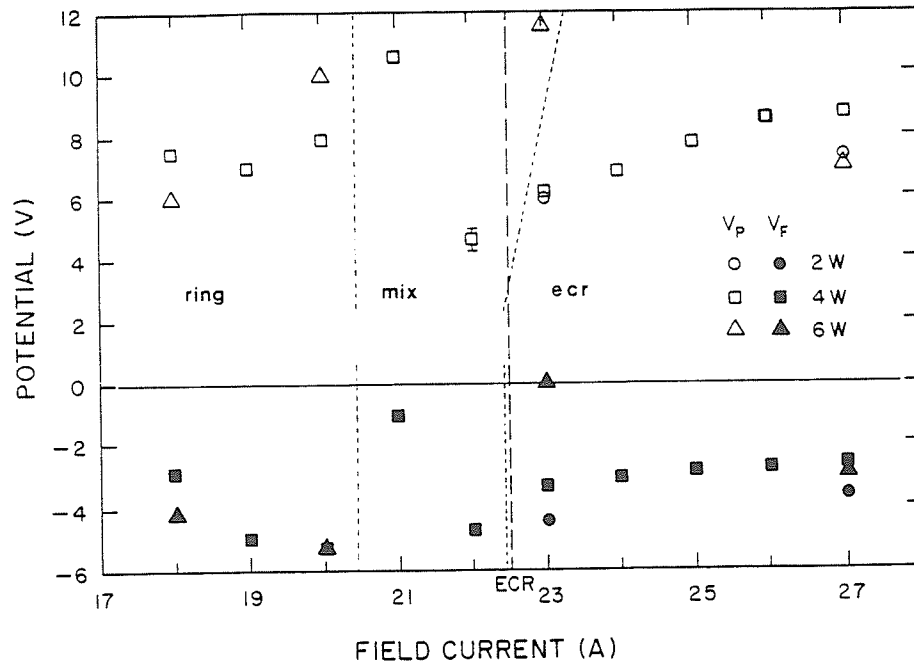


FIGURE 4.6.  $V_p$  and  $V_f$  vs.  $I_B$  at  $P_A = 2, 4$  and  $6$  W. The cumulative effect of measurement errors, except where otherwise indicated, were less than the symbol size.  $V_p$  was calculated from  $T_e$  and  $V_f$ . The results have been grouped according to the shape of the plasma (see sub-section 4.4.2). The dashed line indicates the lowest value of  $I_B$  capable of producing ECR in the chamber.

#### 4.4. DISCUSSIONS

The reader may have noticed that the results of these experiments have not cast much light on the nature of ECR plasmas. A set of useful estimates of the most important plasma parameters has been obtained, and their qualitative behaviour over a restricted but representative range of system variables have been observed. However, these results do little to clarify the *mechanisms* underlying this behaviour.

The main source of this difficulty is clear in retrospect; these experiments were designed with a too simplistic picture of ECR plasmas in mind. Indeed, these results are more remarkable for what was not found, rather than what was. A partial list of expected results makes this point clear: (1) uniform plane (cross-section) plasmas above ECR, (2) uniform disc (cross-section) plasmas below ECR, (3) a linear, or at least monotonic, dependence of  $n$  and  $P_A$  on  $P_I$ , and (4) little to no ECR using this magnetic field configuration. With hindsight it now appears that the true value of this study lay in the clues it contained as to *how to look* for the physics underlying the properties of ECR plasmas. The remainder of this thesis is basically an attempt to exploit these clues. In the rest of this section several of the most important of these clues will be described. First however, improvements to the Langmuir probe diagnostic will be discussed.

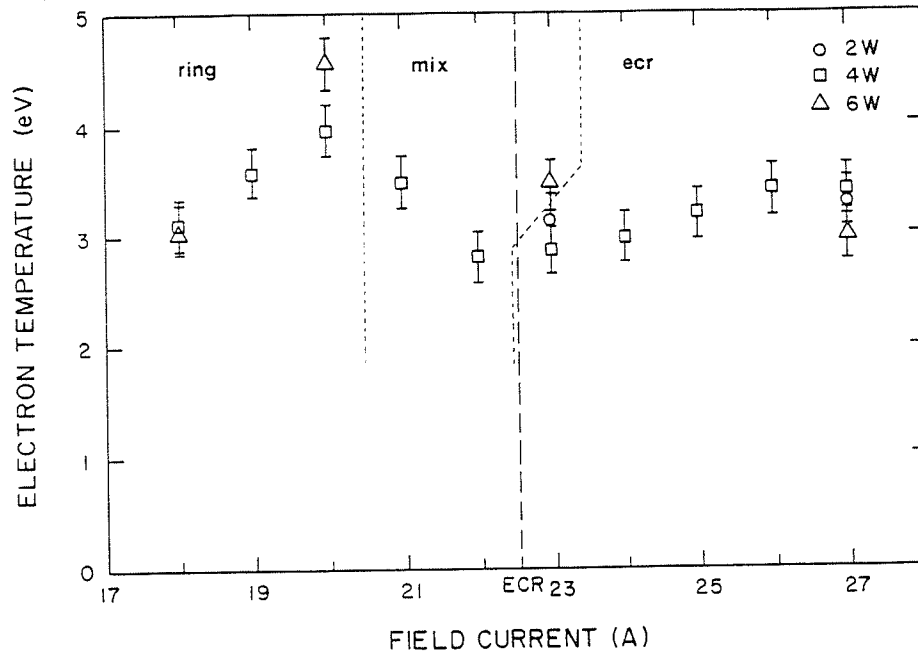


FIGURE 4.7.  $T_e$  vs.  $I_B$  at  $P_A = 2, 4$  and  $6$  W. The results have been grouped according to the shape of the plasma (see sub-section 4.4.2). The dashed line indicates the lowest value of  $I_B$  capable of producing ECR in the chamber.

#### 4.4.1. Improvement of the Langmuir Probe Diagnostic

The probe used in these experiments was well suited for a study of downstream, magnetised plasmas. However, several improvements are clearly called for. The wide range of conditions possible in the ECR system imply that more rigorous characterisations will require a large number of probe measurements. Obviously automation of both the data acquisition and analysis processes will be necessary. The very non-uniform nature of these plasmas means that the probe should also be movable, at least axially, and preferably radially as well. The additional variables added by this will make automation even more necessary.

A more serious question is the accuracy of the plane probe technique itself. Plane probes have two inherent features which limit their accuracy to a qualitative level. The first is that no practical probe can be completely planar; fringing fields and sheath sidewalls will always be present. Although this can be partially compensated for with a guard-ring and/or in the analysis procedure, the fact remains that the true geometry of the collecting surface of the sheath is unknown. Thus  $n$  can only be estimated and determinations of  $T_e$ , though not affected directly, are hindered by the accuracy with which  $I_i(V)$  can be obtained. The second problem is that plane probes, especially with guard-rings, are large and perturb the plasma near the probe in an unpredictable way (which affects both  $n$  and  $T_e$ ). Unfortunately, solutions to these problems are incompatible; smaller probes are less planar and vice versa. The only satisfactory solution is to abandon the planar geometry for one which is amenable to miniaturisation. Of course, the new design must also be immune to the complicating factors present in ECR reactors. As discussed in section 3.4, the solution adopted was the orbital-motion

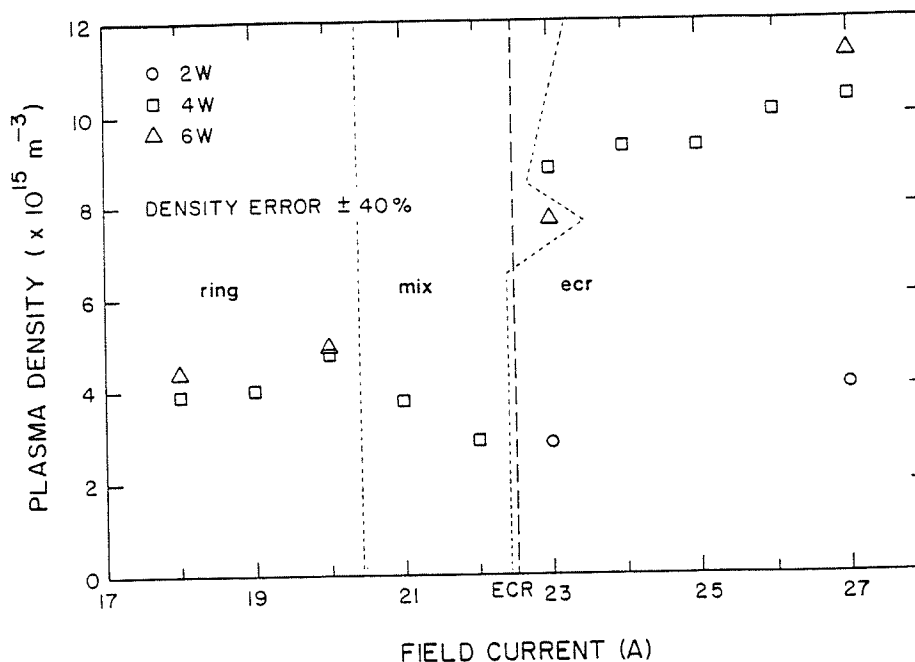


FIGURE 4.8.  $n$  vs.  $I_B$  at  $P_A = 2, 4$  and  $6$  W as obtained from the ion saturation current extrapolated to  $V_p$ . The results have been grouped according to the shape of the plasma (see sub-section 4.4.2). The dashed line indicates the lowest value of  $I_B$  capable of producing ECR in the chamber.

limited cylindrical geometry. Such probes have been shown to yield qualitatively accurate results in magnetised<sup>8</sup> and flowing<sup>6</sup> plasmas.

#### 4.4.2. Global Diagnostics for Global Behaviours

The global diagnostics were originally intended only to facilitate reproducibility of the plasma conditions. However, when it became clear that the plasmas were not behaving as expected, it also became clear that the global measurements were the most sensitive to this problem. Visual inspection in particular appeared to be revealing some kind of underlying order.

Consider any of the probe data; other than the ECR/sub-ECR distinction the data seems to be widely scattered, with little in the way of a monotonic trend apparent. This is especially true of their dependence on  $P_I$ . Consider, however, correlating these results with the shape of the plasma. This was done for figures 4.6 to 4.8. In these figures, "ring" refers to plasmas like those shown in figure 4.2(a) and (b), while "mix" refers to different mixtures of 4.2(b) and (c). "ECR" refers to the complex form shown in figure 4.2(c). There is a clear, if qualitative, correlation between the properties of the plasmas and their visual appearance. For a given shape there appears to be little variation with  $P_A$ , and only a gradual, monotonic dependence on  $I_B$ . Thus for a given shape, the behaviour of the plasma is actually very simple. Perhaps the shape of the plasma can be used to break up the ECR system's parameter space into a collection of different regions, within which the plasmas behave simply.

Considerations of this type led to an examination of how easily performed, qualitative, global diagnostics could be used to organise and classify the overall behaviours of ECR plasmas. The results of these efforts are described in chapter 5.

#### 4.4.3. On the Occurrence of ECR

Finally, the obvious question of how ECR could arise in a peaked magnetic field configuration will be addressed. While partial transmission of microwaves through the cutoff into ECR due to collisions and tunnelling<sup>10,11</sup> might be expected to occur, these should not have allowed ECR to *dominate* the properties of the plasma as appears to have been the case. Indeed, it now appears that these phenomena were enhanced by instabilities in the magnetron, and is a classic example of why the *system* must be fully characterised before being used.

The Phillips YJ1160 is a 500 W to 2.5 kW power magnetron not intended for low power applications. In these experiments the magnetron was typically operated at approximately 300 W, where all but a few watts ( $P_l$ ) were lost/reflected in the convoluted transmission path leading up to the chamber. When operated below its minimum power rating, any magnetron exhibits shifts in operating frequency as well as instabilities in the power output. Such instabilities and shifts were in fact measured in the output of this magnetron shortly before its demise. Oscillations in the kilohertz range and above, on the order of 50% of the signal level, were observed.

The presence of such large oscillations in the microwave power would permit ECR to occur by allowing the plasma density to drop sufficiently between "pulses" to bring the cutoff and resonant frequencies together, since  $\omega_R(n \rightarrow 0) = \omega_C$ . Thus ECR would first occur, building up  $n$  until the cutoff region became strong enough and far enough removed from the ECR plane to prevent resonance. Then as the power dropped the reverse would take place. Thus the plasma would oscillate between conditions of ECR and cutoff. As additional evidence for this hypothesis, it will be shown in chapter 5 that the peaked configuration does *not* exhibit significant ECR-like behaviours when a stable power source is used.

#### References

1. P.K. Shufflebotham, D.J. Thomson, and H.C. Card, "Behavior of Downstream Plasmas Generated in a Microwave Plasma Chemical-Vapor Deposition Reactor," *J. Appl. Phys.* 64, p. 4398, 1988.
2. I.H. Hutchinson, *Principles of Plasma Diagnostics*, p. 50, Cambridge University press, Cambridge, U.K., 1987.
3. L. Schott, "Electrical Probes," in *Plasma Diagnostics*, ed. W. Lochte-Holtgreven, p. 668, North-Holland, Amsterdam, 1968.
4. J.D. Swift and M.J.R. Schwar, *Electrical Probes for Plasma Diagnostics*, Illife, London, 1969.
5. V. Godyak, *Measuring EEDF in Gas Discharge Plasmas*, Alicante, Spain, Sep. 4-16, 1988. NATO Advanced Study Inst. Prog. Plasma Surface Interaction and Processing of Materials
6. P.M. Chung, L. Talbot, and K.J. Touryan, *Electric Probes in Stationary and Flowing Plasmas: Theory and Application*, Springer-Verlag, New York, 1975.
7. F.F. Chen, "Electric Probes," in *Plasma Diagnostic Techniques*, ed. S.L. Leonard, p. 113, Academic, New York, 1965.
8. F.F. Chen, C. Etievant, and D. Mosher, "Measurements of Low Plasma Densities in a Magnetic Field," *Phys. Fluids* 11, p. 811, 1968.

9. B.W. Rice and J.E. Scharer, "Observation of Localized Electron Cyclotron Resonance Heating in a Magnetic Mirror," *IEEE Trans. Plasma Sci.* PS-14, p. 17, 1986.
10. D.G. Swanson, *Plasma Waves*, Academic Press, Boston, 1989.
11. T.H. Stix, *The Theory of Plasma Waves*, McGraw-Hill, New York, 1962.

## CHAPTER 5

### DIAGNOSTICS FOR PLASMA STABILITY\*

*You can observe a lot just by watching.*  
- Yogi Berra.

The results of chapter 4 clearly demonstrate the need for a means of searching the parameter space of the plasma system for regions of instability or other unusual behaviour. This chapter contains a description of three complementary diagnostic techniques which were found to be very useful in identifying, classifying, and delimiting the range of such regions.

The objects of interest in this chapter are the plasma *modes* produced in the ECR plasma processing reactor. As discussed in sub-section 2.3.1, plasma modes are characterised by a distinct shape and properties which vary smoothly with system parameters. Transitions between modes are discontinuous, noisy and sometimes bistable. The astute reader will have guessed that, although not explicitly stated (because it was not recognised at the time), the results presented in chapter 4 were seriously undermined by the occurrence of modes in the plasma. Once the modal nature of the plasmas was recognised, the diagnostic techniques described in this chapter were developed to provide a way of determining the number and extent of the modes which could appear in the parameter space of a given system configuration.

This chapter is in the form of a demonstration by example, where the uses, capabilities and limitations of these diagnostic techniques are indicated by using them to study the modes produced in system configurations of interest to this thesis.

#### 5.1. EXPERIMENTAL

The plasma system was exactly as described in chapter 3. Both the peaked and beach  $B_0$  profiles were used.  $I_B$  was varied over as wide a range as would support a plasma.  $P_I$  could be varied from 0 to 100 W, but these experiments were restricted to the 0 to 50 W range. The pressure was varied from  $10^{-3}$  to  $10^{-1}$  Torr.

The diagnostic measurements consisted of power characteristics, visual inspection, and time-resolved measurements of either  $P_R$  or  $V_F$ . The visual observations were supported by photographs taken with a 35 mm camera equipped with a 200 mm telephoto lens and high contrast black and white film.

The dynamic measurements were performed by connecting a suitable transducer to a digital storage oscilloscope (Tektronix 2221). The transducer was either a microwave diode detector (Microlab/FXR) connected to the  $P_R$  terminal of the

---

\* P.K. Shufflebotham, D.J. Thomson, "Diagnostic Techniques for Plasma Stability in Electron Cyclotron Resonance Plasma Processing", accepted for publication in the *Journal of Vacuum Science and Technology A*.

directional coupler or a floating Langmuir probe inserted into the rear of the chamber (this probe was installed during all the measurements reported in this chapter). Both techniques produced the same results, but the microwave detector method has the advantage of being non-invasive. The output of the diode detector was a voltage proportional to  $P_R$ . Due to the relatively slow response of the thermistor power heads, the value measured by the power meter corresponded roughly to the average value output by the diode detector.

The power characteristics consisted of curves of  $P_R$  versus  $P_I$  obtained from the microwave power meter readings. Data points over the range of  $P_I = 0$  to 50 W were taken in 2 W decrements starting at 50 W. Note that while  $P_A$  is the important quantity as far as the properties of the plasma are concerned,  $P_R$  was used because it was the measured quantity and because it is the *form* of these curves which are of interest. While the plasma properties change within a given power characteristic, we have found that the form of these characteristics changes only at a mode transition. Therefore, power characteristics provide a quantitative way forming a "map" of the modes occurring in the system's parameter space.

## 5.2. RESULTS

Power characteristics are plotted as functions of  $I_B$  for different magnetic field profiles in figures 5.1 and 5.2. Despite their complex appearance, they were completely reproducible within measurement error ( $\pm 3\%$ ). Observe that under any particular set of system settings there was a (non-zero) minimum microwave power required to maintain the plasma. This minimum maintenance power, determined by  $P_I(\min)$ , set the lowest value of  $P_A$  which could generate enough electrons to replace those lost from the plasma.<sup>1</sup> Thus the plasmas did not gradually disappear as  $P_I$  went to zero, but rather became extinct as soon as  $P_I < P_I(\min)$ . Extinction could also be produced by changes in most other system variables.

At very low powers,  $P_I \leq 5$  W, and below 1 W especially, a few new modes appeared to form. These modes appeared in all plasmas sustainable at these power levels, regardless of  $I_B$  or  $p$ . The bump observed at low power in the ECR plasmas of figure 5.2 is an example of this. We believe that these were artifacts associated with noise measured (in vacuum) in the microwave power output by the magnetron at these low levels. The noise was only greater than 10% of the signal level below  $P_I = 5$  W. Below 3 W the output became entirely oscillatory. This was the origin of any universal mode-like features below  $P_I \approx 5$  W. Above 12 W, noise was always less than 1% of the signal level.

Consider the power characteristics of plasmas generated in the peaked magnetic flux density profile of figure 3.5(a). These characteristics, shown in figure 5.1 as a function of  $I_B$  on a single graph, have several of features in common.  $P_R$  in the presence of plasma was a *linear* function of  $P_I$  which did not change with  $I_B$  even with the appearance of ECR conditions above  $I_B = 22.8$  A. These plasmas were also inefficient absorbers of microwave power. Small differences were observed in the shapes of the plasmas and the range of power over which plasma could be sustained. It will be shown later (figure 5.5) that a weak ECR to sub-ECR mode transition did occur, as indicated by visual inspection, but this did not appear in these less sensitive

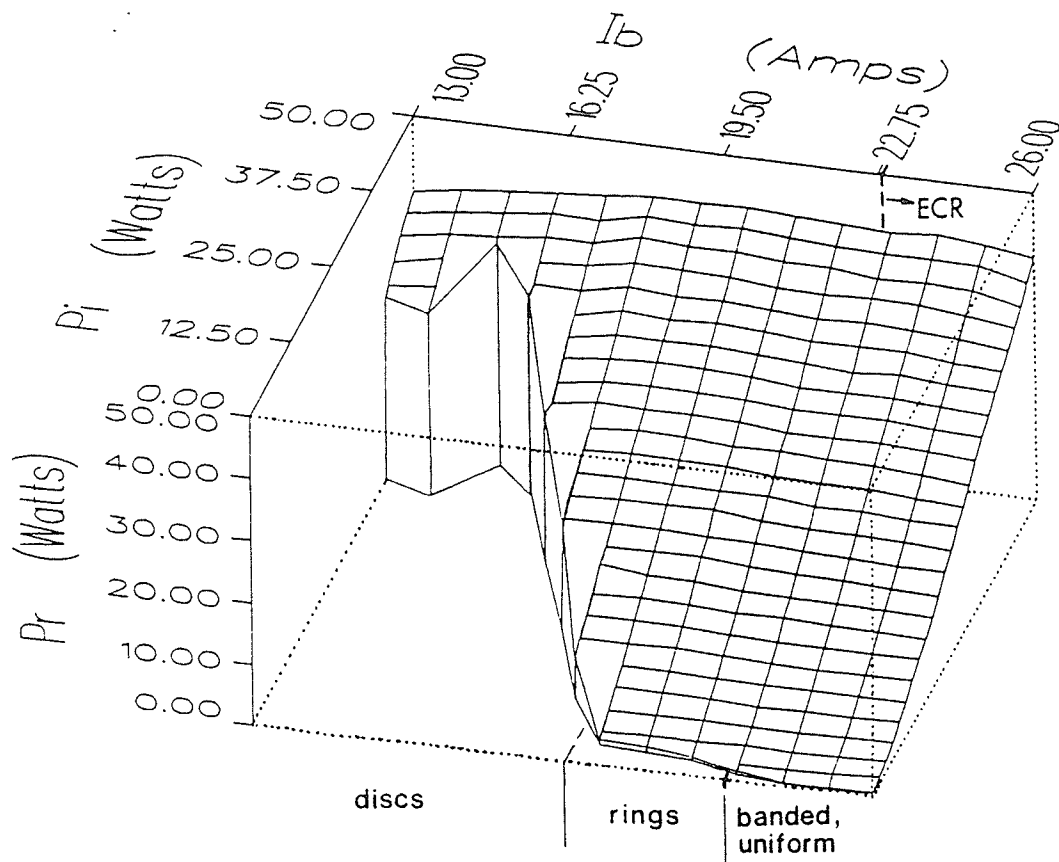


FIGURE 5.1. Power characteristics at 0.01 Torr as functions of  $I_B$  for the peaked magnetic flux density profile of figure 3.5(a). The individual power characteristics have been connected together into a grid pattern. Plasma could not be sustained at  $P_I \leq 50$  W for  $I_B < 13$  A. For clarity,  $P_R$  has been set to zero in regions where no plasma could be sustained ( $P_R/P_I$  of the evacuated chamber was approximately 40%). These regions also do not have the grid pattern. Characteristics above 26 A could not be obtained due to overheating of this coil. The general appearance of the plasmas are noted as a function of  $I_B$  below the lower current axis. "Banded, uniform" refers to plasmas which filled the chamber cross-section uniformly, except for a dark band across the diagonal.

measurements.

We believe that the decrease of  $P_I(min)$  as  $B_0(z)$  increased is well explained by the standard diffusion model of microwave breakdown.<sup>1</sup>  $P_I(min)$  decreases because increasing  $B_0$  reduces the diffusive loss of plasma particles to the chamber walls. In addition, ECR conditions are expected to produce a particularly dramatic decrease in  $P_I(min)$ , as observed.<sup>1</sup>

The overall shapes of these plasmas are determined by  $B_0$ . With  $I_B$  at or above that required to produce ECR the plasma would be expected to fill most of the chamber cross section, as observed, since even the weak fields near the walls would be able to sustain the plasma. However, dark diagonal bands and related patterns of unknown origin were also observed within these plasmas. With  $I_B$  immediately below that required for ECR, the plasma was in the form of a large rectangular ring (with a

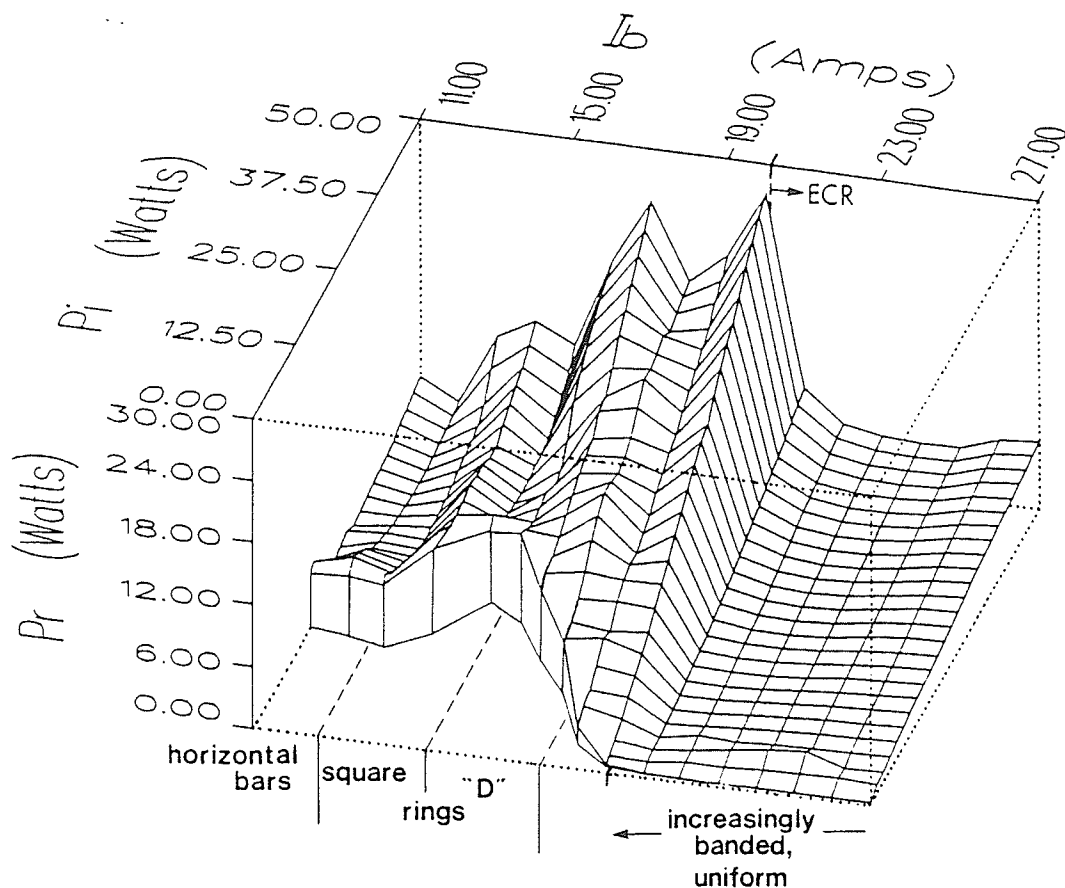


FIGURE 5.2. Power characteristics at 0.01 Torr as functions of  $I_B$  for the magnetic beach flux density profile of figure 3.5(b). The individual power characteristics have been connected together into a grid pattern. Plasma could not be sustained at  $P_I \leq 50$  W for  $I_B < 10.6$  A. For clarity,  $P_R$  has been set to zero in regions where no plasma could be sustained ( $P_R/P_I$  of the evacuated chamber was approximately 40%). These regions also do not have the grid pattern. The general appearance of the plasmas are noted as a function of  $I_B$  below the lower current axis. Hysteresis, which occurred during transitions between several of the modes as a function of  $P_I$  and  $I_B$ , is not shown.

complex, fainter filling), centered on the waveguide axis. Decreasing  $I_B$  caused the ring to first collapse gradually into an oval disc, which in turn decreased in radius until (at a non-zero radius) the plasma suddenly disappeared. Smaller plasma radii at lower  $I_B$  would be expected from decreased confinement since larger microwave electric fields would be required to sustain the plasma,<sup>1</sup> causing the plasma to contract towards the waveguide axis where the electric field was stronger. Again however, the origins of the detailed structure observed in these plasmas, such as why hollow rings should occur instead of larger discs, is not known.

The results for the peaked magnetic field profile are to be contrasted with those for a magnetic beach, figure 3.5(b), where the magnetic field decreases into ECR. Figure 5.2 clearly shows that highly absorbent plasmas were indeed generated in this configuration whenever ECR occurred somewhere in the plasma chamber ( $I_B > 20$  A). While the power characteristics and visual appearances of the ECR plasmas were all very similar, dramatic differences were observed between the ECR and sub-ECR

plasmas. The sub-ECR plasmas produced by the magnetic beach were also different from the plasmas generated using a peaked profile.

The sub-ECR plasmas exhibited a variety of plasma modes. Their overall shapes were similar to those observed in the peaked field configuration, and were also consistent with the confining action of  $B_0$ . However, they exhibited considerable variation in their detailed structure, the origins of which are not known. A striking example of a sub-ECR plasma mode is shown in figure 5.3(d). The modes in the sub-ECR plasmas could easily be identified during an experiment, since they changed both shape and  $P_R$  suddenly, often exhibiting hysteresis. Figure 5.2 is misleading in this regard, as it shows transitions between modes to be continuous, whereas in fact most exhibited hysteresis, and thus many of the actual mode domains overlap. The notes concerning the shapes included in figure 5.2 correspond to the different modes observed in the high  $P_I$  regime (40 to 50 W).

Note that at higher pressures the confining action of the magnetic field on the sub-ECR plasmas was lost as electron-neutral collisions began to dominate the diffusion process. Figure 5.3(c) shows an example of a typical higher  $p$ , sub-ECR plasma. Again, the exact origin of the detailed structures observed in the plasmas is unknown.

The ECR plasmas tended to concentrate near the walls and to one side of the plasma chamber, effects which became more pronounced as  $p$ ,  $I_B$  and/or  $P_I$  increased. The concentration towards the walls is very similar to that observed in several other ECR systems, as described in sub-section 2.3.1. Dark, diagonal bands, similar to those observed in the ECR plasmas produced with the peaked profile, were observed below  $P_I=30$  W. ECR plasmas all appeared to be well localised axially (at least their visible front edges), and moved away from the window with increasing  $I_B$ , following the resonant zone.

The effect of pressure on the ECR plasmas generated in the magnetic beach configuration was examined over the range of  $10^{-3}$  to  $10^{-1}$  Torr. These measurements were restricted to the ECR region, where  $I_B \geq 20$  A. This data was simple enough that full sets of power characteristics, such as figures 5.1 and 5.2 (with  $I_B$  replaced by  $p$ ) were not required. Instead, figure 5.4 shows  $P_R$  at  $P_I = 50$  W as a function of  $p$ . The complete form of the power characteristics was unchanged from that seen at  $10^{-2}$  Torr (figure 5.2) except that their magnitudes varied with  $p$  according to figure 5.4.

The ECR plasmas did not change shape appreciably with  $p$  above  $10^{-2}$  Torr, although they did tend to concentrate closer to the chamber walls, as noted earlier. Decreasing  $p$  below  $10^{-2}$  Torr allowed the plasmas to expand until they filled the entire chamber cross-section at  $6 \times 10^{-3}$  Torr. However, below  $3 \times 10^{-2}$  Torr a small dark hole appeared in the center of the otherwise uniform plasma. Further decreases in  $p$  caused this hole to expand until it virtually filled the waveguide at  $10^{-3}$  Torr, as shown in figures 5.3(a) and 5.3(b) (several ordinary ECR plasmas are shown in figure 5.6). Note that the hole region was not completely dark, but had a deep blue colour. Here we have an example of the importance of direct visual observation: *all* the ECR plasmas underwent a dramatic change as  $p$  dropped below  $3 \times 10^{-3}$  Torr, despite the minor effect implied by most of the power characteristics in figure 5.4.

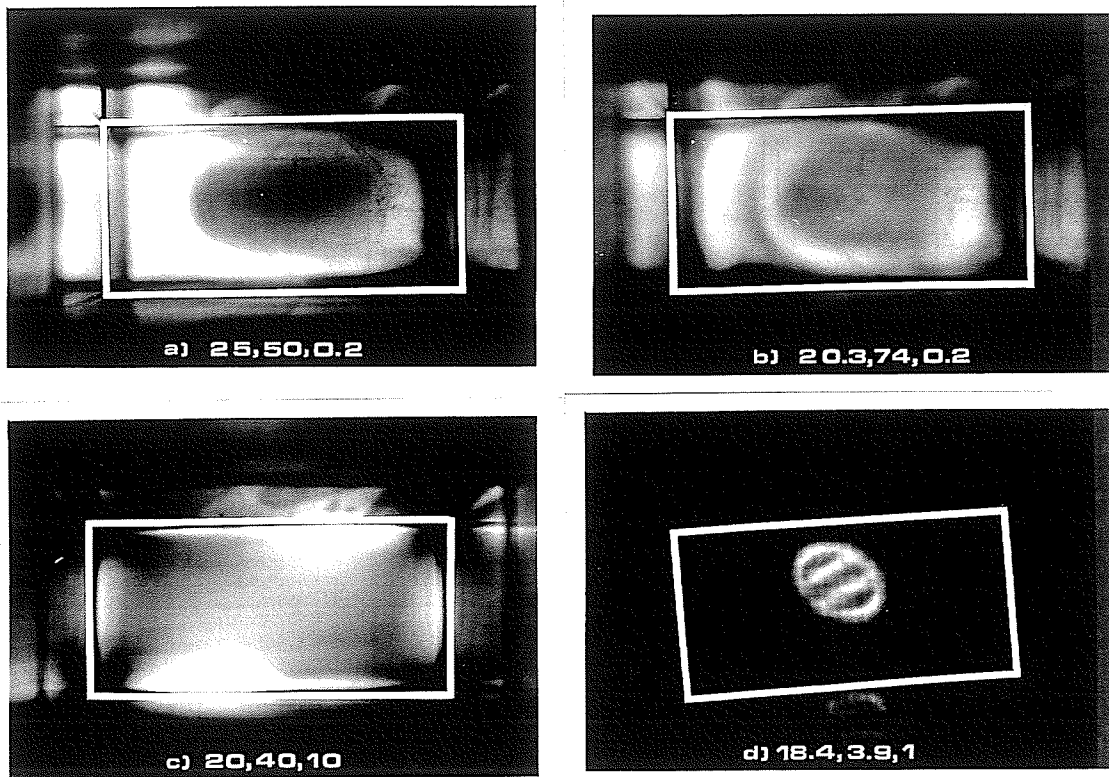


FIGURE 5.3. 35 mm photographs of several plasmas formed in the ECR plasma processing chamber for the magnetic beach configuration of figure 3.5(b). The system settings for each plasma are noted in the following three number format: ( $I_B$  (Amps),  $P_I$  (Watts),  $p$  ( $\times 10^{-2}$  Torr)). The waveguide cross-section at the quartz window has been outlined to prevent confusion of the plasma with wall reflections and to provide a scale reference; the cross-sectional dimensions of the waveguide were 7.2 by 3.6 cm. The screened wall of the waveguide elbow, through which these pictures were taken, was responsible for the faint grid-like patterns. The "dirt" visible in (a) and (b) was due to roughness on the inner surface of the quartz window which scattered the dark blue light produced by the "hole" regions. Note that (d) was taken under low power conditions where noise in  $P_I$  may have affected the plasma.

We have found that the transition between modes could be studied in some detail through the use of dynamic measurements designed to detect oscillations of the plasma as a whole. An example of what occurs during a mode transition is shown in figure 5.5. Originally it was hoped that oscillations associated with drift or other low frequency waves would be detected, which could then be correlated with the different modes. This was not what was typically observed in these measurements. Instead, the signal associated with most modes, away from transition regions, consisted of a DC voltage upon which a weak noise signal of approximately  $\pm 2\%$  was superimposed (as in traces (a) and (e) of figure 5.5). Within a given mode the DC levels changed smoothly, following  $P_R$ , as some system variable was varied. In figure 5.5, traces (a) and (e) both decreased with  $I_B$ . As a transition approached, however, the DC level began to randomly switch to the value associated with the new mode (traces (b) and (c)). This began with sharp, infrequent spikes to the new value of  $P_R$ , which occurred with increasing frequency as the system variable ( $I_B$  in this case) continued to change (decrease). In mid-transition it was sometimes possible to observe this switching behaviour visually, when the switching rate was low enough. More often, the plasma

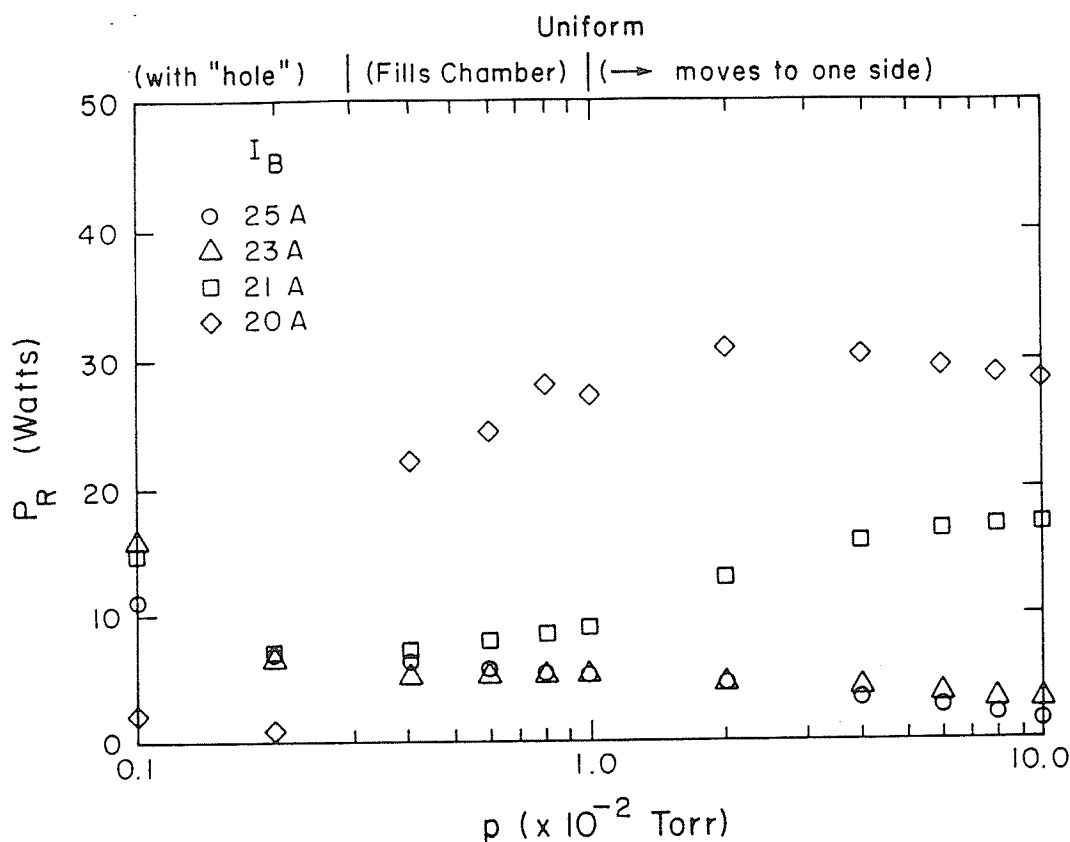


FIGURE 5.4.  $P_R$  vs.  $p$  as a function of  $I_B$  at  $P_I = 50$  W for the "magnetic beach" flux density profile shown in figure 3.5(b). A new mode (see text) appeared at all  $I_B$  shown for pressures below  $3 \times 10^{-3}$  Torr.

would appear as a mixture of the two plasma shapes because of averaging by the eye. Eventually the above process reversed itself as the new mode replaced the old (traces (c) and (d)). The periodic ( $\approx 3$  kHz) sawtooth waveform superimposed on the DC value of the second mode (traces (b), (c), and (d) especially) gradually disappeared (trace (e)) as  $I_B$  continued to decrease. Clearly these dynamic measurements can be used to examine both the range and nature of the unstable plasma regions which occur between plasma modes.

### 5.3. DISCUSSIONS

The three diagnostics reported here form a complementary set, where information obtained from any one fills in some of the gaps left by the other two. In our opinion, visual inspection was the most accurate way to classify and compare modes. Although mode switching was not always evident in the power meter readings, it was always clear in the plasma shape and time-resolved measurements.

The obvious problem with visual inspection is that it does not provide a quantitative measurement. In this regard, the power characteristics have proven most useful, since they can be used to generate a "map" of the plasma modes in parameter space (as in figures 5.1, 5.2 and 5.4). We have found these "maps" to be of considerable use

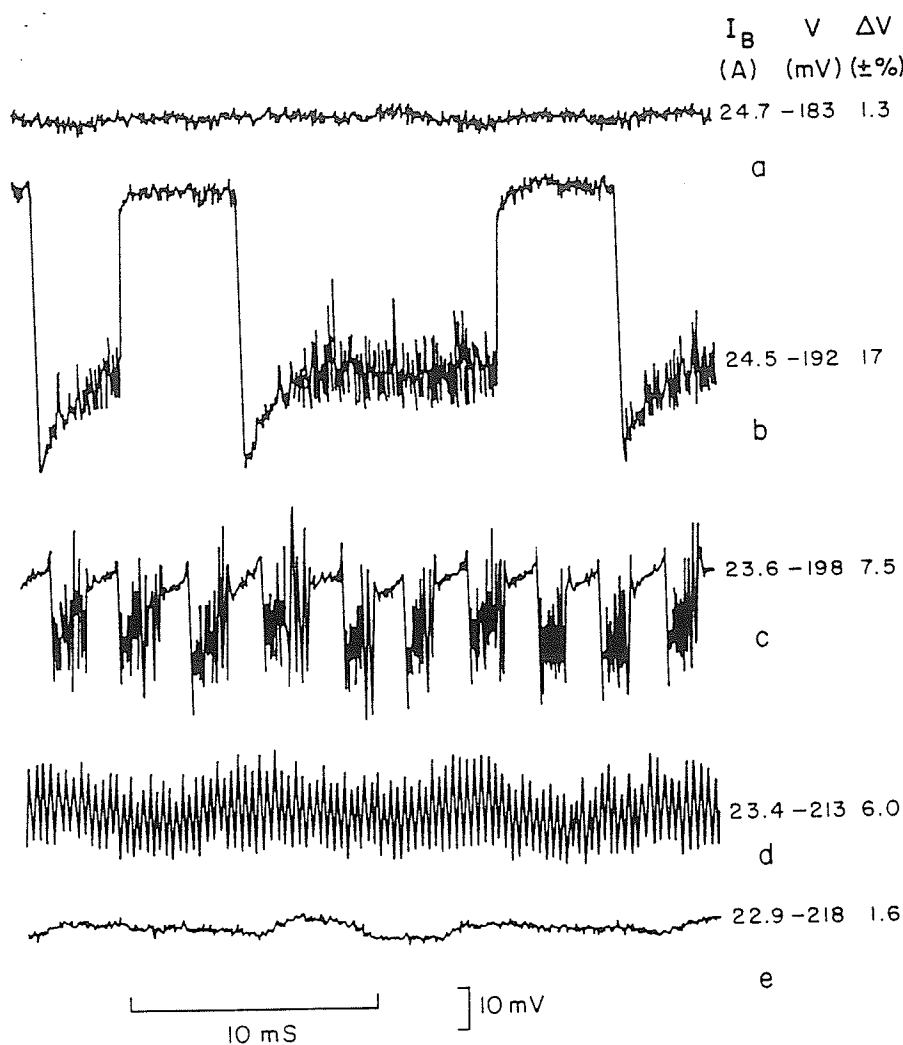


FIGURE 5.5. Output of a microwave diode detector sampling the reflected power during several stages of a mode transition at 0.01 Torr in the peaked magnetic field geometry of figure 3.5(a).  $V$  refers to the time-averaged signal output by the detector,  $\Delta V$  to the percentage variation of the AC component about this value. In this case the magnetic field coil was placed at the rear of the chamber next to a sample table, a configuration used to deposit thin films. This transition corresponds to part of the weak (little effect on the power characteristics, significant effect on the shape) transition from the ECR ("banded uniform") to sub-ECR ("square rings") plasmas noted in figure 5.1.

in the planning of both characterisation and application experiments. Clearly, crossing mode boundaries could cause havoc in the interpretation of experiments, especially the trend studies so important in application development and optimisation.

Neither visual inspection or power measurements provided clear information as to either the nature or extent of the transition regions between modes; this information was obtained using the dynamic measurements. These were directly concerned with the stability of the plasma since rapid oscillations could not be detected with the other two techniques.

### 5.3.1. On the Origin of Modes

The basic power absorption properties of these plasmas can be described using the cold, magnetised Lorentz gas model described in sub-section 2.1.3. While a rigorous analysis of our non-uniformly magnetised plasma-loaded waveguide would be a very complex task, we can certainly say that changes in the wave propagation characteristics of the plasma will affect the impedance characteristics of the waveguide chamber. Thus, an examination of this simple model should be sufficient to understand a number of the qualitative aspects of the microwave absorption problem.

As discussed in sub-section 2.1.3, RCP waves launched into a plasma where the magnetic field increases into ECR experience a cutoff, from which they are reflected, before they reach the ECR zone. Since collisions reduce the efficiency of the cutoff,<sup>2,3</sup> and tunneling of the wave through the cutoff into ECR can occur,<sup>2,4</sup> a small fraction of the incident wave energy will reach the resonant zone. This explains the high values of  $P_R$  observed as well as the weak, but significant, influence of ECR on the properties of plasmas generated in the peaked magnetic field configuration. Note that the LCP waves may also become cut off if the plasma becomes significantly overdense before the ECR zone. No evidence for this was observed.

The magnetic beach configuration is the preferred method for launching waves into ECR since there are no cutoffs for the RCP waves preceding the ECR zone.<sup>4</sup> The power characteristics shown in figure 5.2 clearly reflect this fact. Here also, the LCP waves may be cut off if the magnetic field and/or plasma density preceding ECR are sufficiently large. Again, no evidence for such effects was observed.

There are a host of possible explanations for the variety of modes observed and the complex shapes they exhibit. Possible phenomena which could contribute to complex shapes and/or mode behaviours include the development of structures or waves as a result of diffusion across  $B_0$ ,<sup>5</sup> the excitation of surface<sup>3</sup> or drift waves such as the helical instability,<sup>6</sup> and the occurrence of plasma-modified waveguide cutoffs.<sup>3</sup> Mode conversion<sup>2</sup> should play some role in ECR plasmas, where the RCP waves may be converted into electrostatic plasma<sup>7</sup> or ion acoustic<sup>8</sup> waves. Ordinary ( $\mathbf{k}$  perpendicular,  $\mathbf{E}$  parallel, to  $B_0$ ) and extraordinary ( $\mathbf{k}$  and  $\mathbf{E}$  perpendicular to  $B_0$ ) waves may also become excited where the curvature of the magnetic field lines is sufficient for a significant fraction of the microwaves to be propagating across  $B_0$ . It is also possible that TE waveguide modes can convert at cutoffs to extraordinary waves propagating across  $B_0$ .<sup>3</sup> Finally, non-linear plasma-wave interactions cannot be ruled out,<sup>8</sup> especially in the case of the low  $p$  ECR plasmas, which exhibit some resemblance to the cavitons<sup>9</sup> which result from ponderomotive forces.

Given all the possibilities, it would seem that little progress can be made without an intense experimental and theoretical effort. Nonetheless, there remains one mechanism which appears to be able to explain a number of the modes observed in these experiments. In particular, it is the only mechanism which can account for the *diagonal* symmetries so common in the plasma shapes. We hypothesise that *the plasma modes are a result of the excitation of higher order electromagnetic waveguide modes, whose propagation is made possible by increases in the refractive index of the magnetised plasma.* A thorough exposition of this hypothesis would be beyond the scope of this work. Here we merely justify our hypothesis and propose an experimental test.

We begin by noting that virtually all radiative excited atomic and molecular states of  $H_2$  have very short lifetimes, and thus radiate essentially at their point of generation. The brightness of the plasma at any point is thus proportional to the generation rate at that point. Since the microwaves propagate axially, and  $B_0$  and  $p$  are uniform across the waveguide cross-section, we make the reasonable assumption that the brightness of the plasma across the chamber cross-section (the shape of the plasma) is proportional to  $n$  and the microwave electric field intensity,  $E(\mathbf{r})$ , according to a relationship of the form<sup>10</sup>

$$n_j = n(\mathbf{r})E^\gamma(\mathbf{r}), \quad (5.1)$$

where  $j$  denotes the  $j$ 'th excited state of an atom and  $\gamma$  is a number between 2 and 4. While this relation applies strictly only for electronic levels in atoms, it may reasonably be expected that a similar relation holds for molecular electronic states as well. This also assumes that the EEDF is locally in equilibrium with  $E(\mathbf{r})$ . Of course, the plasma parameters and electric field intensity will adjust themselves over the chamber cross-section in a self consistent manner, and without doing a rigorous analysis we can only hope to explain the overall shapes and symmetries of the plasmas. ECR conditions should be particularly simple in this regard, since the resonance both limits the axial extent of the absorption region and extends generation relatively uniformly across the chamber cross-section.

Our hypothesis assumes that the plasma acts as a dielectric "inserted" into the waveguide, with its relative dielectric constant,  $\epsilon_r$ , a function of  $z$ ,  $B_0$ ,  $p$ , and  $P_A$  through  $\omega_{Ce}$  and  $\omega_{pe}$ . In particular,  $\epsilon_R > 1$  will reduce the cutoff frequencies for the various waveguide modes relative to their vacuum values. For certain conditions, this effect may be sufficient to allow higher order modes to contribute significantly to the microwave electric field distribution, and thus to the shape of the plasma. For reference, the first seven modes in a rectangular waveguide twice as wide as it is high\* are (in order of increasing cutoff frequency):<sup>11,12</sup>  $TE_{10}$ ,  $TE_{20}$ ,  $TE_{11}$  and  $TM_{11}$  (same cutoff),  $TE_{21}$  and  $TM_{21}$  (same cutoff), and  $TE_{30}$ . To clarify the effect of  $\epsilon_R$  in the plasma, consider the general equation for the cutoff frequencies of the TE modes in a dielectric-loaded rectangular waveguide:<sup>12</sup>

$$f_{CO} = \frac{1}{2\sqrt{\mu\epsilon_0\epsilon_R}} \left[ \left( \frac{m}{a} \right)^2 + \left( \frac{n}{b} \right)^2 \right]^{1/2}, \quad (5.2)$$

where  $a$  and  $b$  refer to the width and height ( $a = 2b$ ) of the waveguide, respectively, and  $m$  or  $n$  can be any integer provided they are not both zero.

The mechanism producing the increase in  $\epsilon_R$  in ECR plasmas is just the resonance itself. In the cold plasma approximation  $\epsilon_R$  diverges at ECR; in a real situation it must at least become large. This can be seen qualitatively if we naively assume that  $\epsilon_R$  is given by the expression for an RCP wave in an infinite, cold, magnetised Lorentz plasma;

---

\* Recall that the  $m$  and  $n$  in  $TE_{mn}$  or  $TM_{mn}$  refer to the number of vacuum half-wavelengths that fit along the width and height of the waveguide, respectively.

$$\epsilon_R = 1 - \frac{\omega_{pe}^2}{\omega(\omega - \omega_{ce})} \quad (5.3)$$

The actual behaviour of even this simple function is quite complex along the axis of even a linear magnetic beach. However, as shown in figure 5.6, simply assuming that this increase is sufficient to mix the TE<sub>10</sub> and TE<sub>20</sub> modes fully accounts for the observed plasma shapes in the ECR magnetic beach configuration. In particular, the shift of the plasma to one side, not observed under any other conditions, can be explained by an increased contribution of the TE<sub>20</sub> mode. Since the density of the plasma in the ECR zone increases with  $I_B$ ,  $p$  and/or  $P_A$  (see sub-section 6.3.1), this effect should become more pronounced as these system variables increase. This is exactly what is observed.

The same mechanism explains similar results observed in cylindrical divergent field ECR reactors (as discussed in section 2.3, Miyake et al<sup>13</sup> provide striking photographs of this phenomena). In this case the fundamental mode is TE<sub>11</sub>, which has a single maximum in the microwave electric field strength along the axis. This mode is clearly dominant at low  $p$ , where the plasma appears as a bright central disc. At high  $p$ , our hypothesis predicts that the next higher order mode, TM<sub>01</sub>, should dominate. This mode has the electric field strength localised near the walls, with a null along the waveguide axis. Indeed, at high  $p$  the plasma forms a hollow ring concentrated at the walls.

The hypothesis can explain most of the observed shapes of the plasma. Through various combinations of modes, hollow and solid shapes exhibiting the symmetry of the waveguide cross-section, and diagonal (azimuthal) symmetries in rectangular (circular) waveguides can be modelled. These symmetry properties are particularly difficult to explain using any of the mechanisms mentioned earlier. Also, only the variety of waveguide modes seem able to account for the variety of observed plasma modes.

The hypothesis also accounts for the stability properties of the plasma modes. Which waveguide mode, or modes, will occur under a given set of conditions is determined by a self-consistent interaction between the plasma and microwave field. A given combination will be stable under small changes in  $\epsilon_R$ , but only over a restricted band. As  $\epsilon_R$  increases both the order and number of allowed waveguide modes increases. Thus plasmas which require high order modes to explain their shape are also expected to exhibit more instability, since more waveguide modes are allowed and the spacing between their cutoff frequencies is smaller. The sub-ECR magnetic beach plasmas fulfill both of these criteria.

We now propose a direct experimental test of our hypothesis. This is to simply insert a microwave electric field probe (suitably insulated from the plasma) into the plasma chamber and directly measure the electric field pattern in the absorption region. If the measured field intensity does not correspond to the brightness of the plasma then the hypothesis is incorrect. Some measurements similar to these have been performed,<sup>8</sup> and show that  $E(r)$  and  $n$  both move to the walls with increasing  $p$ . While the visible shape of the plasma was not recorded, equation (5.1) implies that the plasma shape must also have behaved in this way.

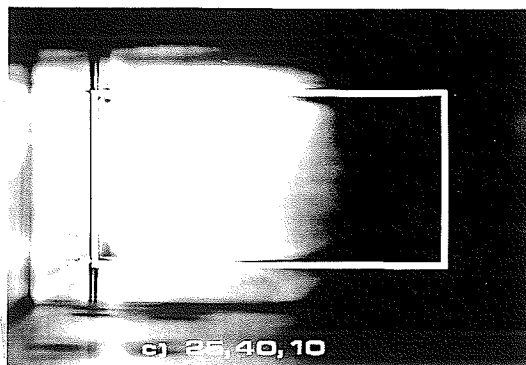
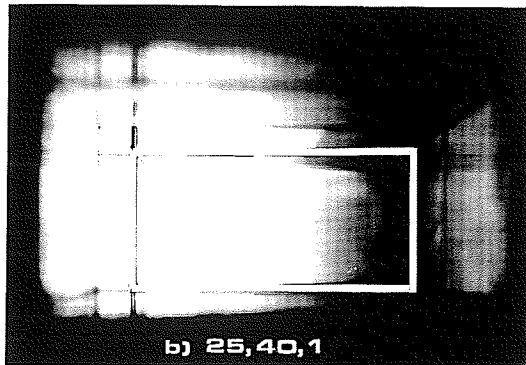
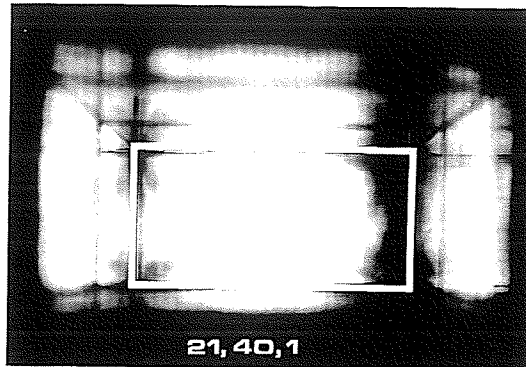
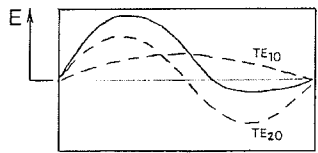
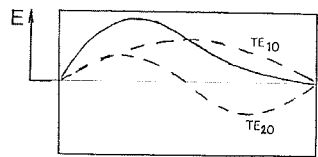
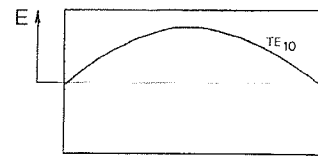


FIGURE 5.6. 35 mm photographs of several plasmas formed in the ECR plasma processing chamber for the magnetic beach configuration of figure 3.5(b), and corresponding mixtures of electromagnetic waveguide modes. These are arranged from top to bottom in order of increasing strength of ECR. The system settings for each plasma are noted in the following three number format:  $\{I_B \text{ (Amps)}, P_1 \text{ (Watts)}, p \text{ (}\times 10^{-2} \text{ Torr)}\}$ . Note that contrast saturation in the reproduction processes has made the plasmas appear more similar than they appear to the eye. The waveguide cross-section at the quartz window has been outlined to prevent confusion of the plasma with wall reflections and to provide a scale reference; the cross-sectional dimensions of the waveguide were 7.2 by 3.6 cm. The screened wall of the waveguide elbow, through which these pictures were taken, was responsible for the faint grid-like patterns.

References

1. A.D. MacDonald, *Microwave Breakdown in Gases*, John Wiley & Sons, New York, 1966.
2. D.G. Swanson, *Plasma Waves*, Academic Press, Boston, 1989.
3. W.P. Allis, S.J. Buchsbaum, and A. Bers, *Waves in Anisotropic Plasmas*, M.I.T. Press, Cambridge, 1963.
4. T.H. Stix, *The Theory of Plasma Waves*, McGraw-Hill, New York, 1962.

5. D. Winske, "Development of Flute Modes on Expanding Plasma Clouds," *Phys. Fluids B* 1, p. 1900, 1989.
6. B.E. Cherrington and L. Goldstein, "Helical Configuration Produced in Gaseous Magnetoplasmas by the Gyro-Resonance Absorption of Microwaves," *Phys. Fluids* 10, p. 613, 1967.
7. J. Musil and F. Žáček, "Penetration of a Strong Electromagnetic Wave in an Inhomogeneous Plasma Generated by ECR Using a Magnetic Beach," *Plasma Phys.* 13, p. 471, 1971.
8. L.A. Ferrari, R.J. LaHaye, and A.W. McQuade, "Anomalous Penetration of High-Frequency Electromagnetic Waves into a Plasma," *Phys. Fluids* 19, p. 457, 1976.
9. A.Y. Wong, "Cavitons," *J. de Physique* 38, Coll. C6, pp. C6-27, 1977.
10. C.M. Ferreira and J. Loureiro, "Electron Energy Distributions and Excitation Rates in High-Frequency Argon Discharges," *J. Phys. D: Appl. Phys.* 16, p. 2471, 1983.
11. R.A. Waldron, in *Theory of Guided Electromagnetic Waves*, Van Nostrand Reinhold, London, 1969.
12. L.C. Shen and J.A. Kong, *Applied Electromagnetism*, Brooks/Cole, Monterey, 1983.
13. K. Miyake, S. Kimura, T. Warabisako, H. Sunami, T. Tokuyama, "Microwave Plasma Stream Transport System for Low Temperature Plasma Oxidation," *J. Vac. Sci. Technol. A* 2, p. 496, 1984.

## CHAPTER 6

### PROBE CHARACTERISATION OF THE MAGNETIC BEACH CONFIGURATION\*

*Nature, it seems, is the popular name  
for milliards and milliards and milliards  
of particles playing their infinite game  
of billiards and billiards and billiards.  
- Piet Hein, Grooms.*

In chapter 5 the domains of the various plasma modes appearing in the ECR plasma processing system were mapped out over a wide range of conditions. This chapter describes a Langmuir probe characterisation of the plasmas produced in the ECR magnetic beach configuration, where the system was in the form of a divergent field ECR plasma processing reactor.

The reader may recall from sections 2.3. and 2.4 that previous plasma characterisations of divergent field ECR plasma processing reactors have left many basic questions concerning the physics of these machines unanswered. The experiments described in this chapter are our attempt to resolve some of these issues. The method used is a systematic, spatially-resolved Langmuir probe characterisation of the plasmas over a wide range of operating conditions. The focus is on the axial variation of basic plasma parameters and potentials as functions of important system variables. To the author's knowledge, this is the first characterisation of a divergent field ECR plasma processing reactor to present a complete set of data over a range of system variables.

At the very least, merely having accumulated a complete set of data will allow unambiguous statements as to how the plasmas depend on the system variables to be made. Because the data is self-consistent as well, correlations between plasma quantities will be possible, providing insight into the physical processes at work. In particular, contributions towards the resolution of a number of the specific issues pointed out in section 2.3 should be possible.

#### 6.1. EXPERIMENTAL

The ECR plasma processing system was exactly as described in chapter 3. The magnetic beach configuration, figure 3.5(b), was used with  $I_B \geq 20$  A so that ECR conditions always occurred within the plasma chamber. All measurements were performed with the cylindrical OML probe described in section 3.4 and appendix A. Measurements were made by first setting the desired system conditions with the probe withdrawn to the rear of the chamber, then taking I-V curves at pre-selected

---

\* The contents of this chapter are currently being prepared for publication.

axial locations. Any changes in the system variables ( $P_R$  in particular) were noted for each measurement. Additional measurements as functions of  $p$  and  $P_I$  were made at fixed locations in order to clarify dependences on system variables.

Most measurements were performed at  $I_B = 25$  A; measurements at other values were also made for comparison. The pressure was varied over the range of  $10^{-3}$  to  $10^{-1}$  Torr. The independent microwave power variable was  $P_I$ , which was varied from 0 to 50 W in 10 W intervals. This meant that the power variable most significant to the results,  $P_A$ , was not in round numbers, and sometimes changed slightly with  $I_B$  and  $p$ . Over 400 I-V measurements were made in  $H_2$ , another 100 in  $O_2$ . All measurements were performed over a one month period, during which no changes to, or other uses of, the plasma system were allowed. Analysis of the results was performed after all measurements had been completed. The plasma parameters were extracted using the cylindrical OML probe equations given in section 3.4 (with the modification described in the next section) and the modelling procedures described in section 3.4 and appendix B.

## 6.2. I-V CHARACTERISTICS

A typical set of probe I-V characteristics are shown in figure 6.1. These curves are very close to those expected from OML theory, with two important exceptions. First, there is a distortion of these curves in the electron saturation region which made it impossible to determine  $V_P$  accurately by inspection. Secondly, the ion saturation current increased faster with  $V$  than anticipated from the cylindrical OML model. This had to be accounted for in the modelling procedure, as discussed below.

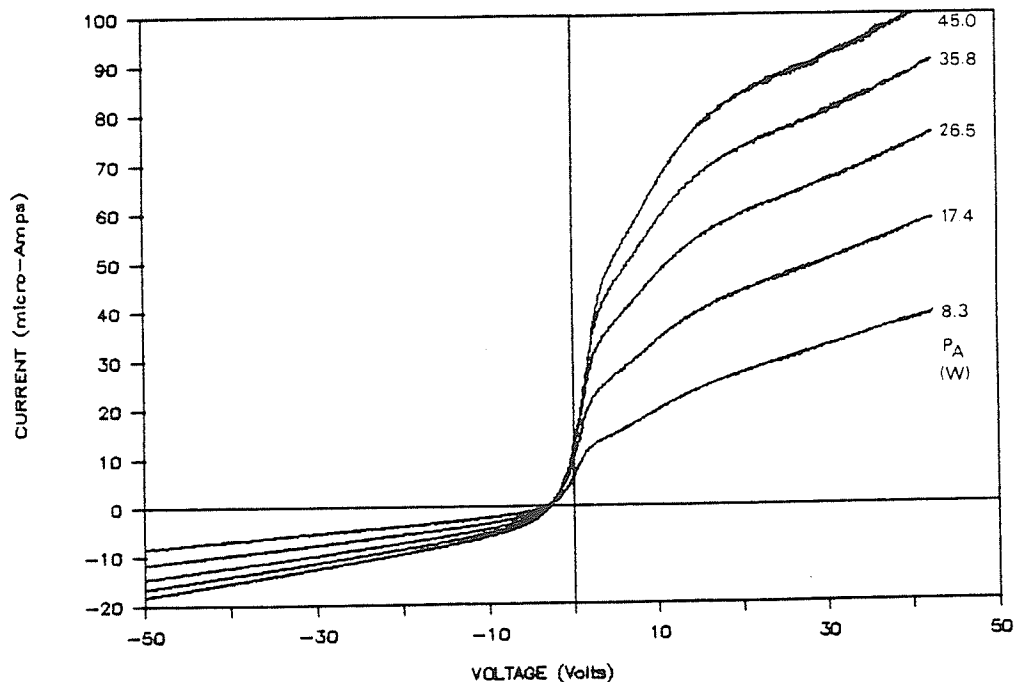


FIGURE 6.1. I-V characteristics of the OML probe as a function of  $P_A$  at  $p=10^{-2}$  Torr,  $I_B=25$  A,  $z=26.5$  cm.

The distortion of the region near and above  $V_p$  was probably a manifestation of moderately magnetised electron collection,<sup>1,2</sup> as discussed in sub-section 3.4.4. The form of the perturbation; a decrease in the magnitude and slope of the electron "saturation" current and a rounding of the electron "saturation" knee are exactly the features expected from collection through a transition magnetosheath.<sup>1</sup> These distortions did not adversely affect the precision of the plasma parameters since the modelling procedure did not use this portion of the I-V characteristic.

Below  $V_p$  most I-V curves could be fitted extremely well. In figure 6.1 the fitted curves would be indistinguishable from the measured ones. Actual program output, showing the high quality of a typical fit, is given in figure B.1 of appendix B. This appendix also contains extensive discussions regarding the precision of the modelling procedure.

The second distortion of the I-V curves occurred in the ion saturation region. Here the collected current increased significantly faster than the parabolic dependence on  $V$  predicted by the OML model. This resulted in a poor fit of the model to many I-V curves. It was found that a term *linear in  $V$*  added to the OML model (3.17) fully accounted for this extra current component;

$$\Psi(\chi_i) \approx \frac{2}{\sqrt{\pi}} \sqrt{\chi_i+1} \rightarrow \frac{2}{\sqrt{\pi}} \sqrt{\chi_i+1} + (\text{constant})V . \quad (6.1)$$

Note that  $n$  can still be obtained as before since it multiplies  $\Psi$ . The values of  $n$  obtained using this correction averaged 70% of those obtained without, and the fit of the model to the data was dramatically improved.

The origin of this linear term is consistent with the probe sheath exhibiting a significant *spherical* character, since spherical OML probes collect saturation currents which vary linearly with  $V$ .<sup>3,4</sup> Although the cylindrical probe has an aspect ratio of 400, there are several mechanisms which may cause it to collect charged particles through a partly spherical sheath. For example, ion beams in the downstream region may cause excessive collection by the non-cylindrical portion of the sheath at the end of the probe. Fringing fields would tend to make this portion of the sheath appear hemispherical, thus explaining the partly spherical nature of the probe sheath. This may have been exacerbated by a small residual curvature retained by the tip wire, as noted in appendix A.

A number of I-V characteristics, especially those taken at low  $p$ , could not be fitted by the model due to the occurrence of non-Maxwellian EEDF's. Probe data from these plasmas appear to show the effect of an excess energetic (or "hot") electron population superimposed upon the high energy tail of an otherwise Maxwellian EEDF. Obviously such a perturbation introduces significant error into the fitting procedure. These perturbations were easily detected from the shape of the I-V curve and the large negative values of  $T_i$  that the fitting procedure produced in these situations. Data points obtained from I-V characteristics subject to this perturbation are duly noted at every occurrence. Such points should be viewed by the reader as estimates considerably less precise than usual.

Some I-V characteristics could not be modelled at all because their magnitudes were either too large or too small for either the diagnostic or the modelling procedure. By too large we mean the curve was virtually a straight vertical line, from which the

modelling procedure could extract essentially no useful information. This condition typically occurred in the ECR zone when both  $n$  and  $T_e$  were large. By too small we primarily mean that the exponential region of the characteristic was not discernible. This occurred when  $n$  was very low, usually well into the downstream region. However, if  $T_e$  was sufficiently small, I-V characteristics with  $n$  as low as  $10^{14} \text{ m}^{-3}$  could sometimes be fitted. More commonly, only regions having  $n \geq 10^{15} \text{ m}^{-3}$  could be modelled.

The measured I-V characteristics were very reproducible. Two sets of ten I-V measurements taken three days apart (between which 3 system shut-downs, 3 re-starts and over 250 intervening measurements were made) were used to check the reproducibility. Differences in  $n$ ,  $T_e$ ,  $V_P$  and  $V_F$  were less than  $\pm 9$ ,  $\pm 3$ ,  $\pm 7$  and  $\pm 30\%$ , respectively. Larger variations were observed only in I-V curves distorted by hot electrons. Other data used to check the reproducibility yielded similar results. The particularly large error value for  $V_F$  resulted from the accumulated variation in the other plasma parameters upon which it depends.

### 6.3. SPATIAL PROFILES

In this section the principal results of the OML probe characterisation of the ECR magnetic beach configuration are described. The primary objective was to measure the spatial variation of the plasma parameters along the chamber axis; that is, along the magnetic beach. Each of the measured plasma parameters are considered separately in this section. Note however, that since four plasma parameters result from a single I-V characteristic, each measurement contributed to three separate graphs; one for each of  $n$ ,  $T_e$  and the pair of  $V_P$  and  $V_F$ . The data in sub-sections 6.3.1 to 6.3.3 are fully comparable since they are different aspects of the same measurements.

Every effort was made to provide as complete a characterisation of the chosen operating regime as possible. However, the anomalous "blue hole" mode which occurred at low pressures will not be considered here as these plasmas exhibited a number of peculiar properties of unknown origin.

#### 6.3.1. Plasma Density

The spatial variation of  $n$  is shown as a function of  $p$  and  $P_A$  in figures 6.2 and 6.3. The form of these curves, with a broad peak at ECR, are in general agreement with the literature.<sup>5,6,7,8</sup> It is not clear whether any significance should be attached to the apparent double peak structure seen in these figures. The overall shape of these profiles is consistent with that expected for diffusion from a source region centered on the ECR plane. Plasma generated near the ECR zone diffused radially and axially, causing  $n$  to decrease away from this region. The increased rate of decay of  $n$  in the region of rapid decrease in  $B_0$  would be expected since the diverging lines of flux help to spread the plasma radially. Note that while  $n$  depends upon  $B_0$ , it does not follow  $B_0(z)$ , as has been suggested elsewhere (see sub-section 2.3.2).

Increasing  $p$  increases the peak value of  $n$  occurring in the plasma chamber. Recall from chapter 5 that plasmas generated over the range of  $4 \times 10^{-3}$  to  $10^{-2}$  Torr were visibly uniform over the chamber cross section, while plasmas at higher pressures concentrated near the walls. This is commonly observed,<sup>6,9,10</sup> and implies that  $n$

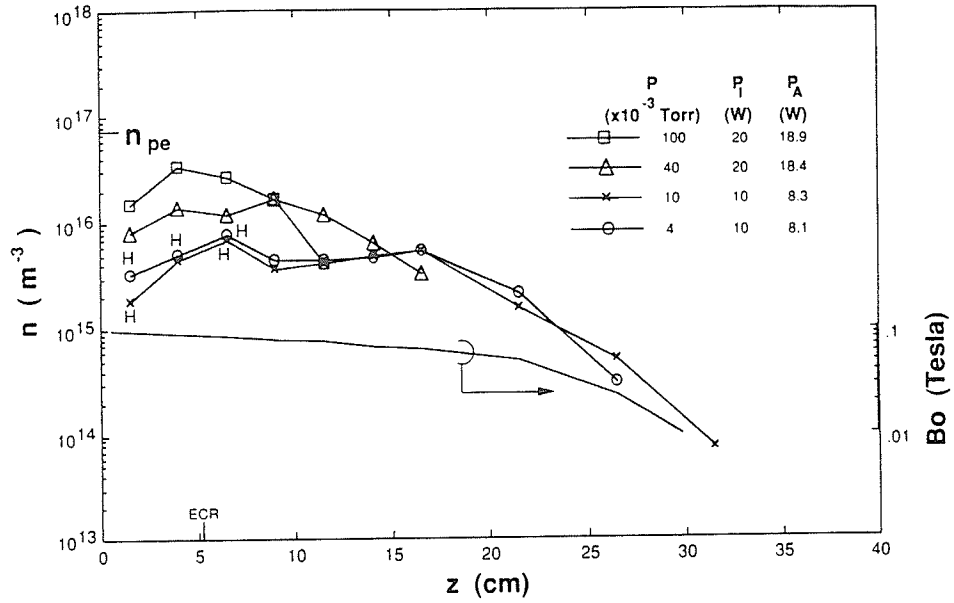


FIGURE 6.2.  $n$  vs.  $z$  as a function of  $p$  at  $I_B=25$  A. Note that the low pressure curve was obtained at  $P_I=10$  W, those at high  $p$  at 20 W. The  $10^{-2}$  Torr curve was essentially the same as that at  $4 \times 10^{-3}$  Torr. ECR occurred at  $z=5.5$  cm. "H" denotes points obtained from I-V curves distorted by excess hot electrons. The logarithmic variation of  $B_0$  is shown for comparison.

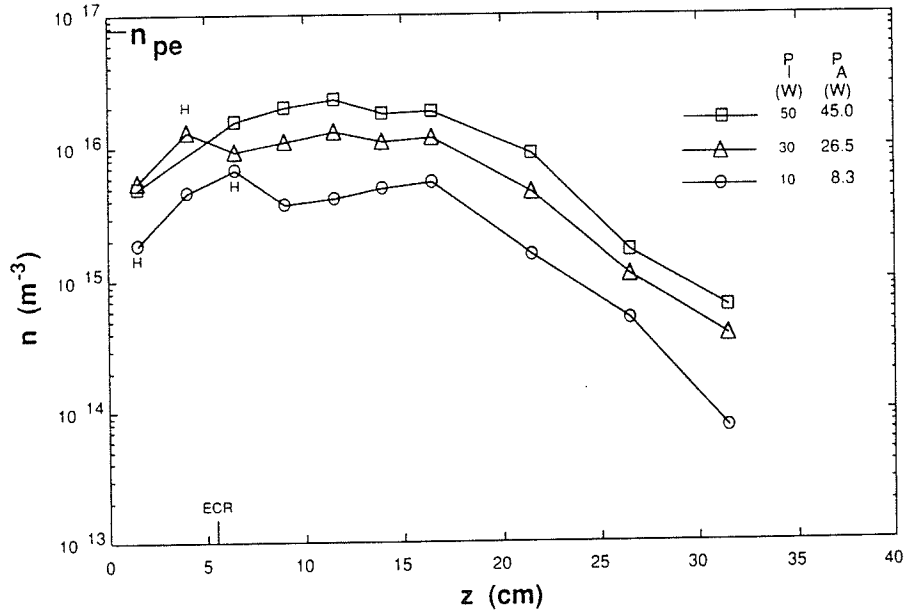


FIGURE 6.3.  $n$  vs.  $z$  as a function of  $P_A$  at  $p=10^{-2}$  Torr and  $I_B=25$  A. ECR occurred at  $z=5.5$  cm. "H" denotes points obtained from I-V curves distorted by excess hot electrons. The I-V curve corresponding to the missing data point at  $z=4$  cm,  $P_I=50$  W could not be modelled. The corresponding logarithmic variation of  $B_0$  is shown in figure 6.2.

off the axis (in the ECR zone) was significantly larger than that measured on the axis at high  $p$ . This has also been reported in the literature.<sup>11,12,13,14</sup>

Increasing  $p$  also increased the rate of decay of  $n$  in the downstream region. The dependence of  $n$  on  $p$  in this region is shown in more detail in figure 6.4. Figure 6.4 is in excellent agreement with the literature.<sup>6,11,12,15,16</sup> The behaviour of  $n$  above  $3 \times 10^{-3}$  Torr in figure 6.4 can be seen to be a direct consequence of the change in the axial profile shown in figure 6.2. A decrease in  $n$  at very low  $p$  has been observed in all studies to date. In our case, the decrease at low  $p$  is correlated with the formation of the "blue hole" mode. Note that  $P_A$  decreased from 28.7 to 26.2 W (8.7% drop) as  $p$  increased from  $2 \times 10^{-3}$  to  $8 \times 10^{-1}$  Torr. This small change cannot account for the order of magnitude variation observed in  $n$ . This comment also applies to figures 6.7 and 6.10.

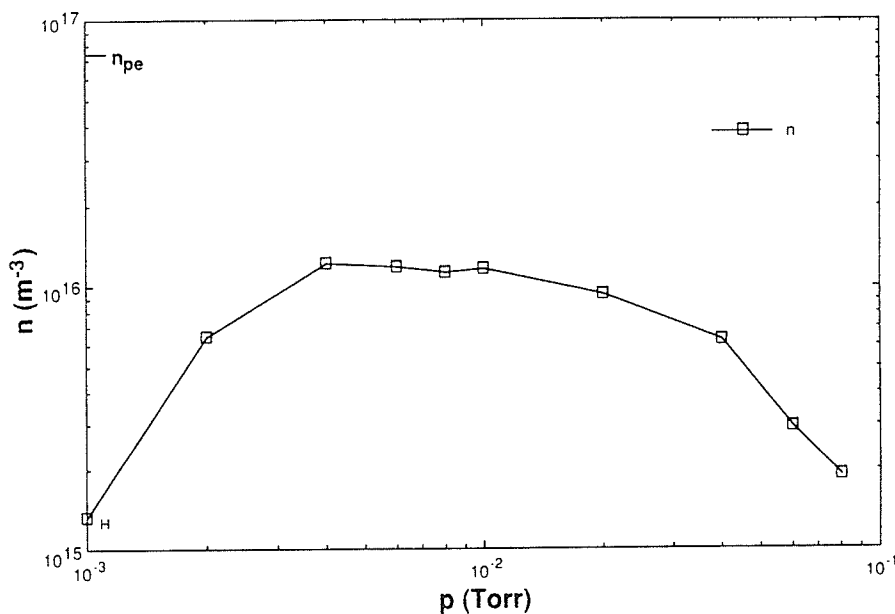


FIGURE 6.4.  $n$  vs.  $p$  at  $P_i=30$  W,  $I_B=25$  A, and  $z=16.5$  cm. "H" denotes points obtained from I-V curves distorted by excess hot electrons.

The effect of  $P_A$  on  $n$  is somewhat simpler than that of  $p$ . As can be seen in figure 6.3, increasing  $P_A$  increases  $n$  throughout the plasma chamber. Overall,  $n$  tends to increase approximately linearly with  $P_A$  but the rate of increase varies with  $z$  and  $p$ . These results are also in agreement with the literature,<sup>6,8,10,11,17</sup> although there are exceptions<sup>12,16</sup> (possibly due to mode changes) and it is often difficult to determine the power densities needed for more accurate comparisons.

Note that  $n$  is always less than the critical plasma density,  $n_{pe} = 7.45 \times 10^{16} \text{ m}^{-3}$ , under the conditions studied in this thesis. By naively extrapolating the power dependence of  $n$  in the ECR zone, a rough estimate of the value of  $P_A$  required to produce a plasma at  $n = n_{pe}$  can be made. Values obtained in this manner vary widely with  $p$  as the power dependence of  $n$  changes, but typically fall within the range of 150 W to 450 W. At  $10^{-1}$  Torr, however,  $n$  shows no dependence on  $P_A$ , and so never extrapolates to  $n_{pe}$ .

In the following sub-sections it will be shown that the profiles of the other plasma parameters simply follow the movement of the ECR zone as  $I_B$  decreases. However, the density profile is not free to follow the ECR zone since its shape is determined primarily by diffusion, which in turn is determined mainly by the geometry of the plasma chamber. Thus decreasing  $I_B$  shifts the  $n$  profile towards lower  $z$ , but also moves the plasma generation region closer to the window, which acts as a sink for plasma particles. This changes the shape of the  $n$  profile as well as its position. The increase in plasma losses, due both to the movement of the source closer to a sink and to the generally reduced confinement provided by the weaker  $B_0$  would also account for the reduced power absorption efficiency observed at lower  $I_B$ . It should be noted that this efficiency was constant for  $I_B \geq 22$  A.

### 6.3.2. Electron Temperature

The spatial variation of  $T_e$  is shown as a function of  $p$ , and  $P_A$  in figures 6.5 and 6.6, respectively. The most obvious feature in these curves is the large temperature spike in the ECR zone, a result of efficient resonant absorption of microwave energy by the electrons. This observation is consistent with the literature.<sup>18,5,6,10</sup> The magnitude of  $T_e$  in the downstream region is in good agreement with the reported values. However, the dependence of  $T_e$  on system variables remains unclear in the literature. In this study, sufficiently detailed measurements of  $T_e$  were made to allow definitive comments concerning its dependence on system variables.

The magnitude of the peak in  $T_e$  decreases with increasing  $p$ . This decrease can be attributed to an increased collision frequency interrupting the cyclotron gyration of the resonating electrons more often, thereby reducing the energy they absorb from the microwaves. In the downstream region, increasing  $p$  decreases  $T_e$  by an amount proportional to the decrease observed in the ECR zone. This behaviour is shown in figure 6.7 and is in agreement with the literature.<sup>11</sup> One exception<sup>15</sup> may be a result of the appearance of a new mode. Increasing  $P_A$  appears to lower  $T_e$  in the ECR zone and decrease its rate of decay in the downstream region. Comparisons with the literature<sup>12</sup> are difficult because of the scarcity of data concerning this dependence.

The dependence of  $T_e$  on  $I_B$  can be explained by a simple shift of the entire profile in response to the movement of the ECR zone, which is towards the window with decreasing  $I_B$ . Small residual differences can be fully accounted for by corresponding small differences in  $P_A$ .

### 6.3.3. Plasma and Floating Potentials

The plasma and floating potentials have also been measured. They depend on the plasma parameters  $n$  and  $T_e$ , as well as the material and geometric properties of the chamber walls. In addition,  $V_F$  depends on the geometry of the probe.

The relationships between the fundamental plasma parameters  $n$  and  $T_e$  and the potentials  $V_P$  and  $V_F$  will be considered in the discussions. Here, we simply present the figures complementary to those given in the previous sections, and point out any novel features which may occur. The axial profiles of  $V_P$  and  $V_F$  are shown in figures 6.8 and 6.9. A more detailed graph of their downstream dependence on  $p$  is shown in figure 6.10.

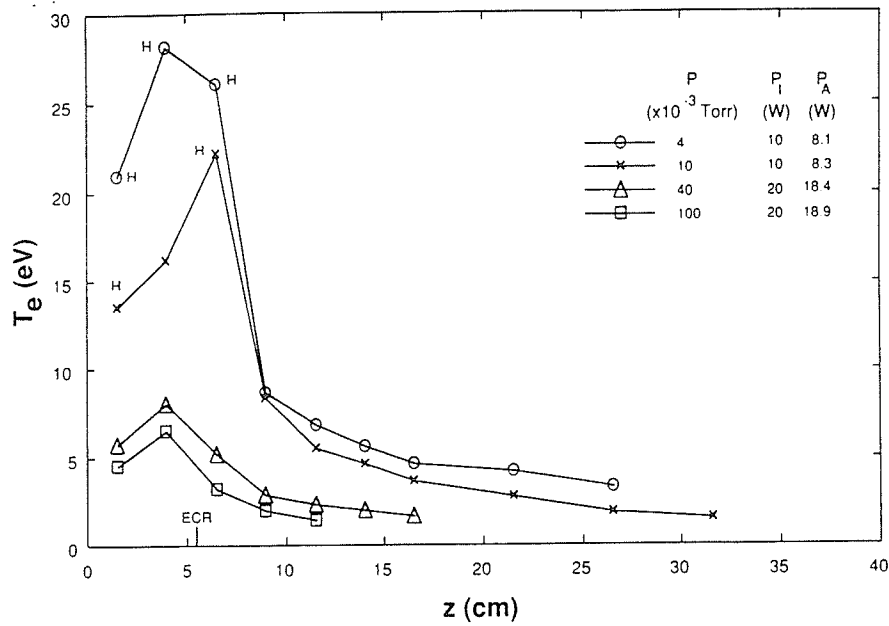


FIGURE 6.5.  $T_e$  vs.  $z$  as a function of  $p$  at  $I_B=25$  A. Note that the low pressure curve was obtained at  $P_I=10$  W, those at high  $p$  at 20 W. ECR occurred at  $z=5.5$  cm. "H" denotes points obtained from I-V curves distorted by excess hot electrons. The corresponding variation of  $B_0$  is shown in figure 3.5(b).

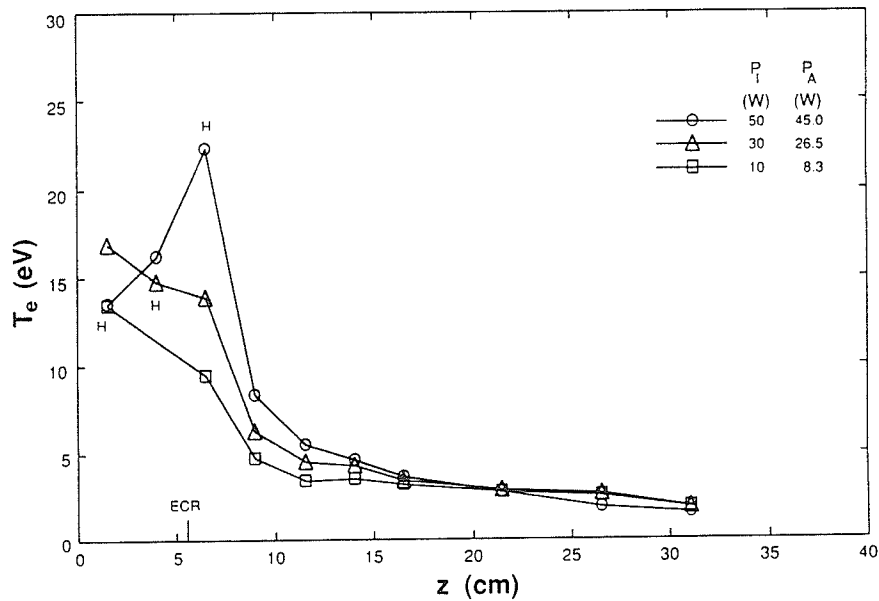


FIGURE 6.6.  $T_e$  vs.  $z$  as a function of  $P_A$  at  $p=10^{-2}$  Torr and  $I_B=25$  A. ECR occurred at  $z=5.5$  cm. "H" denotes points obtained from I-V curves distorted by excess hot electrons. The I-V curve corresponding to the missing data point at  $z=4$  cm,  $P_I=50$  A could not be modelled. The corresponding variation of  $B_0$  is shown in figure 3.5(b).

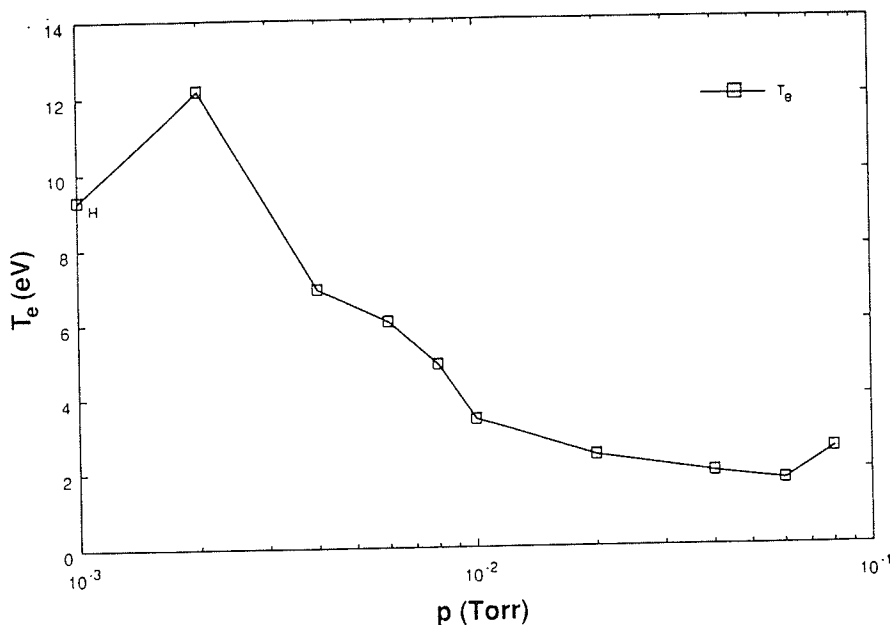


FIGURE 6.7.  $T_e$  vs.  $p$  at  $I_B=25$  A,  $P_I=30$  W,  $z=16.5$  cm. "H" denotes points obtained from I-V curves distorted by excess hot electrons.

The magnitude of  $V_P$  is consistent with the values reported in the literature,<sup>19,6,7,10</sup> but there remains some disagreement as to whether<sup>6</sup> or not<sup>18</sup>  $V_P$  shows a peak in the ECR zone. Regardless,  $V_P$  has been observed to decrease with  $p$  in the downstream region<sup>7</sup> and the ECR zone.<sup>6</sup>  $V_P$  has been found to depend only weakly, if at all, on  $P_A$  in the downstream region.<sup>7,10</sup> These observations are in agreement with those made here.

The dip in  $V_F$  in the ECR zone has been reported elsewhere,<sup>18,8</sup> but it is difficult to make any other comparisons concerning this parameter. As discussed later in subsection 6.4.3,  $V_F$  is a direct consequence of  $V_P$  and  $T_e$ , and should not be treated as an independent plasma parameter.

The resemblance of the  $V_P$  profiles to those of  $T_e$  is striking. The downstream dependence of  $V_P$  on  $p$  also follows that of  $T_e$ . As well,  $V_P$  decreases with increasing  $P_A$  in the ECR zone, while simultaneously increasing in the downstream region, as does  $T_e$ . However, the dependence of  $V_P$  on  $P_A$  in the downstream region is not the same as for  $T_e$ . The dependence of both  $V_P$  and  $V_F$  on  $I_B$  is, like that of  $T_e$ , apparently due simply to a shift of the entire profile along  $z$ , following the ECR zone.

While the  $V_F$  profile bears no obvious resemblance to that of  $T_e$  or  $V_P$ , the pronounced dip in the ECR zone and the slow downstream variation imply a close coupling of  $V_F$  to these quantities, as expected from probe theory. This comment also applies to the detailed dependence of  $V_F$  on  $p$  in the downstream region shown in figure 6.10.

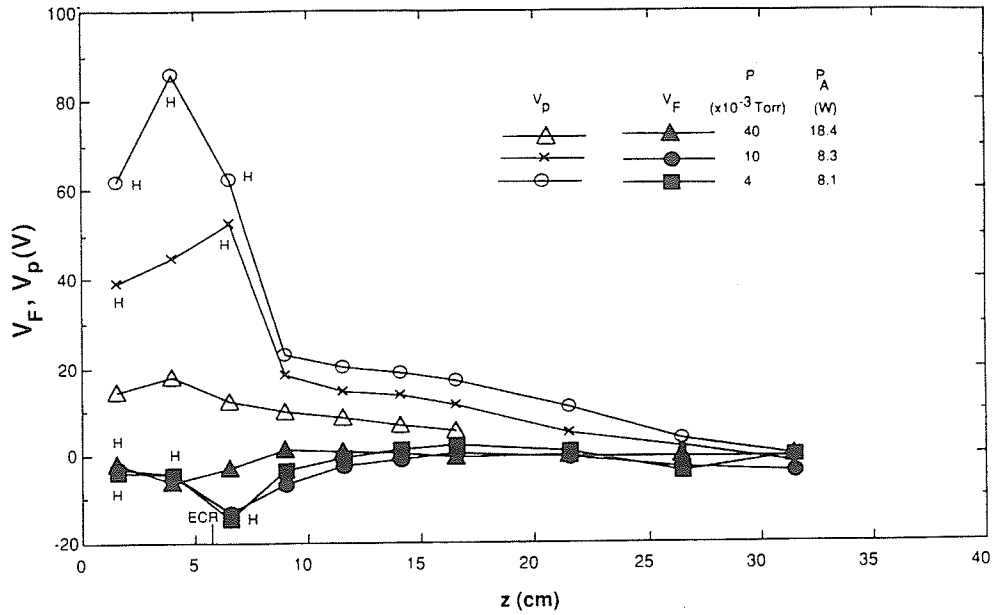


FIGURE 6.8.  $V_p$  and  $V_F$  vs.  $z$  as a function of  $p$  at  $I_B=25$  A. Hollow symbols refer to  $V_p$ , filled ones to  $V_F$ . Note that the low pressure curves were obtained at  $P_I=10$  W, that at  $p=4 \times 10^{-2}$  Torr at 20 W. ECR occurred at  $z=5.5$  cm. "H" denotes points obtained from I-V curves distorted by excess hot electrons. The corresponding variation of  $B_0$  is shown in figure 3.5(b).

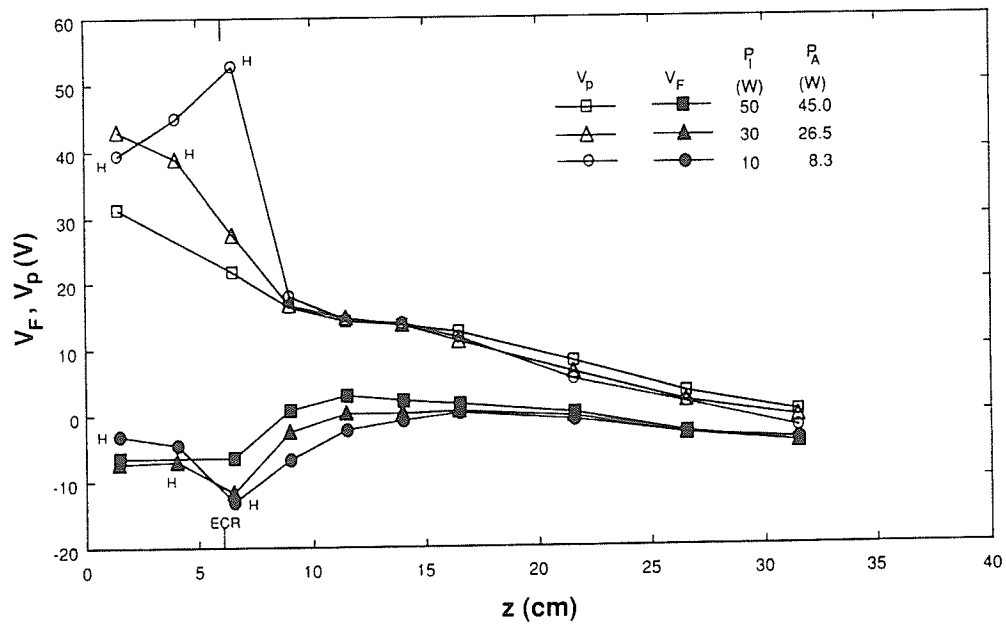


FIGURE 6.9.  $V_p$  and  $V_F$  vs.  $z$  as a function of  $P_A$  at  $p=10^{-2}$  Torr and  $I_B=25$  A. Hollow symbols refer to  $V_p$ , filled ones to  $V_F$ . ECR occurred at  $z=5.5$  cm. "H" denotes points obtained from I-V curves distorted by excess hot electrons. The I-V curve corresponding to the missing data point at  $z=4$  cm,  $P_I=50$  could not be modelled. The corresponding variation of  $B_0$  is shown in figure 3.5(b).

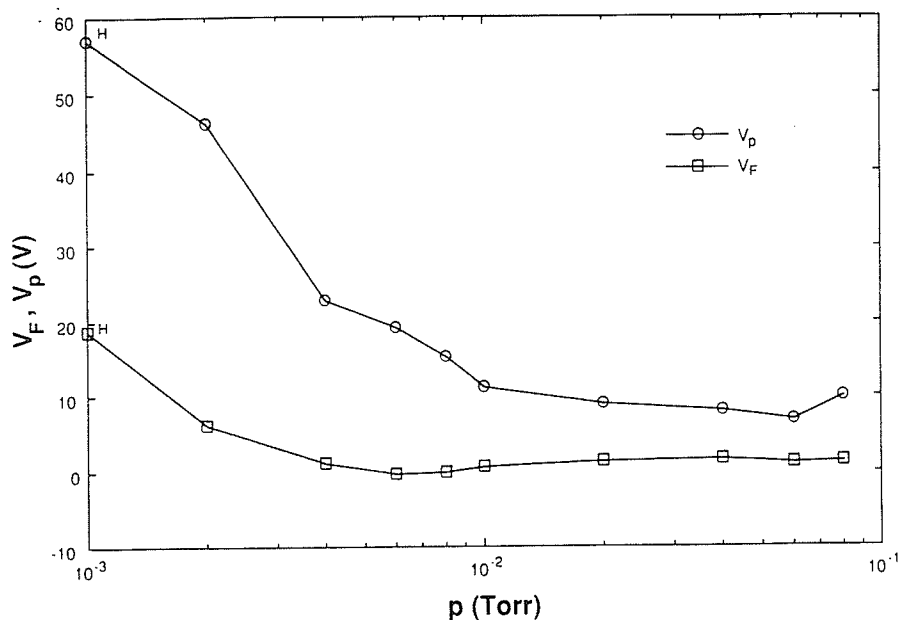


FIGURE 6.10.  $V_p$  and  $V_f$  vs.  $p$  at  $I_B=25$  A,  $P_I=30$  W,  $z=16.5$  cm. The corresponding variation of  $P_A$  is shown in figure 6.10. Hollow symbols refer to  $V_p$ , filled ones to  $V_f$ .

#### 6.4. DISCUSSIONS

The measurements reported in this chapter have been able to reproduce the majority of the results found in the literature concerning plasma characterisations of divergent field ECR plasma processing reactors. However, the detail and completeness of these results make them a significant addition to the body of experimental data concerning these complex plasmas. This was made possible through the work reported in chapter 5, which enabled the selection of stable plasma conditions in which to perform the probe measurements.

The result is a self-consistent, continuous set of data sufficiently detailed to allow the construction of, or comparisons to, analytical models. In general, of course, modelling these plasmas will be a difficult task. Nonetheless, some tentative, phenomenological efforts along these lines will be made in the rest of this section. The primary goals will be to delimit the theoretical problem and suggest initial directions of attack rather than to propose definitive models.

##### 6.4.1. Plasma Generation, Transport and Loss

The density profile,  $n(z)$ , is a reflection of the mass and charge generation, transport and loss mechanisms occurring within the plasma chamber. In ECR plasma processing systems, generation is determined by microwave absorption processes, transport by diffusion and loss by recombination on bounding surfaces. Gas-phase recombination may contribute to plasma loss under certain conditions, such as at high densities and/or pressures in the presence of molecular ions,<sup>7</sup> but it is usually observed that diffusion is the dominant transport/loss process in microwave plasmas.<sup>20</sup> The reason is the very low rates associated with most recombination processes under the conditions typically found in microwave processing plasmas.<sup>21</sup> In this sub-section, the

measured data from section 6.3 will be used to formulate a phenomenological model of plasma generation and transport. A detailed theoretical treatment, which would require extensive numerical modelling, will be left for future work.

We begin by noting that four distinct particle fluxes, the axial and radial electron and ion fluxes, contribute to the net diffusion of plasma. Diffusion is a random walk process, so the diffusive fluxes (in the absence of space-charge fields) will be proportional to the corresponding step lengths in the four cases. For electrons travelling along  $B_0$  the step length is just the mean free path length,

$$l_{en} = \left[ \frac{2 \times 10^{-10}}{p} \right] \sqrt{\frac{2eT_e}{m_e}}, \quad (6.2)$$

with  $p$  in Torr and  $T_e$  in eV. This was arrived at from (2.23) for  $l_{en}$  using the most probable velocity (2.24), and the fact that  $v_{en} \approx 5 \times 10^9 p \text{ s}^{-1}$  (independent of electron energy) in  $H_2$ .<sup>22</sup> Across  $B_0$  the step length is given by the Larmor radius,

$$r_{Le} = \left[ \frac{m_e}{eB_0} \right] \sqrt{\frac{2eT_e}{m_e}}, \quad (6.3)$$

with  $T_e$  in eV. Here (2.24) was used in (2.1) for  $r_{Le}$ . Under the conditions found in these experiments,  $l_{en}$  ranged from about a centimeter at  $10^{-1}$  Torr to a few tens of centimeters at  $4 \times 10^{-3}$  Torr. At the same time,  $r_{Le}$  was on the order of a few tenths of a millimeter and  $\omega_{ce}/v_{en} \approx 100$  at 0.01 Torr in the vicinity of the ECR zone. Thus the Larmor gyration greatly impedes the flux of electrons across  $B_0$  relative to that along  $B_0$ . This difference increases as  $p$  is reduced, since diffusion across  $B_0$  depends on  $v_{en}$ . These comments also apply to the ion fluxes.

Given the strong tendency of the plasma to flow along  $B_0$  (mostly axially) rather than across (mostly radially),  $n(z)$  should have the basic form of the lowest diffusion mode between parallel plates. This would be a cosinusoidal<sup>20,23</sup> variation with the peak at ECR, where the generation rate is presumably the greatest, and with a width proportional to  $l_{en}$ . Increasing  $P_A$  would increase the generation rate and thus the peak value of  $n$ , as observed in figure 6.5. Increasing  $p$  decreases  $l_{en}$ , thus causing the profile "half-width" to decrease, as observed in figure 6.4. Decreasing  $l_{en}$  (increasing  $p$ ) also reduces axial losses, which should produce an increase in the peak value of  $n$ , assuming that axial losses are dominant. This is indeed what was observed.

There are at least three factors which act to perturb  $n(z)$  from an ideal cosinusoidal distribution. The first is that the generation region (the ECR zone) is located near the quartz window, which is a sink for charged particles diffusing along  $B_0$ , thus  $n(z)$  is not symmetrical about the ECR zone. Also, at low  $p$  when  $l_{en}$  is not small compared to the window to ECR zone spacing ( $\approx 6$  cm), the profile will be depressed near the window since  $n$  must be at or near zero on the window surface. This is why the peak of  $n(z)$  appears to move downstream with a reduction of  $p$ ; the profile is expanding in width while simultaneously being depleted at the source.

The second perturbation is due to the divergence of the magnetic lines of flux in the downstream region. This acts to both spread the charged particles radially and to guide them into the side walls of the chamber, thus shortening the distance they must travel to a sink (the walls) along  $B_0$ . Both of these effects serve to add to the

downstream decay of  $n(z)$ . This effect is particularly evident in the region where  $B_0$  decreases exponentially.

The remaining "perturbation" concerns the shape of the generation region. A cosinusoidal axial distribution between parallel plates must be maintained by uniform generation throughout the chamber,<sup>23</sup> which is highly unlikely in the divergent field configuration. At the opposite extreme, a plane source at ECR would support a triangular  $n$  profile.<sup>23</sup> In reality, plasma generation almost certainly occurs nonuniformly over an extended, but limited, axial region centered on the ECR zone. The exact shape of this region presumably also depends on the system conditions. Thus the actual  $n$  profile would, at best, be expected to be only approximately cosinusoidal or triangular. The cross-sectional shape of the generation region, as indicated by the visible shape of the plasma, is also nonuniform and dependent on system variables. This will influence the behaviour of the shape of the profile under changes in the system variables. In particular, the tendency of plasma at high  $p$  and/or  $P_A$  to concentrate along the walls implies that measurements of  $n$  along the axis may underestimate peak values of  $n$  within the chamber.

Finally, some comments concerning the requirements for a rigorous analysis of plasma losses in a divergent field ECR plasma processing reactor. The problems associated with the anisotropy and nonuniformities introduced by  $B_0$  have already been mentioned. The fact that generation occurs over a localised region of unknown shape introduces three additional difficulties. The first is that while the shape of the generation region is important to diffusion, determining its form requires knowledge of the wave absorption properties of the plasma. The second problem is that  $n$  can be so small in regions far from the source that free diffusion may dominate there.<sup>20</sup> Thus ambipolar diffusion conditions may occur only in high density regions of the plasma. This could, in turn, be aggravated by the conducting walls of the plasma chamber, which can support currents connecting fluxes from different regions of the plasma. These complexities place the solution of the diffusion problem well outside the scope of this work.

#### 6.4.2. Plasma Heating and Cooling

The  $T_e$  profiles clearly illustrate the basic nature of ECR plasmas; resonant absorption of microwave energy accelerates plasma electrons to high energies within a narrow region centered at the ECR plane. The energy attained by the resonating electrons is limited by the collision frequency  $\nu_{en}$ . The lower  $\nu_{en}$  is, the longer the electrons can gyrate and thus absorb energy from the microwave field. Therefore, decreasing  $p$  allows  $T_e$  to reach larger values in the ECR zone. At the high temperatures attained in the ECR zone, the majority of the electron population undergoes inelastic, rather than elastic, collisions with neutral species. In an inelastic collision, most of an electron's energy is absorbed by the neutral particle through excitation, dissociation and/or ionisation processes. Thus inelastic collisions rapidly cool the electron population.

Since the extent of ECR along the axis is quite limited, the rapid cooling provided by inelastic collisions accounts for the rapid decay of  $T_e$  away from the resonant zone. In the downstream region, the relatively low value of  $T_e$  does not

change appreciably. At these low values of  $T_e$ , most of the electron population undergoes elastic collisions, in which energy transfer to the much more massive neutral species is very inefficient. Since only a few electrons in the high energy tail of the population collide inelastically, little collisional cooling takes place.

The other major cooling process is due to ambipolar diffusion, where more energetic electrons are able to preferentially escape any space-charge fields occurring as a result of charge imbalances. The details of the diffusion cooling process will depend upon the details of ambipolar diffusion under the complex conditions found in the plasma chamber. It remains to be seen how significant this cooling process is. Since collisions reduce the efficiency of ECR and increase the efficiency of cooling,  $T_e$  decreases as  $p$  increases, as observed in figure 6.5.

The apparent decrease in the magnitude of the  $T_e$  spike with increasing  $P_A$  is explained by the corresponding increase in  $n$  this produces. Since there are more electrons present, there is less microwave energy available *per electron*, so  $T_e$  must be lower.<sup>24</sup> The corresponding movement of the spike towards the window may similarly be a result of the higher electron density absorbing more of the microwave power sooner.

### 6.4.3. Potentials

As mentioned previously,  $V_P$  and  $V_F$  are a consequence of plasma-surface interactions. These potentials are determined by  $n$ ,  $T_e$ ,  $B_0$ , the geometry and materials of the reactor walls, and the geometry of the probe (in the case of  $V_F$ ).

$V_P$  arises as a result of ambipolar diffusion of the charged plasma species to the reactor walls. To predict the value of  $V_P$  in a system as complicated as an ECR plasma processing reactor would be a difficult task indeed. Nonetheless, simply knowing that  $V_P$  must depend on  $n$  and  $T_e$  allows for some simplification of the results to be made. First note that while the shape of the reactor was an invariant in these experiments, the geometry important to diffusion phenomena was not, since  $B_0$  varied with  $z$  and  $I_B$ . Also, since the material of the chamber walls changed at the quartz window, changes in the diffusion process may be expected near  $z = 0$ . Thus the spatial variation of  $V_P$ , under a given set of  $p$ ,  $P_A$  and  $I_B$ , must be a result of spatial variations in  $n$ ,  $T_e$ ,  $B_0$ , or due to the presence of the quartz window.

From a comparison of  $V_P(z)$  with  $T_e(z)$ , it is clear that  $V_P$  depends on  $T_e$ . In fact, through a trial-and-error process, the following empirical relation was found to apply throughout the plasma chamber, except near the quartz window:

$$V_P(z) = C_1 \sqrt{n(z)T_e(z)} + C_2 . \quad (6.4)$$

No systematic dependence on  $B_0(z)$  was found. Note that the "constants"  $C_1$  and  $C_2$  depend on  $p$ ,  $P_A$  and  $I_B$ . These "constants" contain the information pertaining to the ambipolar diffusion process which determines the magnitude of  $V_P$ . Relation (6.4) merely describes how this process varies along the chamber axis.  $C_1$  and  $C_2$  must be determined by experiment, and must be re-determined whenever a change is made in  $p$ ,  $P_A$ ,  $I_B$  or the shape of  $B_0(z)$ . While the origin and meaning of (6.4) is not known, it can be used to reduce sets of  $V_P(z)$  profiles to two parameters,  $C_1$  and  $C_2$ . An understanding of (6.4) will, once again, require rigorous solution of the diffusion problem.

Points measured close to the quartz window,  $z \leq 6.5$  cm, did not always obey relation (6.4), presumably due to a change in the diffusion process at the front of the plasma chamber. It was observed that the extent of this perturbation along  $z$  was greatest at low  $p$  and/or low  $P_A$ . This could be a result of the longer screening and mean free path lengths which occur under such conditions. The presence of this perturbation is obvious on a plot of  $V_P$  versus  $\sqrt{nT_e}$ , which is linear if the perturbed points (near the window) are ignored. In figure 6.11 axial profiles selected from figures 6.8 and 6.9 have been re-plotted to demonstrate (6.4). All measured  $V_P(z)$  profiles could be linearised in this way.

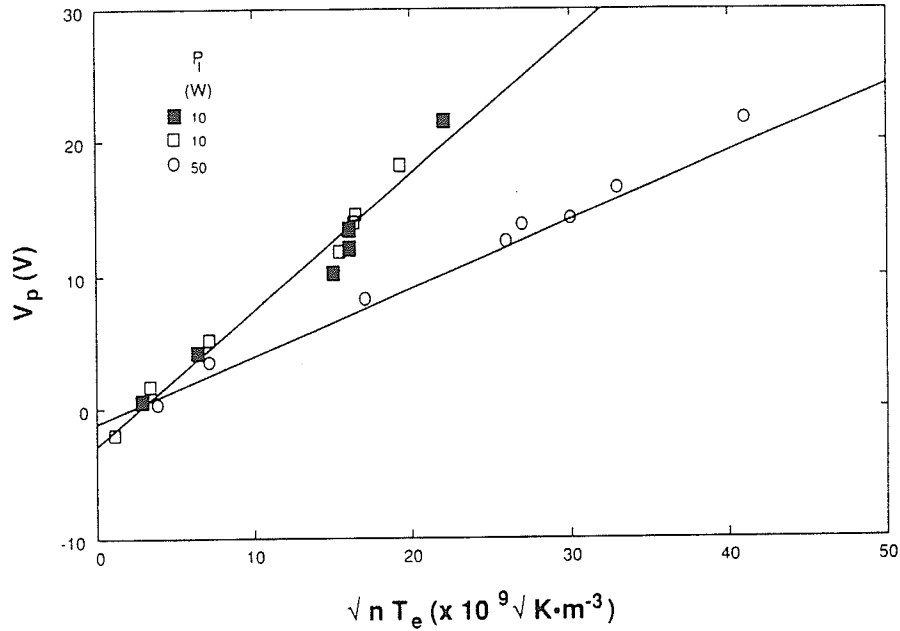


FIGURE 6.11.  $V_P$  vs.  $\sqrt{nT_e}$  as a function of  $P_A$  at  $p=10^{-2}$  Torr and  $I_B=25$  A. The three points nearest to the quartz window were not included. Similar curves were found under all conditions examined in these experiments. The I-V curve corresponding to a missing point at  $z=4$  cm,  $P_i=50$  W could not be modelled. The lines correspond to linear least-square fits to the data.

As mentioned several times previously, probe theory assumes that all potentials are relative to the plasma potential,  $\phi_P \equiv V_P$ . Therefore, in discussing  $V_F$  one must use  $\phi_F = V_F - V_P$ ; the floating potential across the probe sheath. Note that  $\phi_F$  is negative. An expression for  $\phi_F$  can be obtained from the OML current equations (3.10) to (3.17) in the same way as for a plane probe (section 4.3.2). For a plane probe we have, rewriting (4.5) in terms of the normalised potential,

$$\frac{e\phi_F}{\kappa T_e} = \frac{1}{2} \ln \left[ 2\pi \frac{m_e}{m_i} \right] - \frac{1}{2}. \quad (6.5)$$

The corresponding result for a cylindrical OML probe, written in the same format as (6.5), is

$$\frac{e\phi_F}{\kappa T_e} = \frac{1}{2} \ln \left[ 2\pi \frac{m_e}{m_i} \right] + \frac{1}{2} \ln \left[ \left[ \frac{2}{\pi^2} \right] \left[ \frac{T_i}{T_e} - \frac{e\phi_F}{\kappa T_e} \right] \right]. \quad (6.6)$$

Note the unfortunate fact that this equation is nonlinear in  $\phi_F$ , thus requiring numerical solution, and that  $T_i/T_e$  must be known.

According to (6.5),  $\phi_F$  should be a linear function of  $T_e$  only, with the slope given by the term on the right hand side ( $T_e$  in eV). To discover how the measured data actually varied,  $\phi_F$  was plotted as a function of  $T_e$ . The results for *all* probe measurements reported in this chapter are shown in figure 6.12. Clearly the data follows a universal line independent of all system variables and  $n$ . The slope of the line predicted by (6.5) is -3.34, that obtained from the least-squares fit to the data is  $-3.04 \pm 0.05$ .

To compare the experimental results to (6.6), we first note that the complicating terms appear as ratios in a logarithm. This greatly reduces their influence on the final result. Given that  $T_i$  is unknown, but expected to be less than  $T_e$ , we will make the cold ion approximation and assume  $T_i = 0$ . By further assuming that  $e\phi_F/\kappa T_e \approx -3$  in the logarithm of (6.6), the slope predicted by OML theory is -3.09, which is within the margin of error for the fitted slope.

That these equations describe the measured data (or that  $\phi_F$  versus  $T_e$  is a universal line) is unremarkable. This is a direct consequence of probe theory. Failure of the data to follow this curve can only mean that that one or more of the measured values contributing to that point is in error or that the model I-V curve does not fit the data. This relationship is thus another quantitative check on the fit of the model I-V curve to the measured characteristic. Clearly the model I-V curves, from which the plasma parameters were obtained, fit the measured data very well.

#### References

1. J. Rubinstein and J.G. Laframboise, "Theory of Axially Symmetric Probes in a Collisionless Magnetoplasma: Aligned Spheroids, Finite Cylinders, and Disks," *Phys. Fluids* 26, p. 3624, 1983.
2. E.P. Szuszczewicz and P.T. Takacs, "Magnetosheath Effects on Cylindrical Langmuir Probes," *Phys. Fluids* 22, p. 2424, 1979.
3. J.G. Laframboise and L.W. Parker, "Probe Design for Orbit-Limited Current Collection," *Phys. Fluids* 16, p. 629, 1973.
4. J.D. Swift and M.J.R. Schwar, *Electrical Probes for Plasma Diagnostics*, Illife, London, 1969.
5. H. Fujita, H. Handa, M. Nagano, and H. Matsuo, "Characteristics of Microwave Plasma and Preparation of a-Si Thin Film," *Jpn. J. Appl. Phys.* 26, p. 1112, 1987.
6. O.A. Popov, "An Electron Cyclotron Resonance Plasma Stream Source for Low Pressure Thin Film Production," *Surf. Coat. Technol.* 36, p. 917, 1988.
7. Y.H. Lee, J.E. Heidenreich III, and G. Fortuno, "Plasma Characterization of an Electron Cyclotron Resonance-Radio-Frequency Hybrid Plasma Reactor," *J. Vac. Sci. Technol. A* 7, p. 903, 1989.
8. L. Bárdoš and J. Musil, "Axial Decaying of the Microwave ECR Oxygen Plasma," *J. Phys. D: Appl. Phys.* 21, p. 1459, 1988.
9. K. Miyake, S. Kimura, T. Warabisako, H. Sunami, T. Tokuyama, "Microwave Plasma Stream Transport System for Low Temperature Plasma Oxidation," *J. Vac. Sci. Technol. A* 2, p. 496, 1984.
10. O.A. Popov, "Characteristics of Electron Cyclotron Resonance Plasma Sources," *J. Vac. Sci. Technol. A* 7, p. 894, 1989.

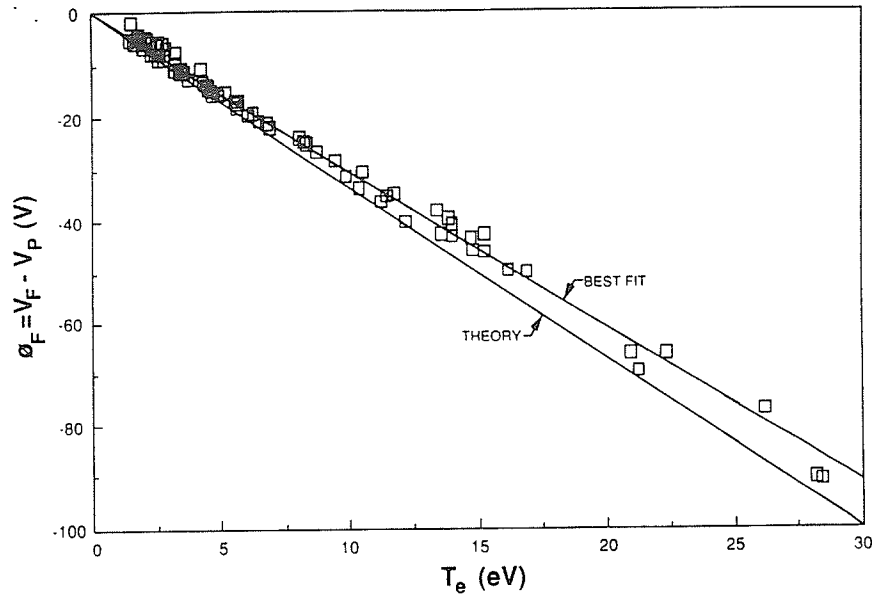


FIGURE 6.12.  $\phi_F$  vs.  $T_e$  for all experimental conditions reported in this chapter except those in which "blue hole" plasmas occurred. The line denoted "best fit" is a linear least-squares fit to the measured data, with the intercept forced to the origin. The line denoted "theory" is a plot of equation (6.5), derived from plane probe theory.

11. J. Forster and W. Holber, "Plasma Characterisation for a Divergent Field Electron Cyclotron Resonance Source," *J. Vac. Sci. Technol. A* 7, p. 899, 1989.
12. E. Ghanbari, I. Trigor, and T. Nguyen, "A Broad-Beam Electron Cyclotron Resonance Ion Source for Sputtering Etching and Deposition of Material," *J. Vac. Sci. Technol. A* 7, p. 918, 1989.
13. L.A. Ferrari, R.J. LaHaye, and A.W. McQuade, "Anomalous Penetration of High-Frequency Electromagnetic Waves into a Plasma," *Phys. Fluids* 19, p. 457, 1976.
14. Y. Sakamoto, "Measurement of Power Transfer Efficiency from Microwave Field to Plasma Under ECR Condition," *Jpn. J. Appl. Phys.* 16, p. 1993, 1977.
15. K. Suzuki, S. Okudaira, N. Sakudo, and I. Kanomata, "Microwave Plasma Etching," *Jpn. J. Appl. Phys.* 11, p. 1979, 1977.
16. C. Keqiang, Z. Erli, W. Jinfa, Z. Hansheng, G. Zuoyao, and Z. Bangwei, "Microwave Electron Cyclotron Resonance Plasma for Chemical Vapor Deposition and Etching," *J. Vac. Sci. Technol. A* 4, p. 828, 1986.
17. Y. Torii, M. Shimada, and I. Watanabe, "Very High Current ECR Ion Source for an Oxygen Ion Implanter," *Nucl. Instrum. Meth. Phys. Res. B* 21, p. 178, 1987.
18. B.W. Rice and J.E. Scharer, "Observation of Localized Electron Cyclotron Resonance Heating in a Magnetic Mirror," *IEEE Trans. Plasma Sci.* PS-14, p. 17, 1986.
19. M. Matsuoka and K. Ono, "Magnetic Field Gradient Effects on Ion Energy for Electron Cyclotron Resonance Microwave Plasma Stream," *J. Vac. Sci. Technol. A* 6, p. 25, 1988.
20. S.C. Brown, *Introduction to Electrical Discharges in Gases*, John Wiley & Sons, New York, 1966.
21. A. von Engel, in *Electric Plasmas, Their Nature and Uses*, Taylor & Francis, New York, 1983.
22. A.D. MacDonald, *Microwave Breakdown in Gases*, John Wiley & Sons, New York, 1966.
23. F.F. Chen, *Introduction to Plasma Physics and Controlled Fusion, Vol. 1: Plasma Physics, 2nd Edn.*, Plenum, New York, 1984.
24. M. Moisan and Z. Zakrzewski, "Plasmas Sustained by Surface Waves at Microwave and RF Frequencies: Experimental Investigation and Applications," in *Radiative Processes in Discharge Plasmas*, ed. L.H. Leussen, p. 381, Plenum, 1986.

## CHAPTER 7

### CONCLUSIONS AND RECOMMENDATIONS

*Truth is never pure, and rarely simple.*

- Oscar Wilde, *The Importance of Being Earnest*.

#### 7.1. CONCERNING THE CHOICE OF GASES

Virtually all plasma processing applications use complex, highly reactive gas mixtures to perform their task. Such plasmas present a complicated and destructive environment to in situ plasma diagnostics such as Langmuir probes. This is why most plasma processing characterisations which use probes are performed with simpler gas mixtures. The results of such experiments must then be extrapolated to the more complex conditions used in practice. It should be obvious that the plasmas studied with probes must be a reasonable approximation to those used in applications if this extrapolation is to be meaningful. In this thesis,  $H_2$  was used exclusively. However, as discussed in section 2.3, most studies reported in the literature were performed in Ar plasmas. We believe that Ar, or any other noble gas, is not an optimum choice for use in characterisations of plasma processing reactors.

Noble gas atoms have relatively simple inelastic collision spectra compared to molecular gases. In particular, molecular gases have numerous excitation (rotational, vibrational, electronic) levels below the ionisation energy which noble gas atoms do not have. This implies that energy transport between electrons and neutrals will be more efficient in molecular gases. For example, electron temperatures may be expected to be lower in molecular gases due to the increased number of low energy inelastic collision processes available.

Consider also dissociation, which obviously is not significant in noble gases. Dissociative recombination is an efficient electron-ion recombination process, and its occurrence at high pressures has been shown to affect the density profiles in ECR plasma processing reactors.<sup>1</sup> The complementary process of dissociative ionisation also does not occur in noble gases. This process can produce energetic ions, as in the case of Franck-Condon dissociation of  $H_2$ .<sup>2,3</sup> Obviously, chemical recombination also does not occur in noble gas plasmas. In molecular gases this can occur in the gas phase or on surfaces, and can significantly affect the transport of energy out of the plasma.<sup>4</sup> Indeed, it appears that energy transport to surfaces in molecular plasmas is dominated by the transfer of the vibrational energy of the plasma molecules to the surface,<sup>4</sup> a pathway not available in noble gas plasmas.

#### Recommendation 1:

We recommend that characterisations of processing plasmas be performed in the simplest *molecular* gas that provides a reasonable approximation to the gas mixture of the intended application.  $H_2$  is obviously the simplest and most

extensively characterised of all the molecular gases, and is a common component of many processing gas mixtures.  $H_2$  is also not particularly corrosive, does not usually leave surface deposits and produces singly charged ions predominantly of one type ( $H^+$ ). It also has the nice property that  $v_{en}/p$  is essentially independent of electron energy,<sup>5</sup> making analytic calculations possible in many situations.

#### Recommendation 2:

In an effort to determine if and when electron-ion recombination is important in ECR processing plasmas, we recommend that afterglow measurements be made at various axial locations under different system conditions. These would involve probe measurements of the rate of decay of  $n$  with time after shutting off the microwave power. Diffusion would produce an exponential decay, recombination a  $1/t$  dependence.<sup>6,7</sup>

## 7.2. CONCERNING THE USE OF LANGMUIR PROBES

The Langmuir probe technique is a deceptively simple way of simultaneously measuring several fundamental plasma properties. However, there exist a host of experimental and interpretive pitfalls awaiting the unwary experimentalist.<sup>8,9,10,11,12,13</sup> The complex environment found in divergent field ECR plasma processing reactors harbours a number of potentially bothersome creatures, including flux tubes, ion beams and plasma fluctuations.

With the exception of this thesis, all probe characterisations of divergent field ECR plasma processing reactors have used cylindrical probes oriented perpendicular to the magnetic field, and have analysed the results using a thin-sheath (planar) theory similar to that described in chapter 4. The use of such probes in magnetic fields is fraught with difficulties.<sup>8,9,10,12</sup> The most serious problems result from flux tubes, which change the collecting surface of the probe in an unpredictable manner and introduce a magnetic field dependence into the I-V characteristics.

In this thesis, the flux tube problem was side-stepped through the use of a probe so small that it was immune to the effects of the magnetic field. This had the additional benefit of reducing the perturbation of the plasma while still allowing interpretation of the I-V curves with an analytic (OML) theory. This theory is only slightly more complex than the thin-sheath model. OML probes have also been shown to be particularly well-suited for use in non-fusion magnetised plasmas.<sup>14</sup> To our knowledge, this thesis is the first reported use of this technique in the diagnosis of ECR processing plasmas.

#### Recommendation 3:

Given the potential problems with using thin-sheath probes in strongly magnetised, beam forming plasmas such as those found in ECR processing plasmas, we recommend that OML Langmuir probes be used instead. While not ideal, they are subject to fewer and less severe problems than standard thin-sheath probes.

**Recommendation 4:**

We recommend that the existing OML Langmuir probe be upgraded by adding: (a) the capability to perform direct EEDF measurements, and (b) the ability to change current ranges by changing the value of the current-to-voltage converter resistor. Calibration of the probe results by other techniques, in order to establish the accuracy of the probe results, should also be undertaken.

**7.3. CONCERNING PLASMA STABILITY**

It was demonstrated in chapter 5 that the plasmas generated in ECR plasma processing reactors generally appear in the form of distinct "plasma modes". These modes are characterised by a distinct structure (radially and axially), are usually quiescent and exhibit properties which vary smoothly with system variables. Transitions between modes, however, are discontinuous, often bistable, and are noisy due to switching between the two modes. It is obvious that such behaviour can have a serious influence on the controllability or reproducibility of plasma and processing conditions, as well as on the interpretation of trend studies.

At present the only way to ensure controllability of the plasma is to avoid the unstable transition regions between modes. This requires knowledge of the number and domains of plasma modes produced in the system's parameter space, and the extent and stability of the corresponding transition regions. The use of three complementary techniques was developed in this thesis (chapter 5) to accomplish this task. Visual inspection of the radial structure of the plasma can be used to identify and classify the different plasma modes. Microwave power "characteristics" ( $P_R$  versus  $P_I$  for example) can then be used to make a map of the mode domains in the system's parameter space. The nature and extent of the unstable transition regions can then be examined using dynamic measurements of  $P_R$  or  $V_F$ . These measurements are easily performed and provide a complete, if highly qualitative, description of the number and extent of plasma modes found in any given system configuration.

Despite the lack of quantitative data, the variety of plasma modes, their curious symmetries (diagonal in our case) and their metastable nature provide sufficient clues to form a reasonable hypothesis concerning their origin. The hypothesis states that the plasma modes are due to modification of the microwave electric field profile within the plasma chamber as a result of the mixing of higher order electromagnetic *waveguide* modes. This mixing is assumed to be brought about by large changes in the refractive index of the magnetised plasma filling the waveguide. This hypothesis can explain virtually all of the shapes observed in ECR and related magnetised microwave plasma processing systems.

**Recommendation 5:**

We propose that the "waveguide mode" hypothesis be tested by direct measurement of the microwave electric field pattern within the modes.

### Recommendation 6:

We also recommend more quantitative characterisation of the plasma modes. In particular, radially-resolved Langmuir probe measurements of the plasma modes are called for.

### 7.4. CONCERNING BASIC PLASMA PROPERTIES

The axial variation of  $n$  within the divergent field ECR reactor configuration was found to have the primarily cosinusoidal form expected from axial diffusion of plasma away from a generation region at ECR. This profile was skewed towards the front of the plasma chamber because the ECR region was located close to the quartz window, which acted as a sink of charged particles.

Increasing  $P_A$  increased the magnitude of  $n(z)$ , a result of an increased rate of generation rate in the ECR zone. Increasing  $p$  increased the rate of axial decay of  $n(z)$  away from the ECR zone. This was caused by an increased  $v_{en}$  reducing the axial diffusion coefficient while simultaneously increasing the radial diffusion coefficient. Since axial diffusion dominated plasma loss, increasing  $p$  reduced this loss and allowed  $n$  to increase in the ECR zone. At lower  $p$ , when the mean free paths were larger than the ECR zone to window spacing, further changes in  $p$  had little effect on  $n(z)$  since losses to the window (sink) and ECR zone (source) were already well-connected. However, as the profile spread with decreasing  $p$ , losses to the window depleted  $n$  in the ECR region; thus the peak appeared to move downstream. Note that  $n(z)$  did *not* appear to follow  $B_0(z)$  as observed in some studies.

The axial  $T_e$  profile was dominated by the efficient heating of the plasma electrons produced by resonant absorption of microwaves at ECR. This resulted in a temperature spike in the ECR zone. Inelastic collisions between the energetic electrons and neutral species resulted both in efficient plasma generation and rapid cooling of the electron population. This produced a rapid decay of  $T_e$  just outside the ECR zone. In the downstream region,  $T_e$  decreased to the point where elastic collisions with neutrals, in which energy transfer from electrons to neutrals is very low, was dominant. Thus little cooling occurred and  $T_e$  changed only slowly.

The magnitude of  $T_e(z)$  decreased with  $p$  as an increased  $v_{en}$  both reduced the efficiency of the resonance and increased the collisional cooling rate. Increasing the  $P_A$  decreased  $T_e$  in the ECR zone and decreased its rate of decay in the downstream region. This resulted from the corresponding increase in  $n$  which caused less wave power per electron to be available for heating.

$T_e(z)$  depended on  $B_0(z)$  only through the axial location of the ECR zone.  $V_p$  and  $V_F$  showed the same behaviour. While  $n(z)$  showed some movement, the fact that its shape and location also depended on the (fixed) location of the nearest particle sink (the quartz window) prevented it from freely following the ECR zone.

$V_p(z)$  and  $V_F(z)$  were determined by  $n(z)$  and  $T_e(z)$ ; they are not fundamental plasma parameters.  $V_p$  was found to vary along the chamber axis according to  $V_p \propto \sqrt{nT_e}$ , where the dependences on system variables appear only in two constants (slope and  $V_p$ -intercept) associated with this function. This relation was obeyed throughout the plasma chamber except between the quartz window and the ECR

zone, presumably due to perturbation of the plasma by the sheath and pre-sheath of the window.

$V_F$  depends directly on  $V_P$  and  $T_e$  according to a relation given by probe theory. Clearly this parameter is not meaningful by itself;  $T_e$  and/or  $V_P$  must also be specified, otherwise it is impossible to tell whether any observed variation in  $V_F$  is due to  $V_P$ ,  $T_e$  or both.

#### Recommendation 7:

Clearly probe measurements must be spatially-resolved if the true causes of variations in plasma or process variables are to be understood. Therefore we strongly recommend that spatial resolution be a *minimum* requirement of any serious characterisation of ECR processing plasmas.

#### Recommendation 8:

Additional diagnostic techniques should be used to measure the properties of ionic and neutral species in the plasma. Ion energy analysis, mass spectroscopy and optical emission spectroscopy would be particularly useful in this regard.

### 7.5. CONCERNING REACTOR DESIGN AND APPLICATION

The general objective of plasma characterisations of processing reactors is to provide a causal link between system variables and the results obtained in applications. The intermediary here is, of course, the plasma itself. The experiments reported in this thesis have provided an empirical connection between the reactor and the plasma as well as the phenomenological roots of a model of reactor-plasma interactions. What our results imply for reactor and application design depends on the exact nature of the intended application. Here we will restrict our comments to general issues.

First we note that  $n$  may not necessarily be a good figure of merit for the reaction rate of a given application. In the downstream region, charged and neutral species follow very different transport pathways, so that  $n$  may be a very poor indicator of the activated neutral species concentration in this region. Also, a significant fraction of  $n$  may be due to recycled neutrals.<sup>15</sup> In applications this implies that a corresponding fraction of the plasma originates from reaction *products*, which may or may not contribute to the desired process.

The nature of ECR plasmas is such that while the plasma and radical neutral species concentrations are large over an extended length of the plasma chamber, energetic species (hot electrons and excited neutrals) are essentially confined to the ECR zone. Clearly processing chemistry will be different inside and outside of the ECR zone. Energetic, damage insensitive processes could be performed within the ECR zone ("contact" plasma processing) to maximise the reaction rate. More damage sensitive applications could be performed just outside the electron temperature spike ("diffusion" plasma processing) to reduce damage while preserving a high reaction rate. Very sensitive processes may best be performed "remotely", in the downstream region, where the processing rate can be sacrificed in favour of reduced damage. In the latter case a well collimated  $B_0(z)$  will effectively transport low energy plasma onto the samples, while a strongly divergent  $B_0(z)$  will greatly reduce the density of

plasma impingent on the samples. In either case the flux of activated neutrals, which usually are responsible for the processing reactions, will be unaffected. Thus quantity of plasma impingent on samples in the downstream region can be controlled *directly* using the magnetic field profile.

Ion energies are relatively low in ECR reactors and are thus amenable to *independent* external control. Radio-frequency sample bias<sup>16</sup> is a particularly elegant method of increasing ion energies, for use in reactive-ion etching for example. Other much less elegant techniques (such as repeller grids) are required to reduce ion energies.

#### Recommendation 9:

To increase the plasma density attainable in our ECR plasma processing system, we recommend that the ECR zone be moved further downstream, away from the quartz window. Note that  $B_0$  must be kept well above that necessary for ECR in the region preceding the ECR zone.

#### Recommendation 10:

To connect the results of these plasma characterisations to the results of applications, we recommend that simple processing experiments be undertaken to, at least, determine the difference between contact, diffusion and remote plasma processing. A simple, informative and important process which could be used is silicon oxidation\*.

#### Recommendation 11:

Finally, and most importantly, we feel that the results of this thesis are sufficiently complete to allow informative comparisons to be made to the results of modelling efforts. We strongly recommend that a strenuous modelling program now be undertaken. We suggest that the problem be separated into its fluid (diffusion) and plasma wave (heating) components.

#### References

1. Y.H. Lee, J.E. Heidenreich III, and G. Fortuno, "Plasma Characterization of an Electron Cyclotron Resonance-Radio-Frequency Hybrid Plasma Reactor," *J. Vac. Sci. Technol. A* 7, p. 903, 1989.
2. A. von Engel, in *Electric Plasmas, Their Nature and Uses*, Taylor & Francis, New York, 1983.
3. I.G. Brown, "Ion Temperature in a 'Cold' Microwave-Produced Plasma," *Plasma Physics* 18, p. 205, 1976.
4. D.E. Rapakoulias and D.E. Gerassimou, "Simulation of Energy Transfer from a Glow Discharge to a Solid Surface," *J. Appl. Phys.* 62, p. 402, 1987.
5. A.D. MacDonald, *Microwave Breakdown in Gases*, John Wiley & Sons, New York, 1966.
6. F.F. Chen, *Introduction to Plasma Physics and Controlled Fusion, Vol. 1: Plasma Physics, 2nd Edn.*, Plenum, New York, 1984.
7. S.C. Brown, *Introduction to Electrical Discharges in Gases*, John Wiley & Sons, New York, 1966.
8. N. Hershkowitz, "How Langmuir Probes Work," in *Plasma Diagnostics Vol. 1; Discharge Parameters and Chemistry*, ed. O. Auciello, D.L. Flamm, p. 113, Academic, Boston, 1989.

---

\* Some work along these lines is presently being carried out by Dr. T.V. Herak, with the assistance of Prof. D.J. Thomson and the author.

9. P.M. Chung, L. Talbot, and K.J. Touryan, *Electric Probes in Stationary and Flowing Plasmas: Theory and Application*, Springer-Verlag, New York, 1975.
10. J.D. Swift and M.J.R. Schwar, *Electrical Probes for Plasma Diagnostics*, Illife, London, 1969.
11. L. Schott, "Electrical Probes," in *Plasma Diagnostics*, ed. W. Lochte-Holtgreven, p. 668, North-Holland, Amsterdam, 1968.
12. F.F. Chen, "Electric Probes," in *Plasma Diagnostic Techniques*, ed. S.L. Leonard, p. 113, Academic, New York, 1965.
13. L.B. Loeb, *Basic Processes of Gaseous Electronics*, University of California Press, Berkeley, 1955.
14. F.F. Chen, C. Etievant, and D. Mosher, "Measurements of Low Plasma Densities in a Magnetic Field," *Phys. Fluids* 11, p. 811, 1968.
15. J. Forster and W. Holber, "Plasma Characterisation for a Divergent Field Electron Cyclotron Resonance Source," *J. Vac. Sci. Technol. A* 7, p. 899, 1989.
16. K. Suzuki, K. Ninomiya, S. Nishimatsu, and S. Okudaira, "Radio-Frequency Biased Microwave Plasma Etching Technique: A Method to Increase SiO<sub>2</sub> Etch Rate," *J. Vac. Sci. Technol. B* 3, p. 1025, 1985.

## APPENDIX A

### LANGMUIR PROBE DIAGNOSTIC SYSTEM

The Langmuir probe and associated data acquisition system was designed and constructed from scratch as part of this thesis. The purpose of this appendix is to describe the hardware and software in detail.

#### A.1. LANGMUIR PROBE

The Langmuir probe is shown in figure 3.8. The glass shields for the probes were drawn by Ian Ward of the chemistry glass shop. The outside diameter of the shield at the tip was approximately 100  $\mu\text{m}$ . The probe was assembled by threading the W wire through the shield and then setting it in place with vacuum epoxy (Torr-Seal) at one end. This was in turn attached to the end of a 1/4 inch diameter, thick-walled glass tube which functioned as the slider in the feedthrough assembly. Inside the slider, Ag paint attached the W wire to the larger Cu wire which led to the external connector. The slider was cemented at both ends to form a secure vacuum seal. The shield to slider connection was enlarged to form a stop to prevent complete withdrawal of the probe from the feedthrough.

The probe tip could not be made perfectly straight due to some residual curvature retained by the wire as a result of being wound on a roll. Thus the tip of the probe was tilted about  $10^\circ$  off axis.

#### A.2. ELECTRICAL SYSTEM

A block diagram of the Langmuir probe data acquisition system was given in figure 3.9. The computer control system consisted of a 640 kB personal computer (IBM-XT clone) equipped with an enhanced 8088 microprocessor (NEC V-20) running at a clock rate of 8 MHz. Data acquisition was performed with a board (Metra-Byte Dascon-1) installed in the computer.

The Dascon-1 was interfaced to the probe through the I-V measurement circuit shown in figure A.1. The overall operation of this circuit was described in section 3.4.5. Other important features are as follows. Amplifiers A1 and A3 were special high-voltage op-amps capable of sourcing up to  $\pm 140$  V DC at 10 mA (Analog Devices 171J). The small ceramic (low inductance) capacitors placed parallel to the feedback resistors compensated for the stray input capacitance of the op-amps, thereby reducing the noise at their outputs. The 20,450  $\Omega$  feedback resistor on A2 determined the conversion ratio of the current-to-voltage converter through Ohm's law. The switch allowed the probe to be connected to other devices (such as an oscilloscope for viewing the floating voltage in real-time). Note that A2 floated on the output of A1. In practice this meant that an external connection from A1 to the common of A2's (floating) power supply was required. While this may have reduced the frequency response of the system considerably, the very low frequency (tens of Hz) of operation of the Dascon1 meant that this was not a problem in these experiments.



$$V = (VDA - ZO - NO) \left[ \frac{VFS \times AMP}{BFS} \right], \quad (A.1)$$

where  $VDA$  was the output value of the D/A (bits),  $ZO$  is the zero offset (2047.5 bits),  $NO$  is the noise offset (2.3 bits),  $VFS$  is the full scale output range of the D/A port (10 volts),  $BFS$  is the corresponding value in bits (4095) and  $AMP$  is the amplification factor provided by A1 (10 $\times$ ). The corresponding current conversion is

$$I = \frac{VAD}{R} \frac{VFS'}{BFS'}, \quad (A.2)$$

where  $VAD$  is the input to the A/D converter (volts),  $VFS'$  is the full scale input range of the A/D port ( $\pm 2.0475$  volts),  $BFS'$  is the corresponding value in bits ( $\pm 4075$ ), and  $R = 20,450 \Omega$  is the value of the feedback resistor on the current to voltage converter A2.

The I-V curves were collected in the following manner. The program first determined the upper and lower voltage limits given the maximum allowed collected current of 100  $\mu$ A. This was to prevent excess perturbation of the plasma and/or damage to the probe tip. The data was then acquired in a run consisting of 4 interlaced scans. A run would proceed as follows: During each scan the voltage was increased from lowest to highest, in 16 byte increments. Each of the following scans repeated the previous procedure, but with a +4 byte shift in its D/A values. The purpose of this somewhat complex process was to take, in effect, a time average of 4 scans in a reasonable length of time (approximately 40 s/run) while maintaining a high voltage resolution.

The data acquisition program was written in GW-BASIC. It did not analyse the I-V curves at the time they were taken, but did display them for inspection. A listing of the data acquisition program is given below. Analysis of the curves was performed after all the experiments were completed. The analysis procedure is discussed in section 3.4.3 and appendix B.

#### A.4. PROGRAM LISTING

```
110 ' PROBE.BAS
120 '
130 ' GW-BASIC Data Acquisition Software for an
140 ' Orbital-Motion Limited Cylindrical Langmuir Probe
150 '
160 ' Last Rev. 17/04/1989
170 ' by Paul K. Shufflebotham
180 '***** Titles:
190 KEY OFF: CLS
200 LOCATE 11,29: PRINT "ORBITAL-MOTION LIMITED"
210 LOCATE 12,27: PRINT "CYLINDRICAL LANGMUIR PROBE"
220 LOCATE 13,28: PRINT "DATA ACQUISITION PROGRAM"
230 '***** Initialisation:
240 ' DASCON1 Workspace
250 CLEAR,32768!
260 DEF SEG = 0
270 SG = 256 * PEEK(&H511) + PEEK(&H510)
280 DASCON1 = 0
290 SG = (32768!/16) + SG
```

```
300 DEF SEG = SG
310 BLOAD "DASCON1.BIN", 0
320 OPEN "I", #1, "DASCON1.ADR": INPUT #1, BASADR%: CLOSE #1
330 ' Variable Initialisation
340 MDDA% = 7: CHDA% = 0: DIM DA%(8)
350 MDAD% = 1: CHAD% = 0: DIM AD%(8,1025)
360 DA%(0) = 2045: CALL DASCON1 (MDDA%,CHDA%,DA%(0),DA%(1),BASADR%)
370 ***** Program Execution Control:
380 EXPT = 0: DIM FTESTS(99)
390 SCREEN 0
400 LOCATE 25,3: PRINT " "
410 LOCATE 25,3: INPUT "Execute Run"; YNS: CLS
420 EXPT = EXPT + 1
430 IF YNS <> "n" AND YNS <> "N" THEN GOTO 450
440 KEY ON: END
450 LOCATE 25,50: PRINT " "
460 LOCATE 25,50: INPUT "Data File Name: ", DFILES$
470 IF DFILES = "" GOTO 460
480 FTESTS(EXPT) = DFILES$
490 FOR M = 1 TO EXPT - 1
500 IF FTESTS(M) <> FTESTS(EXPT) GOTO 550
510 LOCATE 25,3: PRINT " "
520 LOCATE 25,3: INPUT "File Already Exists, OK to Overwrite"; YNS
530 LOCATE 25,3: PRINT " "
540 IF YNS <> "y" AND YNS <> "Y" THEN GOTO 390 ELSE GOTO 560
550 NEXT M
560 ***** Data Acquisition Routine:
570 LOCATE 12,25: PRINT " Collecting Data... "
580 ZERO = 512: LOLIM = 0: UPLIM = 1024: SKIP = 4
590 ' Current Limitation
600 FOR I = ZERO + SKIP TO UPLIM STEP SKIP
610 DA%(0) = SKIP * I
620 CALL DASCON1 (MDDA%,CHDA%,DA%(0),DA%(1),BASADR%)
630 CALL DASCON1 (MDAD%,CHAD%,AD%(0,I),AD%(1,I),BASADR%)
640 IF AD%(4,I) <> &H500 THEN NEXT I ELSE UPLIM = I
650 FOR I = ZERO TO LOLIM STEP -SKIP
660 DA%(0) = ABS(SKIP * I)
670 CALL DASCON1 (MDDA%,CHDA%,DA%(0),DA%(1),BASADR%)
680 CALL DASCON1 (MDAD%,CHAD%,AD%(0,I),AD%(1,I),BASADR%)
690 IF AD%(4,I) <> &H500 THEN NEXT I ELSE LOLIM = I
700 DA%(0) = LOLIM * SKIP: CALL DASCON1 (MDDA%,CHDA%,DA%(0),DA%(1),BASADR%)
710 ' I-V Data Collection
720 FIRST = LOLIM: LAST = UPLIM - SKIP
730 FOR J = 1 TO SKIP STEP 1
740 FOR I = FIRST TO LAST STEP SKIP
750 DA%(0) = SKIP * I
760 CALL DASCON1 (MDDA%,CHDA%,DA%(0),DA%(1),BASADR%)
770 AD%(0,I) = 0
780 CALL DASCON1 (MDAD%,CHAD%,AD%(0,I),AD%(1,I),BASADR%)
790 NEXT I
800 DA%(0) = LOLIM * SKIP: CALL DASCON1 (MDDA%,CHDA%,DA%(0),DA%(1),BASADR%)
810 FIRST = FIRST + 1: LAST = LAST + 1
820 NEXT J
830 DA%(0) = 2045: CALL DASCON1 (MDDA%,CHDA%,DA%(0),DA%(1),BASADR%)
840 BEEP
850 LOCATE 12,22: PRINT " "
860 ***** Filing Routine:
870 LOCATE 12,27: PRINT " Filing Data... "
880 OPEN "O", #1, DFILES
```

```
890 FIRST = LOLIM: LAST = UPLIM - SKIP
900 FOR J = 1 TO SKIP STEP 1
910   FOR I = FIRST TO LAST STEP SKIP
920     DA%(0) = SKIP * I
930     PRINT #1, USING "##### "; DA%(0); AD%(0,I)
940   NEXT I
950   FIRST = FIRST + 1: LAST = LAST + 1
960 NEXT J
970 CLOSE #1
980 ***** Plotting Routine:
990 LOCATE 10,30: PRINT "
1000 LOCATE 25,3: INPUT "Plot I-V Characteristic"; YNS
1010 IF YNS <> "" AND YNS <> "y" AND YNS <> "Y" THEN GOTO 390
1020 KEY OFF: CLS: SCREEN 2:
1030 ' Plot Format Control
1040 LOCATE 25,3: PRINT "
1050 LOCATE 25,3: INPUT "Examine Quadrant (0,1-4)"; QUAD
1060 IF QUAD <> 0 GOTO 1120
1070 LOCATE 25,3: PRINT "
1080 LOCATE 25,3: INPUT "Zoom Factor: ", ZOOM
1090 X1 = -100 / ZOOM: X2 = 100 / ZOOM
1100 Y1 = -100 / ZOOM: Y2 = 100 / ZOOM
1110 GOTO 1200
1120 ON QUAD GOTO 1150, 1130, 1190, 1170
1130 X1 = -10: Y1 = -100: X2 = 100: Y2 = 20
1140 GOTO 1200
1150 X1 = -10: Y1 = -20: X2 = 100: Y2 = 100
1160 GOTO 1200
1170 X1 = -100: Y1 = -20: X2 = 20: Y2 = 100
1180 GOTO 1200
1190 X1 = -100: Y1 = -100: X2 = 20: Y2 = 20
1200 CLS
1210 WINDOW (X1,Y1)-(X2,Y2)
1220 ' Vertical Axis (Current)
1230 LINE (0,-80)-(0,80)
1240 LINE (-1,-80)-(1,-80)
1250 LINE (-1,80)-(1,80)
1260 ' Horizontal Axis (Voltage)
1270 LINE (-90,0)-(90,0)
1280 LINE (-90,-1)-(-90,2)
1290 LINE (90,-1)-(90,2)
1300 ' Plot I-V Curve
1310 FOR I = LOLIM TO UPLIM
1320   XPT = ((SKIP * I) - 2047.5) * 90 / 2047.5
1330   YPT = AD%(0,I) * 80 / 4095
1340   PSET (XPT,YPT)
1350 NEXT I
1360 LOCATE 25,3: INPUT "Examine Further"; YNS
1370 IF YNS <> "y" AND YNS <> "Y" THEN GOTO 390 ELSE GOTO 1040
```

## APPENDIX B

### LANGMUIR PROBE DATA ANALYSIS SOFTWARE

The I-V characteristics obtained from the OML Langmuir probe measurements were analysed using the Levenberg-Marquardt (LM) algorithm described in *Numerical Recipes*.<sup>1</sup> Using routines given in this book, a Pascal program was written which fitted the OML current equations to the measured curves. The plasma parameters were then extracted from the fitted model parameters. In this appendix, the details concerning this procedure are be described.

#### B.1. LEVENBERG-MARQUARDT ALGORITHM\*

The problem is that we have a set of  $N$  data points  $y_i(x_i)$ , to which we wish to fit a model equation  $y(x_i, \mathbf{a})$  which depends nonlinearly on a set of  $M$  parameters  $a_k$  (contained in a vector matrix  $\mathbf{a}$ ). To accomplish this, we minimise the *chi-squared* (least-squares) error;

$$\chi^2 \equiv \sum_{i=1}^N \left[ \frac{y_i - y(x_i, \mathbf{a})}{\sigma_i} \right]^2, \quad (\text{B.1})$$

where  $\sigma_i$  is the standard deviation of a normally distributed ensemble of measurements at  $x_i$ , for which  $y_i$  is the average value. Here,  $\chi$  is a statistical measure which occurs only in this appendix, and should not be confused with the normalised probe voltage  $\chi_j$ , used throughout the rest of this thesis. Since  $y(x_i, \mathbf{a})$  is a nonlinear function of  $\mathbf{a}$ , the minimisation must proceed iteratively. We have two options; the *inverse Hessian* and the *gradient descent* techniques.

The inverse Hessian method assumes that we are close to the minimum of  $\chi^2$ , and that  $\chi^2$  depends in an approximately quadratic fashion on  $\mathbf{a}$ . In this case the iteration proceeds according to

$$\mathbf{a}_{new} = \mathbf{a}_{old} + \mathbf{D}^{-1} \cdot [-\nabla \chi^2(\mathbf{a}_{old})], \quad (\text{B.2})$$

where  $[-\nabla \chi^2(\mathbf{a}_{old})]$  is a vector matrix containing the  $M$  elements of the gradient of  $\chi^2$  with respect to the  $a_k$ , evaluated at  $\mathbf{a}_{old}$ . If  $\chi^2(\mathbf{a})$  is exactly quadratic, then  $\mathbf{a}_{new} = \mathbf{a}_{min}$ . This procedure is named for  $\mathbf{D}^{-1}$ , the inverse of the Hessian matrix, which contains the second derivatives with respect to the  $a_k$ .

If  $\chi^2$  is not quadratic, then the only option is to take a step down the gradient of  $\chi^2$  towards the minimum;

$$\mathbf{a}_{new} = \mathbf{a}_{old} - (\text{constant}) [\nabla \chi^2(\mathbf{a}_{old})], \quad (\text{B.3})$$

where the constant is small relative to the extent of the gradient.

---

\* This section is a condensation of chapter 14.4 of "Numerical Recipes",<sup>1</sup> and is completely general.

In both cases we start with an initial guess of  $\mathbf{a}$  and iterate (B.2) or (B.3) to convergence, which occurs when  $\chi^2$  decreases by a statistically insignificant amount,

$$0 \leq \frac{\chi^2_{new} - \chi^2_{old}}{\chi^2_{old}} < 10^{-3}, \quad (\text{B.4})$$

for example.

To put (B.2) and (B.3) into useful forms, we use (B.1) to find the elements of the gradient

$$\frac{\partial \chi^2}{\partial a_k} = -2 \sum_{i=1}^N \frac{y_i - y(x_i, \mathbf{a})}{\sigma_i^2} \frac{\partial y(x_i, \mathbf{a})}{\partial a_k}, \quad k=1, \dots, M \quad (\text{B.5})$$

and Hessian

$$\frac{\partial^2 \chi^2}{\partial a_k \partial a_l} = 2 \sum_{i=1}^N \frac{1}{\chi_i^2} \left\{ \frac{\partial y(x_i, \mathbf{a})}{\partial a_k} \frac{\partial y(x_i, \mathbf{a})}{\partial a_l} - [y_i - y(x_i, \mathbf{a})] \frac{\partial^2 y_i(x_i, \mathbf{a})}{\partial a_k \partial a_l} \right\} \quad (\text{B.6})$$

matrices. For convenience we define the new variables

$$\beta_k \equiv - \frac{1}{2} \frac{\partial \chi^2}{\partial a_k} \quad (\text{B.7})$$

and

$$\alpha_{kl} \equiv \frac{1}{2} \frac{\partial^2 \chi^2}{\partial a_k \partial a_l}. \quad (\text{B.8})$$

In  $\alpha$  we neglect the second term on the right side of (B.6). The inverse Hessian method (B.2) can now be written

$$\sum_{l=1}^M \alpha_{kl} \delta a_l = \beta_k, \quad (\text{B.9})$$

while the gradient descent method (B.3) becomes

$$\lambda a_{ll} \delta a_l = \beta_k. \quad (\text{B.10})$$

The "fudge factor"  $\lambda$  is a small number which ensures that the constant in (B.3), which is  $\lambda a_{ll}$ , is not too large. These equations are solved for  $\delta a_l = a_{l_{new}} - a_{l_{old}}$ .

The inverse Hessian method is faster, but gradient descent can be used far from the minimum. Levenberg and Marquardt suggested that the two techniques, (B.9) and (B.10), be merged into a single hybrid which starts out as gradient descent (B.10) and continuously changes into inverse Hessian (B.9) as the minimum is approached. The *Levenberg-Marquardt method* is produced by redefining  $\alpha$ ,

$$\alpha'_{jk} \equiv \begin{cases} (1+\lambda)\alpha_{jj} & j=k \\ \alpha_{jk} & j \neq k \end{cases} \quad (\text{B.11})$$

and replacing (B.9) and (B.10) with

$$\sum_{l=1}^M \alpha'_{kl} \delta a_{kl} = \beta_k. \quad (\text{B.12})$$

Observe that as  $\lambda \rightarrow 0$ , the LM equation (B.12) approaches that for the inverse Hessian

(B.9). When  $\lambda \gg 1$ , the off-diagonal terms become negligible compared to the diagonals, and (B.12) approaches the gradient descent equation (B.10).

The LM algorithm proceeds as follows:

- (1) Compute  $\chi^2(\mathbf{a})$ .
- (2) Pick a modest value of  $\lambda$ ; 1 in our case.
- (3) Solve the LM equation (B.12) for  $\delta\mathbf{a}$  and calculate  $\chi^2(\mathbf{a}+\delta\mathbf{a})$ .
- (4a) If  $\chi^2(\mathbf{a}+\delta\mathbf{a}) \geq \chi^2(\mathbf{a})$  the trial failed; reject  $\delta\mathbf{a}$ , *increase*  $\lambda$  by 10 and return to step (3).
- (4b) If  $\chi^2(\mathbf{a}+\delta\mathbf{a}) < \chi^2(\mathbf{a})$  the trial succeeded; accept  $\delta\mathbf{a}$ , *decrease*  $\lambda$  by 10 and return to step (3).
- (5) Stop only after a *successful* trial has produced a statistically insignificant change in  $\chi^2$ , as given by (B.4), for example.

In our case, as is often true, the  $\sigma_i$  were not known, so they were set equal to 1 for convenience. This means that  $\chi^2$  was not dimensionless, but in units of Amps. This does not affect the performance of the LM algorithm. Upon completion, *assuming* the model to be a good fit, an average variance (all  $\sigma_i = \sigma$ ) for the data points can be calculated from

$$\sigma^2 = \frac{1}{N} \sum_{i=1}^N [y_i - y(x_i, \mathbf{a})]^2 . \quad (\text{B.13})$$

Note that  $\sigma$  is in units of Amps. This number provides an estimate of the measurement error, and thus allows error bars to be assigned to the data. However, without knowing the actual  $\sigma_i$ , independent measures of goodness-of-fit *cannot* be assigned to the model.

## B.2. SOFTWARE

The data analysis procedure was performed on an IBM XT clone running at 4.77 MHz equipped with an NEC V-20 enhanced 8088 microprocessor and an Intel 8087 math co-processor. The software was written in Turbo Pascal version 4.0, and requires Turbo Graphix Toolbox version 4.0 for the graphics functions. In the spirit of Turbo Pascal, the analysis program, ANAL.PAS, is very short, consisting primarily of a list of procedure calls. All procedures written for ANAL.PAS are contained in the Turbo Pascal unit OML.PAS. The only Turbo Pascal file which needs modification is the unit GDRIVER.PAS. After running the Turbo Graphix installation program TGINST.BAT, the variable MaxPlotGlb in GDRIVER.PAS must be changed from 100 to 1030 to accommodate the large I-V data sets.

The modelling algorithm is implemented by procedure MrqMin, which calls procedures MrqCof and GaussJ. These were taken with only minor modifications from *Numerical Recipes*.<sup>1</sup> The optional procedure CovSrt was not used. The user-specified procedure containing the function to be modelled is called F\_OML.

Procedure F\_OML must contain both the function to be fitted and its derivatives with respect to the fitting parameters at each  $V$ . The model equation must be written so that none of the fitting parameters are degenerate (indistinguishable).<sup>1</sup> This means that the OML current equation (from sub-section 3.4.2),

$$I = Aen \left\{ \left[ \frac{\kappa T_e}{2\pi m_e} \right]^{1/2} \exp \left[ \frac{e(V-V_P)}{\kappa T_e} \right] - \left[ \frac{2\kappa T_i}{\pi^2 m_i} \right]^{1/2} \left[ 1 - \frac{e(V-V_P)}{\kappa T_i} \right]^{1/2} \right\}, \quad (\text{B.14})$$

must be rewritten in the form

$$I = C_1 \exp \left[ \frac{V}{C_2} \right] - \left[ C_3 - C_4 V \right]^{1/2} + C_5 V. \quad (\text{B.15})$$

With temperatures expressed in electron volts,

$$T \text{ (eV)} = \frac{\kappa T}{e}, \quad (\text{B.16})$$

the first four fitting parameters are

$$C_1 = An \left[ \frac{e^3 T_e}{2\pi m_e} \right]^{1/2} \exp \left[ \frac{-V_P}{T_e} \right], \quad (\text{B.17})$$

$$C_2 = T_e, \quad (\text{B.18})$$

$$C_3 = C_4(V_P - T_i), \quad (\text{B.19})$$

$$C_4 = \frac{2A^2 n^2 e^3}{\pi^2 m_i}. \quad (\text{B.20})$$

The linear term  $C_5 V$  was added to improve the fit of the model to the data. This corresponds to a modification of  $\Psi$  (equation (3.17)), which describes the shape and size of the probe sheath. Determinations of  $n$  are not affected, since it is not contained in  $\Psi$ . As described in sub-section 3.4.4, this term probably resulted from some spherical character in the probe sheath, since spherical probes collect saturation currents proportional to  $V^{2,3,4}$ .

Once the modelling algorithm has fitted (B.15) to the data, the plasma parameters are obtained from the fitted parameters  $C_1$  to  $C_4$  in the following manner: (1) solve (B.18) for  $T_e$  and (B.20) for  $n$ , (2) solve (B.17) for  $V_P$ , and (3) solve (B.19) for  $T_i$  (for completeness). The area of the probe is  $A = \pi DL$ , where the diameter is  $D = 25 \mu\text{m}$  and the length is  $L = 1 \text{ cm}$ . End effects are not included in  $A$ , but may be partly accounted for by the  $C_5 V$  term in (B.15). The plasma parameters are calculated in procedure Param, called from ANAL.PAS.

The partial derivatives of  $I$  with respect to the fitting parameters are:

$$\frac{\partial I}{\partial C_1} = \exp \left[ \frac{V}{C_2} \right], \quad (\text{B.21})$$

$$\frac{\partial I}{\partial C_2} = \frac{-C_1 V}{C_2^2} \exp \left[ \frac{V}{C_2} \right], \quad (\text{B.22})$$

$$\frac{\partial I}{\partial C_3} = \frac{-1}{2\sqrt{C_3 - C_4 V}}, \quad (\text{B.23})$$

$$\frac{\partial I}{\partial C_4} = \frac{V}{2\sqrt{C_3 - C_4 V}} \quad (B.24)$$

$$\frac{\partial I}{\partial C_5} = V \quad (B.25)$$

Procedure F\_OML contains (B.15) and (B.21) to (B.25).

Program ANAL.PAS is organised into three parts. The first reads in the measured data and sorts it into a single I-V characteristic. This non-trivial task is performed by procedure ReadSortIV. The range of the I-V curve to be modelled can then be restricted (to below electron saturation, for example) using graphics procedure Truncate. The measured I-V curve can then be compared to the initial guess with graphics procedure IVComp, which uses graphics procedure GenPoly. Procedure GetEst allows changes to be made to the initial guess using the plasma parameters instead of the fitting parameters.

The second part of ANAL.PAS takes the initial fitting parameters and iteratively fits them to the measured data using the Levenberg-Marquardt algorithm. This loop ends when  $\chi^2$  ("chisq") changes ("test") by less than  $10^{-3}$ . Fudge factor  $\lambda$  ("alambda") starts at 1 by default, but this can be changed interactively if necessary. Any combination of the fitting parameters can be held fixed if desired. The variable fitting parameters are specified in array "clist[]", defined in procedure GetEst. Note that the number of variable fitting parameters ("mfit") must also be changed with "clist[]". All I-V curves analysed in this thesis allowed all of  $C_1$  to  $C_5$  to vary.

The third part of ANAL.PAS takes the fitted model parameters and calculates the plasma parameters using procedure Param.  $V_F$  is obtained from the first  $I=0$  crossing of the measured I-V curve by procedure VF\_Calc. While crude, this method was sufficiently accurate for the purposes of this thesis. The measured and fitted I-V curves are then plotted along with a full list of the analysis results by graphics procedure IVGraph (which also calls procedure GenPoly).

Example program output is shown in figure B.1. Much of this output is self-explanatory. The filename is given top left, the date of analysis (day/month/year) top right. The density is given in  $m^{-3}$ , temperatures in eV and potentials in V. The line slope ( $C_5$ ) is a conductance ( $\times 10^{-7} \Omega^{-1}$ ). The standard deviation, calculated in procedure Param, is just  $\sigma$  obtained from (B.13) and is in units of Amps.

### B.3. PROGRAM USAGE

The analysis program is interactive and simple to use. The only variables that the user may wish to change within the program are the convergence criteria "test", in ANAL.PAS, and the list of variable fitting parameters, "clist[]" and "mfit" of procedure GetEst, in unit OML.PAS.

The program proceeds in a straightforward manner, first asking for the name of the file containing the data to be analysed, then proceeding to a graphics routine which allows the user to specify the truncation voltage. Note that graphics procedure GenPoly will crash if  $V_P < V_T$ . Once completed, the default plasma parameters are listed, and the user is asked for any changes. The initial guess I-V curve is then graphically compared to the measured data. This process can be repeated until the

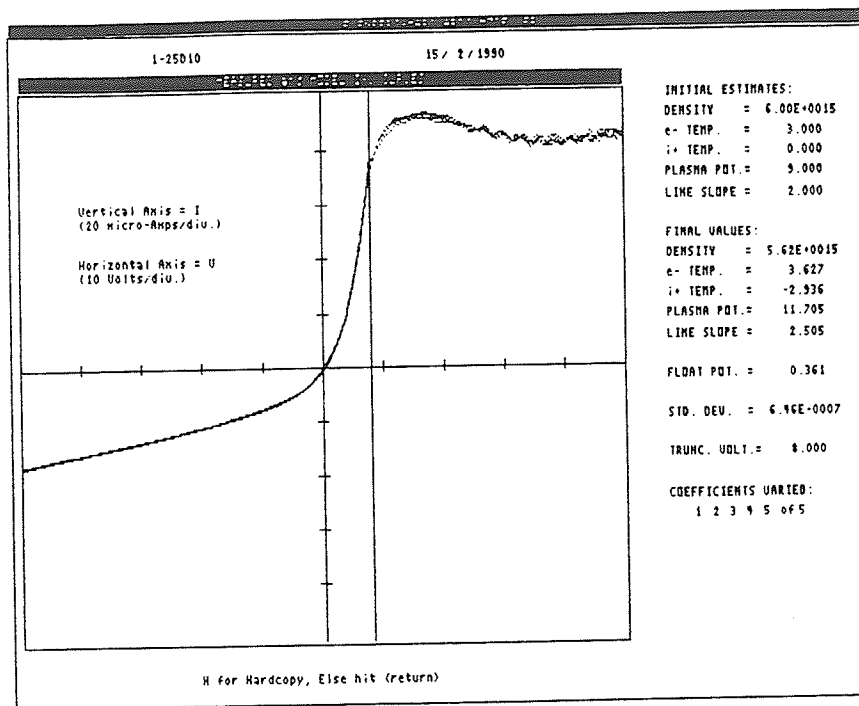


FIGURE B.1. Example output of the cylindrical OML Langmuir probe I-V characteristic analysis program.

initial guess is deemed satisfactory.

As the modelling process begins, the initial value of "alambda" may be changed from the default value of 1. During the modelling iterations (each of which lasts about 10 seconds), the current values of "test" and "alambda" are listed. Upon completion the results are displayed graphically as in figure B.1.

In accordance with Murphy's Law, this process was more difficult and time consuming than the previous discussion may indicate. The problem is the square root term in (B.15). If the initial guess is not close enough to the actual data (close being a relative term dependent on how ideal the measured curve was), then the argument of the square root could go negative, causing the computer to "hang up". Unfortunately, since Turbo Pascal can not handle imaginary numbers and does not provide a means of jumping out of procedure calls, we could not find a way of avoiding this problem without halting execution. Therefore, when this problem occurs (typically within procedure F\_OML), the program pauses and displays a message requesting the user to halt execution by typing CTRL-BREAK. Failure to do so will cause the computer to hang-up, and a reboot will be necessary (CTRL-ALT-DEL or CTRL-RESET). The result is that analysis of many I-V characteristics consisted of repeatedly running ANAL.PAS with different initial guesses until it ran to completion.

In selecting the initial plasma parameters, it is obviously useful to know what effect each has on the I-V characteristic. These effects are shown in figures B.2 to B.6. Observe that, except for  $T_i$ , all parameters have recognizably distinct effects on the shape of the curves. The effect of  $T_i$  is both minor and relatively indistinguishable

from changes in other parameters. This is basically why  $T_i$  cannot be obtained from cylindrical OML probes.<sup>2</sup>

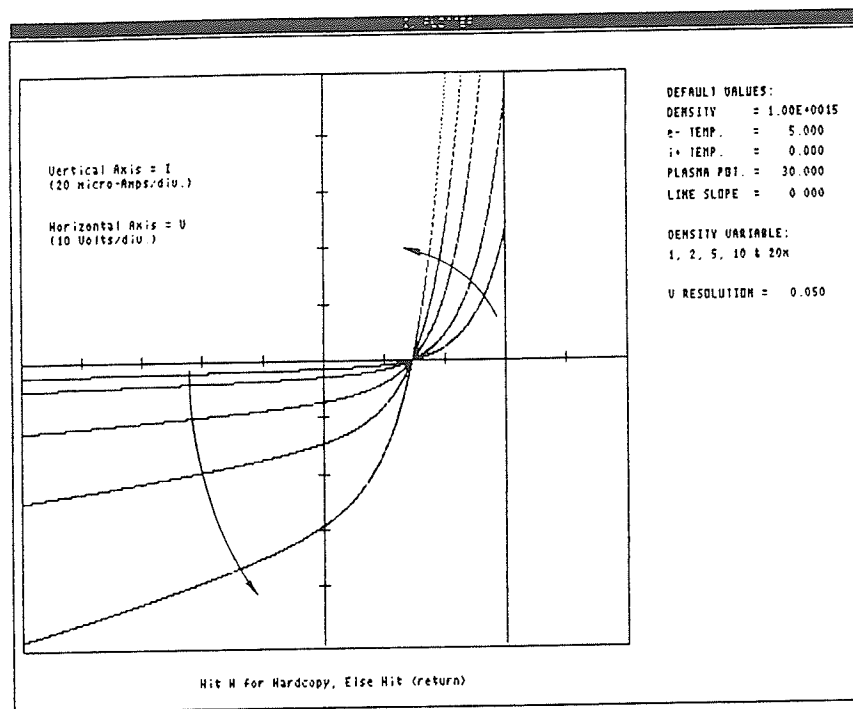


FIGURE B.2. Effect of increasing the plasma density on OML Langmuir probe I-V characteristics. The vertical line corresponds to  $V_p$ .  $n$  determines the magnitude of the current at a given  $V$ . Note the constancy of  $V_p$ .

#### B.4. ACCURACY OF RESULTS

As discussed at the end of section B.1, the amount of measurement error was estimated by comparison to the fitted model. By assuming that the measurement error in  $I$  at each  $V$  was normally distributed and that this distribution did not change with  $V$ , an estimate of the standard deviation of the measurement error,  $\sigma$ , was calculated. This was used to assign error bars to the I-V data points. The value of  $\sigma$  was always less than  $1 \mu\text{A}$ , which is on the order of the pixel size in the analysis program output (figure B.1).

Some measurement error was due to the finite resolution of the data acquisition system;  $0.1 \mu\text{A}/\text{point}$  and  $0.1 \text{ mV}/\text{point}$ . The rest was due to noise in the electronics and, of course, in the plasma itself. Drifts in the plasma (or probe) properties during an I-V measurements would have appeared as shifts in the four interlaced scans from which each I-V curve was assembled. These were not observed. In general, the precision of the measured I-V data was quite good. Two remaining questions concern the precision of the plasma parameters obtained from the I-V characteristics (how well does the model fit the data) and their accuracy (how well do they represent the actual physical properties of the plasma)?

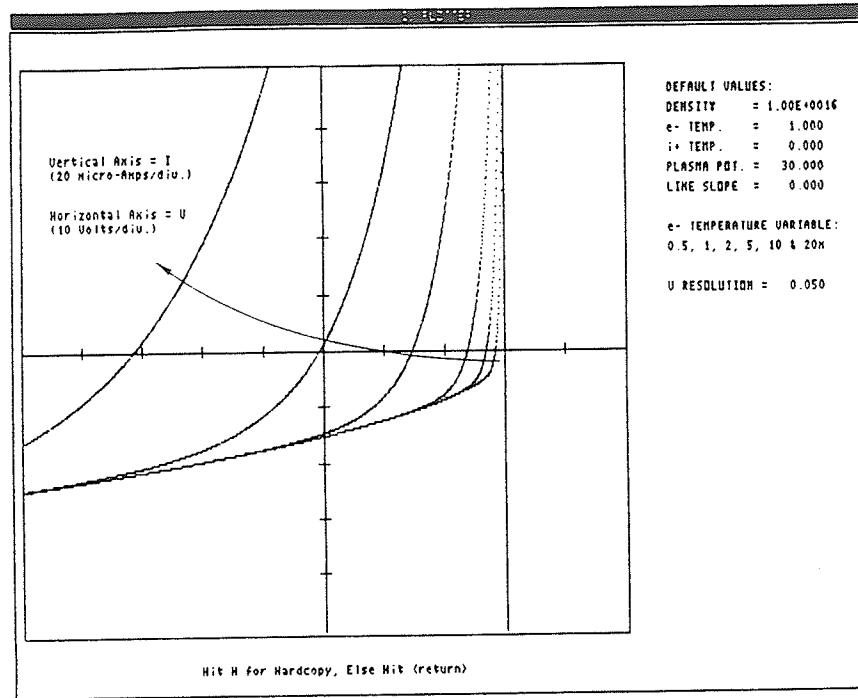


FIGURE B.3. Effect of increasing the electron temperature on OML Langmuir probe I-V characteristics. The vertical line corresponds to  $V_p$ .  $T_e$  determines the rate of increase of the current in the exponential region. Note that the ion saturation current is not affected.

Unfortunately, the question of accuracy cannot be answered unless independent measurements of the plasma parameters are made. This is typically a difficult task, given that probes make local measurements of several variables. The consensus is that probes give approximate results, the primary use of which should be in comparative studies.<sup>5,6</sup> As a rough guide,  $n$  should be considered correct to within an order of magnitude, while  $T_e$  and  $V_p$  should be within a few tens of percent. Fortunately, the accuracy of the plasma parameters is not of primary importance to this thesis, but rather their relative variations as functions of system parameters. The accuracy of these trends is given by the precision of the modelled plasma parameters.

The statistically preferred method of stating the precision of modelling results is to assign confidence limits to the fitted parameters. Assuming normally distributed measurement errors, these can be calculated from the fitted parameters from the covariances (given in matrix "covar[]" calculated by procedures MrqMin and MrqCof in OML.PAS). However, since we do not know the measurement error distribution we cannot, in good faith, calculate the confidence limits. We can only give the covariance matrix as the "formal covariance matrix of the fit on the assumption of normally distributed errors".<sup>1</sup> This would not be particularly informative, as it applies to the fitting parameters, not the plasma parameters which are of interest.

To provide a more physically meaningful (if less so statistically) estimate of the precision of the model plasma parameters, we directly calculated the values of each plasma parameter which was required to produce a given increase in  $\chi^2$ . This was done by simply varying each plasma parameter about its optimal value until  $\chi^2$

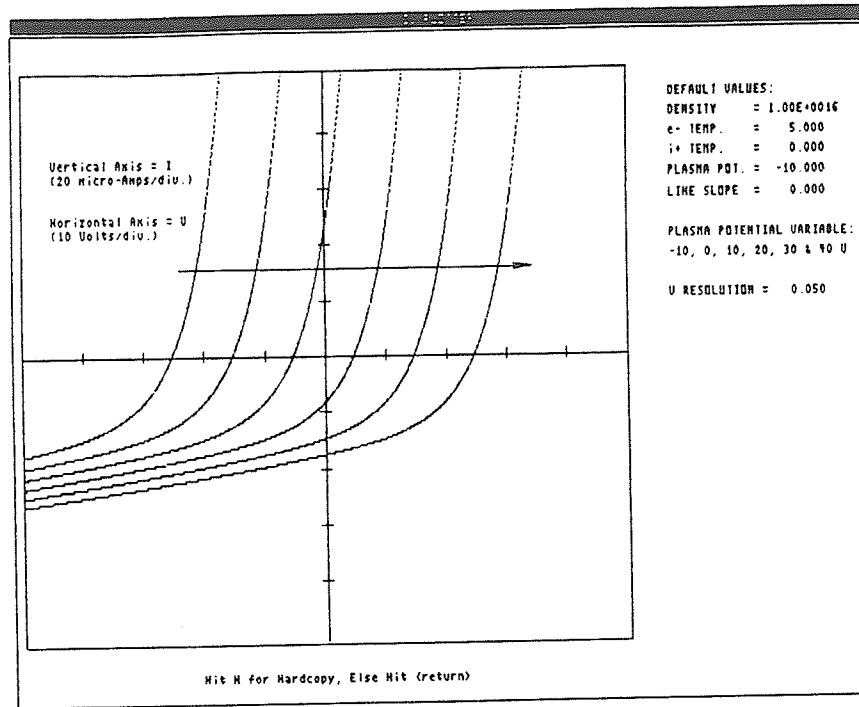


FIGURE B.4. Effect of increasing the plasma potential on OML Langmuir probe I-V characteristics.  $V_p$  determines the location of the I-V curve along the  $V$  axis. Note that the shape of the I-V curve does not change, that  $V_F$  follows  $V_p$ , and that the ion saturation current at a fixed  $V$  decreases with  $V_p$ .

increased by 10%. This provides an (admittedly arbitrary) measure of both the precision and the relative significance of each plasma parameter.

Five I-V characteristics were selected for this analysis from the data set used in this thesis. These were chosen so as to represent the full range of possible forms these curves could adopt; they were *not* "typical" results which would have yielded overly optimistic error estimates. Note that despite the extreme nature of some of these curves, none produced extreme results in more than one plasma parameter. The results of the analysis are summarised in figure B.7. Clearly this confirms that  $T_i$  is an essentially meaningless parameter, as expected. Given the effect of  $T_i$  on the form of the I-V characteristic (figure B.5), about all that can be said about this parameter is that large negative (positive) values may indicate an excess (deficit) of hot electrons in the otherwise approximately Maxwellian EEDF. Since the I-V curves do not contain sufficient information for a meaningful determination of  $T_i$ , this parameter will not be considered in this thesis.  $LS$  is reasonably precise (less than  $\pm 5\%$ ), but since it is not used in any calculations, it too will not be considered in this thesis. However,  $n$ ,  $T_e$  and  $V_p$  all have average variations at about  $\pm 1\%$ , and therefore are quite precise. Thus relative trends in these three parameters will be accurate representations of the properties of the plasma.

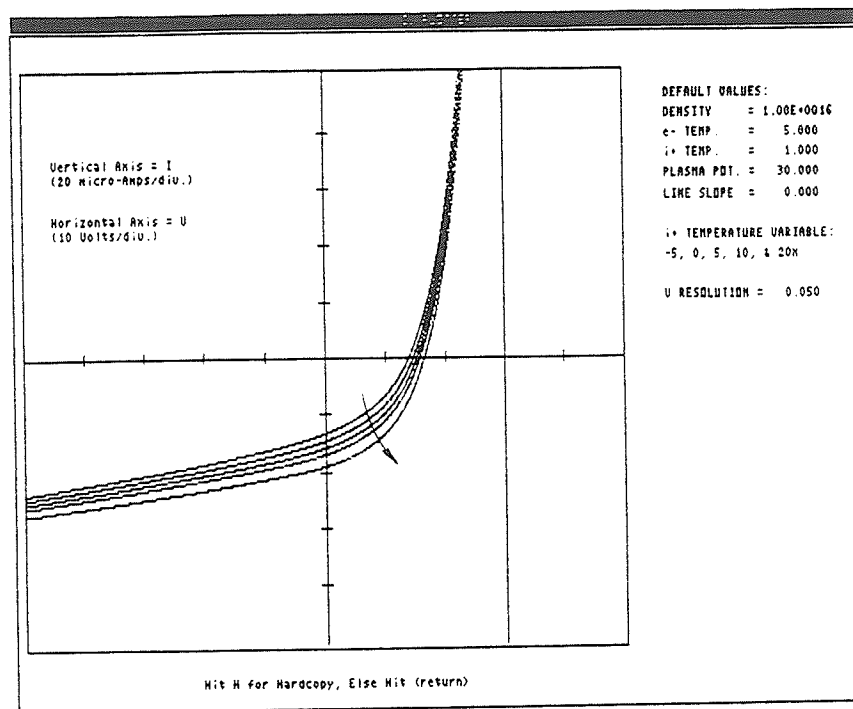


FIGURE B.5. Effect of increasing the ion temperature on OML Langmuir probe I-V characteristics. The vertical line corresponds to  $V_p$ .  $T_i$  influences both the location of the I-V curve along the  $I$  axis and the sharpness of the knee above the ion saturation region. Note that both these effects are relatively minor, especially in the exponential region from which  $T_e$  and  $V_p$  are obtained.

## B.5. PROGRAM LISTING

PROGRAM Anal;

(\* Turbo Pascal ver. 4.0 Data Analysis Software for an \*)  
 (\* Orbital-Motion Limited Cylindrical Langmuir Probe \*)

(\* Requires Turbo Graphix Toolbox ver. 4.0 and math co-processor \*)

(\* Last Rev. 27/10/1989 \*)  
 (\* by Paul K. Shufflebotham \*)

USES

Dos, Crt, GDriver, Printer, GKernel, GWindow, GShell, OML;

VAR

name, go, try: string;  
 ma, mfit, num0, num: integer;  
 alambda, chisq, chiold, test: single;  
 da, ad, v, i, sig: glndata;  
 a: glma;  
 lista: gllista;  
 covar, alpha: glnpbynp;

BEGIN { begin program Anal }  
 InitGraphic; { initialise graphics mode }

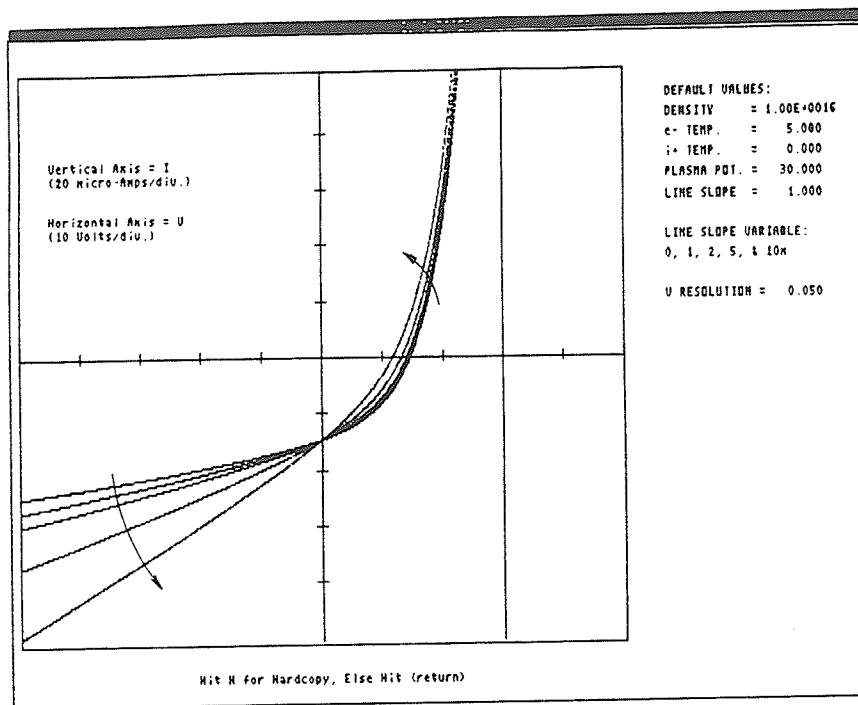


FIGURE B.6. Effect of increasing the linear term in  $V$  added to the OML Langmuir probe current equation (B.15). The vertical line corresponds to  $V_p$ . This parameter is just the slope of a line and is in units of conductance ( $\Omega^{-1}$ ). Note that  $V=0$  is the fixed point, and that the effect of this parameter is relatively minor in the exponential region from which  $T_e$  and  $V_p$  are obtained.

```

LeaveGraphic; { leave graphics initialization }
ReadSortIV(name,num0,da,ad,v,i); { get data file, read and sort data }
Truncate(name,num0,num,v,i,ppin[7]); { truncate I-V curve }
ppin[1] := 1.0e16; { default initial plasma density }
ppin[2] := 3.0; { default initial electron temperature }
ppin[3] := 0.0; { default initial ion temperature }
ppin[4] := 10.0; { default initial plasma potential }
ppin[5] := 0.0; { default initial line slope }
try := 'y';
WHILE (try = 'y') OR (try = 'Y') DO
BEGIN { get initial estimates }
  GetEst(a,ppin,lista,ma,mfit,sig,num); { get initial parameters }
  IVComp(name,num0,num,v,i,a,ppin); { plot trial }
  Writeln("Try again? (Y if Yes, Else hit <return>");
  Readln(try);
END;
alambda := -1.0; { initialization value }
MrqMin(v,i,sig,num,a,ma,lista,mfit,covar,alpha,chisq,alambda);
test := 1.0; { initial value of convergence test variable }
Writeln(test:5:3, ' ,alambda:9);
WHILE test >= 1.0e-3 DO { iterate until change in fit is insignificant }
BEGIN { analysis loop }
  chiold := chisq;
  MrqMin(v,i,sig,num,a,ma,lista,mfit,covar,alpha,chisq,alambda);
  test := (chiold-chisq)/chiold;
  Writeln(test:5:3, ' ,alambda:9);

```

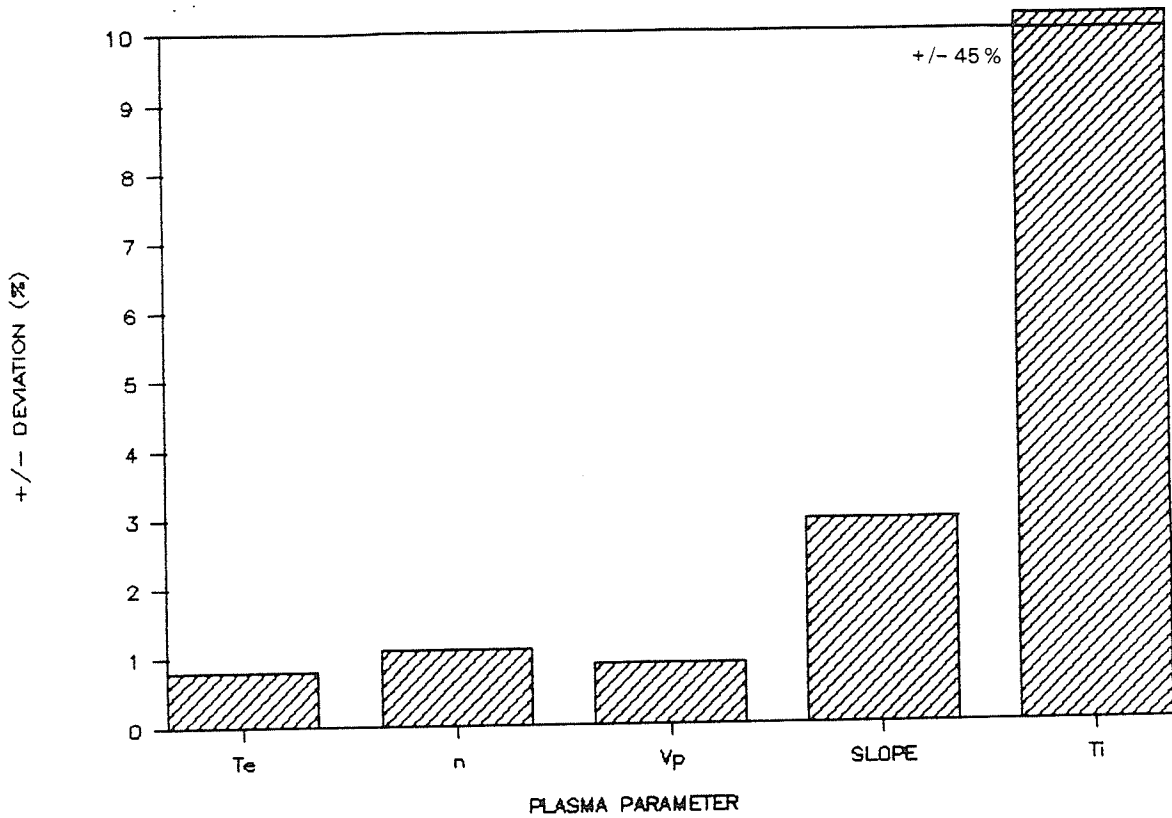


FIGURE B.7. Bar graph indicating the percentage change required in each model plasma parameter to produce a 10% increase in  $\chi^2$ . This summarises the results of an analysis of five I-V characteristics chosen to represent all the observed forms these curves could adopt. Shown is the average  $\pm$  variation and the maximum and minimum total minus-to-plus variation.

```
END;  
Param(a,chisq,ppout,num); { extract plasma parameters from model }  
Vf_Calc(v,i,ppout[6]); { extract Vf from raw data }  
IVGraph(name,num0,num,v,i,a,ppin,ppout,lista,mfit); { plot results }  
END. { end program Anal }
```

UNIT OML;

(\* Turbo Pascal ver. 4.0 Unit for Program ANAL.PAS \*)

(\* Requires Turbo Graphix Toolbox ver. 4.0 and math co-processor \*)

(\* Last Rev. 31/10/1989 \*)

(\* Paul K. Shufflebotham \*)

INTERFACE

USES

Dos, Crt, GDriver, Printer, GKernel, GWindow, GShell;

CONST

pi = 3.141592654; { pi }

```
e = 1.602189246e-19; { unit of charge }
me = 9.10953447e-31; { electron mass }
mi = 1.67264858e-27; { proton mass }
dia = 2.5e-5; { probe diameter }
len = 1e-2; { probe length }
iconv = 2.444987775e-8; { i conversion, amps to bits }
step = 4; { voltage step, in bits }
```

```
TYPE { TYPE single requires co-processor }
  glndata = ARRAY [1..1030] OF single;
  glma = ARRAY [1..9] OF double;
  gllista = ARRAY [1..9] OF integer;
  glnpbynp = ARRAY [1..9,1..9] OF single;
  glnp = ARRAY [1..9] OF integer;
  glstr = ARRAY [1..9] OF string;
```

VAR

```
  glbeta, ppin, ppout: glma;
  glochisq: single;
  j, k, num: integer;
```

```
PROCEDURE ReadSortIV(VAR filename: string; VAR numpts: integer;
  VAR x,y,x1,y1: glndata);
PROCEDURE Truncate(filename: string; numin: integer; VAR numout: integer;
  x,y: glndata; VAR vt: double);
PROCEDURE GetEst(VAR coeff, init: glma; VAR clist: gllista;
  VAR ma,mfit: integer; VAR sigma: glndata; numpts: integer);
PROCEDURE IVComp(filename: string; numin,numpts: integer; x,y: glndata;
  coeff,init: glma);
PROCEDURE Param(coeff: glma; errest: single; VAR fin: glma; numpts: integer);
PROCEDURE Vf_Calc(x,y: glndata; VAR cross: double);
PROCEDURE F_OML(v: single; a: glma; VAR i: single; VAR dyda: glma);
PROCEDURE MrqMin(x,y,sig: glndata; ndata: integer;
  VAR a: glma; ma: integer; lista: gllista; mfit: integer;
  VAR covar,alpha: glnpbynp; VAR chisq,alambda: single);
PROCEDURE MrqCof(x,y,sig: glndata; ndata: integer;
  VAR a: glma; ma: integer; lista: gllista; mfit: integer;
  VAR alpha: glnpbynp; VAR beta: glma; VAR chisq: single);
PROCEDURE GaussJ(VAR covar: glnpbynp; n: integer;
  VAR oneda: glnpbynp; m: integer);
PROCEDURE IVGraph(filename: string; numin,numpts: integer; x,y: glndata;
  coeff,init,fin: glma; list: gllista; numlist: integer);
PROCEDURE GenPoly(x: glndata; a: glma; numpts: integer; VAR xy: plotarray);
```

IMPLEMENTATION

```
PROCEDURE ReadSortIV;
(* Reads in I-V data points and sorts them into increasing order. *)
VAR
  iv: text;
  first, last, jump, count: integer;
BEGIN { begin procedure ReadSortIV }
  Writeln('Enter Filename: '); { get data file }
  Readln(filename);
  numpts := 0;
  first := 1;
  last := 1024;
  jump := 4;
  Assign(iv, filename);
```

```

Reset(iv); { open I-V data file }
Readln(iv,x[first],y[first]); { read and sort I-V data }
x1[first] := (x[first]-2045.2)/40.95;
y1[first] := y[first]*2.477826e-8;
numpts := numpts+1;
FOR count := 1 TO jump DO
BEGIN
  j := first+jump;
  WHILE j <= last+jump-1 DO
  BEGIN
    Readln(iv,x[j],y[j]);
    IF x[j] > x[j-jump] THEN
    BEGIN
      x1[j] := (x[j]-2045.2)/40.95;
      y1[j] := y[j]*2.477826e-8;
      numpts := numpts+1;
      j := j+jump;
    END
    ELSE
    BEGIN
      k := j;
      j := last+jump;
    END;
  END;
  IF count <> jump THEN
  BEGIN
    first := first+1;
    x[first] := x[k];
    y[first] := y[k];
    x1[first] := (x[first]-2045.2)/40.95;
    y1[first] := y[first]*2.477826e-8;
    numpts := numpts+1;
  END;
END;
Close(iv); { close I-V data file }
END; { end procedure ReadSortIV }

PROCEDURE Truncate;
(* Displays raw I-V curve, and allows interactive truncation *)
(* (removal of e- attracting region) to be performed. *)
VAR
  yn, vtstr: string;
BEGIN { begin procedure Truncate }
  vt := 50.0;
  numout := numin;
  Writeln('Plot/Truncate data? (Y if Yes, Else hit <return>');
  Readln(yn);
  WHILE (yn = 'y') OR (yn = 'Y') DO
  BEGIN
    Str(vt:9:3,vtstr);
    EnterGraphic; { enter graphics mode }
    SetHeaderOn;
    DefineWindow(1,1,1,XMaxGlb,YMaxGlb); { background window }
    DefineHeader(1,'I-V CHARACTERISTIC TRUNCATION');
    DefineWorld(1,0,0,100,100);
    SelectWorld(1);
    SelectWindow(1);
    DrawBorder;
    DrawTextW(77,50,1,'TRUNCATE V=');
  END;
END;

```

```
DrawTextW(88,50,1,vtstr);
DrawTextW(19,96,1,'Y to truncate, Then new V, Else hit <return>');
DefineWindow(2,2,30,XMaxGlb-25,YMaxGlb-30); { foreground window }
DefineHeader(2,filename);
DefineWorld(2,-50,-102e-6,50,102e-6);
SelectWorld(2);
SelectWindow(2);
DrawBorder;
SetClippingOn; { prevents screen crashes }
DrawLine(-50,0,50,0); { V axis }
DrawLine(0,-102e-6,0,102e-6); { I axis }
FOR k := -4 TO 4 DO
BEGIN { axis tick marks }
  DrawLine(-1,20e-6*k,1,20e-6*k);
  DrawLine(10*k,-2e-6,10*k,2e-6);
END;
FOR j := 1 TO numin DO DrawPoint(x[j],-y[j]); { draw raw data }
DrawLine(vt,-102e-6,vt,102e-6); { draw truncation indicator }
Readln(yn);
IF (yn = 'y') OR (yn = 'Y') THEN Readln(vt); { retry truncation }
END;
LeaveGraphic; { leave graphics mode }
j := 1; { calculate new total number of data points }
WHILE (x[j] < vt) AND (j < numin) DO j := j+1;
numout := j-1;
END; { end procedure Truncate }
```

```
PROCEDURE GetEst;
(* Sets default first estimates of plasma parameters, and asks *)
(* for changes. Calculates coefficients needed by L-M, and sets *)
(* which are to be varied. Sets variances for measured data *)
(* pairs to 1, since they aren't known. *)
VAR
  yn, pname: string;
  value: single;
BEGIN { begin procedure GetEst }
  Writeln('Trial plasma parameters are: ');
  Writeln;
  Writeln('n=',init[1]:11,' Te=',init[2]:5:3,' Ti=',init[3]:5:3,
    ' Vp=',init[4]:5:3,' L=',init[5]:5:3);
  Writeln;
  yn := 'y';
  WHILE (yn = 'y') OR (yn = 'Y') DO
  BEGIN { get new initial plasma parameters }
    Writeln('Enter name of parameter to change, Then new value,');
    Writeln('Else hit <return> to continue...');
    Readln(pname);
    IF (pname = '') THEN yn := 'no'
    ELSE
      Readln(value);
      IF (pname = 'n') OR (pname = 'N')
      THEN init[1] := value
      ELSE
        IF (pname = 'te') OR (pname = 'TE')
        THEN init[2] := value
        ELSE
          IF (pname = 'ti') OR (pname = 'TI')
          THEN init[3] := value
          ELSE
```

```

        IF (pname = 'vp') OR (pname = 'VP')
        THEN init[4] := value
        ELSE
            IF (pname = 'l') OR (pname = 'L')
            THEN init[5] := value;
    END;
    coeff[1] := pi*dia*len*e*init[1]*Sqrt((e*init[2])/(2*pi*me))
                *Exp(-init[4]/init[2]); { coefficients of OML equation }
    coeff[2] := init[2];
    coeff[4] := (2*Sqr(dia*len*e*init[1])*e)/mi;
    coeff[3] := coeff[4]*(init[3]+init[4]);
    coeff[5] := init[5]*1.0e-7;
    ma := 5; { total no. of coefficients }
    mfit := 5; { no. of variable coefficients }
    clist[1] := 1; { list of coefficients to vary }
    clist[2] := 2;
    clist[3] := 3;
    clist[4] := 4;
    clist[5] := 5;
    FOR j := 1 TO numpts DO sigma[j] := 1; { set variances, since unknown }
END; { end procedure GetEst }

```

PROCEDURE IVComp;

(\* Plots I-V data and model data as Current (Amps) vs. Voltage \*)

(\* (Volts), for comparison of initial guess with data. \*)

VAR

nstrin, testrin, tistrin, vpstrin: string;

vfstr, vtstr, lstr, go: string;

model: plotarray;

BEGIN { begin procedure IVComp }

WriteIn('Wait...');

Str(init[1]:11,nstrin); { convert initial parameters to strings }

Str(init[2]:9:3,testrin);

Str(init[3]:9:3,tistrin);

Str(init[4]:9:3,vpstrin);

Str(init[5]:9:3,lstr);

Str(init[7]:9:3,vtstr);

GenPoly(x,coeff,numpts,model); { generate array for model data }

EnterGraphic; { enter graphics mode }

SetHeaderOn;

DefineWindow(1,1,1,XMaxGlb,YMaxGlb); { background window }

DefineHeader(1,'INITIAL GUESS COMPARATOR');

DefineWorld(1,0,0,100,100);

SelectWorld(1);

SelectWindow(1);

DrawBorder;

DrawTextW(77,9,1,'INITIAL ESTIMATES:'); { write initial guesses }

DrawTextW(77,12,1,'DENSITY =');

DrawTextW(88,12,1,nstrin);

DrawTextW(77,15,1,'e- TEMP. =');

DrawTextW(88,15,1,testrin);

DrawTextW(77,18,1,'i+ TEMP. =');

DrawTextW(88,18,1,tistrin);

DrawTextW(77,21,1,'PLASMA POT. =');

DrawTextW(88,21,1,vpstrin);

DrawTextW(77,24,1,'LINE SLOPE =');

DrawTextW(88,24,1,lstr);

DrawTextW(77,33,1,'TRUNC. VOLT.=');

DrawTextW(88,33,1,vtstr);

```

DrawTextW(25,96,1,'Hit <return> to Continue');
DefineWindow(2,2,30,XMaxGlb-25,YMaxGlb-30); { foreground window }
DefineHeader(2,filename);
DefineWorld(2,-50,-102e-6,50,102e-6);
SelectWorld(2);
SelectWindow(2);
DrawBorder;
SetClippingOn; { prevents screen crashes }
DrawLine(-50,0,50,0); { V axis }
DrawLine(0,-102e-6,0,102e-6); { I axis }
FOR k := -4 TO 4 DO { axis tick marks }
BEGIN
    DrawLine(-1,20e-6*k,1,20e-6*k);
    DrawLine(10*k,-2e-6,10*k,2e-6);
END;
FOR j := 1 TO numin DO DrawPoint(x[j],-y[j]); { draw raw data }
DrawLine(init[7],-102e-6,init[7],102e-6); { draw truncation indicator }
DrawPolygon(model,1,-numpts,0,0,0); { draw model I-V curve }
Readln;
LeaveGraphic; { leave graphics mode }
END; { end procedure IVComp }

```

```

PROCEDURE Param;
(* Calculates plasma parameters from OML equation variables. *)
BEGIN { begin procedure Param }
    IF (coeff[4] <= 0.0) THEN
    BEGIN
        Writeln('Error in procedure Param:');
        Writeln('n is zero or imaginary; Hit CTRL-Break to Exit');
        Readln;
    END;
    fin[1] := Sqrt((coeff[4]*mi)/(2*e))/(e*dia*len); { density }
    IF (coeff[2] <= 0.0) THEN
    BEGIN
        Writeln('Error in procedure Param:');
        Writeln('Te is zero or negative; Hit CTRL-Break to Exit');
        Readln;
    END;
    fin[2] := coeff[2]; { e- temperature }
    IF (coeff[1] <= 0.0) THEN
    BEGIN
        Writeln('Error in procedure Param:');
        Writeln('coeff[1] is zero or negative; Hit CTRL-Break to Exit');
        Readln;
    END;
    fin[4] := -fin[2]*(Ln(coeff[1])-Ln(pi*dia*len*e*fin[1])
        -0.5*Ln((e*fin[2])/(2*pi*me))); { plasma potential }
    fin[3] := coeff[3]/coeff[4]-fin[4]; { i+ temperature }
    fin[5] := coeff[5]/1.0e-7;
    fin[9] := Sqrt(errest/numpts); { estimated std. dev. of avg. data pt. }
END; { end procedure Param }

```

```

PROCEDURE Vf_Calc;
(* Calculates the floating voltage from the raw I-V data. *)
BEGIN
    j := 1;
    WHILE y[j] < 0.0 DO j := j+1;
    cross := x[j];
END; { end procedure Vf_Calc }

```

```
PROCEDURE F_OML;
(* Evaluates OML equation and derivatives wrt/coefficients for *)
(* use in MrqMin *)
VAR
  arg1, arg2: single;
BEGIN { begin procedure F_OML }
  arg1 := v/a[2];
  arg2 := a[3]-a[4]*v;
  IF (arg2 <= 0.0) THEN
  BEGIN
    Writeln('Error in procedure F_Oml at V = ',v:4:2,':');
    Writeln('Negative argument of Sqrt; Hit CTRL-Break to Exit');
    Readln;
  END;
  i := a[1]*Exp(arg1)-Sqrt(arg2)+a[5]*v; { OML current equation }
  dyda[1] := Exp(arg1); { derivatives wrt/ coefficients }
  dyda[2] := -(v*a[1]/(a[2]*a[2]))*Exp(arg1);
  dyda[3] := -1/(2*Sqrt(arg2));
  dyda[4] := v/(2*Sqrt(arg2));
  dyda[5] := v;
END; { end procedure F_OML }
```

```
PROCEDURE MrqMin;
(* Main procedure for Levenberg-Marquardt nonlinear modelling *)
(* method. From Numerical Recipes, Chapter 14.4. Pascal listing *)
(* pp.774-775. *)
LABEL 99;
VAR
  yn: string;
  kk, ihit: integer;
  atry, da: glma;
  oneda: glnpbynp;
BEGIN { begin procedure MrqMin }
  IF (alambda < 0.0) THEN
  BEGIN { initialization sequence }
    kk := mfit+1;
    FOR j := 1 TO ma DO
    BEGIN { check lista for proper permutation of coefficients }
      ihit := 0;
      FOR k := 1 TO mfit DO
      BEGIN
        IF (lista[k] = j) THEN ihit := ihit+1;
      END;
      IF (ihit = 0) THEN
      BEGIN
        lista[kk] := j;
        kk := kk+1;
      END
      ELSE IF (ihit > 1) THEN
      BEGIN
        Writeln('pause 1 in routine MRQMIN');
        Writeln('improper permutation in LISTA');
        Readln;
      END;
    END;
  END;
  IF (kk <> (ma+1)) THEN
  BEGIN
    Writeln('pause 2 in routine MRQMIN');
    Writeln('improper permutation in LISTA');
```

```
      Readln;
    END; { end lista permutation check }
    alambda := 1.0; { initial (default) value }
    Writeln; { change alambda? }
    Writeln('Initial value of Lambda is: ',alambda:5);
    Writeln('Change it? (Y if Yes, Then new value, Else hit <return>');
    Readln(yn);
    IF (yn = 'Y') OR (yn = 'y') THEN Readln(alambda);
    Writeln('Test ALambda');
    Writeln('1.000 ',alambda:9);
    MrqCof(x,y,sig,ndata,a,ma,lista,mfit,alpha,glbeta,chisq);
    glochisq := chisq; { evaluate alpha and beta }
    FOR j := 1 TO ma DO
    BEGIN
      atry[j] := a[j];
    END;
  END; {end initialization }
  FOR j := 1 TO mfit DO
  BEGIN { alter alpha by augmenting diagonal elements }
    FOR k := 1 TO mfit DO
    BEGIN
      covar[j,k] := alpha[j,k];
    END;
    covar[j,j] := alpha[j,j]*(1.0+alambda);
    oneda[j,1] := glbeta[j];
  END; { end alpha augmentation }
  Gaussj(covar,mfit,oneda,1); { solve matrix }
  FOR j := 1 TO mfit DO
  BEGIN
    da[j] := oneda[j,1];
  END;
  FOR j := 1 TO mfit DO
  BEGIN { evaluate success of trial }
    atry[lista[j]] := a[lista[j]]+da[j];
  END;
  MrqCof(x,y,sig,ndata,atry,ma,lista,mfit,covar,da,chisq);
  IF (chisq < glochisq) THEN
  BEGIN { successful trial; accept new solution }
    alambda := 0.1*alambda;
    glochisq := chisq;
    FOR j := 1 TO mfit DO
    BEGIN
      FOR k := 1 TO mfit DO
      BEGIN
        alpha[j,k] := covar[j,k];
      END;
      glbeta[j] := da[j];
      a[lista[j]] := atry[lista[j]];
    END;
  END
  ELSE
  BEGIN { trial failed; increase alambda and exit MrqMin }
    alambda := 10.0*alambda;
    chisq := glochisq;
  END;
99: END; { end procedure MrqMin }
```

```
PROCEDURE MrqCof;
(* Sub-procedure for Levenberg-Marquardt nonlinear modelling *)
```

```
(* method. From Numerical Recipes, Chapter 14.4. Pascal listing *)
(* pp.775-776. *)
VAR
  i: integer;
  ymod, wt, sig2i, dy: single;
  dyda: glma;
BEGIN { begin procedure MrqCof }
  FOR j := 1 TO mfit DO
    BEGIN { initialise alpha and beta }
      FOR k := 1 TO j DO
        BEGIN
          alpha[j,k] := 0.0;
        END;
        beta[j] := 0.0;
      END;
      chisq := 0.0;
      FOR i := 1 TO ndata DO
        BEGIN { begin evaluation of alpha and beta (sum over all data) }
          F_OML(x[i],a,ymod,dyda);
          sig2i := 1.0/(sig[i]*sig[i]);
          dy := y[i]-ymod;
          FOR j := 1 TO mfit DO
            BEGIN
              wt := dyda[lista[j]]*sig2i;
              FOR k := 1 TO j DO
                BEGIN
                  alpha[j,k] := alpha[j,k]+wt*dyda[lista[k]];
                END;
                beta[j] := beta[j]+dy*wt;
              END;
              chisq := chisq+dy*dy*sig2i;
            END; { end evaluation of alpha and beta }
          FOR j := 2 TO mfit DO
            BEGIN { fill in symmetric side of matrices }
              FOR k := 1 TO j-1 DO
                BEGIN
                  alpha[k,j] := alpha[j,k];
                END;
              END; { end fill-in of symmetric sides }
            END; { end procedure MrqCof }
          END; { end procedure MrqCof }

PROCEDURE GaussJ;
(* Gauss-Jordan elimination method for solving sets of linear *)
(* equations. Sub-procedure for Levenberg-Marquardt nonlinear *)
(* modelling method. From Numerical Recipes, Chapter 2.1. *)
(* Pascal listing pp.682-683. *)
VAR
  big, dum, pivinv: single;
  i, icol, irow, l, ll: integer;
  indxc, indxr, ipiv: glnp;
BEGIN { begin procedure GaussJ }
  FOR j := 1 TO n DO
    BEGIN { initialise ipiv }
      ipiv[j] := 0;
    END;
    FOR i := 1 TO n DO
      BEGIN { begin column reduction }
        big := 0.0;
        FOR j := 1 TO n DO
```

```
BEGIN { begin search for pivot point }
  IF (ipiv[j] <> 1) THEN
    BEGIN
      FOR k := 1 TO n DO
        BEGIN
          IF (ipiv[k] = 0) THEN
            BEGIN
              IF (Abs(covar[j,k]) >= big) THEN
                BEGIN
                  big := Abs(covar[j,k]);
                  irow := j;
                  icol := k;
                END;
            END
          ELSE IF (ipiv[k] > 1) THEN
            BEGIN
              Writeln('Pause1 in GAUSSJ - singular matrix');
              Readln;
            END;
          END;
        END;
      END;
    END;
  ipiv[icol] := ipiv[icol]+1;
  IF (irow <> icol) THEN
    BEGIN { begin column interchange, if necessary }
      FOR l := 1 TO n DO
        BEGIN
          dum := covar[irow,l];
          covar[irow,l] := covar[icol,l];
          covar[icol,l] := dum;
        END;
      FOR l := 1 TO m DO
        BEGIN
          dum := oneda[irow,l];
          oneda[irow,l] := oneda[icol,l];
          oneda[icol,l] := dum;
        END;
      END;
    END; { end column interchange }
  indxr[i] := irow;
  indxc[i] := icol;
  IF (covar[icol,icol] = 0.0) THEN
    BEGIN
      Writeln('Pause 2 in GAUSSJ - singular matrix');
      Readln;
    END;
  pivinv := 1.0/covar[icol,icol];
  covar[icol,icol] := 1.0;
  FOR l := 1 TO n DO
    BEGIN
      covar[icol,l] := covar[icol,l]*pivinv;
    END;
  FOR l := 1 TO m DO
    BEGIN
      oneda[icol,l] := oneda[icol,l]*pivinv;
    END;
  FOR ll := 1 TO n DO
    BEGIN { begin row reduction }
      IF (ll <> icol) THEN
        BEGIN
```

```

        dum := covar[l1,icol];
        covar[l1,icol] := 0.0;
        FOR l := 1 TO n DO
        BEGIN
            covar[l1,l] := covar[l1,l]-covar[icol,l]*dum;
        END;
        FOR l := 1 TO m DO
        BEGIN
            oneda[l1,l] := oneda[l1,l]-oneda[icol,l]*dum;
        END;
    END;
END; { end row reduction }
END; { end column reduction }
FOR l := n DOWNTO 1 DO
BEGIN { begin column unscramble }
    IF (indxr[l] <> indxc[l]) THEN
    BEGIN
        FOR k := 1 TO n DO
        BEGIN
            dum := covar[k,indxr[l]];
            covar[k,indxr[l]] := covar[k,indxc[l]];
            covar[k,indxc[l]] := dum;
        END;
    END;
END; { end column unscramble }
END; { end procedure GaussJ }

PROCEDURE IVGraph;
(* Plots I-V data and model data as Current (Amps) vs. Voltage *)
(* (Volts), and prints the fitted parameters. Prints a hardcopy *)
(* if desired. *)
VAR
    hcopy: char;
    year, month, day, doweeek: word;
    lststr: glstr;
    yrstr, mostr, dystr: string;
    nstrin, testrin, tistrin, vpstrin, lstrin, vfstr, vtstr: string;
    nstrout, testrout, tistrout, vpstrout, lstrout, errstr, numstr: string;
    model: plotarray;
BEGIN { begin procedure IVGraph }
    GetDate(year,month,day,doweeek); { get date }
    Str(year:4,yrstr); { convert date parameters to strings }
    Str(month:2,mostr);
    Str(day:2,dystr);
    Str(init[1]:11,nstrin); { convert initial parameters to strings }
    Str(init[2]:9:3,testrin);
    Str(init[3]:9:3,tistrin);
    Str(init[4]:9:3,vpstrin);
    Str(init[5]:9:3,lstrin);
    Str(init[7]:9:3,vtstr);
    Str(fin[1]:11,nstrout); { convert final parameters to strings }
    Str(fin[2]:9:3,testrout);
    Str(fin[3]:9:3,tistrout);
    Str(fin[4]:9:3,vpstrout);
    Str(fin[5]:9:3,lstrout);
    Str(fin[6]:9:3,vfstr);
    Str(fin[9]:11,errstr);
    Str(numlist:1,numstr);
    FOR j := 1 TO numlist DO Str(list[j]:1,lststr[j]);

```

```
GenPoly(x,coeff,numpts,model); { generate array for model data }
EnterGraphic; { enter graphics mode }
SetHeaderOn;
DefineWindow(1,1,1,XMaxGlb,YMaxGlb); { background window }
DefineHeader(1,'LEVENBERG-MARQUARDT MODELLER');
DefineWorld(1,0,0,100,100);
SelectWorld(1);
SelectWindow(1);
DrawBorder;
DrawTextW(17,3,1,filename); { write file name }
DrawTextW(49,3,1,dystr); { write date }
DrawTextW(51,3,1,'/');
DrawTextW(52,3,1,mostr);
DrawTextW(54,3,1,'/');
DrawTextW(55,3,1,yrstr);
DrawTextW(77,9,1,'INITIAL ESTIMATES:'); { write initial guesses }
DrawTextW(77,12,1,'DENSITY   =');
DrawTextW(88,12,1,nstrin);
DrawTextW(77,15,1,'e- TEMP.  =');
DrawTextW(88,15,1,testrin);
DrawTextW(77,18,1,'i+ TEMP.  =');
DrawTextW(88,18,1,tistrin);
DrawTextW(77,21,1,'PLASMA POT.=');
DrawTextW(88,21,1,vpstrin);
DrawTextW(77,24,1,'LINE SLOPE =');
DrawTextW(88,24,1,lstrin);
DrawTextW(77,30,1,'FINAL VALUES:'); { write calculated parameters }
DrawTextW(77,33,1,'DENSITY   =');
DrawTextW(88,33,1,nstrout);
DrawTextW(77,36,1,'e- TEMP.  =');
DrawTextW(88,36,1,testrout);
DrawTextW(77,39,1,'i+ TEMP.  =');
DrawTextW(88,39,1,tistrout);
DrawTextW(77,42,1,'PLASMA POT.=');
DrawTextW(88,42,1,vpstrout);
DrawTextW(77,45,1,'LINE SLOPE =');
DrawTextW(88,45,1,lstrout);
DrawTextW(77,51,1,'FLOAT POT. =');
DrawTextW(88,51,1,vfstr);
DrawTextW(77,57,1,'STD. DEV.  =');
DrawTextW(88,57,1,errstr);
DrawTextW(77,63,1,'TRUNC. VOLT.=');
DrawTextW(88,63,1,vtstr);
DrawTextW(77,69,1,'COEFFICIENTS VARIED:');
DrawTextW(22,96,1,'H for Hardcopy, Else hit <return>');
FOR j := 0 TO numlist-1 DO DrawTextW(80+2*j,72,1,lststr[j+1]);
DrawTextW(80+2*numlist,72,1,'of');
DrawTextW(82+2*numlist,72,1,numstr);
DefineWindow(2,2,30,XMaxGlb-25,YMaxGlb-30); { foreground window }
DefineHeader(2,'MEASURED and MODEL I-V CURVES');
DefineWorld(2,-50,-102e-6,50,102e-6);
SelectWorld(2);
SelectWindow(2);
DrawBorder;
SetClippingOn; { prevents screen crashes }
DrawLine(-50,0,50,0); { V axis }
DrawLine(0,-102e-6,0,102e-6); { I axis }
FOR k := -4 TO 4 DO { axis tick marks }
BEGIN
```

```
DrawLine(-1,20e-6*k,1,20e-6*k);
DrawLine(10*k,-2e-6,10*k,2e-6);
END;
DrawTextW(-40,-60e-6,1,'Vertical Axis = I'); { axis labels }
DrawTextW(-40,-55e-6,1,'(20 micro-Amps/div.)');
DrawTextW(-40,-40e-6,1,'Horizontal Axis = V');
DrawTextW(-40,-35e-6,1,'(10 Volts/div.)'); { draw raw data (next line) }
FOR j := 1 TO numin DO DrawPoint(x[j],-y[j]); { draw raw data }
DrawLine(init[7],-102e-6,init[7],102e-6); { draw truncation indicator }
DrawPolygon(model,1,-numpts,0,0,0); { draw model I-V curve }
hcopy := ReadKey;
IF (hcopy = 'h') OR (hcopy = 'H') THEN HardCopy(false,1); { print }
LeaveGraphic; { leave graphics mode }
END; { end procedure IVGraph }
```

```
PROCEDURE GenPoly;
(* Generates the DrawPolygon array from the model OML I-V curve *)
(* parameters. NOTE: after a TGINST.BAT, set MaxPlotGlb in *)
(* GDRIVER.PAS to 1030 from 100 to avoid an "out of range" *)
(* runtime error in this procedure. *)
VAR
  arg: single;
BEGIN { begin procedure GenPoly }
  FOR j := 1 TO numpts DO
  BEGIN
    xy[j,1] := x[j];
    arg := a[3]-a[4]*xy[j,1];
    IF (arg <= 0.0) THEN
    BEGIN
      Writeln('Error in procedure GenPoly at v= ',x[j]:4:2,':');
      Writeln('Negative argument of Sqrt; Hit CTRL-Break to Exit');
      Readln;
    END;
    xy[j,2] := -a[1]*Exp(xy[j,1]/a[2])+Sqrt(arg)-a[5]*xy[j,1];
    { - because y-axis increases downwards }
  END;
END; { end procedure GenPoly }

END. { end unit OML }
```

#### References

1. W.H. Press, B.P. Flannery, S.A. Teukolsky, and W.T. Vetterling, *Numerical Recipes, The Art of Scientific Computing*, Cambridge University Press, Cambridge, England, 1986.
2. J.G. Laframboise and L.W. Parker, "Probe Design for Orbit-Limited Current Collection," *Phys. Fluids* 16, p. 629, 1973.
3. N. Hershkowitz, "How Langmuir Probes Work," in *Plasma Diagnostics Vol. 1; Discharge Parameters and Chemistry*, ed. O. Auciello, D.L. Flamm, p. 113, Academic, Boston, 1989.
4. J.D. Swift and M.J.R. Schwar, *Electrical Probes for Plasma Diagnostics*, Illife, London, 1969.
5. I.H. Hutchinson, *Principles of Plasma Diagnostics*, p. 50, Cambridge University press, Cambridge, U.K., 1987.
6. B.E. Cherrington, "The Use of Electrostatic Probes for Plasma Diagnostics - A Review," *Plasma Chem. Plasma Proc.* 2, p. 113, 1982.